UNIVERSITA' DEGLI STUDI DI SIENA
DIPARTIMENTO DI BIOTECNOLOGIE, CHIMICA E FARMACIA

DOTTORATO DI RICERCA IN:
CHEMICAL AND PHARMACEUTICAL SCIENCES - CICLO XXXIV
COORDINATORE: Prof. MAURIZIO TADDEI

DESIGN OF NOVEL ORGANIC COMPOUNDS FOR THE DEVELOPMENT OF SOLAR ENERGY CONVERSION DEVICES

SETTORE SCIENTIFICO-DISCIPLINARE: CHIM/06

DOTTORANDA:
Carmen Coppola

TUTOR:
Prof.ssa Adalgisa Sinicropi

ANNO ACCADEMICO: 2021/2022

Acknowledgements

I am really grateful to family, starting from my angel, my grandpa Attilio, for being my first supporter. I shared with him every moment of my life and I could have become the person that I am thank to his constant presence and teachings. I would never forget our endless calls every Sunday morning and still there is not a day in which I cannot feel his presence. I would like to thank my mum Elena, my dad Raffaele and my sister Francesca, for their unconditional love, the constant encouragements and for always letting me the opportunity to follow my passions and pursuing my goals. They often blame me for the little time I spend with them, but I take this opportunity to promise that I will do my best to be more present. You are my everything. Still, I would like to thank all the rest of my family, in particular zio Ciro, Sonia, Sabino, Marilisa, and my little *meatballs* Sofia and Vittoria.

I would like to thank my dearest friends Silvia, Rosanna and Carmen for always having the ability to read inside my mind, Jessica and Ludovica for being one soul in three bodies and all my extraordinary friends for their precious time and dedication.

Last but not least, I am really grateful to Mario. Since we met, we started to share every aspect of us ending to create this wonderful covalent bond that right now would require too much energy to break.

Abstract

In the last decades, the global perception of the energy crisis has encouraged the research to the development of novel technologies from renewable sources. In particular, great emphasis has been devoted to solar energy conversion devices. While the international photovoltaic market is still dominated by silicon-based solar cells, perovskite solar cells (PSCs), dye-sensitized solar cells (DSSCs) and luminescent solar concentrators (LSCs) are considered as promising alternative technologies in terms of improved manufacturability and for the possibility to reduce the costs and enhance the light trapping of high efficiency silicon-based solar cells. Additionally, in the last years PSCs have become potentially competitive to silicon-based solar cells for their high efficiency, while DSSCs and LSCs have the great advantage to work under diffused light and they can be easily incorporated into the building-integrated photovoltaics (BIPV). Despite the attractive features, these technologies still present some efficiency and instability issues related to their components. For this reason, the design of novel materials for highly performant and stable solar energy conversion devices has become an attractive and challenging issue involving worldwide researchers. In this context, this thesis addresses the design of novel organic compounds to be employed in PSCs, DSSCs and LSCs. In particular, the design of novel organic i) hole transport materials (HTMs) in PSCs, ii) sensitizers in DSSCs and iii) fluorophores in LSCs has been carried out with the aim of contributing to the development of potentially more efficient devices. To this end, *state-of-the-art* Density Functional Theory (DFT) and Time Dependent Density Functional Theory (TDDFT) methods represent powerful tools for the discovery of promising materials in the solar energy field. Here, they have mainly been applied for the prediction of the most relevant physical-chemical properties of the designed compounds and for the investigation of the structure-property relationships. In such a way it is possible to make an assessment of their suitability to be employed in the aforementioned devices. The outcomes of these studies would provide the fertile ground for future projects that will hopefully contribute to accelerate the research in this field. Indeed, the increased knowledge on the behavior of these materials is the key for boosting the development of solar energy conversion devices in the near future.

Table of Contents

List of Abbreviations

a-Si	Amorphous Silicon
ACQ	Aggregation-Caused Quenching
AIE	Aggregation-Induced Emission
AO	Atomic Orbital
ASEP	Averaged Solvent Electrostatic Potential
BET	Back Electron Transfer
BIPV	Building-Integrated Photovoltaics
BJ	Becke-Johnson
BZ	Brillouin Zone
CB	Conduction Band
CdTE	Cadmium Telluride
CE	Counter Electrode
CIGS	Copper Indium Gallium Selenide
COP	Conference Of Parties
CSP	Concentrating Solar Power
D-A-D	Donor-Acceptor-Donor
D-A-π-A	Donor-Acceptor-π bridge-Acceptor
DFT	Density Functional Theory
DSSC	Dye-Sensitized Solar Cell
DTCT	Dye-to-TiO_2 Charge Transfer
DZ	Double Zeta
DZP	Double Zeta Polarization
D-π-A	Donor-π bridge-Acceptor
ETM	Electron Transport Material
FF	Fill Factor
FTO	Fluorine-doped Tin Oxide
GGA	Generalized Gradient Approximation
GHG	GreenHouse Gas
GTO	Gaussian Type Orbital
HF	Hartree-Fock
HOMO	Highest Occupied Molecular Orbital
HTM	Hole Transport Material

ICCP	Intergovernmental Panel on Climate Change
ICT	Intramolecular Charge Transfer
KS	Kohn-Sham
LDA	Local Density Approximation
LSC	Luminescent Solar Concentrator
LSDA	Local Spin Density Approximation
LUMO	Lowest Unoccupied Molecular Orbital
MAPI	Methylammonium Lead Triiodide
MD	Molecular Dynamics
MLCT	Metal to Ligand Charge Transfer
MM	Molecular Mechanics
MO	Molecular Orbital
NAO	Numerical Atomic Orbital
NIR	Near-Infrared
NREL	National Renewable Energy Laboratory
$O(N)$	Order-N
OPV	Organic Photovoltaics
PBC	Periodic Boundary Conditions
PCE	Power Conversion Efficiency
PCM	Polarizable Continuum Model
PSC	Perovskite Solar Cell
PTZ	Phenothiazine
PV	Photovoltaics
QDPV	Quantum Dot Photovoltaics
RIR	Restriction of Intramolecular Rotation
SCF	Self Consistent Field
STO	Slater Type Orbital
TCO	Transparent Conductive Oxide
TDDFT	Time Dependent Density Functional Theory
TPA	Triphenylamine
VB	Valence Band

Chapter 1. Introductory Remarks

In the very recent years the global awareness of climate change and energy issues has risen. In this regard, Greta Thunberg, the most famous and debated activist for the climate change, has catalyzed the attention of many youngers to environmental problems. Considering the international scenario, many countries have been adopting new policies to limit the use of fossil fuels as primary source for energy production and to contrast greenhouse gases (GHGs) emissions, in particular CO_2 emissions, which are the main responsible for the global warming [1]. As matter of fact, the first real steps in the pathway to the environmental sustainability have been accomplished in 2015. On one side, signed by 190 Parties, the Paris agreement has been adopted during the Paris Climate Conference (COP21), targeting to limit the rise of global surface temperature to well below 2ºC (better if 1.5ºC) compared to pre-industrial levels [2]. On the other side, the United Nations have defined the Sustainable Development Goals for 2030 [3]. Among them, the 7th goal reported in the 2030 Agenda, *"Ensure access to affordable, reliable, sustainable and modern energy for all"*, defines the real need to replace fossil fuels with renewables sources [3].

More recently, the *green* European revolution is dated to 14 July 2021, the day in which the European Member States have adopted a climate legislative package, part of the European Green Deal presented in 2019. In order to achieve the carbon neutrality by 2050, it aims to reduce the greenhouse gas emissions to 55%, to increase the energy efficiency to 36-39% and to increase the renewable share to 40% by 2030 [4]. The European Green Deal is considered a lifeline to left behind the sanitary, emotional, economic and energetic crisis that the world had to face from March 2020, due to Covid-19 pandemic. Because of worldwide lockdowns, the global energy demand decreased by 4% in 2020, mostly affecting oil, coal and gas demand, while the renewable energies demand surprisingly inverted the trend. In fact, their usage increased by 3% in 2020 and, as predicted, it increased to almost 30% in 2021 [5]. However, as consequence of activities recovery after lockdowns, the global energy demand increased again during 2021, together with the fossil fuels request, making the overall scenario dramatic again (Figure 1) [5,6]. Indeed, in the last Intergovernmental Panel on Climate Change (ICCP) report (August 2021) it emerged that the major sources of CO_2 emissions are human activities, which have warmed the climate more than what had been registered in the last 2000 years [7]. For this reason, in the last COP26 held in Glasgow in November 2021,

cooperation between governments, businesses and society has become an imperative to accelerate actions to face the climate crisis [8].

(a)

(b)
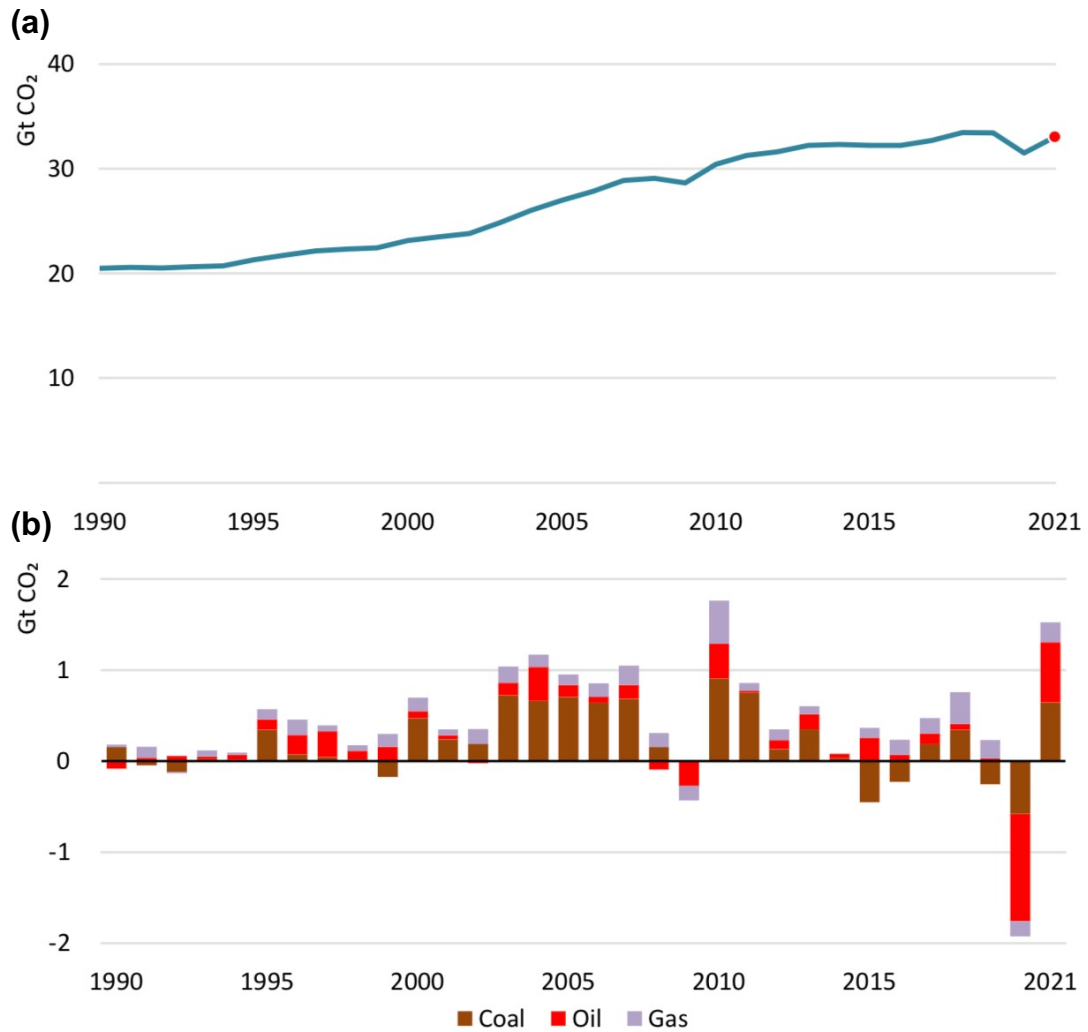
Figure 1. (a) CO_2 emissions related to global energy demand from 1990 to 2021; (b) CO_2 emissions related to fossil fuels exploitation from 1990 to 2021 [5].

The linear dependence between emitted CO_2 and the global warming has also been mathematically proven by Prof. Manabe and Prof. Hasselmann (2021 Nobel Prize in Physics along with prof. Parisi), demonstrating that climate models are consistent, despite the chaotic behavior of weather [9]. It sounds clear that the energy transition is an urgency and an imperative.

As matter of fact, all the scientific community has the responsibility to join forces to accelerate the energy transition. With the aim of developing more efficient technologies

from renewable sources, chemists' work gives a fundamental contribution for the design of novel materials and the investigation of their working principles.

In this context, the research carried out by the PhD candidate has been dedicated to the *in silico* design of novel organic compounds for solar energy conversion devices. To this end, Density Functional Theory (DFT) and Time Dependent Density Functional Theory (TDDFT) methods are universally recognized as powerful computational chemistry methods for the identification of promising materials in the solar energy field. Indeed, they consent to predict their ground- and excited-states properties, such as molecular geometries, molecular orbitals energies, vertical excitations and emission maxima, ground- and excited-states redox potentials. Additionally, these methods can help to clarify the interface phenomena into the devices. Hence, the DFT and TDDFT methods allow the prediction of the main relevant properties of candidates for solar energy conversion devices prior to their synthesis in laboratory. This is essential to save time and raw materials, such as expensive chemicals, accelerating the research in this field and offering strategies for the construction of more efficient devices [10].

In this thesis work, DFT and TDDFT methods have been applied to:

i) the design of a novel family of phenothiazine and triphenylamine-based molecules (**HTM1-4**) through the investigation of the well-known structural and electronic properties that they should possess to be considered as suitable hole transport materials (HTMs) candidates for applications in perovskite solar cells (PSCs);

ii) the study of interfacial phenomena between the MAPI perovskite and **HTM1** to provide new insights into the hole transport mechanism for the construction of potentially more efficient PSCs;

iii) the investigation of the structural, electronic and photophysical properties of novel organic dyes containing the **Indigo core** and the prediction of ground state oxidation potentials of 16 organic dyes, to increase our knowledge on how to design potentially more efficient sensitizers for dye-sensitized solar cells (DSSCs);

iv) the *in silico* characterization of a series of catechol-based molecules, **Cat-I-XV**, to explore their suitability as sensitizers for type-II DSSCs, by investigating the *one-step* and the dye-to-TiO$_2$ charge transfer (DTCT) mechanisms;

v)   the computational study of the structural, electronic and photophysical properties of three novel class of fluorophores, **BBT1-3**, **DQ1-5** and **TPa-c**, characterized by the same peculiar structure Donor-Acceptor-Donor (D-A-D), but endowed by different donor and acceptor groups for applications in thin-film luminescent solar concentrators (LSCs).

This thesis is composed of 5 Chapters, including this Chapter 1: Introductory remarks, and two Appendix sections. Solar energy potentials and the main photovoltaic technologies are presented in Chapter 2. In Section 2.1 perovskite solar cells (PSCs) are described, focusing the attention on hole transport materials (Section 2.1.1). Dye-sensitized solar cells (DSSCs) and luminescent solar concentrators (LSCs) are illustrated in Section 2.2 and Section 2.3, respectively. Chapter 3 is dedicated to the computational methodologies employed. The results obtained during the PhD research work are presented in Chapter 4 proceeded by a description of the candidate's contribution. All the results have been the subject of seven manuscripts (Manuscript 1, 3-8) published in peer-reviewed international journals plus a last one (Manuscript 2) which is to be submitted. Chapter 5 contains the conclusions of this research work. Appendix A includes the description of the main photovoltaic parameters used for the characterization of solar energy devices' performances and Appendix B contains additional published and submitted manuscripts not reported in this thesis.

1.1. References

[1] C. Le Quéré, J.I. Korsbakken, C. Wilson, J. Tosun, R. Andrew, R.J. Andres, J.G. Canadelll, A. Jordan, G.P. Peters, and D.P. van Vuurem, Drivers of declining CO_2 emissions in 18 developed economies, Nat. Clim. Chang. 9, 213–217 (2019). https://doi.org/10.1038/s41558-019-0419-7

[2] Conference of the Parties, Adoption of the Paris Agreement, Dec. 12, 2015, U.N. Doc. FCCC/CP/2015/L.9/Rev/1 (December 2015).

[3] United Nations, Resolution adopted by General Assembly on 25 September 2015–transforming our world: the 2030 Agenda for Sustainable Development, Gen. Assem. 70th Sess. A/RES/70/1, 1-35 (2015).

[4] European Commission, Communication from the Commission to the European Parliament, the European Council, the Council, the European Economic and Social Committee and the Committee of the Regions, The European Green Deal (2019).

[5] IEA (INTERNATIONAL ENERGY AGENCY), Global Energy Review 2021 (April 2021).

[6] M. A. Aktar, M. M. Alamb, and A. Q. Al-Amin, Global economic crisis, energy use, CO_2 emissions, and policy roadmap amid COVID-19, Sustainable Production and Consumption 26, 770–781 (2021). https://doi.org/10.1016/j.spc.2020.12.029

[7] IPCC (INTERGOVERNMENTAL PANEL ON CLIMATE CHANGE), Climate Change 2021: The Physical Science Basis, Working Group I contribution to the Sixth Assessment Report (August 2021).

[8] www.ukcop26.org

[9] "For groundbreaking contributions to our understanding of complex physical systems" Advanced information, NobelPrize.org, Nobel Prize Outreach AB 2021, (October 2021). https://www.nobelprize.org/prizes/physics/2021/advanced-information/

[10] X. Wu, F. Kang, W. Duan, J. Li, Density functional theory calculations: A powerful tool to simulate and design high-performance energy storage and conversion materials, Progress in Natural Science: Materials International 29, 247–255 (2019). https://doi.org/10.1016/j.pnsc.2019.04.003

Chapter 2. Photovoltaic Technologies

The sun has the largest potential to completely fulfil the global energy demand, as it is an inexhaustible and easily accessible source of energy [1]. Indeed, it has been calculated that the energy reaching the Earth in one hour is more than its usage in a year [2]. Even if a proper exploitation of this energy source could contribute to mitigate climate changes, its influence on energy supply is still negligible [3]. In general, solar-based devices are classified in photovoltaic (PV), solar thermal, solar fuels and concentrating solar power (CSP) technologies. PV devices are based on semiconductors materials which exploit the photovoltaic effect to directly convert the sunlight into electrical energy [4]. Electricity generation from PV increased to almost 18% in 2021, approaching 1000 TWh [5]. Considering the active material, PV technologies are classified in three main groups: Generation 1. Crystalline silicon-based solar cells; Generation 2. Thin-film solar cells; Generation 3. Emerging solar cells. Their power conversion efficiencies (PCE) are collected by the National Renewable Energy Laboratory (NREL) in a chart updated every year (Figure 2.1) [6].
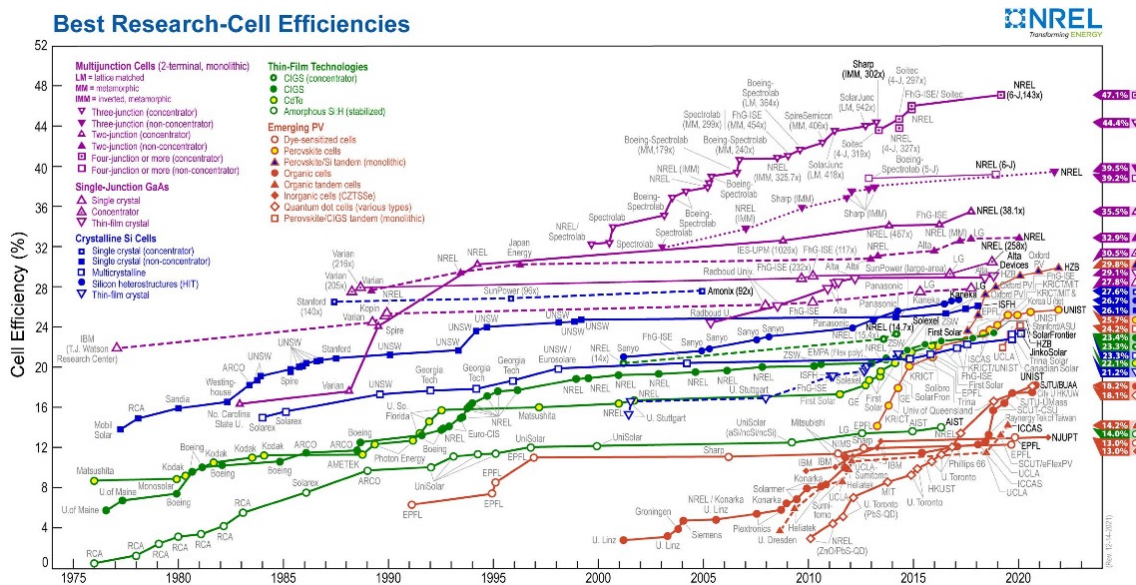
Figure 2.1. Solar cells' efficiency chart [6].

Crystalline silicon (Si)-based solar cells have been the first commercially available PV technology and they present many advantages. First, silicon is non-toxic, and it is the second widely diffused element on the Earth. It has a large refractive index, that makes it an efficient light absorber, and a suitable band gap (1.12 eV), which can be translated into

6

very efficient (up to 26%) and long-lasting (almost 30 years) devices [7]. Silicon can be used in its monocrystalline and polycrystalline forms. In the first case, silicon has a defect-free crystal structure which results in more efficient although more expensive devices than polycrystalline Si-based solar cells which are formed by several small silicon crystals that reduce the overall performance of the devices [8]. In order to diminish global costs, researchers tried to reduce the quantity of the semiconductor employed into the fabrication of cells, giving rise to thin-film solar cells [8]. The most employed semiconductor materials are cadmium telluride (CdTe), copper indium gallium selenide (CIGS), gallium arsenide (GaAs) and amorphous silicon (a-Si). Thin-film solar cells are not only cheaper than crystalline Si-based solar cells, but they are also flexible, which allows their commercialization in independent markets and in the building-integrated photovoltaics (BIPV) market [9]. However, nowadays, their PCE is still low compared to that of crystalline Si-based PV (Figure 2.1) [6]. Hence, to minimize the energy losses and maximize the PCE, multijunction devices made of different semiconductor materials able to absorb different wavelengths of solar radiation have been introduced. Despite their ideal features, their production costs are very high, limiting their commercial applications [10].

In this context, the born of emerging solar cells can be found in the necessity to achieve a balance between high PCE and low costs by using hybrid and abundant materials. Emerging solar cells include a variety of technologies such as perovskite solar cells (PSCs), dye-sensitized solar cells (DSSCs), organic photovoltaics (OPV) and quantum dot photovoltaics (QDPV) [10]. Nowadays, while the international market is still dominated by crystalline Si-based solar cells whose production costs have been gradually diminishing, worldwide research efforts are focused on the improvement of emerging solar cells' technologies in terms of efficiency, stability and scalability.

Additionally, Si-based solar cells have the disadvantage to be efficient only under direct light irradiation and all the unconverted energy becomes heat in excess that should be dissipated in a proper way [11]. In this context and being devices able to work under diffused light, also the luminescent solar concentrators (LSCs) have recently caught great attention within the PV community [12].

2.1. Perovskite Solar Cells

Perovskite solar cells (PSCs) have been introduced in 2009 when lead halide perovskite compounds have been investigated as sensitizers in PV cells, and, since then, their PCE progressed from 3.9% to 25.5% in 2021 [13, 14]. The name perovskite was originally given to the mineral $CaTiO_3$ and nowadays is used to indicate all the materials having the general formula ABX_3 (where A and B are cations, while X is an anion) and having the same crystal structure of $CaTiO_3$. [15]. Among them, organic-inorganic halide-based perovskites have shown suitable electrical and optical properties to be applied in PV technologies. In this case, A is an organic monovalent cation (i.e., $CH_3NH_3^+$, $CH_3CH_2NH_3^+$, $NH_2CHNH_2^+$), B is a divalent cation (i.e., Pb^{2+}, Sn^{2+}, Ge^{2+}), and X are halogen anions (i.e., Cl^-, Br^-, I^-, F^-) [16]. The most common perovskites are the formamidinium lead trihalides, such as $FAPbI_3$, and methylammonium lead trihalides, such as $CH_3NH_3PbI_3$, which is generally known as MAPI. The latter, which has also been used in the simulations done in this PhD thesis' work, is characterized by different structural phases: the cubic at high temperature (T>330 K), the tetragonal at $160 \leq T \leq 330$ K and the orthorhombic at low temperature (T<160 K). The cubic structure has been proven to be the most stable and, in this case, MA and Pb cations coordinate with 6 I anions, creating a PbI_6 octahedral network that occupies the corners of the structure, while MA cations are located among them (Figure 2.2) [15].
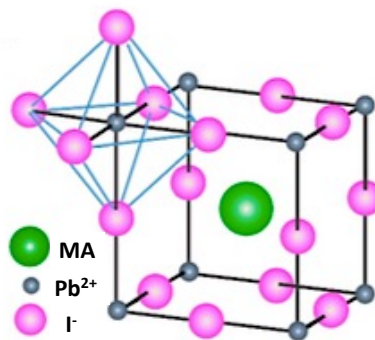
Figure 2.2. MAPI crystal structure, adapted from ref. 15.

The stability of perovskites can be estimated by the tolerance factor t, defining the formation of an ideal cubic structure, and by the octahedral factor μ, determining its distortions (Equations 2.1 and 2.2, respectively):

$$t = \frac{R_A + R_X}{\sqrt{2}(R_B + R_X)} \quad (2.1)$$

$$\mu = \frac{R_B}{R_X} \quad (2.2)$$

where R_A, R_B, and R_x are the ionic radii of A and B cations and X anion, respectively. Generally, perovskites are expected to be stable when $0.8 \leq t \leq 1.1$ and $0.45 \leq \mu \leq 0.89$ [16]. The high PCE of PSCs can be partially related to the unique electronic and optical properties of perovskites. For example, MAPI possesses a tunable band gap of approximately 1.55 eV, strong absorption, weak exciton binding energy and, consequently, good free carriers' mobility [17].

The device architecture of a PSC is characterized by the transparent conductive oxide (TCO), which is generally fluorine-doped tin oxide (FTO), the electron transport material (ETM), the perovskite material, the hole transport material (HTM) and the metal electrode (typically Au, Ag and Al). Two different configurations are available, the first one is called "normal" (n-i-p) (Figure 2.3 (a), (b)) and the second one "inverted" (p-i-n) (Figure 2.3 (c), (d)) depending on the position of the ETM and HTM layers. In both arrangements, the perovskite material can be present in a planar (Figure 2.3 (a), (c)) or in a mesoporous form (Figure 2.3 (b), (d)). The planar form, which has demonstrated to be easier to produce, consists of a compact nanometer perovskite layer, while in the mesoporous configuration the perovskite is deposited on TiO_2 (Figure 2.3) [18].

(a) n–i–p planar	(b) n–i–p mesoporous	(c) p–i–n planar	(d) p–i–n mesoporous
Metal anode	Metal anode	Metal cathode	Metal cathode
HTM	HTM	ETM	ETM
Perovskite	Perovskite	Perovskite	Perovskite
ETM	ETM	HTM	HTM
TCO (cathode)	TCO (cathode)	TCO (anode)	TCO (anode)
Glass	Glass	Glass	Glass
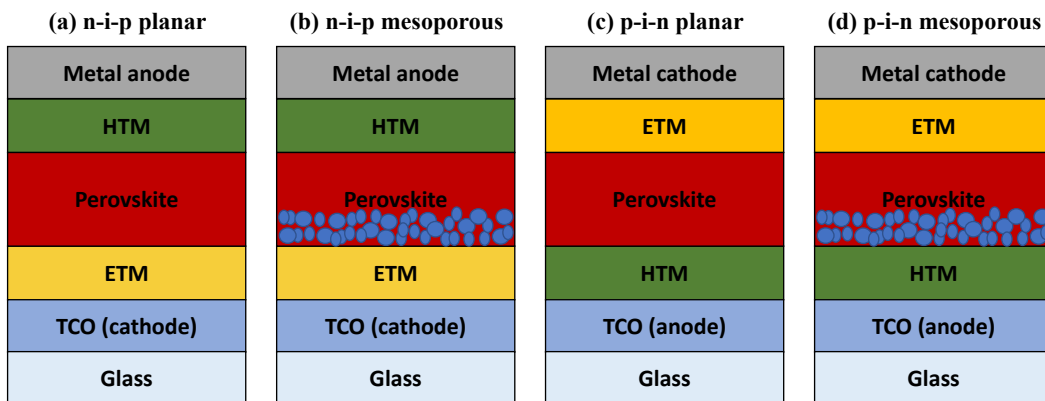
Figure 2.3. Representation of (a) normal planar configuration, (b) normal mesoporous configuration, (c) inverted planar configuration and (d) inverted mesoporous configuration of a PSC.

The working principle of a PSC consists in the photoexcitation of the perovskite that leads to the creation of excitons (electron-hole pairs), followed by the injection of the electrons into the ETM and the injection of the holes into the HTM. Lastly, the charges are collected at their respective electrodes and the current is generated (Figure 2.4) [19].
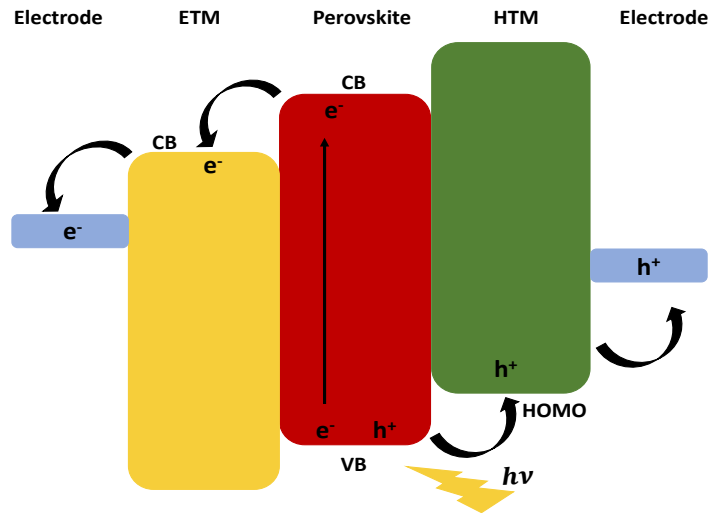
Figure 2.4. Working principle of a PSC.

Nevertheless, some undesired reactions, such as the recombination of photogenerated carriers and the back electron (or hole) transfer to the perovskite, can occur and they are detrimental to the PSCs performances [19]. Regarding performances, the ETM and the HTM materials play a key role. Indeed, n-type semiconductor materials having high carrier mobility fit well for ETMs and can also contribute to prevent the charge recombination. Other important requirements that n-type semiconductor materials should satisfy to be suitable as ETMs are the transparency to the visible light and an appropriate conduction band (CB) alignment, lower than that of the perovskite [19]. Concerning HTMs, they must be able to efficiently extracts the holes from the perovskite and to transport them to the counter electrode, preventing their direct contact, hence the degradation at the metal-perovskite interface. At present, the most employed ETM and HTM are TiO_2 and Spiro-OMeTAD, respectively [15].

PSCs have rapidly caught the worldwide research interest, not only for their high PCE, but also for the potential low costs of raw materials, simple manufacturing techniques and for the possibility to realize flexible devices [20]. However, large-scale PSCs production is still hindered by some environmental drawbacks, mainly deriving from the use of lead in conventional perovskites, and the lack of long-term stability of devices, which is

compromised by the rapid degradation of PSCs components. In this regard, the encapsulation technique has been proposed as a strategy to cover, and hence protect, the devices to external agents. Additionally, the encapsulation method has also been proven to be efficient in reducing the Pb release [21]. However, the most valid strategy to overcome instability issues is definitely the optimization of PSCs components, in particular the HTMs, which have demonstrated to largely affect the stability and the efficiency of PSCs. In section 2.1.2. the importance and the main features of HTMs are presented.

2.1.2. Hole transport materials

To guarantee an efficient hole extraction and transport, HTMs should fulfill a series of requirements: the highest occupied molecular orbital (HOMO) of HTMs has to be higher in energy than the valence band (VB) of perovskite (-5.4 eV for MAPI), as well as the lowest unoccupied molecular orbital (LUMO) has to be higher in energy than the CB of perovskite (-3.9 eV for MAPI); they must be transparent to visible light, to avoid the competition with perovskite absorption, and they should have an ideal hole mobility higher than 10^{-3} cm^2 V^{-1} s^{-1}; additionally, they should present chemical and photochemical stability and low-cost preparation methods. Several inorganic molecules, polymers and small organic molecules have been investigated as HTMs [22]. Among inorganic molecules, the most common are nickel oxides (NiO$_x$), copper-based materials, such as CuSCN, CuI, CuO and Cu$_2$O, and transition metal oxides, such as MoO$_3$. Even if these molecules have good hole mobility and a suitable band alignment, they still have poor efficiency compared to conventional PSCs using Spiro-OMeTAD, which can achieve 25.2% of PCE employing FAPbI$_3$ perovskite [14]. Indeed, the highest reached PCE is c.a. 20% and it has been achieved by devices employing NiO$_x$ compounds [15,23]. Concerning polymers, the most employed are poly(3-hexylthiophene) (P3HT), poly (3,4-ethylenedioxythiphene): poly(styrenesulfonate) (PEDOT:PSS) and poly-triarylamine (PTAA). In this case, the molecular weight (MW) of polymers plays a crucial role in affecting the efficiency and the stability of PSCs devices. Indeed, it has been recently demonstrated that doped-PTAA with high MW can achieve more than 20% of efficiency on small cells and more than 17% of efficiency on modules, which are among the best performances for these molecules [24]. Even if the aforementioned HTMs are under widespread investigation, those made of small organic molecules are by far the most

explored, due to the possibility to tune their optoelectronic properties thanks to appropriate design rules. The most commonly used small organic molecule is Spiro-OMeTAD, (2,2',7,7'-tetrakis[*N,N*-di(4-methoxyphenyl)amino]- 9,9'-spirobifluorene), employed for the first time in DSSCs [25]. Its molecular structure (Figure 2.5) consists of two extended π-systems linked to a carbon sp^3 hybridized atom. The dimethoxydiphenylamines (DPA-OMe) moieties are responsible for the molecule's donor properties and the OMe groups can act as binding sites to the perovskite [26].
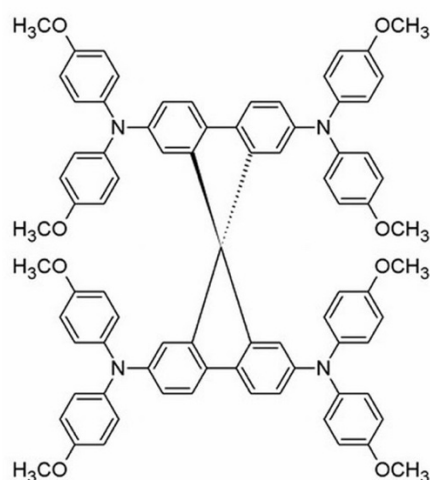
Figure 2.5. Spiro-OMeTAD molecular structure.

Until now, Spiro-OMeTAD is the most popular HTM employed in high efficiency PSCs. Indeed, its energy levels are well aligned with common perovskites, it is soluble in many organic solvents, and it has high melting temperature, which is fundamental for the thermal stability of PSCs. Nevertheless, as it shows low conductivity and hole mobility, it requires the addition of dopants, such as lithium bis(trifluoromethanesulfonyl)imide (LiTFSI) and 4-tert-butylpyridine (TBP), to enhance its electrical properties. Anyway, these dopants are detrimental to the stability of PSCs devices: LiFTSI has the tendency to absorb water and it aggregates in Spiro-OMeTAD films, affecting the interfacial energy levels, while TBP corrodes the perovskite and it has the tendency to evaporate over time [27]. For this reason, many doped or dopant-free spiro-liked HTMs, and HTMs based on triphenylamines (TPA), phenothiazines (PTZ), carbazoles, thiophenes, phenoxazines and triazines have been proposed. In particular, great research interest has been devoted to TPA moieties, for their unique hole transport properties, and to PTZ unit, which has an electron-donating butterfly structure that produces stable radical cations

[28]. In particular, HTMs based on a combination of TPA and PTZ-moieties, such as the **PTZ2** compound reported by Grisorio et al. [29], have shown efficiencies comparable to those obtained employing Spiro-OMeTAD. With the aim of contributing to the development of potentially more efficient HTMs, in this research work the design of four novel TPA and PTZ-based HTMs (**HTM1-4**) has been carried out. The molecular and electronic properties of **HTM1-4** have been deeply investigated by means of DFT and TDDFT methods and the results are reported in Section 4.1 of Chapter 4.

Nowadays, even if a wide library of organic HTMs is available, still a deep understanding of their electronic features at the interface with the perovskite is missing. Indeed, considering the statement *"the interface is the device"*, it is evident that the optimization of the interfacial phenomena is also essential to guarantee a further development of PSCs devices in terms of efficiency and stability [18]. As matter of fact, it is well known that a correct energy-levels alignment between the perovskite and the HTM directly drives the charge extraction and transfer. Moreover, it can largely influence the open-circuit voltage (V_{oc}) of the cells [30]. Even if MAPI is the most popular perovskite, the adsorption mechanisms at MAPI/organic HTMs interface is still not fully understood and it has never been explored for HTMs based on both TPA and PTZ moieties. In this regard, the electronic properties of the recently designed **HTM1** have been studied at the interface with MAPI by means of DFT-D3 method. The same kind of investigation has also been carried out considering the *state-of-the-art*, Spiro-OMeTAD, and well-known TPA and PTZ-based HTMs, with the aim of providing additional knowledge on the interfacial phenomena. The results of this study are presented in Section 4.2 of Chapter 4.

2.2. Dye-Sensitized Solar Cells

A *Nature* paper of 1991 by Michel Grätzel and co-workers sets off the born of dye-sensitized solar cells (DSSCs), also known as Grätzel cells, which showed PCE of 7-8% [31]. Since then, the efficiency of these devices has not improved a lot and the last certified one is 13% [6, 32]. At the beginning DSSCs were presented as a low-cost technology in comparison to silicon PV, but in the recent years the manufacturing costs of Si-based solar cells are diminished, thanks to a cooperation between the Chinese manufacturing and the support of US investors [33]. However, DSSCs are characterized by basic manufacturing processes based on low-costs and scalable raw materials and, in comparison to Si-based solar cells, they show the great advantage to work well also under ambient and diffused light at high temperature. For these reasons, they find application as a low-power technology in electronic devices, aesthetic devices powering lamps, environmental and security sensors and, in general, in *smart* objects for indoor applications. Moreover, they consent the realization of flexible and colorful devices that allow their integration into building-integrated photovoltaics (BIVP) [2]. All these applications make DSSCs still placeable in the PV market.

The device architecture of a DSSC is composed by the transparent conductive oxide (TCO), generally fluorine-doped tin oxide (FTO), deposited on a glass substrate, the nanocrystalline semiconductor, the sensitizer (dye), the redox electrolyte and the counter electrode [34]. The electrical current in DSSCs can be generated following two different electron injection pathways, according to which they can be classified in type-I or type-II DSSCs [35]. The working principle of type-I DSSCs, which is characterized by a "two-step" or "indirect" electron injection mechanism, is based on the photoexcitation of the dye that promotes the electrons from the ground-state to the excited-state. Then, the excited electrons are injected into the CB of the semiconductor, from which they diffuse to the photoanode (FTO) and, through an external circuit, they arrive to the counter electrode generating the current. The oxidized dye is in contact with the electrolyte, which contains the redox couple that regenerates the dye, oxidizing itself. Then, the regeneration of the redox couple occurs at the counter electrode (Figure 2.6).
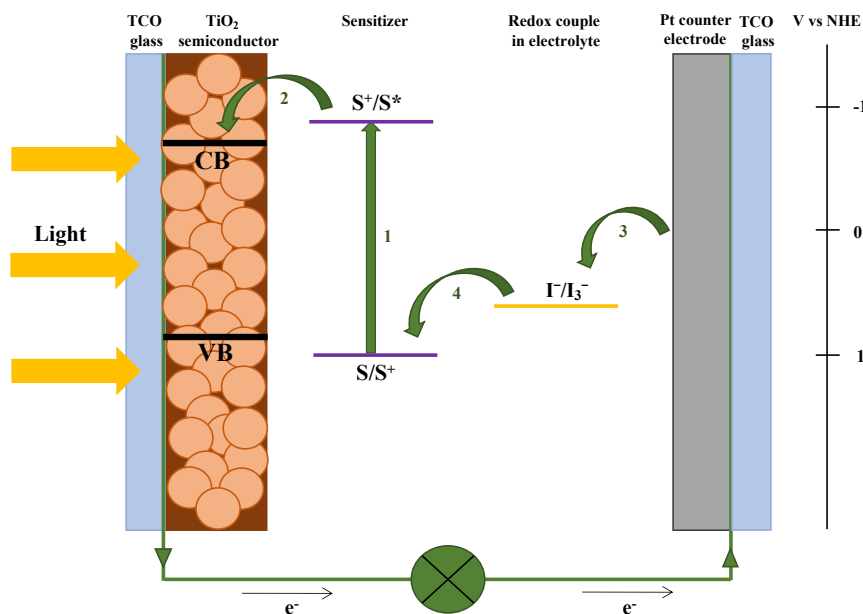
Figure 2.6. Working principle of a type-I DSSC.

Nevertheless, some undesired reactions can occur, and they involve the recombination of excited electrons from the CB of semiconductor to the HOMO of the oxidized dye or to the oxidized form of the redox couple into the electrolyte. To avoid electrons recombination phenomena, it is important to adjust the kinetic of fundamental reactions and, consequently, the choice of DSSCs components is crucial to achieve improved performances [36].

Since now, the most employed semiconductor has been a network of TiO_2 nanoparticles in their anatase crystal structure, having an indirect band gap of 3.2 eV. This arrangement is characterized by 50% of porosity and it allows a better adsorption of the dye molecule [34]. On the other side, the electrolytes should be chemically stable solvents (generally organic solvents or ionic liquids), capable to dissolve the redox couple. The first employed redox mediator was iodide/triiodide (I^-/I_3^-), as it presents a series of advantages. First, it shows a suitable redox potential allowing the regeneration of many dyes, it has good stability, and it can be solubilized by lots of organic solvents. However, I^-/I_3^- also presents some drawbacks, such as absorption in the 400–500 nm range of the visible spectrum and it can corrode some DSSCs components. For these reasons, alternative electrolyte compositions have been explored, such as copper redox shuttles, transition metal coordination complexes and iodine-free electrolytes [36].

The counter electrode (CE) should have a correct energy alignment and high catalytic activity to the electrolyte's redox couple. Moreover, it should have high conductivity, reflectance and low costs. Since now, platinum (Pt) fulfills most of these requirements, but it is a rare material and it has high costs. Hence, alternative CE have been proposed, such as carbon-based materials and conductive polymers [37].

The core of DSSCs is represented by the sensitizer, which is responsible for light absorption. An efficient photosensitizer should have the absorption spectrum covering the whole visible and even part of the near-infrared (NIR) regions. It should have suitable anchoring groups to be adsorbed on the semiconductor surface and it should be electrochemically and thermally stable. In order to ensure the adequate driving force for the electron injection into the semiconductor, the LUMO energy level of the sensitizer has to be higher (more negative) than the CB of the semiconductor. Additionally, to ensure the adequate driving force for the regeneration of the oxidized sensitizer, its HOMO energy level has to be lower (more positive) than the redox potential of the redox mediator (0.4 vs NHE for I^-/I_3^-) [35]. Based on these requirements, many sensitizers have been proposed in literature and they can be classified in two main classes: metal complexes sensitizers and metal free sensitizers (or organic sensitizers). The formers have been crucial to the early development of DSSCs, they are still used as benchmark materials and some of them have also been commercialized. Their structure consists of a central metal ion with auxiliary ligands. The metal ion is responsible for the light absorption through a metal to ligand charge transfer (MLCT) transition, while the overall photo and electrochemical properties of the sensitizer can be tuned by introducing different substituents to ligands. The most adopted are Ru(II) complexes, as well as porphyrin- and phthalocyanine-based complexes [38]. As an alternative to metal complexes, the organic sensitizers (e.g., the standard D5) include low-cost and more environmentally friendly organic molecules that can be synthetized from a wide range of raw materials. Most of them are characterized by the peculiar structure donor group-π bridge-acceptor group (D-π-A) that consents to tune the photophysical and electrochemical properties of the dyes by exploring a wide array of D and A substituents. Indeed, the increase of the electron-donating and the electron-accepting abilities of D and A, respectively, results in a decrease of the HOMO-LUMO energy gap with a consequent redshifting of absorption. The photoabsorption in D-π-A sensitizers is associated with an intramolecular charge transfer (ICT) transition from the donor to the acceptor moiety that promotes a rapid injection of the electron into the CB of the semiconductor. In figure 2.7

a schematic representation of the photoabsorption process in organic sensitizers is illustrated, taking as reference the molecular structure of the D5 dye.
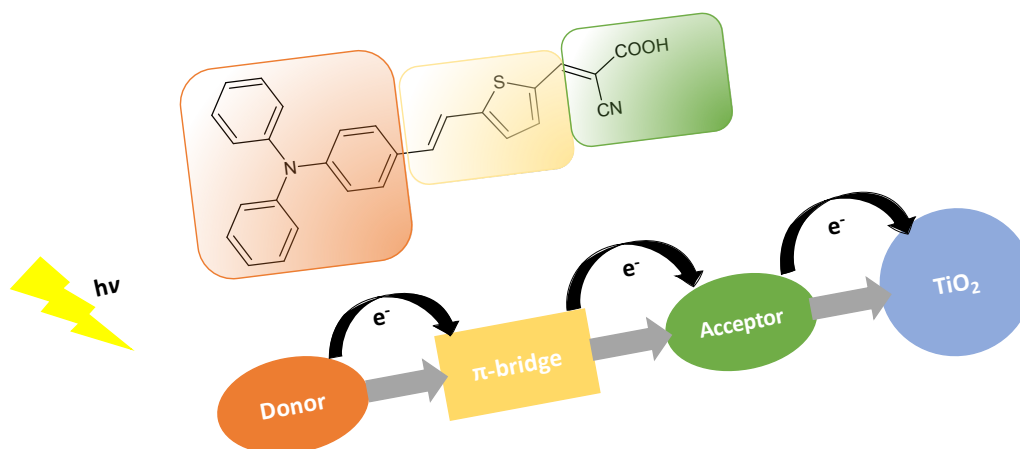
Figure 2.7. Schematic representation of D-π-A structure of organic sensitizers.

The absorption properties and the energy levels of organic dyes can be modulated adding auxiliary electron-acceptor units, giving rise to D-A-π-A motif [39]. Sensitizers having this molecular structure are characterized by blue and green colors and they have been demonstrated to enhance the photovoltaic performances of DSSCs, as well as their commercial appeal [40].

In the context of this thesis, to assess the possibility of using the Indigo scaffold for the design of green dyes for DSSCs application, a novel organic Indigo-based dye bearing D-A-π-A motif, has been designed. The results of the theoretical investigation, carried out by using DFT and TDDFT methods, and the experimental characterization are reported in Section 4.3 of Chapter 4, together with the results obtained from the design of novel Indigo-based dyes having donor-acceptor-donor (D-A-D) structure. Additionally, as previously reported, the correct energy levels alignment between the dye and the redox couple is one of the main parameters that influence the overall DSSCs performances, hence the prediction of ground-state redox potentials of the photosensitizers can help to identify the most promising candidates for such application. In this regard, the ground-state redox potentials of 16 organic D-π-A and D-A-π-A dyes have been computed by means of DFT and TDDFT methods and compared with the available experimental data. The results are shown in Section 4.4 of Chapter 4.

2.2.1. Type-II Dye-Sensitized Solar Cells

Differently from type-I DSSCs, where the electron is injected into the CB of the semiconductor after the photoexcitation of the dye ("two-step" or "indirect" mechanism), type-II DSSCs are characterized by a "one-step" or "direct" electron injection mechanism. Indeed, the electron is directly injected from the HOMO of the sensitizer into the CB of the semiconductor by photoexcitation of the dye-to-TiO$_2$ charge transfer (DTCT) bands [41]. This pathway is faster than the indirect mechanism and it is shown in Figure 2.8.
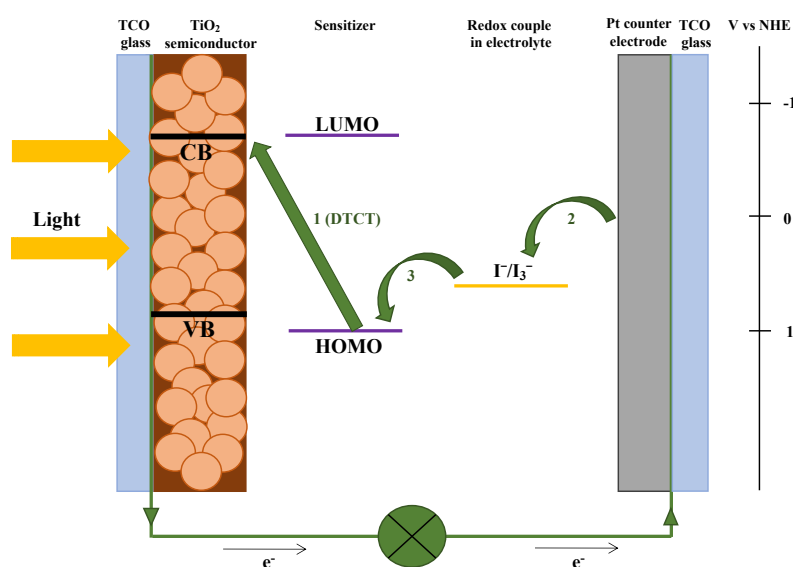
Figure 2.8. Working principle of a type-II DSSC.

The most explored type-II sensitizers are catechol-based compounds, known as Cat-dyes, (e.g. dopamine and fluorone), as well as natural pigments (e.g. Bromopyrogallol Red and anthocyanins), which are all characterized by the DTCT bands in the visible region upon binding to TiO$_2$ [42]. For this reason, they are able to absorb a wide spectral range of sunlight. In contrast to type-I DSSCs, the efficiency of type-II DSSCs is not affected by the correct energy levels alignment between the LUMO of the sensitizer and the CB of the semiconductor, but it is determined by a suitable interfacial level alignment between the HOMO of the dye and the CB of the semiconductor [43]. However, despite the promising light-harvesting capabilities of type-II dyes, the PCE of type-II DSSCs is still very low compared to that of type-I DSSCs, as it never exceeded the 2.5%. Additionally, the back electron transfer (BET) for type-II mechanism is faster than that of type-I [44]. Trying to overcome these problems, several Cat-dyes have been proposed in literature,

with the aim of investigating their performances on type-II mechanism. In particular, from theoretical and experimental studies, it emerged that the design of Cat-dyes follows some specific rules: i) moderate or strong electron-donating and electron-withdrawing substituents to the catechol moiety can modulate the electron-injection mechanism; ii) the LUMO of the dye-TiO$_2$ complex should be localized on d orbitals of Ti; iii) the DTCT band should be associated to transitions from the HOMO of the dye to unoccupied orbitals of the dye-TiO$_2$ complex, formed by the interaction between d orbitals of Ti atoms closest to the catechol-moiety and p orbitals of catechol oxygen atoms; iv) the HOMO of the dye should be well aligned with the CB of TiO$_2$ to slower the BET [44-47]. Moreover, it has been found that some dyes can present an intermediate charge injection mechanism between pure type-I and pure type-II, upon varying the dye conjugation in the anchoring group [48]. In this context and with the aim of increasing the knowledge about the one-step mechanism and the DTCT features, 15 Cat-dyes have been designed for a possible application in type-II DSSCs. The effect of substituents in different positions and the effect of conjugation due to the introduction of an ethylene π spacer have been investigated by means of DFT and TDDFT methods. The results of this study are reported in Section 4.5 of Chapter 4.

2.3. Luminescent Solar Concentrators

The idea of concentrating the solar radiation to lower the price of PV has born at the end of 1970s [49, 50]. In that context, luminescent solar concentrators (LSCs) have been introduced as devices able to concentrate direct and diffused solar radiation on small PV cells, reducing the number of photoactive materials, while preserving their overall efficiency. These outstanding features make them exploitable also in cloudy weather countries [12, 51]. A LSC consists of a plastic or a glass matrix containing a dispersed luminophore, which is able to absorb direct and indirect solar radiation and to re-emits it at longer wavelengths. Thanks to the refraction index of the matrix material, which is higher than that of the air, the emitted photons, through total internal reflection, are concentrated in solar cells placed at the edge of the collector and the electricity is then generated (Figure 2.9) [52].
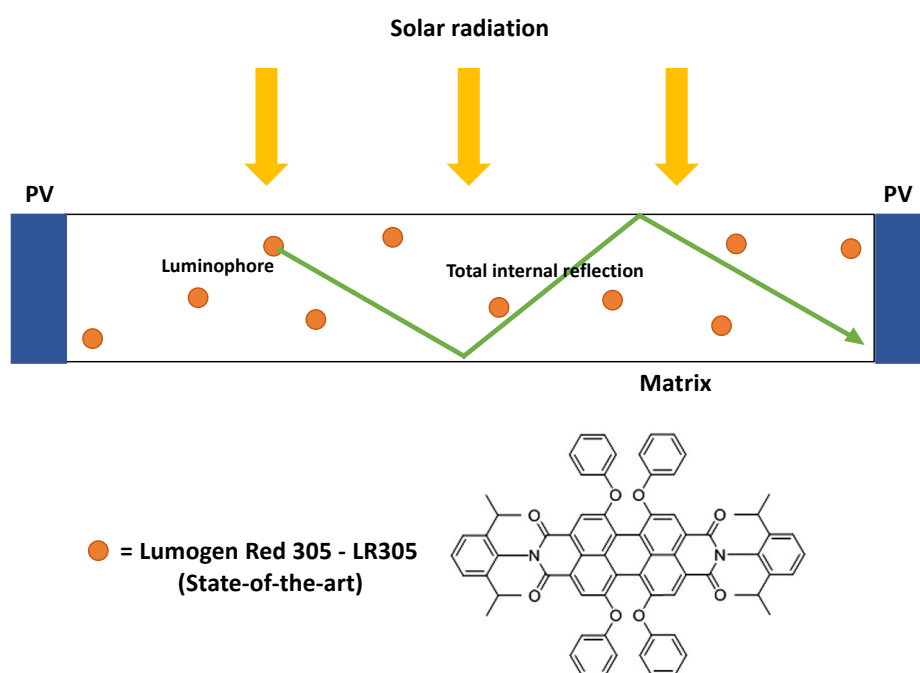
Figure 2.9. Working principle of a LSC.

After 20 years in which they have been almost overlooked, in the early 2000s the interest in LSCs has reawaken again in a global context characterized by decreased PV prices [12]. Hence, nowadays the research on LSCs is essentially oriented to the optimization of the fluorophores and the matrix [52], while their aesthetic features make them active

actors in the *green architecture revolution.* Indeed, they consent the realization of transparent and colorful devices that drive their application in the BIPV market [53].

Regarding the matrix, the most employed is the poly(methyl methacrylate) (PMMA), which has high refractive index, it is transparent, and it has a good compatibility with lots of fluorophores, contributing to achieve good performances. Additionally, during the past years, the research has devoted great attention towards biopolymers and biomaterials obtained from renewable sources or through more ecofriendly processes, which would further help the integration of LSCs in modern urban areas [54, 55].

Concerning the fluorophores, they are key components to realize highly performant LSCs, and they should fulfill several requirements. Indeed, they should have: i) wide absorption range, ii) high fluorescence quantum yield, that is the number of emitted photons with respect to those absorbed, iii) large Stokes shift, in order to limit the overlap between the absorption and the emission spectra, iv) long-term thermal and photo-stability, v) good solubility in the host matrix [56]. Several fluorophores have been reported in literature, such as quantum dots, colloidal nanocrystals, rare earths complexes and organic molecules [57-60]. Among them, organic molecules are the most investigated, because their optical properties can be easily modulated by changing the nature of functional groups to reach high quantum yield and absorption coefficients. Most of them are based on coumarins, rhodamines, bipyridines, phthalocyanines, BODIPY oligomers and benzothiadiazoles [61-63]. The *state-of-the-art is* represented by the Lumogen Red 305 (LR305, Figure 2.9) [12], which has a quantum yield≈ 97% in PMMA and its red emission is well matched with the bandgap of Si-based solar cells (≈ 1.1 eV). However, it has a small Stokes Shift, which can lead to the reabsorption of emitted photons by neighboring luminophores [64].

With the aim of developing more efficient fluorophores having absorption and emission in different spectral ranges, hence high Stokes Shift, in this thesis two novel series of D-A-D fluorophores are presented. In particular, the molecules of the first series have the benzo[1,2-*d*:4,5-*d'*]bisthiazole (BBT) acceptor core, while the molecules of the second series are endowed with the quinoxaline acceptor scaffold. The fluorophores of both series carry different donor groups. The electronic properties of these compounds have been investigated by means of DFT and TDDFT methods (Sections 4.6 and 4.7 of Chapter 4).

The reabsorption of emitted photons is quite a common feature in red-emitting organic fluorophores, and it can limit the generation of electric current by the PV cells. For this

reason, near-infrared (NIR) emissive fluorophores, with emissions beyond 750 nm, have been proposed as alternatives for LSCs applications. They are generally based on donor-acceptor (D-A) structures, which are characterized by charge-transfer excited states and small bandgaps. However, due to the rigid conjugated structure, they can be responsible for the aggregation-caused quenching (ACQ) phenomenon, which can limit their application in the solid state. The solution to this problem has been found with the introduction of aggregation-induced emission (AIE) molecules, which have a non-emissive behavior when dissolved in good solvents but became highly luminescent in poor solvents or in solid state. This phenomenon is caused by the restriction of the intramolecular rotation (RIR) that affects molecules in solid state, hence their limited molecular motions bring to energy dissipation through radiative decay [65-67]. For this reason, in the last years the research on LSCs has been mainly focused on the development of novel NIR fluorophores having AIE properties.

In this context, in Section 4.8 of Chapter 4 are reported the results of the theoretical and the experimental investigation of a novel class of NIR emitting AIEgens featuring D-A-D structure. These luminophores have been endowed with a thieno[3,4-*b*]pyrazine acceptor core, while the donor group is represented by a triarylamine unit carrying the tetraphenylethylene (TPE) moiety, whose introduction is a common strategy to increase the emission from the condensed phase.

2.4. References

[1] N. Kannan, and D. Vakeesan, Solar energy for future world: - A review, Renewable and Sustainable Energy Reviews 62, 1092-1105 (2016). http://dx.doi.org/10.1016/j.rser.2016.05.022

[2] A. B. Muñoz-García, I. Benesperi, G. Boschloo, J. J. Concepcion, J. H. Delcamp, E. A. Gibson, G. J. Meyer, M. Pavone, H. Pettersson, A. Hagfeldt, and M. Freitag, Dye-sensitized solar cells strike back, Chemical Society Reviews 50, 12450-12550 (2021). https://doi.org/10.1039/D0CS01336F

[3] E. Kabir, P. Kumar, S. Kumar, A. A. Adelodun, and K.H. Kim, Solar energy: Potential and prospects, Renewable and Sustainable Energy Reviews 82, 894-900 (2018). http://dx.doi.org/10.1016/j.rser.2017.09.094

[4] A. Einstein, The Quantum Theory of Radiation, Physikalische Zeitschrift 18, 121–128 (1917).

[5] IEA (INTERNATIONAL ENERGY AGENCY), Global Energy Review 2021 (April 2021).

[6] NREL. Best Research-Cell Efficiency Chart. (Accessed January 2022). https://www.nrel.gov/pv/assets/pdfs/best-research-cell-efficiencies-rev211214.pdf

[7] J. Singh, and A. Agrahari, The progression of silicon technology acting as substratum for the betterment of future photovoltaics, International Journal of Research Energy 43, 3959–3980 (2019). https://doi.org/10.1002/er.4402

[8] E. Pulli, E. Rozzi, and F. Bella, Transparent photovoltaic technologies: Current trends towards upscaling, Energy Conversion and Management 219, 112982 (2020). https://doi.org/10.1016/j.enconman.2020.112982

[9] J. Ramanujam, D. M. Bishop, T. K. Todorov, O. Gunawan, J. Rath, R. Nekovei, E. Artegiani, and A. Romeo, Flexible CIGS, CdTe and a-Si:H based thin film solar cells: A review, Progress in Materials Science 110, 100619 (2020). https://doi.org/10.1016/j.pmatsci.2019.100619

[10] S. Ghosh, and R. Yadav, Future of photovoltaic technologies: A comprehensive review, Sustainable Energy Technologies and Assessments 47, 101410 (2021). https://doi.org/10.1016/j.seta.2021.101410

[11] G. M Wilson, M. Al-Jassim, W. K Metzger, S. W Glunz, P. Verlinden, G. Xiong, L. M. Mansfield, B. J. Stanbery, K. Zhu, Y. Yan, J. J. Berry, A. J Ptak, F. Dimroth, B. M. Kayes, A. C. Tamboli, R. Peibst, K. Catchpole, M. O. Reese, C. S. Klinga, P. Denholm,

M. Morjaria, M. G. Deceglie, J. M. Freeman, M. A. Mikofski, D. C. Jordan, G. TamizhMani, and D. B. Sulas-Kern, The 2020 photovoltaic technologies roadmap, Journal of Physics D: Applied Physics 53, 493001 (2020). https://doi.org/10.1088/1361-6463/ab9c6a

[12] J. Roncali, Luminescent Solar Collectors: Quo Vadis?, Advanced Energy Materials 10, 2001907 (2020). https://doi.org/10.1002/aenm.202001907

[13] A. Kojima, K. Teshima, Y. Shirai, and T. Miyasaka, Organometal Halide Perovskites as Visible-Light Sensitizers for Photovoltaic Cells, J. Am. Chem. Soc. 131, 6050–6051 (2009). https://doi.org/10.1021/ja809598r

[14] J. Jeong, M. Kim, J. Seo, H. Lu, P. Ahlawat, A. Mishra, Y. Yang, M. A. Hope, F. T. Eickemeyer, M. Kim, Y. J. Yoon, I. W. Choi, B. P. Darwich, S. J. Choi, Y. Jo, J. H. Lee, B. Walker, S. M. Zakeeruddin, L. Emsley, U. Rothlisberger, A. Hagfeldt, D. S. Kim, M. Grätzel, and J. Y. Kim, Pseudo-halide anion engineering for α-FAPbI$_3$ perovskite solar cells, Nature 592, 381–385 (2021). https://doi.org/10.1038/s41586-021-03406-5

[15] J. Y. Kim, J.-W. Lee, H. S. Jung, H. Shin, and N.-G. Park, High-Efficiency Perovskite Solar Cells, Chem. Rev. 120, 7867−7918 (2020). https://dx.doi.org/10.1021/acs.chemrev.0c00107

[16] P. Roy, N. K. Sinha, S. Tiwari, and A. Khare, A review on perovskite solar cells: Evolution of architecture, fabrication techniques, commercialization issues and status, Solar Energy 198, 665-688 (2020). https://doi.org/10.1016/j.solener.2020.01.080

[17] M. Grätzel, The light and the shade of perovskite solar cells, Nature Materials 13, 838–842 (2014). https://doi.org/10.1038/nmat4065

[18] S. A. Olaleru, J.K. Kirui, D.Wamwangi, K.T.Roro, and B. Mwakikunga, Perovskite solar cells: The new epoch in photovoltaics, Solar Energy 196, 295-309 (2020). https://doi.org/10.1016/j.solener.2019.12.025

[19] D. Zhou, T. Zhou, Y. Tian, X. Zhu, and Y. Tu, Perovskite-Based Solar Cells: Materials, Methods, and Future Perspectives, Journal of Nanomaterials 2018, 8148072 (2018). https://doi.org/10.1155/2018/8148072

[20] M. L. Parisi, and A. Sinicropi, Closing the loop for perovskite solar modules, Nature Sustainability 4, 754-755 (2021). https://doi.org/10.1038/s41893-021-00735-1

[21] S. Maranghi, M. L. Parisi, R. Basosi, and A. Sinicropi, The critical issue of using lead for sustainable massive production of perovskite solar cells: a review of relevant literature [version 1; peer review: 2 approved], Open Research Europe NaN 1, 1-44 (2021). https://doi.org/10.12688/openreseurope.13428.2

[22] P. Vivo, J.K. Salunke, and A. Priimagi, Hole-transporting materials for printable perovskite solar cells, Materials 10, 1-45 (2017). https://doi.org/10.3390/ma10091087

[23] R. Singh, P. K.Singh, B.Bhattacharya, and H.-W. Rhee, Review of current progress in inorganic hole-transport materials for perovskite solar cells, Applied Materials Today 14, 175-200 (2019). https://doi.org/10.1016/j.apmt.2018.12.011

[24] N. Y. Nia, M. Zendehdel, M. Abdi-Jalebi, L. A. Castriotta, F. U. Kosasih, E. Lamanna, M. M. Abolhasani, Z. Zheng, Z. Andaji-Garmaroudi, K. Asadi, G. Divitini, C. Ducati, R. H. Friend, and A. Di Carlo, Beyond 17% stable perovskite solar module via polaron arrangement of tuned polymeric hole transport layer, Nano Energy 82, 105685 (2021). https://doi.org/10.1016/j.nanoen.2020.105685

[25] M. Vasilopoulou, A. Fakharuddin, A. G. Coutsolelos, P. Falaras, P. Argitis, A. R. b. M. Y., and M. K. Nazeeruddin, Molecular materials as interfacial layers and additives in perovskite solar cells, Chem. Soc. Rev. 49, 4496-4526, (2020). https://doi.org/10.1039/C9CS00733D

[26] J. Urieta-Mora, I. García-Benito, A. Molina-Ontoria, and N. Martin, Hole transporting materials for perovskite solar cells: a chemical approach, Chem. Soc. Rev. 47, 8541-8571 (2018). https://doi.org/10.1039/C8CS00262B

[27] G. Ren, W. Han, Y. Deng, W. Wu, Z. Li, J. Guo, H. Bao, C. Liu, and W. Guo, Strategies of modifying spiro-OMeTAD materials for perovskite solar cells: a review, J. Mater. Chem. A 9, 4589-4625 (2021). https://doi.org/10.1039/D0TA11564A

[28] L. M. Nhari, R. M. El-Shishtawya, and A. M. Asiri, Recent progress in organic hole transport materials for energy applications, Dyes and Pigments 193, 109465 (2021). https://doi.org/10.1016/j.dyepig.2021.109465

[29] R. Grisorio, B. Roose, S. Colella, A. Listorti, G. P. Suranna, and A. Abate, Molecular Tailoring of Phenothiazine-Based Hole-Transporting Materials for Highly Performing Perovskite Solar Cells, ACS Energy Lett. 2, 1029–1034 (2017). https://doi.org/10.1021/acsenergylett.7b00054

[30] R. J. E. Westbrook, I. Sanchez-Molina, J. M. Marin-Beloqui, H. Bronstein, and S. A. Haque, Effect of Interfacial Energetics on Charge Transfer from Lead Halide Perovskite to Organic Hole Conductors, J. Phys. Chem. C 122, 1326−1332 (2018). https://doi.org/10.1021/acs.jpcc.7b09178

[31] B. O' Regan, and M. Grätzel, A low-cost, high-efficiency solar cell based on dye-sensitized colloidal TiO_2 films, Nature 353, 737–740 (1991). https://doi.org/10.1038/353737a0

[32] D. Zhang, M. Stojanovic, Y. Ren, Y. Cao, F. T. Eickemeyer, E. Socie, N. Vlachopoulos, J.-E. Moser, S. M. Zakeeruddin, A. Hagfeldt, and M. Grätzel, A molecular photosensitizer achieves a V_{oc} of 1.24 V enabling highly efficient and stable dye-sensitized solar cells with copper(II/I)-based electrolyte, Nat Commun 12, 1777 (2021). https://doi.org/10.1038/s41467-021-21945-3

[33] M. A. Green, How Did Solar Cells Get So Cheap?, Joule 3, 631-633 (2019). https://doi.org/10.1016/j.joule.2019.02.010

[34] A. Hagfeldt, G. Boschloo, L. Sun, L. Kloo, and H. Pettersson, Dye-Sensitized Solar Cells, Chem. Rev. 110, 6595–6663 (2010). https://doi.org/10.1021/cr900356p

[35] Y. Ooyama, and Y. Harima, Photophysical and electrochemical properties, and molecular structures of organic dyes for dye-sensitized solar cells, ChemPhysChem 13, 4032–4080 (2012). https://doi.org/10.1002/cphc.201200218.

[36] H. Iftikhar, G. G. Sonai, S. G. Hashmi, A. F. Nogueira, and P. D. Lund, Progress on Electrolytes Development in Dye-Sensitized Solar Cells, Materials 12, 1998 (2019). https://doi.org/10.3390/ma12121998

[37] J. Wu, Z. Lan, J. Lin, M. Huang, Y. Huang, L. Fan, G. Luo, Y. Lin, Y. Xie, and Y. Wei, Counter electrodes in dye-sensitized solar cells, Chem. Soc. Rev. 46, 5975-6023 (2017). https://doi.org/10.1039/C6CS00752J

[38] C.A. Bignozzi, R. Argazzi, R. Boaretto, E. Busatto, S. Carli, F. Ronconi, S. Caramori, The role of transition metal complexes in dye sensitized solar devices, Coordination Chemistry Reviews 257, 1472-1492 (2013). https://doi.org/10.1016/j.ccr.2012.09.008

[39] Y. Wu, W.-H. Zhu, S. M. Zakeeruddin, and M. Grätzel, Insight into D-A-π-A Structured Sensitizers: A Promising Route to Highly Efficient and Stable Dye-Sensitized Solar Cells, ACS Appl. Mater. Interfaces 7, 9307-9318 (2015). https://doi.org/10.1021/acsami.5b02475

[40] A. Dessì, A. Sinicropi, S. Mohammadpourasl, R. Basosi, M. Taddei, F. Fabrizi de Biani, M. Calamante, L. Zani, A. Mordini, P. Bracq, D. Franchi, and G. Reginato, New Blue Donor–Acceptor Pechmann Dyes: Synthesis, Spectroscopic, Electrochemical, and Computational Studies, ACS Omega 4, 7614-7627 (2019). https://doi.org/10.1021/acsomega.8b03560

[41] Y. Ooyama, K. Yamaji, and J. Ohshita, Photovoltaic performances of type-II dye-sensitized solar cells based on catechol dye sensitizers: retardation of back-electron

transfer by PET (photo-induced electron transfer), Mater. Chem. Front. 1, 2243-2255 (2017). https://doi.org/10.1039/C7QM00211D

[42] Y. Ooyama, T. Yamada, T. Fujita, Y. Harima, and J. Ohshita, Development of D–π–Cat fluorescent dyes with a catechol group for dye-sensitized solar cells based on dye-to-TiO$_2$ charge transfer, J. Mater. Chem. A 2, 8500-8511 (2014). https://doi.org/10.1039/C4TA01286K

[43] D. J. Mowbray, and A. Migani, Optical Absorption Spectra and Excitons of Dye-Substrate Interfaces: Catechol on TiO$_2$ (110), J. Chem. Theory Comput. 12, 2843−2852 (2016). https://doi.org/10.1021/acs.jctc.6b00217

[44] Y.Ooyama, M. Kanda, K. Uenaka, and J. Ohshita, Effect of Substituents in Catechol Dye Sensitizers on Photovoltaic Performance of Type II Dye-Sensitized Solar Cells, ChemPhysChem 16, 3049-57 (2015). https://doi.org/10.1002/cphc.201500419

[45] Y. Ooyama, K.Furue, T. Enoki, M. Kanda, Y. Adachi, and J. Ohshita, Development of type-I/type-II hybrid dye sensitizer with both pyridyl group and catechol unit as anchoring group for type-I/type-II dye-sensitized solar cell, Phys.Chem.Chem.Phys. 18, 30662-30676 (2016). https://doi.org/10.1039/C6CP06513A

[46] Y.-C. Chen, and J. T. Lin, Multi-anchored sensitizers for dye-sensitized solar cells, Sustainable Energy Fuels 1, 969-985 (2017). https://doi.org/10.1039/C7SE00141J

[47] R. Sánchez-de-Armas, M.A. San-Miguel, J. Oviedo, and J. F. Sanz, Direct vs. indirect mechanisms for electron injection in DSSC: Catechol and alizarin, Computational and Theoretical Chemistry 975, 99–105 (2011). https://doi.org/10.1016/j.comptc.2011.01.010

[48] R. Sánchez-de-Armas, J. Oviedo, M.A. San-Miguel, and J. F. Sanz, Direct vs Indirect Mechanisms for Electron Injection in Dye-Sensitized Solar Cells, J. Phys. Chem. C 115, 11293–11301 (2011). https://doi.org/10.1021/jp201233y

[49] W. H. Weber, and J. Lambe, Luminescent greenhouse collector for solar radiation, Applied Optics 15, 2299-2300 (1976). https://doi.org/10.1364/AO.15.002299

[50] A. Goetzbergerand, and W.Greubel, Solar Energy Conversion with Fluorescent Collectors, Applied Physics 14, 123-139 (1977). https://doi.org/10.1007/BF00883080

[51] W. G. J. H. M. van Sark, Luminescent solar concentrators: A low cost photovoltaics alternative, Renewable Energy 49, 207-210 (2013). https://doi.org/10.1016/j.renene.2012.01.030

[52] G. Griffini, Host Matrix Materials for Luminescent Solar Concentrators: Recent Achievements and Forthcoming Challenges, Frontiers in Materials 6, 29 (2019). https://doi.org/10.3389/fmats.2019.00029

[53] F. Meinardi, F. Bruni, and S. Brovelli, Luminescent solar concentrators for building-integrated photovoltaics, Nature Reviews Materials 2, 17072 (2017). https://doi.org/10.1038/natrevmats.2017.72

[54] M. Sottile, G. Tomei, S. Borsacchi, F. Martini, M. Geppi, G. Ruggeri, and A. Pucci, Epoxy resin doped with Coumarin 6: Example of accessible luminescent collectors, European Polymer Journal 89, 23–33 (2017). http://dx.doi.org/10.1016/j.eurpolymj.2017.02.003

[55] T. A. Geervliet, I. Gavrila, G. Iasilli, F. Picchioni, and A. Pucci, Luminescent Solar Concentrators Based on Renewable Polyester Matrices, Chem. Asian J. 14, 877 – 883 (2019). https://doi.org/10.1002/asia.201801690

[56] C. Papucci, T. A. Geervliet, D. Franchi, O. Bettucci, A. Mordini, G. Reginato, F. Picchioni, A. Pucci, M. Calamante, and L. Zani, Green/Yellow-Emitting Conjugated Heterocyclic Fluorophores for Luminescent Solar Concentrators, Eur. J. Org. Chem. 2018, 2657–2666 (2018). https://doi.org/10.1002/ejoc.201800242

[57] F. Meinardi, A. Colombo, K. A. Velizhanin, R. Simonutti, M. Lorenzon, L. Beverina, R. Viswanatha, V. I. Klimov, and S. Brovelli, Large-area luminescent solar concentrators based on 'Stokes-shift-engineered' nanocrystals in a mass-polymerized PMMA matrix, Nature Photonics 8, 392–399 (2014). https://doi.org/10.1038/nphoton.2014.54

[58] J.-C. G. Bünzli, and A.-S. Chauvin, Lanthanides in Solar Energy Conversion, Handbook on the Physics and Chemistry of Rare Earths 44, 169-281 (2014). https://doi.org/10.1016/B978-0-444-62711-7.00261-9

[59] P. Minei, E. Fanizza, A. M. Rodríguez, A. B. Muñoz-García, P. Cimino, M. Pavone, and A. Pucci, Cost-effective solar concentrators based on red fluorescent Zn(II)–salicylaldiminato complex, RSC Adv. 6, 17474–17482 (2016). https://doi.org/10.1039/C5RA23049G

[60] P. Della Sala, N. Buccheri, A. Sanzone, M. Sassi, P. Neri, C. Talotta, A. Rocco, V. Pinchetti, L. Beverina, S. Brovelli, and C. Gaeta, First demonstration of the use of very large Stokes shift cycloparaphenylenes as promising organic luminophores for transparent luminescent solar concentrators, Chem. Commun. 55, 3160-3163 (2019). https://doi.org/10.1039/C8CC09859J

[61] J. Lucarelli, M. Lessi, C. Manzini, P. Minei, F. Bellina, A. Pucci, N-alkyl diketopyrrolopyrrole-based fluorophores for luminescent solar concentrators: Effect of the alkyl chain on dye efficiency, Dyes and Pigments 135, 154-162 (2016). http://dx.doi.org/10.1016/j.dyepig.2016.03.036

[62] G. Albano, T. Colli, T. Bivera, L. A. Aronica, and A. Pucci, Photophysical properties of new p-phenylene- and benzodithiophene-based fluorophores for luminescent solar concentrators (LSCs), Dyes and Pigments 178, 108368 (2020). https://doi.org/10.1016/j.dyepig.2020.108368

[63] N. J. L. K. Davis, R. W. MacQueen, S. T. E. Jones, C. Orofino-Pena, D. Cortizo-Lacalle, R. G. D. Taylor, D. Credgington, P. J. Skabarac, and N. C. Greenham, Star-shaped fluorene–BODIPY oligomers: versatile donor–acceptor systems for luminescent solar concentrators, J. Mater. Chem. C 5, 1952-1962 (2017). https://doi.org/10.1039/C6TC05298C

[64] B. McKenna, and R. C. Evans, Towards Efficient Spectral Converters through Materials Design for Luminescent Solar Devices, Adv. Mater. 29, 1606491 (2017). https://doi.org/10.1002/adma.201606491

[65] A. Barbieri, E. Bandini, F. Monti, V. K. Praveen, and N. Armaroli, The Rise of Near-Infrared Emitters: Organic Dyes, Porphyrinoids, and Transition Metal Complexes, Top Curr Chem (Z) 374, 47 (2016). https://doi.org/10.1007/s41061-016-0048-9

[66] R. Mori, G. Iasilli, M. Lessi, A. B. Muñoz-García, M. Pavone, F. Bellina, and A. Pucci, Luminescent solar concentrators based on PMMA films obtained from a red-emitting ATRP initiator, Polym. Chem. 9, 1168-1177 (2018). https://doi.org/10.1039/C7PY01933E

[67] F. De Nisi, R. Francischello, A. Battisti, A. Panniello, E. Fanizza, M. Striccoli, X. Gu, N. L. C. Leung, B. Z. Tang, and A. Pucci, Red-emitting AIEgen for luminescent solar concentrators, Mater. Chem. Front. 1, 1406-1412 (2017). https://doi.org/10.1039/C7QM00008A

Chapter 3. Computational Methods

The computational chemistry plays a key role in the design of novel materials for solar energy conversion devices. In particular, Density Functional Theory (DFT) methods represent a good compromise between accuracy and computational costs, hence they are largely employed for the prediction of the electronic and the spectroscopical properties of novel compounds in the solar energy field [1].

In this chapter, a brief overview of the theoretical framework concerning the computational methodologies employed in this thesis is given.

3.1. Density Functional Theory

The naissance of Density Functional Theory (DFT) methods can be found in the necessity to finding approaches to solve the time-independent Schrödinger equation for many-electrons systems at lower computational costs with respect to post Hartee-Fock (HF) methods, reaching, however, high accuracy. The time-independent Schrödinger equation is an eigenvalue problem, and it can be written as Eq. 3.1:

$$\hat{H}\Psi = E\Psi \quad \text{(Eq. 3.1)}$$

where $\hat{H}$ is the Hamiltonian, Ψ is the wavefunction and E is the eigenvalue, i.e. the energy of the system. Indeed, post HF methods are wavefunction-based methods, where the wavefunction depends on 4N variables (3 spatial coordinates and 1 spin coordinate), hence its complexity increases exponentially with the number of electrons of the system. On the contrary, using DFT approach, the total energy of a system can be described as a functional of the electron density which is a real-space function with only 3 variables, independently from the system size. The electron density is defined as in Eq. 3.2:

$$\rho\,(r) = \ \sum_{i}^{N}|\Phi_i|^2 \quad \text{(Eq. 3.2)}$$

where N is the number of electrons in the system and Φ_i are the molecular orbitals (MOs), linear combination of atomic orbitals (AOs) [2-4].

In 1964, Hohenberg and Kohn demonstrated that the ground-state energy of a many-electrons system with a non-degenerate ground-state, as well as its ground-state properties, depends only on the electron density. Therefore, the Hohenberg-Kohn

Existence Theorem assumes that the ground-state energy is a unique functional of the electron density $\rho(r)$ [5]. The second Hohenberg-Kohn Variational Theorem assumes that the density obeys a variational principle. Therefore, in order to find the true ground-state electron density, which minimizes the energy functional, the energy should be minimized by varying the electron-density [5]. Because of the exact form of the universal functional $E[\rho(r)]$ is not known, in 1965 Kohn and Sham proposed an expression for the energy functional considering the kinetic energy of non-interacting electrons, which will lead to a ground state density same as that of the interacting-electrons system (Eq. 3.3) [6]:

$$E[\rho(r)] = T[\rho(r)] + V_{ne}[\rho(r)] + V_{ee}[\rho(r)] + E_{xc}[\rho(r)] \quad \text{(Eq. 3.3)}$$

where $T[\rho(r)]$ is the kinetic energy of the non-interacting system, $V_{ne}[\rho(r)]$ is the external potential, i.e. nucleus-electron attraction term, $V_{ee}[\rho(r)]$ is the Coulomb term, i.e. electron-electron repulsion term, and $E_{xc}[\rho(r)]$ is the exchange-correlation functional, which accounts for the kinetic energy deriving from the interacting electrons and all the other aspects of the true system, which are the non-classical electron-electron interactions, i.e. the exchange and the correlation.

The Kohn-Sham (KS) approach is based on the solution of an eigenvalue problem (Eq. 3.4):

$$\hat{h}_i^{KS} \, \Phi_i = \varepsilon_i \Phi_i \quad \text{(Eq. 3.4)}$$

where $\hat{h}_i^{KS}$ is the KS operator (Eq. 3.5), Φ_i are the Kohn-Sham orbitals and ε_i are the orbital energies.

$$\hat{h}_i^{KS} = -\frac{1}{2}\nabla_i^2 - \frac{1}{2}\sum_j^N \frac{Z_j}{|r_i - r_j|} + \int \frac{\rho(r)}{|r_i - r|} + \frac{\partial E_{xc}}{\rho(r)} \quad \text{(Eq. 3.5)}$$

KS approach will return the exact energy only if the exact form of the exchange-correlation functional is known. To this end, a Self-Consistent Field (SCF) procedure is used to solve the equation: the starting point is an initial guess of the density from which a set of orbitals can be derived, leading to a better value for the density that is used in the second iteration and so on, until an approximate solution is reached [2,3].

3.1.1. Exchange-Correlation Functionals

Exchange-correlation functionals are key points in the DFT approach. Several approximations have been developed for this term and the simplest is the Local Density Approximation (LDA). It is based on the uniform electrons gas model, in which the electron density is taken constant throughout the space, i.e. it is assumed that a constant electron density with the same value as at *r* replaces the real electron density distribution around a volume element at point *r*. The total exchange-correlation energy is expressed as Eq. 3.6:

$$E_{xc}[\rho(r)] = \int \rho(r)\, \varepsilon_{XC}\big(\rho(r)\big) dr \quad \text{(Eq. 3.6)}$$

where ε_{XC} is the energy density, the sum of individual exchange and correlation contributions [2]. The LDA approximation can be extended to the Local Spin Density Approximation (LSDA) for systems with unpaired electrons. However, in molecular systems the electron density is usually not uniform, thus this approximation results often inadequate. For this reason, extensions have been developed, such as the gradient-corrected functionals, i.e. the Generalized Gradient Approximation (GGA), which is based on the gradient of the density at each point in the space and not only on its pure value. In these functionals, the exchange and the correlation contributions are treated separately. In particular, the exchange part of E_{XC}^{GGA} can be written as in Eq. 3.7:

$$E_{XC}^{GGA} = E_X^{LDA} - \sum_{\sigma} \int F(s_{\sigma})\, p^{\frac{4}{3}}\, \vec{r}\, \mathrm{d}\vec{r} \quad \text{(Eq. 3.7)}$$

where s_{σ} is the reduced density gradient, which is a local inhomogeneity parameter assuming large values both for large gradients and for small region densities. For the function *F,* two approaches have been developed. The first one is based on a GGA exchange-correlation functional which includes an empirical parameter. A functional developed considering this approach is the Perdew-Wang (PW91) [7-10]. In this thesis, it has been used combined with the Time Dependent extension of DFT method to investigate the main UV absorption properties of catechol-based sensitizers, as discussed in Section 4.5 of Chapter 4. Indeed, PW91 pure functional can satisfy several conditions, incorporating some inhomogeneity effects while retaining many features of LDA functionals [9]. The second class of GGA functionals does not contain semiempirical

parameters, such as the Perdew, Burke and Ernzerhof (PBE) functional [9], which has been used in this thesis to determine some of the electronic properties of isolated **HTM1**, but mainly to characterize its interaction with the MAPI surface (See Section 4.2 of Chapter 4). Indeed, PBE is one of the most employed functionals within GGA to determine extended systems properties.

In principle, exchange functionals should be combined with any of correlation functionals, but only few combinations are currently in use. As the exchange contributions are larger than the corresponding correlation effects, an accurate expression for the exchange functional is essential to obtain accurate results. For this reason, the functionals have been improved including a certain percentage of the HF *exact* exchange energy, which has brought to hybrid functionals. In the approach proposed by Becke [10], the exchange-correlation energy is written as Eq. 3.8:

$$E_{xc} = \int_0^1 U_{XC}^\lambda \, d\lambda \quad \text{(Eq. 3.8)}$$

where λ is a coupling parameter and it can assume values from 0 to 1. When $\lambda = 0$, the Coulomb repulsion between electrons is not considered, while $\lambda = 1$ accounts for the real system with full interactions. The simplest approximation of this integral is a linear interpolation (Eq. 3.9).

$$E_{xc} = \frac{1}{2} \left(U_{XC}^0 + U_{XC}^1 \right) \quad \text{(Eq. 3.9)}$$

When $\lambda = 0$, U_{XC}^0 is the exchange-correlation energy of the non-interacting system, then it represents the pure exchange energy of the KS determinant that can be exactly determined. U_{XC}^1 is then the exchange-correlation energy of the full interacting system and it can be determined by introducing the LSDA exchange-correlation functional. This approach is also known as half-and-half combination of exact exchange and exchange-correlation functional. A further improvement consisted in eliminating the U_{XC}^0 term (Eq. 3.10):

$$E_{xc} = E_{XC}^{LSDA} + \alpha_0 \left(E_X^{exact} - E_{XC}^{LSDA} \right) + \alpha_x \Delta E_X^{GC} + \alpha_c \Delta E_C^{GC} \quad \text{(Eq. 3.10)}$$

where: E_X^{exact} is the exact exchange energy, E_{XC}^{LSDA} is the exchange energy under the LSDA approximation, ΔE_X^{GC} is the gradient correction for the exchange and ΔE_C^{GC} is the gradient correction for the correlation. α_0, α_x and α_c are empirical coefficients and they have values of 0.2, 0.7 and 0.8, respectively. Among these hybrid functionals, the most popular is the B3LYP that includes the Becke's exchange functional along with the Lee-Yang-Parr (LYP) correlation functional (Eq 3.11) [10,11]:

$$E_{XC}^{B3LYP} = (1-a)E_X^{LSDA} + aE_X^{exact} + b\Delta E_X^{B88} + (1-c)E_C^{LSDA} + cE_C^{LYP} \quad \text{(Eq. 3.11)}$$

The popularity of this functional can be attributed to its good performances for lots of chemical applications. In this thesis, it has been largely employed to determine the ground-state geometries of lots of the designed compounds, to calculate frequencies, as well as for the calculation of their molecular orbitals' energies (See Chapter 4).

Another hybrid functional employed in this thesis to calculate the spectroscopic properties of some of the designed fluorophores, combined to the Time Dependent extension of DFT, and to predict the ground-state redox potential of 16 dyes is the modified Perdew-Wang 1-parameter model for kinetics, the MPW1K (Sections 4.4, 4.6 and 4.7 of Chapter 4) [12]. This functional includes ca. 42% of the HF *exact* exchange and it involves a single semiempirical parameter.

However, to provide a better description of properties which are not only dependent from the quality of the occupied KS orbitals, but also on the quality of virtual orbitals, i.e. excitation energies, CAM-B3LYP functional has been proven to provide very stable and reliable results combined to the Time Dependent extension of DFT. Indeed, it associates the hybrid quality of B3LYP to a long-range correction to the exchange potential, known as the Coulomb attenuating method (CAM), that accounts for both short- and long-range interactions [13]. CAM-B3LYP functional has been used to calculate the excitation energies of the designed HTMs, as well as those of NIR-emitting fluorophores (Sections 4.1 and 4.8, respectively, of Chapter 4).

3.1.2. DFT in crystalline solids

In crystalline systems, a given set of atoms, i.e. the unit cell, are repeated along the three dimensions of the real space according to a given symmetry. The unit cell is characterized by three lattice vectors (**a**, **b**, **c**) and three angles between them (α, β, γ). All the atomic

positions in the unit cell can be expressed as fractional coordinates of such cell vectors (Eq. 3.12):

$$\mathbf{r} = x\mathbf{a} + y\mathbf{b} + z\mathbf{c} \quad \text{(Eq. 3.12)}$$

The periodicity of the lattice implicates that every property, i.e. the electron density value, is the same at equivalent positions in the lattice (PBC: Periodic Boundary Conditions). Considering that a crystal contains an infinite number of electrons, the Bloch theorem (Eq. 3.13) connects the wavefunction of an electron in an external periodic potential with the wavefunction at any point of the crystal [14]:

$$\psi^k(\mathbf{r} + \mathbf{T}) = e^{i\mathbf{kT}} \psi^k(\mathbf{r}) \quad \text{(Eq. 3.13)}$$

where $\mathbf{T}$ is a translational vector and $e^{i\mathbf{kT}}$ is an imaginary phase factor arising from the translational symmetry, which is called plane wave. For a particular class of vectors $\mathbf{k}$, the plane wave has the same periodicity of the crystal ($e^{i\mathbf{kT}}=1$). They are called reciprocal space and any vector of the reciprocal space can be expressed with three primitive vectors (Eq 3.14):

$$\mathbf{K} = x\mathbf{d} + y\mathbf{e} + z\mathbf{f} \quad \text{(Eq. 3.14)}$$

These primitive vectors are connected to real-space vectors as Eq. 3.15:

$$\mathbf{d} = 2\pi \frac{\mathbf{b} \, x \, \mathbf{c}}{V}; \quad \mathbf{e} = 2\pi \frac{\mathbf{c} \, x \, \mathbf{a}}{V}; \quad \mathbf{f} = 2\pi \frac{\mathbf{a} \, x \, \mathbf{b}}{V} \quad \text{(Eq. 3.15)}$$

where V is the volume of the real-space unit cell $V = \mathbf{a}(\mathbf{a} \, x \, \mathbf{b})$. $\mathbf{K}$ value should be confined in a unit cell of the reciprocal space, called Brillouin Zone (BZ), which contains all the information of the infinite crystal. In principle, all the equations in solid state should be solved within the BZ in the reciprocal space, hence the number of electrons is limited to that contained in the unit cell. However, only a finite number of k-points is practically selected (k-points sampling), considering the volume of the unit cell and which kind of chemical problem should be analyzed. The discrete sampling of the BZ is possible because the wavefunctions at close points in the $\mathbf{k}$ space are almost identical. A common

method for generating *k*-points sets has been developed by Monkhorst and Pack. It is based on an equally spaced *k*-point mesh by performing **nd** × **ne** × **nf** divisions along the d, e and f directions of the BZ [15]. In this thesis, 8 x 8 x 8 Monkhorst-Pack *k*-point grid for sampling the BZ has been considered for the optimization of MAPI bulk, while 8 x 8 x 1 and 1 x 1 x 1 Monkhorst-Pack *k*-point grid have been employed for the slabs and HTMs optimizations within PBC and to calculate the binding energies of HTMs/MAPI systems (see Section 4.2 of Chapter 4).

3.1.3. Time Dependent Density Functional Theory

As a ground-state theory, DFT has some limitations. Indeed, it is not adequate for the description of many-electrons systems in time-dependent fields, as well as for the calculation of excitation energies and the excited-state properties. For this reason, a time dependent extension of DFT, known as Time Dependent Density Functional Theory (TDDFT) has been developed to deal with any time-dependent phenomena. TDDFT can be considered as an alternative formulation of time-dependent quantum mechanics based on the Schrödinger equation, but it has the advantage to consider the one-body electron density. The TDDFT finds its origin in the Runge-Gross theorem that is a time-dependent extension of the Hohenberg-Kohn theorem [16]. Indeed, while in DFT the ground-state energy can be determined minimizing the total energy functional, in TDDFT the energy is not a conserved quantity, but it is substituted by the quantum mechanical action (Eq. 3.16):

$$A\,[\Phi] = \int_{t_0}^{t_1} dt < \Phi(t) \left| i\, \frac{\partial}{\partial t} - \hat{H}\,(t) \right| \Phi(t) > \quad \text{(Eq. 3.16)}$$

where $\Phi(t)$ is the N_e-body function. This theorem asserts that there is a unique correspondence between the potential $v(r, t)$ and the density $\rho(r, t)$ for systems evolving from a fixed many-body state (Eq. 3.17). Hence, all the observables of a many-electrons system can be calculated knowing the one-body density.

$$v(r, t) \neq v'(r, t) + c(t) \rightarrow \rho(r, t) \neq \rho'(r, t) \quad \text{(Eq. 3.17)}$$

To calculate the electron density, an auxiliary system of non-interacting electrons, the KS electrons, subjected to an external local potential v_{KS}, is used. This potential is unique,

and it is chosen such that the density of the KS electrons is the same as the density of the original interacting system. For this reason, the KS electrons obey to the time-dependent Schrödinger equation (Eq. 3.18) and the density of the interacting system can be determined from the time-dependent KS orbitals (Eq. 3.19).

$$i\frac{\delta}{\delta t}\,\varphi_i(r,t) = \left[-\frac{\nabla^2}{2} + v_{KS}(r,t)\right]\varphi_i(r,t) \quad \text{(Eq. 3.18)}$$

$$\rho(r,t) = \sum_i^{occ}|\varphi_i\,(r,t)^2| \quad \text{(Eq. 3.19)}$$

This implicates that the exact KS potential v_{KS} (Eq. 3.20) determines the exact KS orbitals, thus the exact density of the system.

$$v_{KS}(r,t) = v_{ext}(r,t) + v_{Hartree}(r,t) + v_{XC}(r,t) \quad \text{(Eq. 3.20)}$$

In Eq. 3.20 the first term is the external potential, the second term is the Hartree potential that accounts for the classic electrostatic interactions between electrons and the last term is the exchange-correlation potential, accounting for the all the aspects of the true system. $v_{XC}\,(r,t)$ can be written as the functional derivative of the exchange-correlation part of a new action functional Ã (Eq. 3.21):

$$v_{XC}(r,t) = \frac{\delta \tilde{A}_{XC}}{\delta \rho(r,\tau)}\Big|_{\rho(r,t)} \quad \text{(Eq. 3.21)}$$

As for the ground-state DFT, the exact form of the $v_{XC}(r,t)$ is unknown, hence several approximations have been proposed [17].

TDDFT method has been used throughout this thesis to determine the excitation energies and excited-state properties of the designed HTMs for PSCs, sensitizers for DSSCs and fluorophores for LSCs (See Chapter 4).

3.2. Basis Sets

A key aspect of the KS approach is represented by the KS molecular orbitals (MOs), which yield the ground state density associated with the choice of the exchange-correlation potential. For this reason, it is fundamental to have a good description of the atomic orbitals, also known as basis sets. The Slater Type Orbitals (STOs) would represent the best choice (Eq 3.22).

$$\xi_{\zeta,n,l,m_l}(r,\theta,\varphi,) = NY_{l,m_l}(\theta,\varphi)r^{n-1}e^{-\zeta r} \quad \text{(Eq. 3.22)}$$

They are composed by a radial part defined by *r* that depend on the distance between the nucleus and the electrons, and a spherical harmonic part, defined by θ,φ that describes the shape of the orbitals. *N* is the normalization constant and the value of ζ for every STO is determined by minimizing the atomic energy with respect to it. STOs are very accurate, however the exponential part e^{-r} is very expensive to compute, in particular for large systems. Therefore, Gaussian Type Orbitals (GTOs) have been introduced (Eq. 3.23) where the exponential e^{-r^2} make them faster to compute. However, they are less accurate, falling too rapidly far away from the nucleus.

$$\xi_{\zeta,n,l,m_l}(r,\theta,\varphi,) = NY_{l,m_l}(\theta,\varphi)r^{2n-2-l}e^{-\zeta r^2} \quad \text{(Eq. 3.23)}$$

Therefore, at least three GTOs are required to represent a single STO and STO-3G is known as the minimal basis set, in which 3 primitive Gaussian functions are combined in a fixed linear combination to give one contracted Gaussian function. To improve the description of valence electrons, Split Valence Double Zeta (DZ) basis sets have been introduced, doubling the functions for each orbital, while the core electrons are still treated as a minimal basis set (e.g. 6-31G). An additional improvement is to consider the change in the shape of the orbitals. For this reason, polarization functions are introduced. They have more angular nodal planes than the occupied atomic orbitals, ensuring that the orbitals can distort from their original atomic symmetry to better adapt to the molecular environment. A typical example of a basis set containing polarization function is the 6-31G**, or equivalently, 6-31G(d,p), which considers d functions for heavy atoms and p functions for hydrogen and helium. To also provide for a description of species such as anions and molecules with lone pairs, which have a significant portion of the electron

density away from nucleus, the diffuse functions can be added to the basis set. They are indicated with the plus sign (+) and only a single + denotes a single set of diffuse functions on heavy atoms, two plus signs indicate that they are extended also on hydrogen [2,3]. Most of the calculation in this thesis have been performed with the TZVP (triple zeta valence polarized), 6-31G*, 6-31+G*, 6-31G(d,p), 6-311G(d,p), 6-311+G(2d,p) and 6-311++G** basis sets (Chapter 4).

3.2.1. Numerical Atomic Orbitals

Order-N methods, $O(N)$, have become popular to simulate many-atoms systems because the computer time and the memory scale linearly with the simulated system size. In addition to solving the Schrödinger equation, they require the determination of the self-consistent Hamiltonian in $O(N)$ iterations, which is a difficult task to perform using plane waves. For this reason, strictly localized basis sets, i.e. orbitals that are strictly zero beyond a given cutoff radius r_c, appear to be the best choice. These kinds of orbitals, also known as NAO's, Numerical Atomic Orbitals, are generated by numerically solving the atomic KS equations with the corresponding approximate exchange-correlation functional. They can be employed to perform fast simulations using minimal basis sets, but also very accurate computations using expanded bases. NAO's can be described considering three main features that are the size (number of orbitals for atom), the range (cutoff radius of orbitals) and the shape, and they are generated adapting known principles of quantum chemistry, such as the split-valence method. For an atom I, located at $\mathbf{R}_I$, NAO's are defined as the product of a numerical radial function and a spherical harmonic function (Eq. 3.24):

$$\phi_{Ilmn}(r) = \phi_{Iln}(r_I)Y_{lm}(\hat{r}_I) \quad \text{(Eq. 3.24)}$$

Where $r_I = \text{r-}\mathbf{R}_I$. Within this approach, multiple zeta basis sets can be generated by adding to each basis orbital a new basis function that reproduces exactly the tail of the original orbital but ensuring continuity towards the origin in a given cutoff radius r_c (size feature). In this way, they combine the decay of the atomic eigenfunctions with a smooth behavior inside r_c. Each radial function can have a different cutoff radius, hence a systematic way of defining all the different cutoff radii has been found in setting the split norm to 0.15

(range feature). The last feature is represented by the shape; hence polarization orbitals are added to the basis set (Eq. 3.25):

$$\phi_{l+1,m}(r) = N\phi_{l+1}(r)Y_{l+1,m}(\hat{r}) \text{ (Eq. 3.25)}$$

Where N is a normalization constant.

Within this approach, the DZP (double zeta polarized) is considered the standard basis set, as it represents a good compromise between computational cost and accurate results, which are comparable to those obtained with plane-waves calculations [18-20]. DZP has been employed in this thesis to simulate the electronic properties of HTMs/MAPI interfaces, as implemented in Siesta software [20] (Section 4.2 of Chapter 4).

3.3. Pseudopotentials

Calculations on periodic systems are usually performed considering only the valence electrons explicitly, while pseudopotential functions are used to treat core electrons. They give wavefunctions with the same shape as the true wavefunction outside of the core region (cutoff radius), while they have only few nodes inside the core region. Such pseudopotentials that require few plane waves are defined "soft" pseudopotentials and they have large cutoff radius. On the other hand, pseudopotentials having small cutoff radius are defined "hard" and they are more computationally expensive. If the valence electrons pseudopotential reproduces the behavior of the valence electrons in the all-electrons calculation, i.e. the total valence electron density in the core region is equal to that of the all-electron atoms, they are defined as "non-local norm-conserving" [3]. The most common pseudopotentials are the Ultrasoft [21], the Projector Augmented Wave [22] and the Troullier-Martins [23]. Troullier-Martins pseudopotentials (Eq. 3.26) consent to describe elements of the entire periodic table:

$$\left[-\frac{1}{2r}\frac{d^2}{dr^2}r + \frac{l(l+1)}{2r^2} + V_l(r) + V^H(r) + V^{XC}(r)\right]\psi_{ln}(r) = \epsilon_{ln}\psi_{ln}(r) \text{ (Eq. 3.26)}$$

where V_l, V^H and V^{XC} are the semilocal potential, the Hartree potential and the exchange-correlation potential for the pseudo-valence charge density, while ψ_{ln} are the eigenstates of the semilocal pseudopotential at energy ϵ_{ln} [20].

Troullier-Martins pseudopotentials are implemented in Siesta software [20], and they have been used in this thesis to characterize the HTMs/MAPI properties (Section 4.2 of Chapter 4). Indeed, even if their usage is not strictly necessary with atomic basis sets, they allow to accurately represent a smooth charge density in a real-space grid [20].

3.4. Dispersion Forces

One limit of the DFT theory concerns the inability to describe dispersion forces, which have a crucial role in interfacial phenomena. Indeed, when two systems are close to each other, there is a repulsion between their electron densities, but at intermediate distances, a weak attracting force is created: the electron density of system A induces a perturbation in the electron density of system B and a temporary dipole moment is created. This attracting force decays with r^{-6}, where r is the intermolecular distance between the two considered systems [2, 24]. In order to include dispersion forces, van der Waals-based functionals and the DFT-D approach have been developed [25-27]. The latter consists in adding a semi-empirical dispersion potential to the KS DFT energy and it is more convenient in terms of computational costs. The total DFT-D3 energy has been defined by Grimme as Eq. 3.27:

$$E_{DFT-D3} = E_{KS-DFT} + E_{disp} \quad \text{(Eq. 3.27)}$$

where E_{disp} is the dispersion term, defined as Eq. 3.28:

$$E_{disp}^{D3(BJ)} = -\frac{1}{2} \sum_{i \neq j} s_6 \frac{C_{6ij}}{r_{ij}^6} f_{d,6}(r_{ij}) + s_8 \frac{C_{8ij}}{r_{ij}^8} f_{d,8}(r_{ij}) \quad \text{(Eq. 3.27)}$$

Where s_6 and s_8 are scaling parameters, depending on the density functional, C_{6ij} and C_{8ij} are the dispersion coefficients for the ij atoms, r_{ij} is the interatomic distance, $f_{d,6}$ and $f_{d,8}$ are damping functions that regulate the attractive term. The dispersion coefficients in DFT-D3 are geometry dependent and they are calculated from first-principles. One of the most common damping schemes is that proposed by the Becke-Jonson (BJ) [27] and it is adopted in this thesis to determine the structural features of HTMs/MAPI systems (Section 4.2 of Chapter 4).

3.5. Solvation Methods

As solvents may largely affect the properties of systems of interest, solvation models have been proposed to include solvents contribution in calculations. In this thesis, two solvation methods have been used: the Polarizable Continuum Model (PCM) [28] and the Averaged Solvent Electrostatic Potential from Molecular Dynamics (ASEP/MD) [29], briefly introduced in the next sections.

3.5.1. Polarizable Continuum Model

In continuum models the solvent acts as a perturbation on the gas-phase behavior of the system. The solvation free energy is described as the energy change when a molecule is transferred from the vacuum to the solvent (Eq. 3.28):

$$\Delta G_{solv} = \Delta G_{elec} + \Delta G_{vdW} + \Delta G_{cav} + (\Delta G_{hb}) \quad \text{(Eq. 3.28)}$$

where ΔG_{elec} is the electrostatic component, ΔG_{vdW} addresses for the van der Waals interactions between the solvent and the solute and it can be divided into a repulsive and an attractive term, ΔG_{rep} and ΔG_{disp}, respectively, while ΔG_{cav} is the free energy required to form the solute cavity within the solvent. (ΔG_{hb}) is an auxiliary hydrogen-bonding term that can be added in systems where localized hydrogen bonds between solvent and solute are present. This model considers the solvent as a continuous dielectric medium creating a cavity that contains the solute. The cavity is created from the van der Waals radii of the atoms and its surface is divided into small surface elements, each of them associated to a point charge which represent the polarization of the solvent. The total electrostatic potential at each surface element is described as Eq. 3.29:

$$\varphi(r) = \varphi_\rho(r) + \varphi_\sigma(r) \quad \text{(Eq. 3.29)}$$

where $\varphi_\rho(r)$ is the potential due to the solute and $\varphi_s(r)$ is the potential due to the surface charges. The initial value of the point charges is calculated from the electric field gradient of the solute (Eq. 3.20):

$$q_i = - \left[\frac{\varepsilon-1}{4\pi\varepsilon}\right] E_i \Delta S \quad \text{(Eq. 3.30)}$$

where ε is the dielectric constant of the medium, E_i is the electric field gradient and ΔS is the area of the surface element. The contribution from other point charges is calculated through the Coulomb's law and they are modified until the self-consistency is reached. The resulting potential $\varphi_\sigma(r)$ is then added to the solute Hamiltonian (Eq 3.31) and an iterative SCF calculation starts, until the solute wavefunction and the surface charges are self-consistent [2,28].

$$H = H_0 + \varphi_\sigma(r) \quad \text{(Eq 3.31)}$$

This solvation method has been included in several calculations throughout this thesis (see Chapter 4).

3.5.2. Averaged Solvent Electrostatic Potential from Molecular Dynamics

The Averaged Solvent Electrostatic Potential from Molecular Dynamics (ASEP/MD) solvation method is a combination of continuum and quantum mechanics/molecular mechanics (QM/MM) methods, allowing a good description of the solute and of the solute-solvent interactions too. Indeed, as in continuum models, the solvent effect is introduced in the solute Hamiltonian as a perturbation in an averaged way (mean field approximation): the solvent perturbation is the averaged value of the potential generated by the solvent in the volume occupied by the solute. However, this distribution is obtained from QM/MM simulations: the solute is described with QM methods, while the solvent is described with MM force fields, i.e. ignoring the electronic motions and only considering the nuclear positions. The ASEP/MD Hamiltonian is then the combination of the solute and the solvent Hamiltonians plus the Hamiltonian of the interaction between the two subsystems, as described in Eq. 3.32.

$$\hat{H} = \hat{H}_{QM} + \hat{H}_{MM} + \hat{H}_{QM/MM} \quad \text{(Eq. 3.32)}$$

The $\hat{H}_{MM}$ does not involve the quantum subsystem, then it is computed separately, while the energy of the solvated solute is obtained solving the effective Schrödinger equation (Eq. 3.33).

$$\left(\hat{H}_{QM} + \hat{H}_{QM/MM}\right)| \psi > = E \,| \psi > \quad \text{(Eq. 3.33)}$$

The $\hat{H}_{QM/MM}$ term accounts for the electrostatic and the van der Waals interaction (Eq. 3.34):

$$\hat{H}_{QM/MM} = \hat{H}_{QM/MM}{}^{elec} + \hat{H}_{QM/MM}{}^{vdW} \quad \text{(Eq. 3.34)}$$

where $\hat{H}_{QM/MM}{}^{vdW}$ depends only on the nuclear coordinates of solvent and solute, thus it does not affect the solute wavefunction, while $\hat{H}_{QM/MM}{}^{elec}$ term is defined as follows (Eq. 3.35):

$$\hat{H}_{QM/MM}{}^{elec} = \int dr \, \hat{\rho} < V_s(r; \rho) > \quad \text{(Eq. 3.35)}$$

where $\hat{\rho}$ is the solute charge density operator and $< V_s(r; \rho) >$ is the ASEP term: the average electrostatic potential generated by the solvent at position *r*, obtained from molecular dynamics (MD) calculations where the solute molecule is taken at fixed geometry. This potential is represented by a set of point charges q_i (Eq. 3.36) that simulate the electrostatic potential generated by the continuous solvent distribution:

$$< V_s(r; \rho) > = \sum_i \frac{q_i}{r - r_i} \quad \text{(Eq. 3.36)}$$

The ASEP/MD method proceeds as follows:

1. The solute charge distribution is obtained from a QM calculation in gas-phase;
2. The obtained charge distribution is used as input in a MD calculation to find the structure of the solvent around the solute;
3. The ASEP charges are determined and introduced in the solute Hamiltonian;
4. The electronic wavefunction of the solute is determined by solving the effective Schrödinger equation;
5. A new charge distribution for the solute is found and it represents the input for a new MD simulation.

This procedure is repeated until convergence in the solute charges is achieved [29].

In this thesis, ASEP/MD method has been used to study the influence of the selected solvent on the absorption properties of **DQ3** fluorophore designed for LSCs application. In particular, the results obtained with this method have been compared to those obtained employing PCM as solvation method (Section 4.7.1 of Chapter 4).

3.6. Software used

The main software used in this thesis are:

1. Gaussian, Inc.: a computational chemistry software that allows to calculate the electronic structure and the main properties of molecules in gas-phase and in solution. In this thesis Gaussian09 and Gaussian16 versions have been used [30,31].

2. Siesta: a method and a computer program implementation that allow to calculate the electronic structure and the main properties of molecules and solids [20].

3. ASEP/MD: a method and a computer program that allow to study the solvent effects in a specific case study. External programs are implemented in ASEP/MD such as Gaussian, Inc. package [30, 31], to perform QM simulations, and GROMACS [32], to perform MD simulations.

4. Avogadro: a molecular editor and a visualization tool that allows to construct molecular geometries in 3D and analyze chemical and molecular data [33].

5. VESTA: a 3D visualization tool that allows to analyze the crystal structures from crystallographic studies and electronic state calculations [34].

3.7. References

[1] R. Nashed, Y. Ismail, and N. K. Allam, Recent advances in the use of density functional theory to design efficient solar energy-based renewable systems, Journal of Renewable and Sustainable Energy 5, 022701 (2013). https://doi.org/10.1063/1.4798483

[2] A. R. Leach, Molecular modelling: principles and applications, Pearson Education, Second Edition (2001).

[3] W. Koch, and M. C. Holthausen, A Chemist's Guide to Density Functional Theory, II. Wiley-VCH (2001).

[4] C. Cramer, Essentials of Computational Chemistry: Theories and Models, John Wiley & Sons Inc. (2002).

[5] P. Hohenberg, and W. Kohn, Inhomogeneous Electron Gas, Phys. Rev. 136, B864–B871 (1964). https://doi.org/10.1103/PhysRev.136.B864

[6] W. Kohn, and L. J. Sham, Self-consistent Equations Including Exchange and Correlation Effects, Phys. Rev. 140, A1133–A1138 (1965). https://doi.org/10.1103/PhysRev.140.A1133

[7] J.P. Perdew, Electronic Structure of Solids '91, Eschrig (Akademie Verlag), Berlin 11 (1991).

[8] K. Burke, J.P. Perdew, and Y. Wang, Derivation of a Generalized Gradient Approximation: The PW91 Density Functional, in: Electron. Density Funct. Theory, Springer US, Boston, MA, 81–111 (1998). https://doi.org/10.1007/978-1-4899-0316-7_7

[9] J. P. Perdew, K. Burke, and M. Ernzerhof, Generalized Gradient Approximation Made Simple, Phys. Rev. Lett. 77, 3865–3868 (1996). https://doi.org/10.1103/PhysRevLett.77.3865

[10] A. D. Becke, Density-functional thermochemistry. III. The role of exact exchange, J. Chem. Phys. 98, 5648 (1993). https://doi.org/10.1063/1.464913

[11] C. Lee, W. Yang, and R. G. Parr, Development of the Colle-Salvetti correlation-energy formula into a functional of the electron density, Phys. Rev. B. 37, 785-789 (1988). https://doi.org/10.1103/PhysRevB.37.785

[12] B. J. Lynch, P. L. Fast, M. Harris, and D. G. Truhlar, Adiabatic Connection for Kinetics, J. Phys. Chem. A 104, 4811–4815 (2000). https://doi.org/10.1021/jp000497z

[13] T. Yanai, D. P. Tew, and N. C. Handy, A new hybrid exchange–correlation functional using the Coulomb-attenuating method (CAM-B3LYP), Chemical Physics Letters 393, 51–57 (2004). https://doi.org/10.1016/j.cplett.2004.06.011

[14] F. Bloch, Über die Quantenmechanik der Elektronen in Kristall- gittern, Z. Phys. 52, 555–600 (1929). http://dx.doi.org/10.1007/BF01339455

[15] H. J. Monkhorst, and J. D. Pack, Special points for Brillouin-zone integrations, Phys. Rev. B 13, 5188–5192 (1976). https://doi.org/10.1103/PhysRevB.13.5188

[16] E. Runge, and E. K. U. Gross, Density-Functional Theory for Time-Dependent Systems, Physical Review Letters 52, 997-1000 (1984). https://doi.org/10.1103/PhysRevLett.52.997

[17] E. K. U. Gross, J. F. Dobson, and M. Petersilka, Density functional theory of time-dependent phenomena, in R.F Nalewajski (eds) Density Functional Theory II. Topics in Current Chemistry, 181. Springer, Berlin, Heidelberg (1996). https://doi.org/10.1007/BFb0016643

[18] D. Sánchez-Portal, P. Ordejón, E. Artacho, J. M. Soler, Density-functional method for very large systems with LCAO basis sets, Internation Journal of Quantum Chemistry 65, 453–461 (1997). https://doi.org/10.1002/(SICI)1097-461X(1997)65:5<453::AID-QUA9>3.0.CO;2-V

[19] J. Junquera, O. Paz, D. Sánchez-Portal, and E. Artacho, Numerical atomic orbitals for linear-scaling calculations, Phys. Rev. B 64, 235111 (2001). https://doi.org/10.1103/PhysRevB.64.235111

[20] J. M. Soler, E. Artacho, J. D. Gale, A. García, J. Junquera, P. Ordejón, and D. Sánchez-Portal, The SIESTA method for ab initio order-N materials simulation, Journal of Physics: Condensed Matter 14, 2745-2779 (2002). https://doi.org/10.1088/0953-8984/14/11/302

[21] D. Vanderbilt, Soft self-consistent pseudopotentials in a generalized eigenvalue Formalism, Phys. Rev. B 41, 7892–7895 (1990). https://doi.org/10.1103/PhysRevB.41.7892

[22] G. Kresse, and D. Joubert, From ultrasoft pseudopotentials to the projector augmented-wave method, Phys. Rev. B 59, 1758–1775 (1999). https://doi.org/10.1103/PhysRevB.59.1758

[23] N. Troullier, and J. L. Martins, Efficient pseudopotentials for plane-wave calculations, Phys. Rev. B 43, 1993–2006 (1991). https://doi.org/10.1103/PhysRevB.43.1993

[24] C. Díaz, Y. Wang, and F. Martín, Including London Dispersion Forces in Density Functional Theory (DFT + D): Applications to Molecule(Atom)/Surface Phenomena,

Encyclopedia of Interfacial Chemistry, Surface Science and Electrochemistry, 1-9 (2018). https://doi.org/10.1016/B978-0-12-409547-2.13029-X

[25] F. Tran, L. Kalantari, B. Traoré, X. Rocquefelte, and P. Blaha, Nonlocal van der Waals functionals for solids: Choosing an appropriate one, Phys. Rev. Materials 3, 063602 (2019). https://doi.org/10.1103/PhysRevMaterials.3.063602

[26] S. Grimme, J. Antony, S. Ehrlich, and H. Krieg, A consistent and accurate *ab initio* parametrization of density functional dispersion correction (DFT-D) for the 94 elements H-Pu, J. Chem. Phys. 132, 154104 (2010). https://doi.org/10.1063/1.3382344

[27] S. Grimme, S. Ehrlich, and L. Goerigk, Effect of the damping function in dispersion corrected density functional theory, J. Comp. Chem. 32, 1456–1465 (2011). https://doi.org/10.1002/jcc.21759

[28] J. Tomasi, B. Mennucci, and R. Cammi, Quantum Mechanical Continuum Solvation Models, Chem. Rev. 105, 2999−3093 (2005). https://doi.org/10.1021/cr9904009

[29] I. F. Galván, M. L. Sánchez, M. E. Martín, F. J. Olivares del Valle, and M. A. Aguilar, ASEP/MD: A program for the calculation of solvent effects combining QM/MM methods and the mean field approximation, Computer Physics Communications 155, 244–259 (2003). https://doi.org/10.1016/S0010-4655(03)00351-5

[30] Gaussian 09, Revision C.01, M.J. Frisch, G.W. Trucks, H.B. Schlegel, G.E. Scuseria, M.A. Robb, J.R. Cheeseman, G. Scalmani, V. Barone, B. Mennucci, G.A. Petersson, H. Nakatsuji, M. Caricato, X. Li, H.P. Hratchian, A.F. Izmaylov, J. Bloino, G. Zheng, J.L. Sonnenberg, M. Hada, M. Ehara, K. Toyota, R. Fukuda, J. Hasegawa, M. Ishida, T. Nakajima, Y. Honda, O. Kitao, H. Nakai, T. Vreven, J.A. Montgomery, Jr., J.E. Peralta, F. Ogliaro, M. Bearpark, J.J. Heyd, E. Brothers, K.N. Kudin, V.N. Staroverov, T. Keith, R. Kobayashi, J. Normand, K. Raghavachari, A. Rendell, J.C. Burant, S.S. Iyengar, J. Tomasi, M. Cossi, N. Rega, J.M. Millam, M. Klene, J.E. Knox, J.B. Cross, V. Bakken, C. Adamo, J. Jaramillo, R. Gomperts, R.E. Stratmann, O. Yazyev, A.J. Austin, R. Cammi, C. Pomelli, J.W. Ochterski, R.L. Martin, K. Morokuma, V.G. Zakrzewski, G.A. Voth, P. Salvador, J.J. Dannenberg, S. Dapprich, A.D. Daniels, O. Farkas, J.B. Foresman, J.V. Ortiz, J. Cioslowski, and D.J. Fox, Gaussian, Inc.: Wallingford, CT, USA (2010).

[31] Gaussian 16, Revision C.01, M. J. Frisch, G. W. Trucks, H. B. Schlegel, G. E. Scuseria, M. A. Robb, J. R. Cheeseman, G. Scalmani, V. Barone, G. A. Petersson, H. Nakatsuji, X. Li, M. Caricato, A. V. Marenich, J. Bloino, B. G. Janesko, R. Gomperts, B. Mennucci, H. P. Hratchian, J. V. Ortiz, A. F. Izmaylov, J. L. Sonnenberg, D. Williams-Young, F. Ding, F. Lipparini, F. Egidi, J. Goings, B. Peng, A. Petrone, T. Henderson, D.

Ranasinghe, V. G. Zakrzewski, J. Gao, N. Rega, G. Zheng, W. Liang, M. Hada, M. Ehara, K. Toyota, R. Fukuda, J. Hasegawa, M. Ishida, T. Nakajima, Y. Honda, O. Kitao, H. Nakai, T. Vreven, K. Throssell, J. A. Montgomery, Jr., J. E. Peralta, F. Ogliaro, M. J. Bearpark, J. J. Heyd, E. N. Brothers, K. N. Kudin, V. N. Staroverov, T. A. Keith, R. Kobayashi, J. Normand, K. Raghavachari, A. P. Rendell, J. C. Burant, S. S. Iyengar, J. Tomasi, M. Cossi, J. M. Millam, M. Klene, C. Adamo, R. Cammi, J. W. Ochterski, R. L. Martin, K. Morokuma, O. Farkas, J. B. Foresman, and D. J. Fox, Gaussian, Inc.: Wallingford CT, USA (2016).

[32] M. D. Hanwell, D. E. Curtis, D. C. Lonie, T. Vandermeersch, E. Zurek, and G. R Hutchison, Avogadro: An advanced semantic chemical editor, visualization, and analysis platform, Journal of Cheminformatics 4, 1-17 (2012). https://doi.org/10.1186/1758-2946-4-17

[33] H. J. C. Berendsen, D. van der Spoel, and R. van Drunen, GROMACS: A message-passing parallel molecular dynamics implementation, Computer Physics Communications 91, 43-56 (1995). https://doi.org/10.1016/0010-4655(95)00042-E

[34] K. Momma, and F. Izumi, VESTA 3 for three-dimensional visualization of crystal, volumetric and morphology data, Journal of Applied Crystallography 44, 1272-1276 (2011). https://doi.org/10.1107/S0021889811038970

Chapter 4. Results and Discussion

The results of the research carried out by the PhD candidate are presented here. They are collected in seven manuscripts published in peer-reviewed international journals plus a last one which is to be submitted. More specifically, this Chapter reports the results concerning PSCs in Sections 4.1 and 4.2, the results related to the DSSCs technology in Sections 4.3, 4.4 and 4.5 and those obtained in the LSCs framework in Sections 4.6, 4.7 and 4.8.

4.1. Manuscript 1: "DFT and TDDFT investigation of four triphenylamine/phenothiazine-based molecules as potential novel organic hole transport materials for perovskite solar cells"

Authors: C. Coppola, R. Infantino, A. Dessì, L. Zani, M. L. Parisi, A. Mordini, G. Reginato, R. Basosi, and A. Sinicropi.

In this work, the *in silico* design of four novel hole transport materials (**HTM1-4**) based on triphenylamine and phenothiazine moieties has been carried out. The well-known structural and electronic optimal properties that a good HTM should possess to be considered as a suitable candidate for the construction of potentially efficient PSCs have been investigated by means of DFT and TDDFT methods. The results of this study suggest that **HTM1-4** possess appropriate electronic properties that contribute to promote the hole transport process, i.e. HOMO and LUMO energy levels well aligned with the VB and CB of MAPI perovskite, respectively, and a suitable electron density and spin density distributions. Additionally, their absorption properties do not compete with the MAPI absorption, and they have good chemical hardness. Comparing the results with those of two of the most performant HTMs reported in literature, Spiro-OMeTAD and PTZ2, it has been demonstrated that **HTM1-4** could be considered as valid HTMs candidates.

As first author of the manuscript, the PhD candidate's contribution refers to the conceptualization and application of computational methodologies to investigate the HTMs properties, as well as the writing of the original draft.
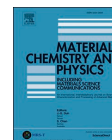
DFT and *TDDFT* investigation of four triphenylamine/phenothiazine-based molecules as potential novel organic hole transport materials for perovskite solar cells

Carmen Coppola [a,b], Rossella Infantino [c,d], Alessio Dessì [c], Lorenzo Zani [c], Maria Laura Parisi [a,b,c], Alessandro Mordini [c], Gianna Reginato [c], Riccardo Basosi [a,b,c], Adalgisa Sinicropi [a,b,c,*]

[a] *Università di Siena, R²ES Lab, Dipartimento di Biotecnologie, Chimica e Farmacia, via Aldo Moro 2, 53100, Siena, Italy*
[b] *CSGI, Consorzio per lo Sviluppo dei Sistemi a Grande Interfase, via della Lastruccia 3, 50019, Sesto Fiorentino, Italy*
[c] *CNR- Istituto di Chimica dei Composti Organometallici (CNR-ICCOM), Via Madonna del Piano del 10, 50019, Sesto Fiorentino, Italy*
[d] *Università di Siena, Dipartimento di Biotecnologie, Chimica e Farmacia, via Aldo Moro 2, 53100, Siena, Italy*

HIGHLIGHTS

- Four novel triphenylamine/ phenothiazine-based **HTM1-4** have been *in silico* designed.
- HOMO and LUMO energy levels of **HTM1-4** are well aligned with VB and CB of $CH_3NH_3PbI_3$.
- The wide spin density delocalization enhances hole transport ability of **(HTM1-4)**.[*+] .
- **HTM1-4** absorption maxima do not compete with perovskite absorption.

GRAPHICAL ABSTRACT
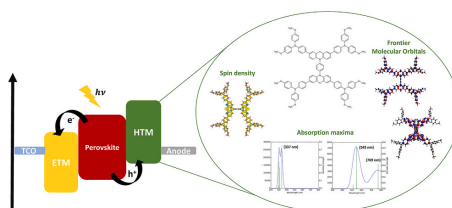
ABSTRACT

Hole transport materials (HTMs) based on conductive organic molecules are crucial components to prepare highly efficient perovskite solar cells (PSCs). To overcome the limitations arising from the use of the most common Spiro-OMeTAD, hindering large-scale PSCs production, alternative HTMs are highly desirable. Therefore, several fully organic molecules mainly based on triphenylamine moieties have already been proposed. However, there is still room for the development of more efficient and easily obtainable HTMs. Within this framework, the *in silico* design of four novel triphenylamine/phenothiazine-based HTMs (**HTM1-4**) is presented here. Their electronic and molecular properties have been investigated by means of Density Functional Theory (DFT) and Time Dependent DFT (TDDFT) methods and the results have been compared to those of Spiro-OMeTAD and a previously reported phenothiazine-based HTM (PTZ2). The analysis suggests that **HTM1-4** fulfil the requirements that enable hole extraction and transport processes in PSCs. Therefore, they should be considered as possible alternatives to Spiro-OMeTAD for the construction of potentially efficient PSCs.

* Corresponding author. Università di Siena, R²ES Lab, Dipartimento di Biotecnologie, Chimica e Farmacia, via Aldo Moro 2, 53100, Siena, Italy.
  E-mail address: adalgisa.sinicropi@unisi.it (A. Sinicropi).

1. Introduction

First introduced in 2009 as light-harvesting materials in Dye-Sensitized Solar Cells (DSSC) [1], mixed organic-inorganic lead perovskites have immediately intrigued the scientific and industrial photovoltaic communities. Indeed, since 2009, perovskite solar cells (PSCs) have been extensively investigated as an efficient alternative to the currently adopted silicon-based solar cells and their power conversion efficiency (PCE) has extraordinarily increased over the years, from 3.9% to 25.5% in 2020 [2–5]. Such outstanding photovoltaic performances can be ascribed, on one hand, to the promising optoelectronic properties of perovskite, and, on the other, to the great efforts devoted to the optimization of PSCs components [6,7]. The most studied PSC devices consist of a methylammonium lead iodide ($CH_3NH_3PbI_3$) layer in between an electron and a hole transport material layers. Both direct (n-i-p) and inverted (p-i-n) configurations are available (Fig. 1(a) and (b), respectively) [8,9]. The working principle of a PSC consists in the photoexcitation of the perovskite that leads to the creation of excitons (electron-hole pairs). Then, the electrons are injected into the electron transport material (ETM), while the holes are transferred to the hole transport materials (HTM). Lastly, the charges are collected at their respective electrodes (Fig. 1(c)) [10].

Among key materials in PSCs, HTMs have a crucial role in enhancing their PCE by extracting the holes from the perovskite and transporting them to the cathode [9]. Additionally, they are essential in preventing the direct contact between the perovskite and the electrode, avoiding the possible degradation at the metal-perovskite interface, and contributing to minimize the charge recombination as well [11,12]. For the reasons stated above, HTMs are under widespread investigation and, even though a large number of inorganic [12–16], polymeric [17–20], and hybrid [21,22] HTMs has been designed, those made of small organic molecules attracted more attention for their chemical versatility and easily tuneable optoelectronic properties [7,11]. Among them, Spiro-OMeTAD (2,2′,7,7′-tetrakis[*N,N*-di(4-methoxyphenyl)amino]- 9, 9′-spirobifluorene) (Fig. 2(a)) is the most widely used in direct (n-i-p) cells due to its suitable molecular properties [11,23–27] and the very high efficiencies obtained with the corresponding cells (up to 23.32%) [28,29]. On the other hand, its drawbacks (i.e. high costs of production, tedious multistep synthesis, negative impact on long-term stability and absorption of its oxidized species in the visible range) are hindering large-scale PSCs production [23,26,29–31]. For this reason, great research efforts have been devoted to the design of novel and potentially more efficient doped or dopant-free HTMs [29,32–40]. Among them, triphenylamine (TPA) moieties [36,37,41–45] and phenothiazine (PTZ)-based compounds [46–54] have been largely investigated. Indeed, the outstanding electro-optical properties of the TPA system, given by its non-planar geometry which influences the packing of the molecules, contribute to improve the hole mobility of HTMs [11,36,44]. On the other hand, because of its chemical stability, favorable optoelectronic properties, good solubility in common organic solvents and good film-forming properties, PTZ system has been largely adopted as a building block for the development of high-performing, low-cost and environmental friendly HTMs [46,49,53,54]. PTZ has a butterfly symmetrical structure, allowing different kinds of functionalization and it produces stable radical cations, displaying low oxidation potentials and high hole mobility [52–56]. In particular, Grisorio et al. [57], reported the synthesis and characterization of PTZ2 (Fig. 2(b)), based on both TPA and PTZ systems, which showed performances comparable to those obtained with Spiro-OMeTAD.

As potential improvement of these encouraging performances, in this work, the *in silico* design of four new TPA and PTZ-based HTMs, **HTM1-4** (Fig. 3), is presented. In particular, **HTM1-3** differ only for the central core, which is benzene in **HTM1**, 3,4-ethylenedioxythiophene (EDOT) in **HTM2** and dibenzofuran in **HTM3**. **HTM4**, instead, has benzene as central core, but it is substituted with three TPA and PTZ-based moieties in 1,3,5 positions.

HTM1-4 are very electron-rich molecules, formed by the combination of large π-conjugated systems and by the presence of heteroatoms. The *p*-methoxy substituted triphenylamines (MeOTPA), together with the PTZ, contribute to align HOMO and LUMO levels with VB and CB of hybrid perovskites. In addition, their dimeric or trimeric structures should favour a wide delocalization of the radical cation spin density. All these features should promote the hole transport process, allowing a better hole extraction and an increase of the charge carriers lifetime [49, 51,58]. Furthermore, in **HTM4** the introduction of an additional electron-donating unit should enhance also the stabilization of the radical cation state through 3D homoconjugation [59].

To understand the correlation between the molecular structures and the optoelectronic properties of the designed **HTM1-4**, key aspects for the development of efficient HTMs for PSCs, a computational study by means of Density Functional Theory (DFT) and Time Dependent Density Functional Theory (TDDFT) methods has been carried out. The results of such fully *in silico* investigation are presented below. The synthesis, the spectroscopic characterization together with the measurements of PSCs devices performances constructed using two of the designed molecules will be published shortly in a separate paper.

2. Computational methods

All QM calculations have been performed using Gaussian09 [60].

The neutral and oxidized forms of **HTM1-4** have been optimized in *vacuo* by DFT [61,62] at B3LYP/6-31G(d,p) level of theory [63,64]. Vibrational frequency calculations have been performed at the same level of theory to check that the stationary points were true energy minima (See Section 1 of Supporting Information for more details). B3LYP/6-311G(d,p) single point calculations at ground-state optimized geometries have been carried out to obtain the ground-state electron density and the frontier molecular orbitals (FMOs), including the solvent
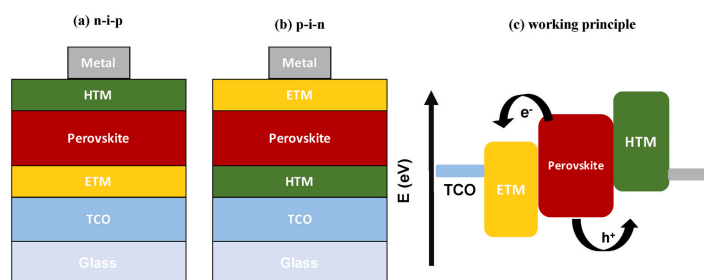

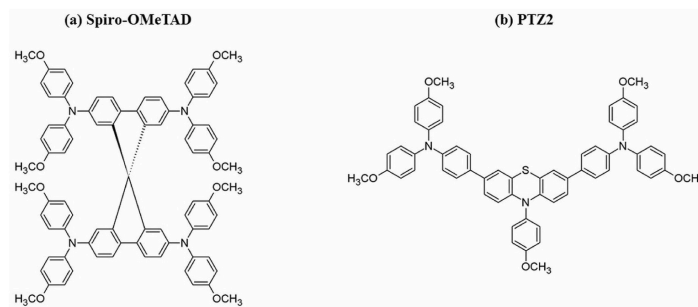**Fig. 1.** Direct (a) and inverted (b) configurations and working principle (c) of a PSC.

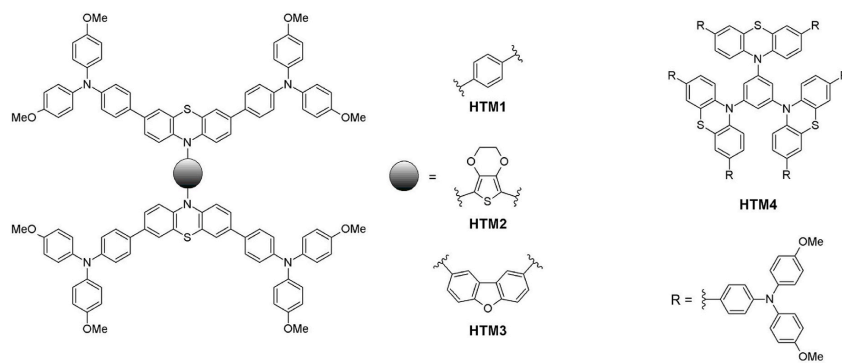**Fig. 2.** Spiro-OMeTAD (a) and PTZ2 (b) molecular structures.

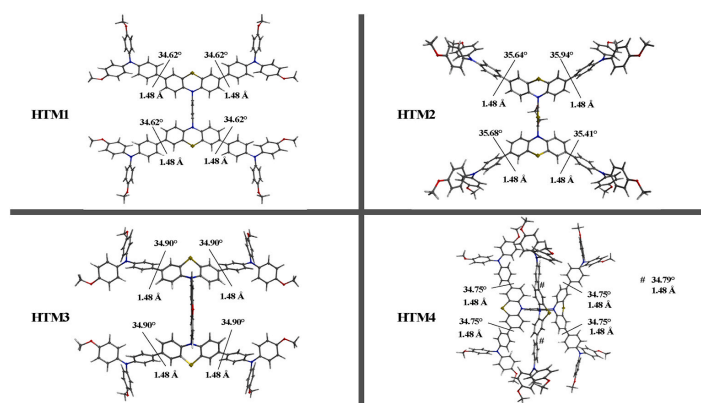

Fig. 3. **HTM1-4** molecular structures.

Fig. 4. DFT-B3LYP/6-31G(d,p) optimized ground-state molecular geometries of **HTM1-4**.

Table 1
FMOs energy levels (eV) of **HTM1-4** and Spiro-OMeTAD calculated at B3LYP/6-311G(d,p) level of theory in CH₂Cl₂, including the solvent effects by C-PCM, compared to those of Spiro-OMeTAD computed in EtOH at B3LYP/6-31G** [23] and PTZ2 in CH₂Cl₂ at B3LYP/6-311G(d,p) levels of theory [57].

Molecule	HOMO-1	HOMO	LUMO	LUMO+1
HTM1	−4.89	−4.88	−1.35	−1.35
HTM2	−4.93	−4.90	−1.31	−1.25
HTM3	−4.88	−4.87	−1.71	−1.32
HTM4	−4.91	−4.87	−1.45	−1.45
Spiro-OMeTAD	−4.76	−4.74	−1.23	−1.22
Spiro-OMeTAD [23]	−4.45	−4.42	−0.83	−0.80
PTZ2 [57]	−5.03	−4.96	−1.32	/

effects by the conductor-like polarizable continuum model (C-PCM) [65, 66]. Analogously to the previous work of Grisorio et al. [57], and to allow a direct comparison to PTZ2 molecular and electronic properties, CH₂Cl₂ was selected as the solvent. Spin densities and absorption maxima of neutral and oxidized states of **HTM1-4** in CH₂Cl₂ have been calculated by means of TDDFT [67,68] at CAM-B3LYP/6-31G(d,p) level [69], yet using C-PCM. The absolute chemical hardness has been evaluated both from the computed adiabatic ionization potential and the adiabatic electron affinity [70] at B3LYP/6-311G(d,p) level of theory in CH₂Cl₂ (using C-PCM), and by using Koopman's theorem [71]. UV–Vis spectra have been simulated with GaussSum considering a Gaussian distribution and an arbitrary line width of 0.03 eV [72].

3. Results and discussion

3.1. Ground-state geometries and electronic properties

HTM1-4 ground-state molecular geometries optimized in *vacuo* are shown in Fig. 4 and they are compared to (**HTM1-4**)•+ geometries in Fig. S1 of Supporting Information. They display similar dihedral angles between the MeOTPA and the PTZ units, ranging between 34° and 36°, while the PTZ N-substituents, which are the core of **HTM1-4**, adopt a

perpendicular position with respect to the lateral chains.

To determine if an efficient hole transfer from perovskite to **HTM1-4** is possible, the FMOs and the ground-state electron density have been calculated. Indeed, an eligible HTM should have the highest occupied molecular orbital (HOMO) and the lowest unoccupied molecular orbital (LUMO) well aligned with the perovskite valence band (VB) and conduction bands (CB), respectively, in order to drive the hole extraction and minimize the charge recombination processes, respectively [46]. Moreover, it has been also proven that a wide distribution of HOMO ground-state electron density leads to a larger overlap with the perovskite VB, ensuring a more efficient charge extraction, while LUMO electron density localization within the core of the molecule contributes to block the electron recombination. Therefore, a slight overlap between HOMO and LUMO orbitals is required to assist the formation of excitons and the following hole migration [23,32,36,48,58,73].

As shown in Table 1, the computed Kohn-Sham energy levels of **HTM1-4** are in good agreement with those calculated for Spiro-OMeTAD from Ref. [23] and PTZ2 from Ref. [57]. As required, they are well aligned with the VB and CB of the CH₃NH₃PbI₃ perovskite (−5.43 eV and −3.93 eV, respectively) [37,58,74] suggesting an efficient charge extraction, as well as a reduced electron recombination. Moreover, HOMO levels of **HTM1-4** are in accordance with the experimental HOMO value of Spiro-OMeTAD in CH₂Cl₂ (−5.07 eV) [75].

Additionally, FMOs energies of **HTM1-4** are lower in energy than those of Spiro-OMeTAD calculated at the same level of theory, which should help enhancing the cell V_{oc} [31], and, as reported for Spiro-OMeTAD [23], HOMO and HOMO-1 levels of **HTM1-4** are quasidegenerate.

The inspection of the wavefunction plots of the designed **HTM1-4**, Fig. 5 and Fig. 6, reveals that the LUMO ground-state electron density is confined on the central core of the molecules, while that of the HOMO is fully delocalised over the entire molecules, in line with Spiro-OMeTAD [26] and PTZ2 [57]. Therefore, the formation of excitons and the following hole migration are promoted by the overlapping between HOMO and LUMO orbitals [48,58,73], which indicates that **HTM1-4** should have good intermolecular hole-transport ability.
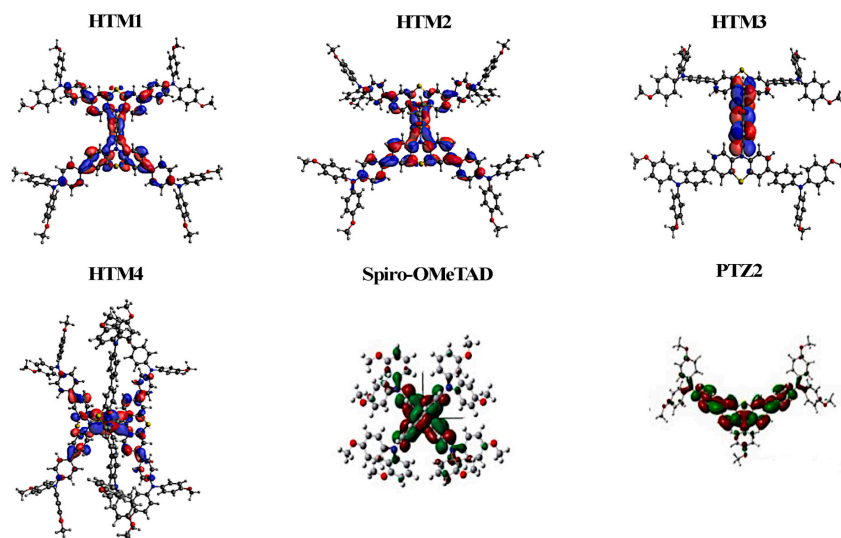

Fig. 5. LUMO DFT ground-state electron density distribution of **HTM1-4** compared to those of Spiro-OMeTAD from Ref. [26] and PTZ2 from Ref. [57].

HTM1   **HTM2**   **HTM3**

HTM4   **Spiro-OMeTAD**   **PTZ2**

Fig. 6. HOMO DFT ground-state electron density distribution of **HTM1-4** compared to those of Spiro-OMeTAD from Ref. [26] and PTZ2 from Ref. [57].
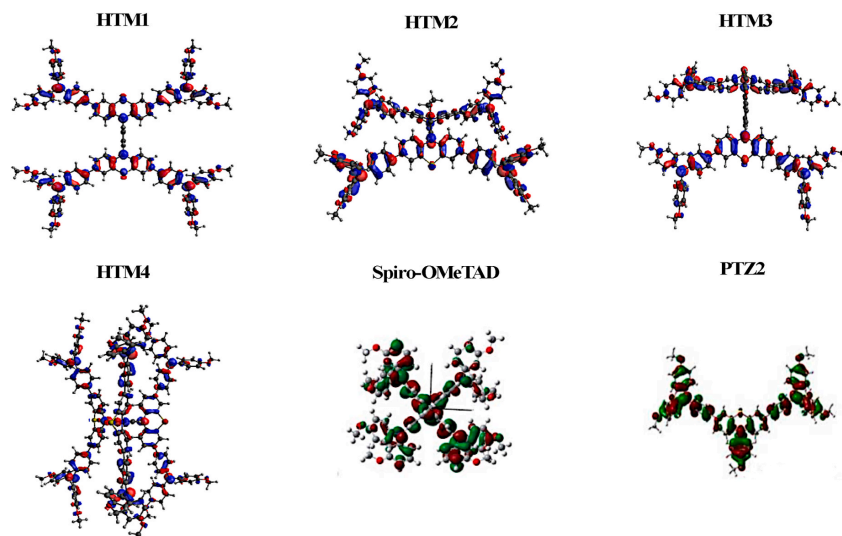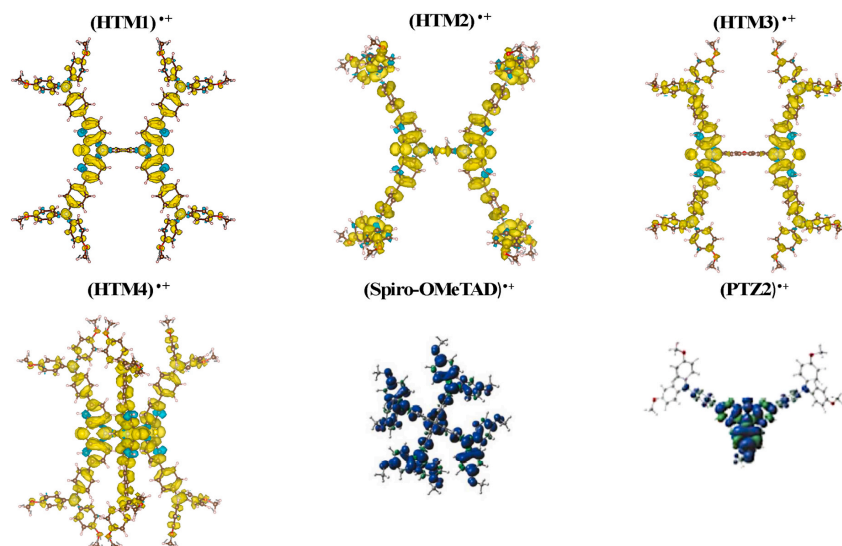
(HTM1)$^{\bullet+}$ **(HTM2)$^{\bullet+}$**   **(HTM3)$^{\bullet+}$**

(HTM4)$^{\bullet+}$ **(Spiro-OMeTAD)$^{\bullet+}$**   **(PTZ2)$^{\bullet+}$**

Fig. 7. TDDFT spin density distribution of (**HTM1-4**)$^{\bullet+}$ compared to those of (Spiro-OMeTAD)$^{\bullet+}$ from Ref. [34] and (PTZ2)$^{\bullet+}$ from Ref. [57].

As the charge transport process involves HTMs also in their radical cation (doublet state) form, to investigate the electronic structure of the oxidized forms of **HTM1-4**, an electron has been removed from the π system and the TDDFT spin density distribution of (**HTM1-4**)$^{\bullet+}$ has been calculated. The results have been compared with those of (Spiro-

OMeTAD)$^{\bullet+}$ from Ref. [34] and (PTZ2)$^{\bullet+}$ from Ref. [57]. Indeed, the excellent ability of Spiro-OMeTAD as HTM has already been ascribed to its wide charge distribution in the radical cation state [34].

The wavefunction plot analysis (Fig. 7) reveals that the singly occupied molecular orbital (SOMO) of (**HTM1-4**)$^{\bullet+}$ has a similar
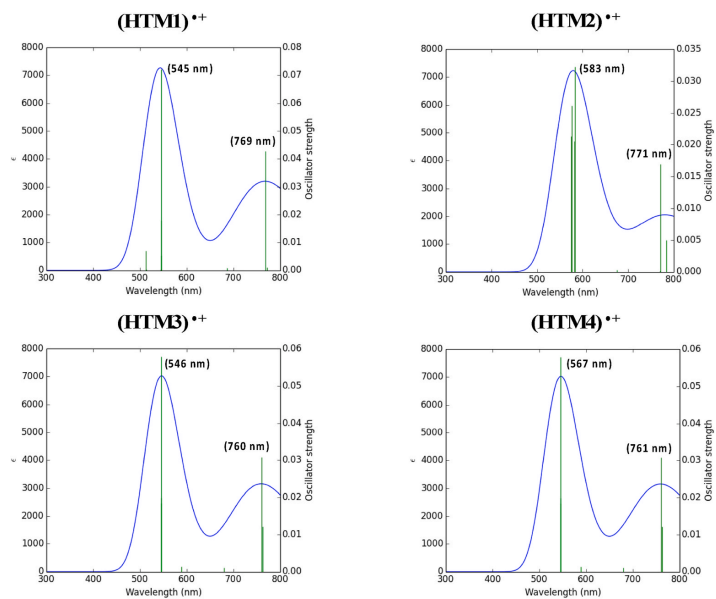
Fig. 8. Simulated TDDFT UV–Vis absorption spectra in CH$_2$Cl$_2$ of **(HTM1-4)**$^{\bullet+}$.
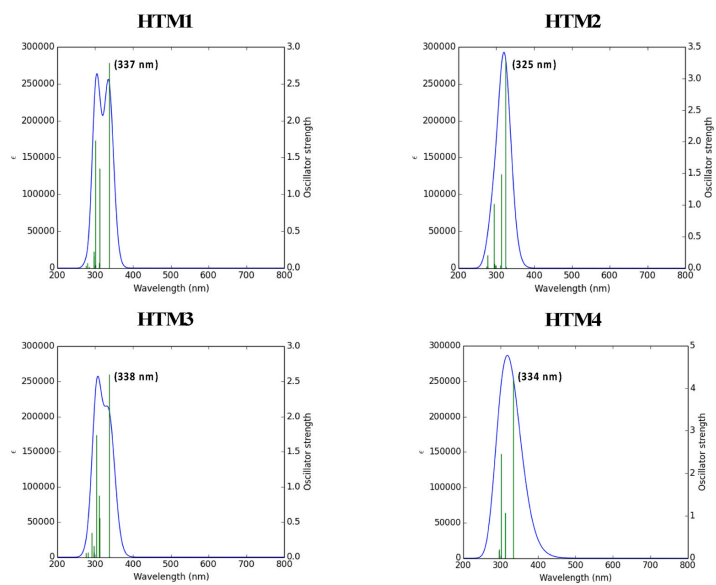

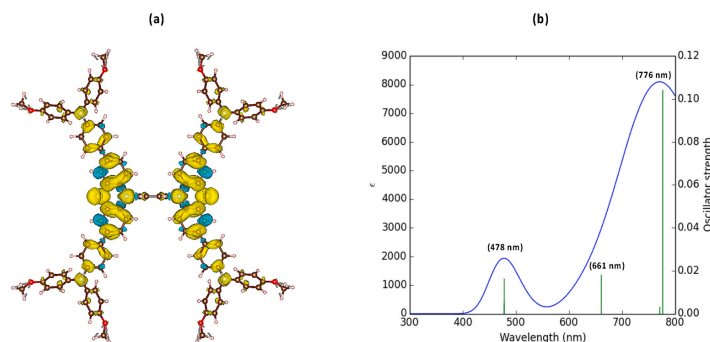**Fig. 9.** Simulated TDDFT UV–Vis absorption spectra in CH$_2$Cl$_2$ of **HTM1-4**.

6

Fig. 10. TD-CAM-B3LYP/6-31G(d,p) spin density distribution (a) and simulated UV–Vis absorption spectrum of **HTM1**$^{2+}$ in CH$_2$Cl$_2$ (b).

electronic structure with respect to its analogue ground-state HOMO, as the spin density is widely delocalised over the entire molecules, reproducing the behavior of (Spiro-OMeTAD)$^{•+}$ [34]. In particular, it is possible to observe that **(HTM2)**$^{•+}$ has the widest charge distribution in the radical cation state. Moreover, the delocalization is more widespread than that of PTZ2. Therefore, this result was a further indication of the favorable hole transport ability of the designed **HTM1-4**.

3.2. UV–Vis vertical excitation properties

The vertical excitation properties of HTMs are considered a decisive factor for estimating the performance of PSCs as well [43]. Indeed, HTMs should have minimal light absorption in the visible spectrum to avoid the competition with the perovskite absorption [7,10,47]. Hence, the first 15 excited states of **(HTM1-4)**$^{•+}$, as well as the first 15 excited states of neutral **HTM1-4**, have been computed, in order to exclude a competition with the perovskite absorption. TD-CAM-B3LYP/6-31G(d, p) absorption maxima (λ_{max}^a), vertical excitation energies (E$_{exc}$) and oscillator strengths (f), computed in CH$_2$Cl$_2$ on B3LYP/6-31G(d,p) minimized structures, of **(HTM1-4)**$^{•+}$ and neutral **HTM1-4** are reported in Table S3 and Table S4 of the Supporting Information, respectively.

Simulated UV–Vis spectra are shown in Fig. 8 and Fig. 9, respectively for **(HTM1-4)**$^{•+}$ and neutral **HTM1-4**.

Considering the radical cation states, the absorption maxima with higher oscillator strengths are in the near-mid infrared region and because they are not of direct interest for this work, they will not be discussed here (Table S3). More significant, the formation of **HTM1-4** radical cations is also evident by the presence of absorption maxima around 500–771 nm, that correspond to the experimental signature of the formation of TPA$^{•+}$ radical cations (Table S3 and Fig. 8) [76]. Even though these absorption maxima could compete with the perovskite absorption, being in the visible region, they have very small oscillator strengths (c.a. 0.01–0.06). Moreover, they are also less intense than those of (Spiro-OMeTAD)$^{•+}$ (oscillator strengths c.a. 0.01–0.79) [23]. The analysis of the TDDFT eigenvectors reveals that these bands involve transitions within the β-orbitals from HOMOs to LUMO, as found for the Spiro-OMeTAD [23].

Concerning the neutral molecules, **HTM1-4** show very intense absorption maxima, having f = 2.79, 3.30, 2.60 and 4.24, respectively for **HTM1**, **HTM2**, **HTM3** and **HTM4** (Fig. 9 and Table S4). Indeed, due to the significant hole and electron distributions overlap present in **HTM1-4** (Figs. 5 and 6), their transition dipole moments are very high, resulting in very high oscillator strengths [74]. In particular, **HTM1** absorption maximum with the highest oscillator strength is at 337 nm (3.68 eV) and it is mainly governed by a HOMO→LUMO transition, while the most

intense **HTM2** absorption maximum is at 325 nm (3.81 eV) and it is largely characterized by a HOMO→LUMO+1 transition. Likewise, **HTM3** absorption maximum with the highest oscillator strength is at 338 nm (3.67 eV), mainly governed by a HOMO-1→LUMO+1 transition, while that of **HTM4** is at 334 nm (3.71 eV), principally corresponding to HOMO→LUMO+2 transition. Other bands, corresponding to higher energy excitations, are present and they are governed by HOMOs→LUMOs transitions (Table S4). All these absorptions in the UV region of the spectrum do not compete with the perovskite absorption and they could also contribute to amplify the short-circuit current density of PSCs [31].

Moreover, to deepen the study of the hole transport ability of **HTM1-4**, which similarly to Spiro-OMeTAD may undergo multiple oxidation processes [23], we investigated the doubly oxidized **(HTM1)**$^{2+}$ (triplet state) features by removing one more electron from neutral **HTM1**. TD-CAM-B3LYP/6-31G(d,p) spin density distribution and simulated UV–Vis absorption spectrum in CH$_2$Cl$_2$ are shown in Fig. 10 and in Table S5.

Even in this case, the spin density is delocalised over the entire molecule in **HTM1**$^{2+}$, confirming its suitable hole transport ability. Moreover, beyond the absorptions in the IR-region (Table S5), **HTM1**$^{2+}$ shows a very weak absorption maximum (f = 0.01) at 478 nm (2.60 eV), while other excited states are found at 661 nm (1.88 eV) and 776 nm (1.58 eV), which found also correspondence in the Spiro-OMeTAD^{2+} [23]. The analysis of the TDDFT eigenvectors reveals that all the transitions involve β-orbitals, and they consist of HOMOs → LUMOs transitions.

3.3. Stability of HTMs

As the degradation of HTMs, and more in general of PSCs, is one of the crucial aspects preventing their commercialization [32], the stability of the designed **HTM1-4** has been estimated and compared with that of

Table 2

Absolute chemical hardness for molecular stability (in eV) of **HTM1-4** and Spiro-OMeTAD, calculated via the adiabatic ionization potential and electron affinity (η^a), and the Koopman's theorem (η^b) at B3LYP/6-311G(d,p) level of theory in CH$_2$Cl$_2$ (using C-PCM).

Molecule	η^a	η^b
HTM1	1.67	1.77
HTM2	1.71	1.80
HTM3	1.52	1.58
HTM4	1.64	1.71
Spiro-OMeTAD	1.55	1.75

7

Spiro-OMeTAD. Theoretically, stability can be evaluated as the absolute chemical hardness, the resistance of a chemical species to change the number of its electrons, according to the formula $\eta = (IP - EA)/2$ (Eq. 1), where IP is the adiabatic ionization potential, while EA is the adiabatic electron affinity. To a larger hardness value has been associated a higher presumed stability [26,31,32,58,74]. Computationally, chemical hardness can be also estimated applying Koopman's theorem, using the formula $\eta = (E_{LUMO} - E_{HOMO})/2$ (Eq. 2), where E_{LUMO} and E_{HOMO} are the Kohn-Sham eigenvalues associated to LUMO and HOMO from an approximate calculation on the neutral species at B3LYP/6-311G(d,p) level of theory (Table 2).

The values of chemical hardness calculated with both methods (η^a and η^b) are similar (Table 2) for all the designed HTMs and follow the order of stability: **HTM2**>**HTM1**>**HTM4**>**HTM3**. In particular, calculations suggest that **HTM2** and **HTM1** could have higher stability than Spiro-OMeTAD, while **HTM4** and **HTM3** could show a similar or slight lower degree of stability.

4. Conclusions

In this work, the *in silico* design of four novel organic triphenylamines and phenothiazine-based HTMs, **HTM1-4**, has been presented. The electronic structures of neutral and oxidized species, the excited state properties and the chemical hardness for molecular stability have been analysed by means of DFT and TDDFT methods, comparing the results with two of the most performant HTMs reported in literature, Spiro-OMeTAD [23,26,34] and PTZ2 [57] (Table S6).

The computed properties suggest that **HTM1-4** could be suitable candidates as HTMs in PSCs. Indeed, they possess HOMO and LUMO energy levels well aligned with VB and CB of the most common perovskite material and, appropriately, the HOMO electron density distribution, as well as the SOMO spin density of radical cation states, are delocalised over the entire molecules, while the LUMO electron density is more localized over the core of **HTM1-4**. All these properties are fundamental to facilitate the hole extraction and to promote the hole transport process, contributing to avoid the electron recombination too. Additionally, neutral **HTM1-4** absorption maxima are in the UV region of the spectrum, thus they do not compete with the perovskite absorption, while (**HTM1-4**)$^{\bullet+}$ have only weak absorptions in the visible range, with very weak oscillator strengths, which correspond to the experimental signature of the formation of the TPA$^{\bullet+}$ radical cations. Moreover, from the evaluation of the absolute chemical hardness, **HTM1-4** show notable stability, with those of **HTM1** and **HTM2** higher than that of Spiro-OMeTAD. Considering all the investigated properties, **HTM1-4** could be valid alternative to Spiro-OMeTAD, similarly to PTZ2, in the construction of potentially efficient PSCs. Ongoing measurements on PSC devices constructed using the designed molecules will hopefully confirm our computational findings.

CRediT authorship contribution statement

Carmen Coppola: Conceptualization, Investigation, Writing – original draft, Writing – review & editing. **Rossella Infantino:** Writing – review & editing. **Alessio Dessì:** Writing – review & editing. **Lorenzo Zani:** Conceptualization, Writing – review & editing. **Maria Laura Parisi:** Writing – review & editing. **Alessandro Mordini:** Writing – review & editing. **Gianna Reginato:** Writing – review & editing. **Riccardo Basosi:** Writing – review & editing. **Adalgisa Sinicropi:** Conceptualization, Writing – original draft, Writing – review & editing, Supervision.

Declaration of competing interest

The authors declare that they have no known competing financial interests or personal relationships that could have appeared to influence the work reported in this paper.

Appendix A. Supplementary data

Supplementary data to this article can be found online at https://doi.org/10.1016/j.matchemphys.2021.125603.

References

[1] A. Kojima, K. Teshima, Y. Shirai, T. Miyasaka, Organometal halide perovskites as visible-light sensitizers for photovoltaic cells, JACS Commun. 131 (2009) 6050–6051, https://doi.org/10.1021/ja809598r.

[2] best-research-cell-efficiencies.20200925.pdf, n.d. https://www.nrel.gov/pv/cell-efficiency.html. (Accessed 12 December 2020).

[3] A decade of perovskite photovoltaics. https://doi.org/10.1038/s41560-018-0323-9, 2019, 4, 20181221.

[4] J. Li, J. Duan, X. Yang, Y. Duan, P. Yang, Q. Tang, Review on recent progress of lead-free halide perovskites in optoelectronic applications, Nano Energy 80 (2021) 105526, https://doi.org/10.1016/j.nanoen.2020.105526.

[5] Y. Zhou, W. Chen, Hybrid organic-inorganic halide perovskites, J. Appl. Phys. 128 (2020) 200401, https://doi.org/10.1063/5.0034825.

[6] M. Grätzel, The light and shade of perovskite solar cells, Nat. Mater. 13 (2014) 838–842, https://doi.org/10.1038/nmat4065.

[7] E. Sheibani, L. Yang, J. Zhang, Recent advances in organic hole transporting materials for perovskite solar cells, Sol. RRL. 4 (2020) 1–16, https://doi.org/10.1002/solr.202000461.

[8] R. Iacobellis, S. Masi, A. Rizzo, R. Grisorio, M. Ambrico, S. Colella, P.F. Ambrico, G. P. Suranna, A. Listorti, L. De Marco, Addressing the function of easily synthesized hole transporters in direct and inverted perovskite solar cells, ACS Appl. Energy Mater. 1 (2018) 1069–1076, https://doi.org/10.1021/acsaem.7b00208.

[9] G.W. Kim, H. Choi, M. Kim, J. Lee, S.Y. Son, T. Park, Hole transport materials in conventional structural (n–i–p) perovskite solar cells: from past to the future, Adv. Energy Mater. 10 (2020), https://doi.org/10.1002/aenm.201903403.

[10] J.Y. Kim, J.W. Lee, H.S. Jung, H. Shin, N.G. Park, High-efficiency perovskite solar cells, Chem. Rev. 120 (2020) 7867–7918, https://doi.org/10.1021/acs.chemrev.0c00107.

[11] P. Vivo, J.K. Salunke, A. Priimagi, Hole-transporting materials for printable perovskite solar cells, Materials (Basel). https://doi.org/10.3390/ma10091087, 2017, 10, 1-45.

[12] A. Fakharuddin, M. Vasilopoulou, A. Soultati, M.I. Haider, J. Briscoe, V. Fotopoulos, D. Di Girolamo, D. Davazoglou, A. Chroneos, A.R. bin Mohd Yusoff, A. Abate, L. Schmidt-Mende, M.K. Nazeeruddin, Robust inorganic hole transport materials for organic and perovskite solar cells: insights into materials electronic properties and device performance, Sol. RRL. 5 (2021) 2000555, https://doi.org/10.1002/solr.202000555.

[13] J. Chen, N.-G. Park, Inorganic hole transporting materials for stable and high efficiency perovskite solar cells, J. Phys. Chem. C 25 (2018) 14039–14063, https://doi.org/10.1021/acs.jpcc.8b01177.

[14] K.C. Wang, P.S. Shen, M.H. Li, S. Chen, M.W. Lin, P. Chen, T.F. Guo, Low-temperature sputtered nickel oxide compact thin film as effective electron blocking layer for mesoscopic NiO/CH3NH3PbI3 perovskite heterojunction solar cells, ACS Appl. Mater. Interfaces 6 (2014) 11851–11858, https://doi.org/10.1021/am503610u.

[15] J.A. Christians, R.C.M. Fung, P.V. Kamat, An inorganic hole conductor for Organo-lead halide perovskite solar cells. Improved hole conductivity with copper iodide, J. Am. Chem. Soc. 136 (2014) 758–764, https://doi.org/10.1021/ja411014k.

[16] S. Ye, W. Sun, Y. Li, W. Yan, H. Peng, Z. Bian, Z. Liu, C. Huang, CuSCN-based inverted planar perovskite solar cell with an average PCE of 15.6, Nano Lett. 15 (2015) 3723–3728, https://doi.org/10.1021/acs.nanolett.5b00116.

[17] N.Y. Nia, F. Matteocci, L. Cinà, A. Di Carlo, High-efficiency perovskite solar cell based on Poly(3-Hexylthiophene): influence of molecular weight and mesoscopic Scaffold layer, ChemSusChem 10 (2017) 3854–3860, https://doi.org/10.1002/cssc.201700635.

[18] T. Matsui, I. Petrikyte, T. Malinauskas, K. Domanski, M. Daskeviciene, M. Steponaitis, P. Gratia, W. Tress, J.P. Correa-Baena, A. Abate, A. Hagfeldt, M. Grätzel, M.K. Nazeeruddin, V. Getautis, M. Saliba, Additive-free transparent Triarylamine-based polymeric hole-transport materials for stable perovskite solar cells, ChemSusChem 9 (2016) 2567–2571, https://doi.org/10.1002/cssc.201600762.

[19] Y. Kim, E.H. Jung, G. Kim, D. Kim, B.J. Kim, J. Seo, Sequentially fluorinated PTAA Polymers for enhancing VOC of high-performance perovskite solar cells, Adv. Energy Mater. 8 (2018) 1–9, https://doi.org/10.1002/aenm.201801668.

[20] N. Van Trang, T.N. Dung, N.T. Cuong, L.T.H. Hai, D. Escudero, M.T. Nguyen, H.M. T. Nguyen, Theoretical study of a class of organic D-π-A dyes for polymer solar cells: influence of various π- spacers, Crystals 10 (2020) 163, https://doi.org/10.3390/cryst10030163.

8

[21] S.N. Habisreutinger, T. Leijtens, G.E. Eperon, S.D. Stranks, R.J. Nicholas, H. J. Snaith, Carbon nanotube/polymer composites as a highly stable hole collection layer in perovskite solar cells, Nano Lett. 14 (2014) 5561–5568, https://doi.org/10.1021/nl501982b.

[22] Z. Li, S.A. Kulkarni, P.P. Boix, E. Shi, A. Cao, K. Fu, S.K. Batabyal, J. Zhang, Q. Xiong, L.H. Wong, N. Mathews, S.G. Mhaisalkar, Laminated carbon nanotube networks for metal electrode-free efficient perovskite solar cells, ACS Nano 8 (2014) 6797–6804, https://doi.org/10.1021/nn501096h.

[23] S. Fantacci, F. De Angelis, M.K. Nazeeruddin, M. Grätzel, Electronic and optical properties of the spiro-MeOTAD hole conductor in its neutral and oxidized forms: a DFT/TDDFT investigation, J. Phys. Chem. C 115 (2011) 23126–23133, https://doi.org/10.1021/jp207968b.

[24] Z. Hawash, L.K. Ono, Y. Qi, Recent advances in spiro-MeOTAD hole transport material and its applications in organic–inorganic halide perovskite solar cells, Adv. Mater. Interfac. 5 (2018) 1–22, https://doi.org/10.1002/admi.201700623.

[25] A.T. Murray, J.M. Frost, C.H. Hendon, C.D. Molloy, D.R. Carbery, A. Walsh, Modular design of SPIRO-OMeTAD analogues as hole transport materials in solar cells, Chem. Commun. 51 (2015) 8935–8938, https://doi.org/10.1039/c5cc02129d.

[26] H. Ashassi-Sorkhabi, P. Salehi-Abar, How the change of OMe substituent position affects the performance of spiro-OMeTAD in neutral and oxidized forms: theoretical approaches, RSC Adv. 8 (2018) 18234–18242, https://doi.org/10.1039/c8ra01879k.

[27] W.-J. Chi, Q.-S. Li, Z.-S. Li, Exploring the electrochemical properties of hole transport materials with spiro-cores for efficient perovskite solar cells from first-principles, Nanoscale 8 (2016) 6146–6154, https://doi.org/10.1039/C6NR00235H.

[28] Q. Jiang, Y. Zhao, X. Zhang, X. Yang, Y. Chen, Z. Chu, Q. Ye, X. Li, Z. Yin, J. You, Surface passivation of perovskite film for efficient solar cells, Nat. Photonics 13 (2019) 460–466, https://doi.org/10.1038/s41566-019-0398-2.

[29] H.D. Pham, T.C.J. Yang, S.M. Jain, G.J. Wilson, P. Sonar, Development of dopant-free organic hole transporting materials for perovskite solar cells, Adv. Energy Mater. 10 (2020) 1903326, https://doi.org/10.1002/aenm.201903326.

[30] B. Li, S. Zhang, F. Xia, Y. Huang, X. Ran, Y. Xia, Y. Chen, W. Huang, Insights into the hole transport properties of LiTFSI-doped spiro-OMeTAD films through impedance spectroscopy, J. Appl. Phys. 128 (2020), 085501, https://doi.org/10.1063/5.0011868.

[31] Z. Sun, S. Feng, C. Gu, C. Nian, J. Liu, Probing effects of molecular conformation on the electronic and charge transport properties in two- and three-dimensional small molecule hole-transporting materials: a theoretical investigation, Phys. Chem. Chem. Phys. 21 (2019) 15206–15214, https://doi.org/10.1039/c9cp01986c.

[32] H. Ashassi-Sorkhabi, P. Salehi-Abar, The role of molecular structure in the functions of novel imidazole-based hole-transporting materials to predict the electrochemical properties of perovskite solar cells: a theoretical approach, J. Mol. Liq. (2020) 114853, https://doi.org/10.1016/j.molliq.2020.114853.

[33] M. Saliba, S. Orlandi, T. Matsui, S. Aghazada, M. Cavazzini, J.-P. Correa-Baena, P. Gao, R. Scopelliti, E. Mosconi, K.-H. Dahmen, F. De Angelis, A. Abate, A. Hagfeldt, G. Pozzi, M. Graetzel, M.K. Nazeeruddin, A molecularly engineered hole-transporting material for efficient perovskite solar cells, Nat. Energy 1 (2016) 15017, https://doi.org/10.1038/nenergy.2015.17.

[34] R. Grisorio, R. Iacobellis, A. Listorti, L. De Marco, M.P. Cipolla, M. Manca, A. Rizzo, A. Abate, G. Gigli, G.P. Suranna, Rational design of molecular hole transporting materials for perovskite solar cells: direct versus inverted device configurations, ACS Appl. Mater. Interfaces 9 (2017) 24778–24787.

[35] Y. Ou, A. Sun, H. Li, T. Wu, D. Zhang, P. Xu, R. Zhao, L. Zhu, R. Wang, B. Xu, Y. Hua, L. Ding, Developing D-π-D hole-transport materials for perovskite solar cells: the effect of the π-bridge on device performance, Mater. Chem. Front. 5 (2021) 876–884, https://doi.org/10.1039/d0qm00719f.

[36] S. Naqvi, A. Patra, Hole transport materials for perovskite solar cells: a computational study, Mater. Chem. Phys. 258 (2021) 123863, https://doi.org/10.1016/j.matchemphys.2020.123863.

[37] Z.Z. Sun, W.L. Ding, S. Feng, X.L. Peng, Tailoring of the core structure towards promising small molecule hole-transporting materials for perovskite solar cells: a theoretical study, Phys. Chem. Chem. Phys. 22 (2020) 16359–16367, https://doi.org/10.1039/d0cp02643c.

[38] B. Xu, J. Zhang, Y. Hua, P. Liu, L. Wang, C. Ruan, Y. Li, G. Boschloo, E.M. J. Johansson, L. Kloo, A. Hagfeldt, A.K.Y. Jen, L. Sun, Tailor-making low-cost spiro [fluorene-9,9′-xanthene]-based 3D Oligomers for perovskite solar cells, Inside Chem. 2 (2017) 676–687, https://doi.org/10.1016/j.chempr.2017.03.011.

[39] I.M. Abdellah, T.H. Chowdhury, J.J. Lee, A. Islam, M.K. Nazeeruddin, M. Gräetzel, A. El-Shafei, Facile and low-cost synthesis of a novel dopant-free hole transporting material that rivals Spiro-OMeTAD for high efficiency perovskite solar cells, Sustain. Energy Fuels 5 (2021) 199–211, https://doi.org/10.1039/d0se01323d.

[40] M. Jeong, I.W. Choi, E.M. Go, Y. Cho, M. Kim, B. Lee, S. Jeong, Y. Jo, H.W. Choi, J. Lee, J.H. Bae, S.K. Kwak, D.S. Kim, C. Yang, Stable perovskite solar cells with efficiency exceeding 24.8% and 0.3-V voltage loss, Science 369 (2020) 1615–1620, https://doi.org/10.1126/science.abb7167, 80-.

[41] R. Hussain, M.Y. Mehboob, M.U. Khan, M. Khalid, Z. Irshad, R. Fatima, A. Anwar, S. Nawab, M. Adnan, Efficient designing of triphenylamine-based hole transport materials with outstanding photovoltaic characteristics for organic solar cells, J. Mater. Sci. 56 (2021) 5113–5131, https://doi.org/10.1007/s10853-020-05567-6.

[42] M. Li, S. Ma, M. Mateen, X. Liu, Y. Ding, J. Gao, Y. Yang, X. Zhang, Y. Wu, S. Dai, Facile donor (D)-π-D triphenylamine-based hole transporting materials with different π-linker for perovskite solar cells, Sol. Energy 195 (2020) 618–625, https://doi.org/10.1016/j.solener.2019.11.071.

[43] M.R.S.A. Janjua, How does bridging core modification alter the photovoltaic characteristics of triphenylamine-based hole transport materials? Theoretical understanding and prediction, Chem. Eur J. 27 (2020) 4197, https://doi.org/10.1002/chem.202004299.

[44] S.A. Siddique, M.B.A. Siddique, R. Hussain, X. Liu, M.Y. Mehboob, Z. Irshad, M. Adnan, Efficient tuning of triphenylamine-based donor materials for high-efficiency organic solar cells, Comput. Theor. Chem. 1191 (2020) 113045, https://doi.org/10.1016/j.comptc.2020.113045.

[45] Z.Z. Sun, M. Hao, S. Feng, W.L. Ding, X.L. Peng, Boosting the performance of D-A-D type hole-transporting materials for perovskite solar cells via tuning the acceptor group, New J. Chem. 44 (2020) 15244–15250, https://doi.org/10.1039/d0nj03306e.

[46] J. Salunke, X. Guo, Z. Lin, J.R. Vale, N.R. Candeias, M. Nyman, S. Dahlström, R. Österbacka, A. Priimagi, J. Chang, P. Vivo, Phenothiazine-based hole-transporting materials toward eco-friendly perovskite solar cells, ACS Appl. Energy Mater. 2 (2019) 3021–3027, https://doi.org/10.1021/acsaem.9b00408.

[47] M.R. Maciejczyk, R. Chen, A. Brown, N. Zheng, N. Robertson, Beyond efficiency: phenothiazine, a new commercially viable substituent for hole transport materials in perovskite solar cells, J. Mater. Chem. C 7 (2019) 8593–8598, https://doi.org/10.1039/c8tc05773g.

[48] F. Zhang, S. Wang, H. Zhu, X. Liu, H. Liu, X. Li, Y. Xiao, S.M. Zakeeruddin, Impact of peripheral groups on phenothiazine-based hole-transporting materials for perovskite solar cells, ACS Energy Lett. 3 (2018) 1145–1152, https://doi.org/10.1021/acsenergylett.8b00291.

[49] X. Liu, X. Tan, Q. Chen, H. Shan, C. Liu, J. Xu, Z.K. Chen, W. Huang, Z.X. Xu, Facile synthesis of a dopant-free hole transporting material with a phenothiazine core for planar perovskite solar cells, RSC Adv. 7 (2017) 53604–53610, https://doi.org/10.1039/c7ra10677g.

[50] X. Ding, C. Chen, L. Sun, H. Li, H. Chen, J. Su, H. Li, H. Li, L. Xu, M. Cheng, Highly efficient phenothiazine 5,5-dioxide-based hole transport materials for planar perovskite solar cells with a PCE exceeding 20, J. Mater. Chem. A 7 (2019) 9510–9516, https://doi.org/10.1039/c9ta00654k.

[51] C. Lu, M. Paramasivam, K. Park, C.H. Kim, H.K. Kim, Phenothiazine functionalized multifunctional A-π-D-π-D-π-A-type hole-transporting materials via sequential C-H Arylation approach for efficient and stable perovskite solar cells, ACS Appl. Mater. Interfaces 11 (2019) 14011–14022, https://doi.org/10.1021/acsami.8b20646.

[52] S. Revoju, A. Matuhina, L. Canil, H. Salonen, A. Hiltunen, A. Abate, P. Vivo, Structure-induced optoelectronic properties of phenothiazine-based materials, J. Mater. Chem. C. 8 (2020) 15486–15506, https://doi.org/10.1039/d0tc03421e.

[53] J. Salunke, X. Guo, M. Liu, Z. Lin, N.R. Candeias, A. Priimagi, J. Chang, P. Vivo, N-substituted phenothiazines as environmentally friendly hole-transporting materials for low-cost and highly stable halide perovskite solar cells, ACS Omega 5 (2020) 23334–23342, https://doi.org/10.1021/acsomega.0c03184.

[54] S. Thokala, S.P. Singh, Phenothiazine-based hole transport materials for perovskite solar cells, ACS Omega 5 (2020) 5608–5619, https://doi.org/10.1021/acsomega.0c00065.

[55] K. Memminger, T. Oeser, T.J.J. Müller, Phenothiazinophanes: synthesis, structure, and intramolecular electronic communication, Org. Lett. 10 (2008) 2797–2800, https://doi.org/10.1021/ol800920d.

[56] D.B. Shinde, J.K. Salunke, N.R. Candeias, F. Tinti, M. Gazzano, P.P. Wadgaonkar, A. Priimagi, N. Camaioni, P. Vivo, Crystallisation-enhanced bulk hole mobility in phenothiazine-based organic semiconductors, Sci. Rep. 7 (2017) 1–10, https://doi.org/10.1038/srep46268.

[57] R. Grisorio, B. Roose, S. Colella, A. Listorti, G.P. Suranna, A. Abate, Molecular tailoring of phenothiazine-based hole-transporting materials for high-performing perovskite solar cells, ACS Energy Lett. 2 (2017) 1029–1034, https://doi.org/10.1021/acsenergylett.7b00054.

[58] Z. Zhang, R. He, Effect of heterocyclic spacer on property of hole-transporting materials with silafluorene core for perovskite solar cells, Comput. Theor. Chem. 1161 (2019) 10–17, https://doi.org/10.1016/j.comptc.2019.06.002.

[59] Q. Yan, Y. Guo, A. Ichimura, H. Tsuji, E. Nakamura, Three-dimensionally homoconjugated carbon-bridged oligophenylenevinylene for perovskite solar cells, J. Am. Chem. Soc. 138 (2016) 10897–10904, https://doi.org/10.1021/jacs.6b04002.

[60] M.J. Frisch, G. Trucks, H.B. Schlegel, G.E. Scuseria, M.A. Robb, J.R. Cheeseman, G. Scalmani, V. Barone, B. Mennucci, G.A. Petersson, H. Nakatsuji, M. Caricato, X. Li, H.P. Hratchian, A.F. Izmaylov, J. Bloino, G. Zheng, J.L. Sonnenberg, M. Hada, M. Ehara, K. Toyota, R. Fukuda, J. Hasegawa, M. Ishida, T. Nakajima, Y. Honda, O. Kitao, H. Nakai, T. Vreven, J.A. Montgomery Jr., J.E. Peralta, F. Ogliaro, M. Bearpark, J.J. Heyd, E. Brothers, K.N. Kudin, V.N. Staroverov, T. Keith, R. Kobayashi, J. Normand, K. Raghavachari, A. Rendell, J.C. Burant, S.S. Iyengar, J. Tomasi, M. Cossi, N. Rega, J.M. Millam, M. Klene, J.E. Knox, J.B. Cross, V. Bakken, C. Adamo, J. Jaramillo, R. Gomperts, R.E. Stratmann, O. Yazyev, A. J. Austin, R. Cammi, C. Pomelli, J.W. Ochterski, R.L. Martin, K. Morokuma, V. G. Zakrzewski, G.A. Voth, P. Salvador, J.J. Dannenberg, S. Dapprich, A.D. Daniels, O. Farkas, J.B. Foresman, J.V. Ortiz, J. Cioslowski, D.J. Fox, Gaussian 09 , Revision C.01, Gaussian, Inc., Wallingford, CT, USA, 2010.

[61] P. Hohenberg, W. Kohn, Inhomogeneous electron gas, Phys. Rev. B 7 (1973) 1912–1919, https://doi.org/10.1103/PhysRevB.7.1912.

[62] W. Kohn, L.J. Sham, Self-consistent equations including exchange and correlation effects, Phys. Rev. 140 (1965) A1134–A1138, https://doi.org/10.1103/PhysRev.140.A1133.

[63] A.D. Becke, Density-functional thermochemistry. III. The role of the exact exchange, J. Chem. Phys. 98 (1993) 5648, https://doi.org/10.1063/1.464913.

[64] C. Lee, W. Yang, R.G. Parr, Development of Colle-Salvetti correlation-energy formula into a functional of the electron density, Phys. Rev. B 37 (1988) 785–789, https://doi.org/10.1103/PhysRevB.37.785.

[65] J. Tomasi, B. Mennucci, R. Cammi, Quantum mechanical continuum solvation models, Chem. Rev. 105 (2005) 2999–3093, https://doi.org/10.1021/cr9904009.

[66] M. Cossi, N. Rega, G. Scalmani, V. Barone, Energies, structures, and electronic properties of molecules in solution with the C-PCM solvation model, J. Comput. Chem. 24 (2003) 669–681.

[67] C. Adamo, D. Jacquemin, The calculations of excited-state properties with time-dependent density functional theory, Chem. Soc. Rev. 42 (2013) 845–856, https://doi.org/10.1039/c2cs35394f.

[68] A.D. Laurent, C. Adamo, D. Jacquemin, Dye chemistry with time-dependent density functional theory, Phys. Chem. Chem. Phys. 16 (2014) 14334–14356, https://doi.org/10.1039/c3cp55336a.

[69] T. Yanai, D.P. Tew, N.C. Handy, A new hybrid exchange-correlation functional using the Coulomb-attenuating method (CAM-B3LYP), Chem. Phys. Lett. 393 (2004) 51–57, https://doi.org/10.1016/j.cplett.2004.06.011.

[70] R. Shankar, K. Senthilkumar, P. Kolandaivel, Calculation of ionization potential and chemical hardness: a comparative study of different methods, Int. J. Quant. Chem. 109 (2009) 764–771, https://doi.org/10.1002/qua.

[71] T. Koopmans, Über die Zuordnung von Wellenfunktionen und Eigenwerten zu den Einzelnen Elektronen Eines Atoms, Physica 1 (1934) 104–113, https://doi.org/10.1016/S0031-8914(34)90011-2.

[72] N.M.O. Boyle, A.L. Tenderholt, K.M. Langner, Software News and Updates cclib : A Library for Package-Independent Computational Chemistry Algorithms. https://doi.org/10.1002/jcc, 2008, 29, 839-845.

[73] C. Chen, X. Ding, H. Li, M. Cheng, H. Li, L. Xu, F. Qiao, H. Li, Highly efficient phenoxazine core unit based hole transport materials for hysteresis-free perovskite solar cells, ACS Appl. Mater. Interfaces. 10 (2018) 36608–36614, https://doi.org/10.1021/acsami.8b12678.

[74] Q. Wang, Z. Zeng, Y. Li, X. Chen, Efficient strategies for improving the performance of EDOT derivatives and TPA derivatives-based hole transport materials for perovskite solar cells, Sol. Energy. 208 (2020) 10–19, https://doi.org/10.1016/j.solener.2020.06.117.

[75] P. Ganesan, K. Fu, P. Gao, I. Raabe, K. Schenk, R. Scopelliti, J. Luo, L.H. Wong, M. Grätzel, M.K. Nazeeruddin, A simple spiro-type hole transporting material for efficient perovskite solar cells, Energy Environ. Sci. 8 (2015) 1986–1991, https://doi.org/10.1039/c4ee03773a.

[76] S. Amthor, B. Noller, C. Lambert, UV/Vis/NIR spectral properties of triarylamines and their corresponding radical cations, Chem. Phys. 316 (2005) 141–152, https://doi.org/10.1016/j.chemphys.2005.05.009.

4.2. Manuscript 2: **"Electronic structure and interfacial features of triphenylamine- and phenothiazine-based hole transport materials for methylammonium lead iodide perovskite solar cells"**

Authors: C. Coppola, A. Pecoraro, A. B. Muñoz-García, R. Infantino, A. Dessì, G. Reginato, R. Basosi, A. Sinicropi, and M. Pavone.
Publication: submitted, 2022.

In this section, the results of a first-principles investigation of the interfacial electronic properties between the recently designed **HTM1** (See Section 4.1) and the most popular MAPI perovskite are presented. Noteworthy, the design of novel HTMs should be accompanied by the study of their electronic properties that could be strongly influenced by the interaction with the perovskite material. Currently, the phenomena occurring at the interface are still not fully understood [1] and, in particular, the interfacial properties of MAPI/HTMs based on both TPA and PTZ moieties have never been investigated so far. Additionally, only few computational studies exploring the interfacial behavior of the *state-of-the-art* **Spiro-OMeTAD** with the MAPI are present [2-5]. For these reasons, in this work the interfacial phenomena of the system **HTM1**/MAPI have been investigated and compared to those of **Spiro-OMeTAD**/MAPI and **PTZ1,2**/MAPI [6]. The results of this study confirm the suitability of **HTM1** as HTM. Additionally, it has been proven that it has good interaction phenomena with MAPI, but this is not enough to guarantee an effective hole transport process. An inadequate driving force for the hole injection/extraction has been also found for **Spiro-OMeTAD**/MAPI and **PTZ1** and **PTZ2**/MAPI, showing that the binding motif is not the only parameter influencing the charge transport process, while the perovskite composition has also an important impact. The difficulty in applying MAPI for real devices' fabrication with TPA and PTZ-based HTMs is thus supported, in agreement with experimental results obtained in collaboration with ICCOM-CNR and CHOSE [7].

Computational details
Neutral and oxidized geometries of **HTM1**, **Spiro-OMeTAD**, **PTZ1** and **PTZ2** have been optimized by means of Density Functional Theory (DFT) [8,9] at B3LYP/6-31G(d,p) [10,11] and PBE/6-31G(d,p) [12] levels of theory in *vacuo,* including dispersion

forces within the Grimme's D3 framework [13] and using the damping scheme by Becke and Johnson (D3BJ) [14,15], as implemented in Gaussian 16, Revision C.01 suite of programs [16]. Frequency calculations have been performed at the same levels of theory to check that stationary points were true energy minima.

The reorganization energies of compounds **HTM1**, **Spiro-OMeTAD**, **PTZ1** and **PTZ2** have been calculated at PBE/6-31G(d,p) and B3LYP/6-31G(d,p) levels of theory in *vacuo* and in toluene on the lowest energy neutral and oxidized optimized geometries at PBE/6-31G(d,p) and B3LYP/6-31G(d,p) levels of theory, respectively. The adiabatic potential energy surface method has been employed (Eq. 4.2.1) [17, 18] and the solvent effects have been included by using the polarizable continuum model (PCM) [19]:

$$\lambda = (E_0^* - E_0) + (E_+^* - E_+) \quad \text{(Eq. 4.2.1)}$$

where E_0^* is the total energy of the neutral molecule at the cation geometry, E_0 represents the total energy of the neutral molecule, E_+^* stands for the total energy of the cation at the neutral molecule geometry and E_+ is the total energy of the cation.

The oxidation potentials (G_{ox}) in *vacuo* of compounds **HTM1**, **Spiro-OMeTAD**, **PTZ1** and **PTZ2** have been calculated at PBE/6-31G(d,p) and B3LYP/6-31G(d,p) levels of theory as reported in Eq. 4.2.2:

$$G_{OX} = G^0 - G^+ \quad \text{(Eq. 4.2.2)}$$

where G^0 stands for the free energy of the neutral molecules and G^+ represents the free energy of the oxidized molecules.

Compounds **HTM1**, **Spiro-OMeTAD**, **PTZ1** and **PTZ2** have been further optimized with Periodic Boundary Conditions (PBC), as well as the cubic structure of the MAPI bulk, to investigate the electronic properties at HTMs/MAPI interface. DFT-GGA-PBE level of theory implemented in SIESTA 4.1 program package [20] has been employed, together with DZP basis set, including $5d^{10}$ semicore electrons for Pb atoms [21], and Troullier-Martins norm-conserving pseudopotentials [22]. A mesh cutoff of 400 Ry and 1 x 1 x 1 and 8 x 8 x 8 Γ–centered Monkhorst-Pack k-point grids for sampling the BZ have been considered to optimize the four compounds and the MAPI bulk, respectively. The two symmetric (non-stochiometric) 5-layers slabs of the MAPI (001) surface, identified as MAPI:MAI and MAPI:PbI$_2$, and the HTMs/MAPI energy minima have been

optimized at GGA-PBE, using DZP basis set (including $5d^{10}$ semicore electrons for Pb atoms) and Troullier-Martins norm-conserving pseudopotentials. A mesh cutoff of 400 Ry and 8 x 8 x 1 and 1 x 1 x 1 Γ–centered Monkhorst-Pack k-point grids have been considered respectively for the optimization of MAPI slabs and HTMs/MAPI energy minima. SCF energy threshold and total forces threshold have been set at 10^{-5} eV and 0.01 eV·Å-1, respectively, for each geometry optimization. HTMs/MAPI binding energies have been determined through single point calculations on the optimized systems at 8 x 8 x 1 Γ–centered Monkhorst-Pack k-point grid as follows (Eq. 4.2.3):

$$E_{binding} = E_{interface} - E_{MAPI} - E_{molecule} \quad (\text{Eq. } 4.2.3)$$

where $E_{interface}$ is the energy of the HTMs/MAPI system, E_{MAPI} is the energy of the isolated MAPI slabs and $E_{molecule}$ is the energy of the isolated HTMs.

Dispersion forces calculated by D3BJ damping scheme have been included to correct the energies of all the investigated systems.

Results

The molecular structures of the four considered compounds (**HTM1**, **Spiro-OMeTAD**, **PTZ1** and **PTZ2**) are shown in Figure 4.2.1.
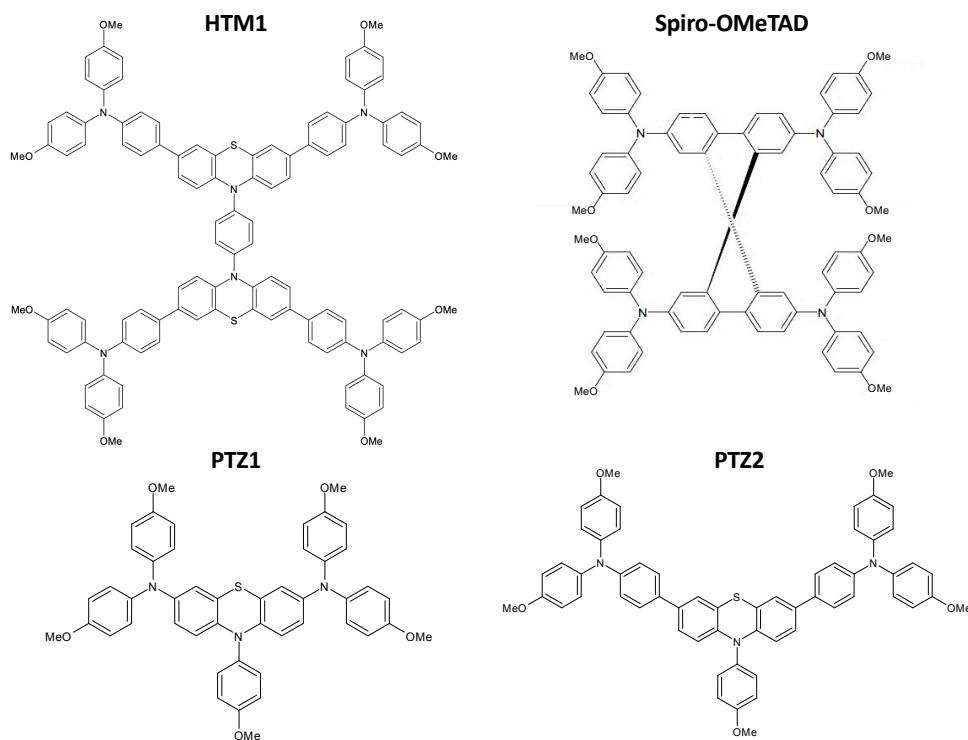
Figure 4.2.1. Molecular structures of compounds **HTM1**, **Spiro-OMeTAD**, **PTZ1** and **PTZ2**.

The reorganization energy λ can strongly influence the hole transport behavior of HTMs. Indeed, the smaller is λ, more rapid could be the hole transport, according to Marcus theory [17,18,23,24]. λ can be separated into internal reorganization energy (λ_{in}) and external reorganization energy (λ_{ext}). Here, only the contribution from λ_{in} is considered, as it represents the energy related to changes occurring in molecules' nuclear coordinates during the charge transfer, while λ_{ext} is often neglected as it accounts for the effect of the polarized medium on the charge transfer and it is usually small [17,18]. The reorganization energies of compounds **HTM1**, **Spiro-OMeTAD**, **PTZ1** and **PTZ2** calculated in *vacuo* and in toluene are shown in Table 4.2.1. It can be noticed that the values have the same trend at both levels of theory and mediums. Additionally, data computed at B3LYP/6-31G(d,p) for **Spiro-OMeTAD** agree with those reported in literature by Chi *et al.* at B3LYP/6-31G(d,p) in dichloromethane (0.131 eV) [25]. λ values follow this order: **HTM1** < **Spiro-OMeTAD** < **PTZ2** < **PTZ1**, indicating that **HTM1** may have a good hole mobility, hence it could be used without the addition of dopants for the construction of devices, differently from the other three HTMs, whose usage in combination with p-doping has already been reported in literature [6,26].

64

Table 4.2.1. Reorganization energies (λ in eV) in *vacuo* and in toluene of **HTM1**, **Spiro-OMeTAD**, **PTZ1** and **PTZ2** calculated at PBE/6-31G(d,p) and B3LYP/6-31G(d,p) levels of theory, including the solvent effects by PCM.

Molecule	λ (eV) PBE/6-31G(d,p)		λ (eV) B3LYP/6-31G(d,p)	
	#	$	#	$
HTM1	0.064	0.061	0.092	0.090
Spiro-OMeTAD	0.087	0.076	0.132	0.120
PTZ1	0.233	0.222	0.381	0.372
PTZ2	0.139	0.132	0.217	0.213

Calculated values in *vacuo*

$ Calculated values in toluene

To further investigate the suitability of HTMs in PSCs, it is important to check if their oxidation potentials (G_{ox}) are well aligned with the VB of MAPI [17,27]. For this reason, the G_{ox} in *vacuo* of **HTM1** has been calculated at PBE/6-31G(d,p) and B3LYP/6-31G(d,p) levels of theory and it has been compared to calculated G_{ox} of **Spiro-OMeTAD**, **PTZ1** and **PTZ2** calculated at the same levels of theory (Table 4.2.2).

Table 4.2.2. Oxidation potentials (G_{ox} in eV) in *vacuo* of **HTM1**, **Spiro-OMeTAD**, **PTZ1** and **PTZ2** calculated at PBE/6-31G(d,p) and B3LYP/6-31G(d,p) levels of theory.

Molecule	G_{ox}(eV) PBE/6-31G(d,p)	G_{ox} (eV) B3LYP/6-31G(d,p)
HTM1	-4.48	-4.99
Spiro-OMeTAD	-4.61	-5.00
PTZ1	-4.66	-4.95
PTZ2	-4.71	-5.10

Table 4.2.2 shows that the obtained G_{ox} values follow the trend expected for both DFT functionals: pure functionals, such as PBE, tend to underestimate G_{ox}, while the increase of the Hartree-Fock exchange increases G_{ox} values, as recently reported by Wang et al. [28]. The calculated G_{ox} of **Spiro-OMeTAD** at B3LYP/6-31G(d,p) is in agreement with that reported by Wang et al. (-4.98) and with its experimental oxidation potential (-5.09 eV in CH_2Cl_2) [5], while those of **PTZ1** and **PTZ2** are in accordance with the experimental oxidation potentials at -4.77 eV and -5.15 eV reported by Grisorio et al. [6]. G_{ox} values of **HTM1** are very similar to those of the other three compounds and they are higher in energy than the VB of MAPI (-5.4 eV) [27]. All these results confirm that

HTM1 is a valid candidate as HTM in PSCs. To further investigate HTM1 potential applicability in MAPI solar cells, its electronic properties at the interface with MAPI have been characterized here. In this regard, the cubic structure (*Pm3m*) of MAPI bulk, the most stable by single-crystal X-ray diffraction analysis, has been fully optimized at GGA-PBE level of theory. The lattice constants resulted to be *a*=6.256 Å, in very good agreement with the experimental ones (*a*=6.276 Å) [29]. The MAPI (001) surface, one of the most stable of cubic and tetragonal phases [2,30], has been selected to build the two symmetric (non-stochiometric) slabs with the two possible MAPI terminations: the MAPI:PbI$_2$ and the MAPI:MAI. A surface energy convergence test has been carried out considering slabs composed of 5, 7 and 9 crystal planes. The surface's energy ($E_{surface}$) is calculated as reported in Eq. 4.2.4, where E_{slab}^{MAI} and $E_{slab}^{PbI_2}$ are the energy of the MAI- and the PbI$_2$-terminated slabs, while E_{bulk} is the energy of the MAPI unit cell. The energies of the considered slabs are reported in Table 4.2.3.

$$E_{surface} = \frac{(E_{slab}^{MAI}+E_{slab}^{PbI_2})-E_{bulk}}{2*Area_{slab}} \quad \text{(Eq. 4.2.4)}$$

Table 4.2.3. Surface's energy (in eV/Å^2) of 5, 7 and 9-layers MAPI (001) slabs.

Slab	$E_{surface}$ (eV/Å^2)	$E_{surface}$ including D3BJ (eV/Å^2)
5-layers	1.97	0.03
7-layers	1.45	0.02
9-layers	2.24	0.03

As reported in Table 4.2.3, the surface's energy of the 5-layers slab of MAPI (001) converged. Hence, as it represents a good compromise between accuracy and computational costs, it has been used to build the supercells for the investigation of the adsorption mechanisms of the considered molecules.

The MAPI bulk structure and the symmetric 5-layers slabs of MAPI:PbI$_2$ and MAPI:MAI here considered are reported in Figure 4.2.2.

(a) unit cell of cubic MAPI
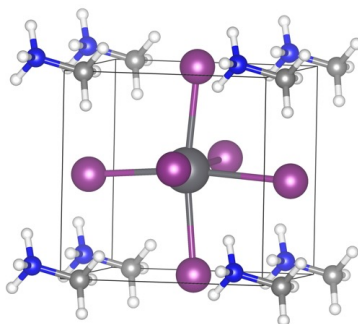
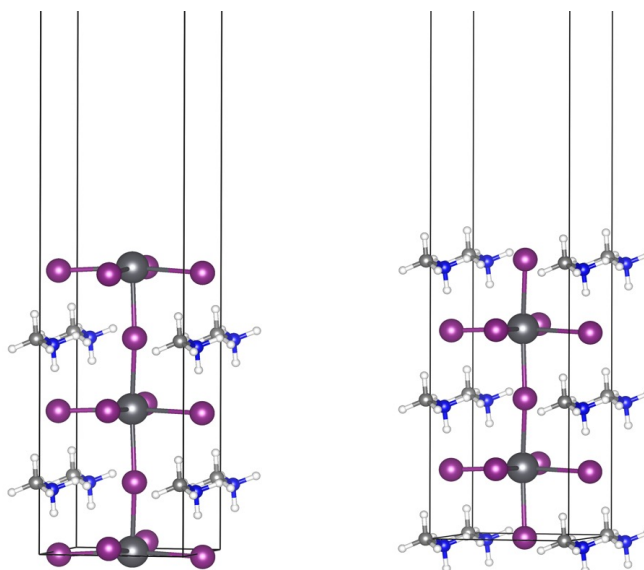**(b) MAPI:PbI$_2$**   **(c) MAPI:MAI**

Figure 4.2.2. (a) MAPI unit cell; 5-layers slabs of (b) MAPI:PbI$_2$ and (c) MAPI:MAI. Color label of atomic spheres: Pb-dark gray; I-violet; C-light grey; N-blue; H-white.

Supercells of 7 x 7 for **HTM1**, 4 x 4 for **Spiro-OMeTAD** and **PTZ1** and 6 x 6 for **PTZ2** for each MAPI termination have resulted to be large enough to accommodate the molecules. In order to account for the molecules' complex structures and to obtain reliable energy minima for each termination, **HTM1, PTZ1** and **PTZ2** have been placed on the MAPI (001) surface considering two possible orientations: in the down orientation the PTZ moieties are exposed on the MAPI surface, while in the up orientation are the methoxybenzene of TPA moieties to be exposed (Figures 4.2.3, 4.2.4, 4.2.6. and 4.2.7). Considering **Spiro-OMeTAD**, it is known that it interacts with the MAPI by exposing the methoxybenzene of the arylamine moieties [2-5], hence the up and down orientations are referred to the exposition of the methoxybenzene of the two different facets of the 9,9'-spirobifluorene core. The energy minima of HTMs/MAPI:PbI$_2$ and

HTMs/MAPI:MAI systems have been found by moving the molecules at different distances on the MAPI (001) surface. During this process, neither the molecules nor the surface atoms have been allowed to relax. Indeed, only the energy minima for each system have been optimized and their binding energies have been calculated according to Eq. 4.2.3. The binding energies considering both up and down orientations of **HTM1**/MAPI:PbI$_2$ and **HTM1**/MAPI:MAI are shown in Table 4.2.4. For **Spiro-OMeTAD**/MAPI, **PTZ1**/MAPI and **PTZ2**/MAPI, only the binding energies of the most stable interface for each MAPI termination are reported (Table 4.2.4).

Table 4.2.4. Binding energies (E$_{binding}$ in eV) of the considered systems calculated at GGA-PBE, including D3BJ dispersion forces.

Interface	E$_{binding}$ (eV)
HTM1/MAPI:PbI$_2$ (up)	-1.49
HTM1/MAPI:PbI$_2$ (down)	-1.00
HTM1/MAPI:MAI (up)	-5.01
HTM1/MAPI:MAI (down)	-2.63
Spiro-OMeTAD/MAPI:PbI$_2$ (down)	-2.83
Spiro-OMeTAD/MAPI:MAI (down)	-2.14
PTZ1/MAPI:PbI$_2$ (up)	-1.61
PTZ1/MAPI:MAI (up)	-2.99
PTZ2/MAPI:PbI$_2$ (down)	-7.30
PTZ2/MAPI:MAI (down)	-6.08

The results in Table 4.2.4 reveal that for **HTM1**/MAPI:PbI$_2$ the interaction is stabilized when **HTM1** adopts the up orientation, i.e. when the methoxybenzene of the TPA moieties are exposed on the MAPI surface. In this case, some distortions in the overall MAPI surface are present (Figure 4.2.3 (a)). On the other hand, when **HTM1** adopts the down orientation, the resulting interaction with the MAPI (001) surface is promoted by the sulfur atoms of the PTZ moieties and it is just a localized event, hence the binding energy results to be higher (less negative) than in the previous case (Figure 4.2.3 (b)). The electronic properties of **HTM1**/MAPI:PbI$_2$ systems have also been analyzed in terms of projected Density of States (pDOS), and they are reported in Figure 4.2.3 (c,d). Despite **HTM1** has a good interaction with the MAPI:PbI$_2$ surface, in particular when it adopts the up orientation, from the pDOS plots emerge that the VB of MAPI has always higher energy than the HOMO level of **HTM1**. This outcome suggests that the hole has not the sufficient driving force to be injected into **HTM1** and undesired charge recombination events can occur.
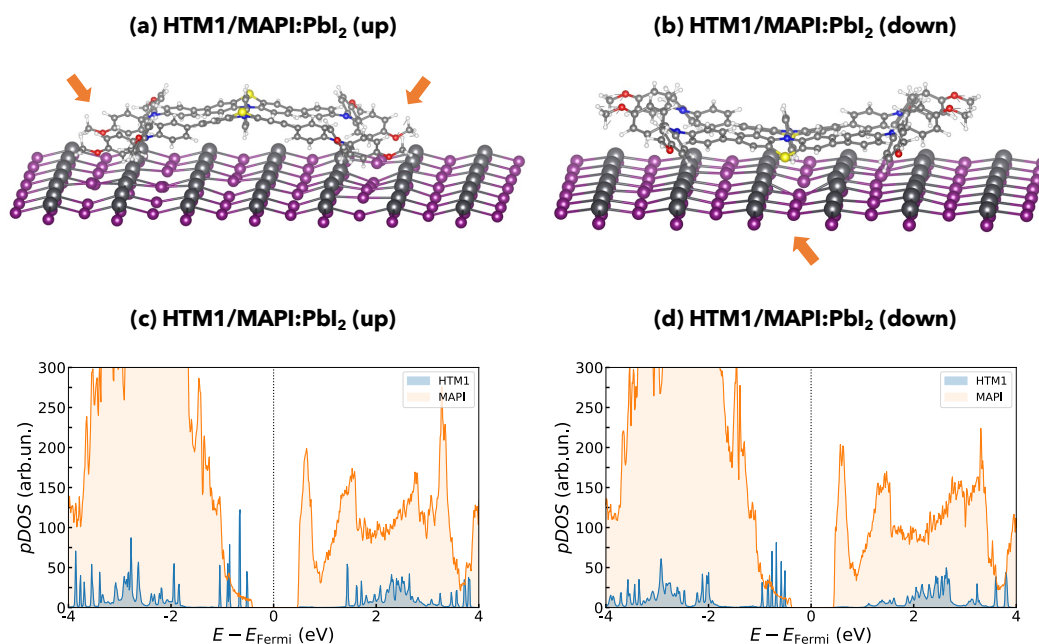
(a) HTM1/MAPI:PbI₂ (up)

(b) HTM1/MAPI:PbI₂ (down)

(c) HTM1/MAPI:PbI₂ (up)

(d) HTM1/MAPI:PbI₂ (down)

Figure 4.2.3. Energy minima of: (a) **HTM1**/MAPI:PbI$_2$ (up), (b) **HTM1**/MAPI:PbI$_2$ (down) and pDOS plots of (c) **HTM1**/MAPI:PbI$_2$ (up) and (d) **HTM1**/MAPI:PbI$_2$ (down). Color label of atomic spheres: Pb-dark gray; I-violet; C-light grey; N-blue; H-white; O-red; S-yellow.
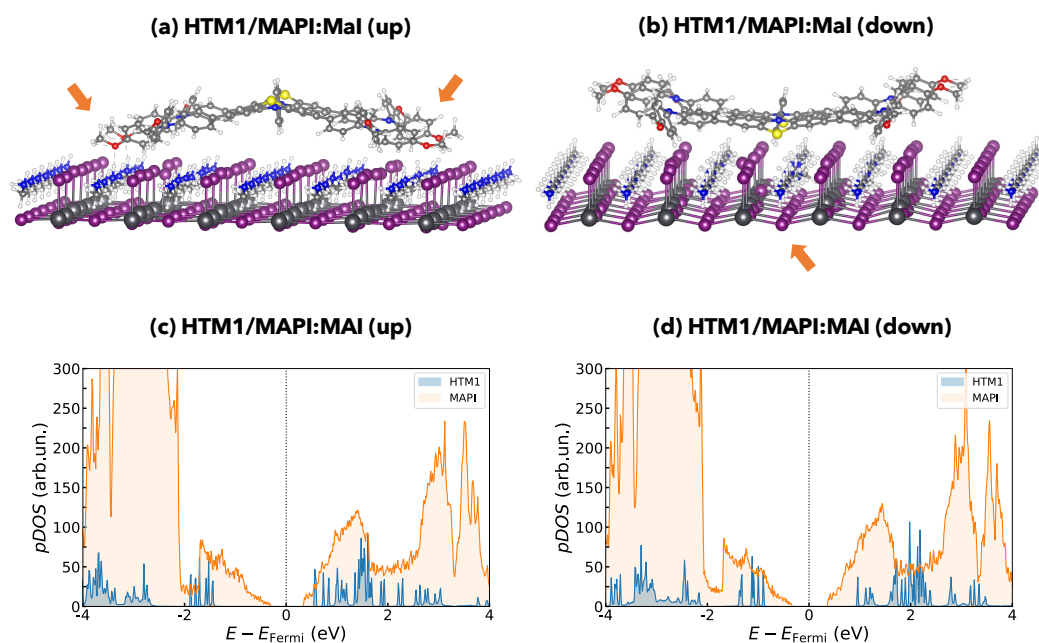
(a) HTM1/MAPI:MaI (up)

(b) HTM1/MAPI:MaI (down)

(c) HTM1/MAPI:MAI (up)

(d) HTM1/MAPI:MAI (down)

Figure 4.2.4. Energy minima of: (a) **HTM1**/MAPI:MAI (up), (b) **HTM1**/MAPI:MAI (down) and pDOS plots of (c) **HTM1**/MAPI:MAI (up) and (d) **HTM1**/MAPI:MAI (down). Color label of atomic spheres: Pb-dark gray; I-violet; C-light grey; N-blue; H-white; O-red; S-yellow.

The binding energies of **HTM1**/MAPI:MAI are lower (more negative) that those of **HTM1**/MAPI:PbI$_2$ systems. However, even for this MAPI termination, the interaction is favored when **HTM1** exposes the methoxybenzene of the TPA moieties (up orientation). Additionally, in this last case, the binding energy results to be the most stabilized thanks to the formation of hydrogen bonds between the oxygen atoms of **HTM1** methoxybenzene moieties and the hydrogen atoms of MAPI methylammonium cations (Figure 4.2.4(a)). On the other side, when **HTM1** adopts the down orientation exposing the PTZ moieties, the sulfur atoms are responsible for a localized interaction with the MAPI surface, as occurs also for the PbI$_2$- termination (Figure 4.2.4(b)). Looking at the pDOS plots (Figure 4.2.4(c,d)), it can be noticed that the VB of MAPI always lies at higher energy than the HOMO level of **HTM1** and this finding is also more evident with respect to what reported for the PbI$_2$- termination. Hence, it is possible to affirm again that there is not the adequate driving force for the hole injection/extraction. Considering these results, the chemical doping of **HTM1** could be considered as a valid approach to increase its HOMO energy level when MAPI is adopted for the construction of PSCs devices. Nevertheless, two aspects should be considered: i) the doping could lead to perovskite degradation [1,27,31,32]; ii) isolated **HTM1** possesses optimal properties to be used as dopant-free HTM. For these reasons, the exploration of different perovskite compositions could allow to understand the real potential of this molecule in PSCs devices. Indeed, **HTM1** has recently been synthetized, fully characterized, and investigated as a dopant-free HTM in a methylammonium-free p-i-n PSC together with our collaborators at ICCOM-CNR and CHOSE [7, see also Appendix B]. The PSC built with **HTM1** and Cs$_{0.17}$FA$_{0.83}$Pb(I$_{0.9}$Br$_{0.1}$)$_3$ perovskite achieved the 17.26% of PCE, while that obtained employing the standard PTAA in the same experimental conditions resulted to be 17.96% [7]. This result confirms our computational findings: **HTM1** has a great potential as HTM, and the perovskite formulation has an important impact on the hole transport process.

The energy minima of **Spiro-OMeTAD**/MAPI are shown in Figure 4.2.5. The lowest binding energy values have been found when the molecule has the down orientation on both PbI$_2$- and the MAI-exposing facets of MAPI. Indeed, the oxygens of methoxybenzene moieties interact with the Pb atoms of the MAPI in **Spiro-OMeTAD**/MAPI:PbI$_2$ (Figure 4.2.5(a)) and with the hydrogens of methylammonium cations in **Spiro-OMeTAD**/MAPI:MAI (Figure 4.2.5(b)). From the pDOs plots (Figure 4.2.5(c,d)), it emerges that the HOMO of **Spiro-OMeTAD** has the same energy of the

VB of MAPI considering the **Spiro-OMeTAD**/MAPI:PbI$_2$ system, while its HOMO level has lower energy than the VB of MAPI in **Spiro-OMeTAD**/MAPI:MAI system. Hence, also in the case of **Spiro-OMeTAD** interacting with the (001) surface of cubic MAPI, there is not the adequate driving force for the hole injection/extraction.
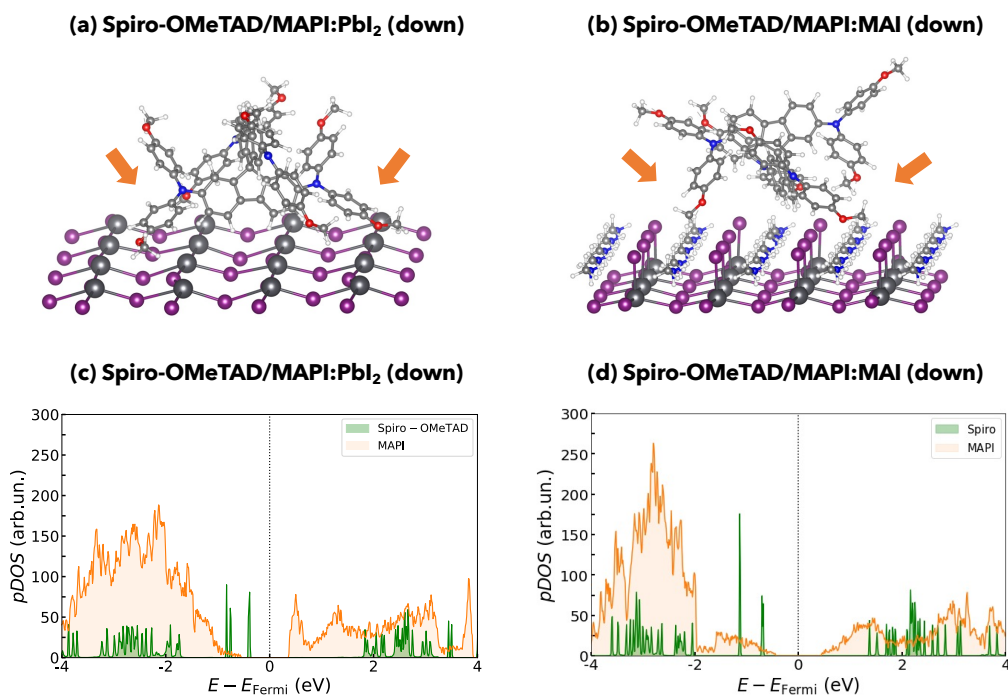

Figure 4.2.5. Energy minima of: (a) **Spiro-OMeTAD**/MAPI:PbI$_2$ (down), (b) **Spiro-OMeTAD**/MAPI:MAI (down) and pDOS plots of (c) **Spiro-OMeTAD**/MAPI:PbI$_2$ (down) and (d) **Spiro-OMeTAD**/MAPI:MAI (down). Color label of atomic spheres: Pb-dark gray; I-violet; C-light grey; N-blue; H-white; O-red.

Considering the energy minima of **PTZ1**/MAPI (Figure 4.2.6(a,b)), the interaction is favored when the molecule adopts the up orientation, i.e. exposing the methoxybenzene of arylamines moieties on both MAPI surface terminations. In particular, the most negative binding energy is associated to **PTZ1**/MAPI:MAI (up) and it is justified by the formation of hydrogen bonds between the oxygens of **PTZ1** methoxybenzene moieties and the hydrogens of MAPI methylammonium cations (Figure 4.2.6(a)), as it also occurs for **HTM1**/MAPI:MAI (up). While the pDOS plots (Figure 4.2.6(c,d)) of **PTZ1**/MAPI:MAI (up) reveal the same behavior found for **HTM1** and **Spiro-OMeTAD**, for **PTZ1**/MAPI:PbI$_2$ (up) the trend is inverted. Indeed, the HOMO level of **PTZ1** lies at higher energy than the VB of MAPI, thus it should be able to extract the holes from the perovskite.
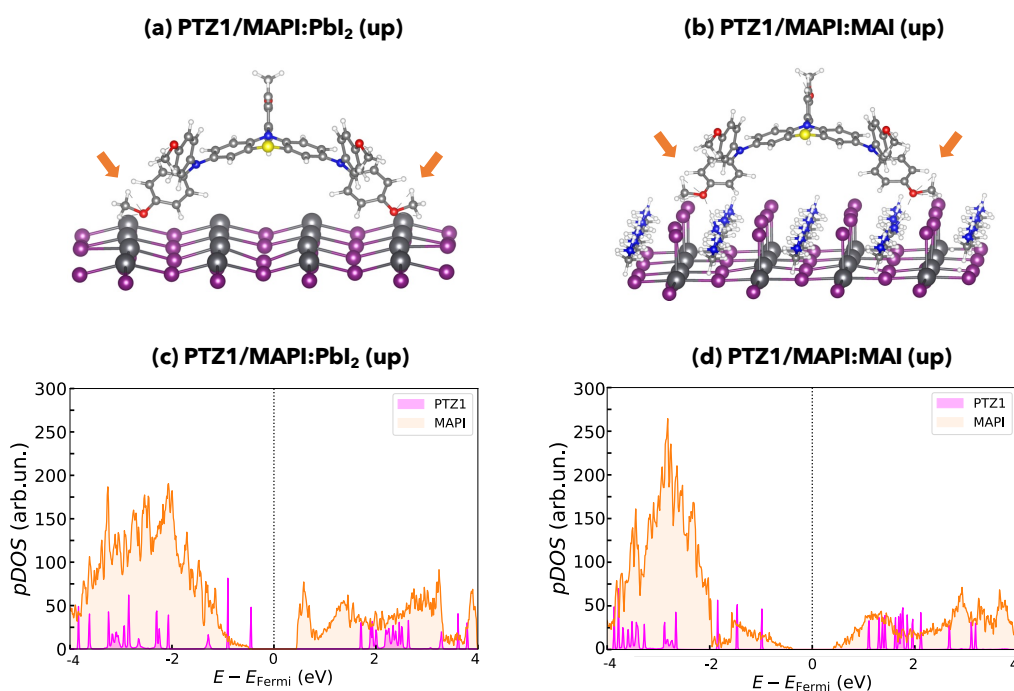
(a) PTZ1/MAPI:PbI₂ (up)

(b) PTZ1/MAPI:MAI (up)

(c) PTZ1/MAPI:PbI₂ (up)

(d) PTZ1/MAPI:MAI (up)

Figure 4.2.6. Energy minima of: (a) **PTZ1**/MAPI:PbI₂ (up), (b) **PTZ1**/MAPI:MAI (up) and pDOS plots of (a) **PTZ1**/MAPI:PbI₂ (up) and (b) **PTZ1**/MAPI:MAI (up). Color label of atomic spheres: Pb-dark gray; I-violet; C-light grey; N-blue; H-white; O-red; S-yellow.

In Figure 4.2.7 are reported the energy minima of **PTZ2**/MAPI. In this case, the binding energies result stabilized when **PTZ2** adopts the down orientation on MAPI (001). This is because **PTZ2** interacts with the MAPI by exposing the sulfur atom, but also the methoxybenzene directly linked to the PTZ nitrogen. Indeed, this methoxybenzene assumes an almost parallel position with respect to the nitrogen, becoming responsible for additional interactions (Figure 4.2.8(a,b)) that are not present in **PTZ1**/MAPI systems. This binding mode contributes to lower the binding energy to more negative values. On the contrary, when **PTZ1** adopts the down orientation in **PTZ1**/MAPI systems, the methoxybenzene directly linked to the PTZ nitrogen has a more pronounced torsion than in **PTZ2** case, which hampers the sulfur atom to interact with the MAPI (Figure 4.2.8(c,d)). Even if **PTZ2** has the most stabilized binding energies, from the pDOS plots (Figure 4.2.7(c,d)) an inadequate driving force for the hole injection/extraction process can be noticed, as also found for **HTM1** and **Spiro-OMeTAD**. This outcome could appear inconsistent with the good performance of this molecule in PSCs devices reported by Grisorio et al. [6]. Nevertheless, the authors also reported that: i) PSCs devices have been built adding dopants to **PTZ1** and **PTZ2**, ii) the employed perovskite was not the

MAPI, but the mixed halide (bromine and iodine) and cations (methylammonium, formamidinium and cesium).
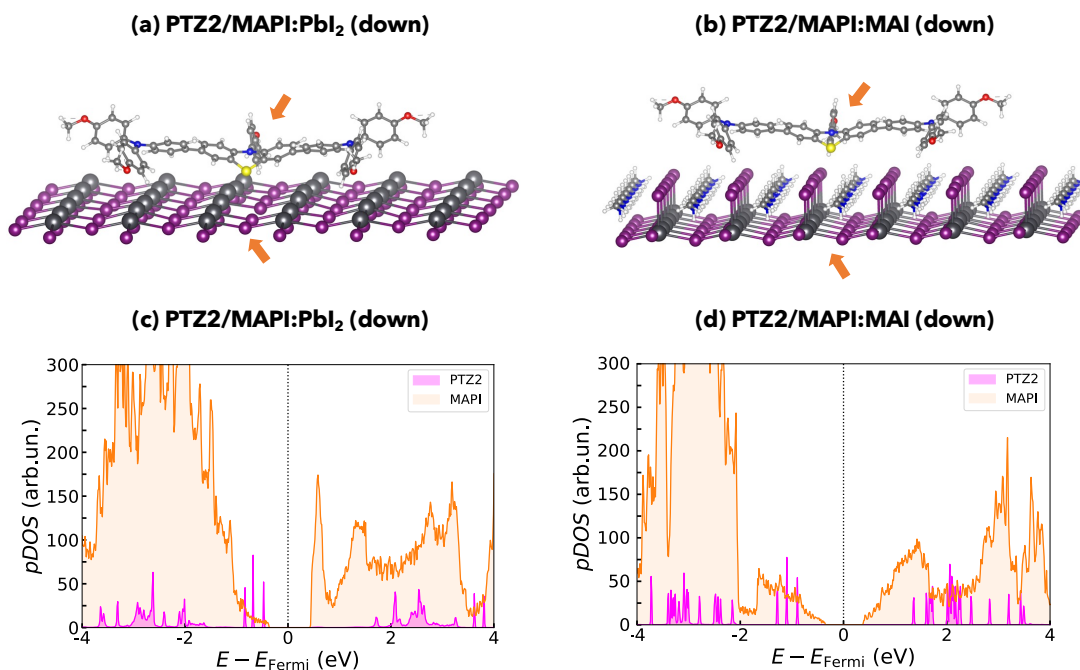

Figure 4.2.7. Energy minima of: (a) **PTZ2**/MAPI:PbI$_2$ (down), (b) **PTZ2**/MAPI:MAI (down) and pDOS plots of (a) **PTZ2**/MAPI:PbI$_2$ (down) and (b) **PTZ2**/MAPI:MAI (down). Color label of atomic spheres: Pb-dark gray; I-violet; C-light grey; N-blue; H-white; O-red; S-yellow.
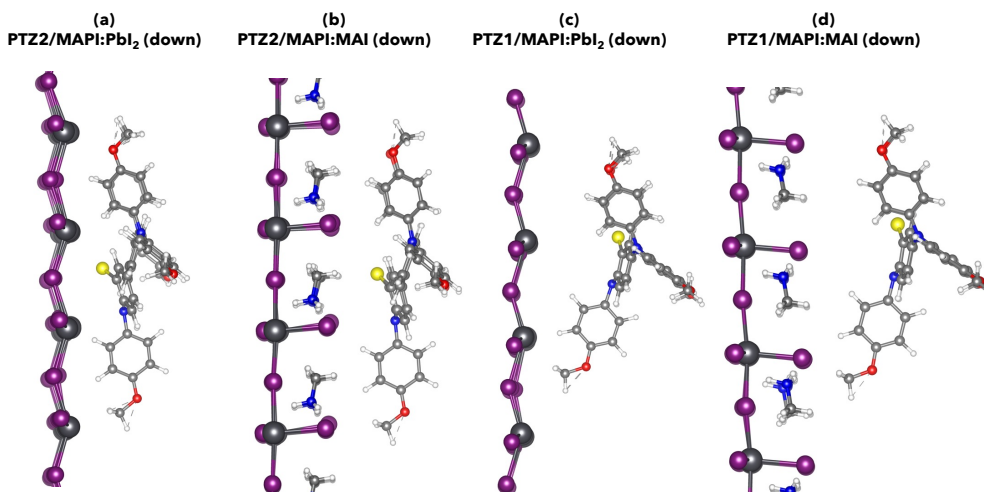

Figure 4.2.8. (a) **PTZ2** down orientation on MAPI:PbI$_2$ surface, (b) **PTZ2** down orientation on MAPI:MAI surface, (c) **PTZ1** down orientation on MAPI:PbI$_2$ surface and (d) **PTZ1** down orientation on MAPI:MAI surface.

In conclusion, the results obtained from the investigation of **PTZ2**/MAPI are an additional proof that a good binding motif is not the only parameter affecting the charge transport process. Indeed, it is not sufficient to determine the adequate driving force for the hole injection/extraction, but the perovskite formulation has also a fundamental impact. In this regard, the MAPI perovskite does not contribute to an efficient charge transport process when combined to TPA and PTZ-based HTMs. This outcome supports the difficulty in applying MAPI for real devices' fabrication with the aforementioned HTMs. A future perspective of this work implicates additional computational studies involving different perovskite compositions, with the aim of providing new insights into interfacial processes in PSCs.

References

[1] F. M. Rombach, S. A. Haque, and T. J. Macdonald, Lessons learned from spiro-OMeTAD and PTAA in perovskite solar cells, Energy Environ. Sci. 14, 5161-5190 (2021). https://doi.org/10.1039/D1EE02095A

[2] A. Torres, and L. G. C. Rego, Surface Effects and Adsorption of Methoxy Anchors on Hybrid Lead Iodide Perovskites: Insights for Spiro-MeOTAD Attachment, J. Phys. Chem. C 118, 26947−26954 (2014). https://doi.org/10.1021/jp510595s

[3] J. Yin, D. Cortecchia, A. Krishna, S. Chen, N. Mathews, A. C. Grimsdale, and C. Soci, Interfacial Charge Transfer Anisotropy in Polycrystalline Lead Iodide Perovskite Films, J. Phys. Chem. Lett. 6, 1396−1402 (2015). https://doi.org/10.1021/acs.jpclett.5b00431

[4] M. Saliba, S. Orlandi, T. Matsui, S. Aghazada, M. Cavazzini, J.-P. Correa-Baena, P. Gao, R. Scopelliti, E. Mosconi, K.-H. Dahmen, F. De Angelis, A. Abate, A. Hagfeldt, G. Pozzi, M. Graetzel, and M. K. Nazeeruddin, A molecularly engineered hole-transporting material for efficient perovskite solar cells, Nature Energy 1, 15017 (2016). https://doi.org/10.1038/nenergy.2015.17

[5] Q. Wang, E. Mosconi, C. Wolff, J. Li, D. Neher, F. De Angelis, G. P. Suranna, R. Grisorio, and A. Abate, Rationalizing the Molecular Design of Hole-Selective Contacts to Improve Charge Extraction in Perovskite Solar Cells, Adv. Energy Mater. 9, 1900990 (2019). https://doi.org/10.1002/aenm.201900990

[6] R. Grisorio, B. Roose, S. Colella, A. Listorti, G. P. Suranna, and A. Abate, Molecular Tailoring of Phenothiazine-Based Hole-Transporting Materials for Highly Performing

Perovskite Solar Cells, ACS Energy Lett. 2, 1029–1034 (2017). https://doi.org/10.1021/acsenergylett.7b00054

[7] L. A. Castriotta, R. Infantino, L. Vesce, M. Stefanelli, A. Dessì, C. Coppola, M. Calamante, G. Reginato, A. Mordini, A. Sinicropi, A. Di Carlo, L. Zani, Methylammonium-Free Wide Band-Gap p-i-n Perovskite Solar Cells and Mini-Modules with Phenothiazine Dimers as Dopant-Free Hole Transporting Materials, submitted manuscript, 2022.

[8] P. Hohenberg, and W. Kohn, Inhomogeneous Electron Gas, Phys. Rev. 136, B864–B871 (1964). https://doi.org/10.1103/PhysRev.136.B864

[9] Kohn, and L. J. Sham, Self-consistent Equations Including Exchange and Correlation Effects, Phys. Rev. 140, A1133–A1138 (1965). https://doi.org/10.1103/PhysRev.140.A1133

[10] A. D. Becke, Density-functional thermochemistry. III. The role of exact exchange, J. Chem. Phys. 98, 5648 (1993). https://doi.org/10.1063/1.464913

[11] C. Lee, W. Yang, and R. G. Parr, Development of the Colle-Salvetti correlation-energy formula into a functional of the electron density, Phys. Rev. B. 37, 785-789 (1988). https://doi.org/10.1103/PhysRevB.37.785

[12] J. P. Perdew, K. Burke, and M. and Ernzerhof, Generalized Gradient Approximation Made Simple, Physical Review Letters 77, 3865–3868 (1996). https://doi.org/10.1103/PhysRevLett.77.3865

[13] S. Grimme, J. Antony, S. Ehrlich, and S. Krieg, A consistent and accurate ab initio parametrization of density functional dispersion correction (DFT-D) for the 94 elements H-Pu, Journal of Chemical Physics 132, 154104 (2010). https://doi.org/10.1063/1.3382344

[14] S. Grimme, S. Ehrlich, and L. Goerigk, Effect of the damping function in dispersion corrected density functional theory, Journal of Computational Chemistry 32, 1456 (2011). https://doi.org/10.1002/jcc.21759

[15] A. D. Becke, and E. R. J. Johnson, A density-functional model of the dispersion interaction, Chemical Physics 122, 154101 (2005). https://doi.org/10.1063/1.2065267

[16] Gaussian 16, Revision C.01, M. J. Frisch, G. W. Trucks, H. B. Schlegel, G. E. Scuseria, M. A. Robb, J. R. Cheeseman, G. Scalmani, V. Barone, G. A. Petersson, H. Nakatsuji, X. Li, M. Caricato, A. V. Marenich, J. Bloino, B. G. Janesko, R. Gomperts, B. Mennucci, H. P. Hratchian, J. V. Ortiz, A. F. Izmaylov, J. L. Sonnenberg, D. Williams-Young, F. Ding, F. Lipparini, F. Egidi, J. Goings, B. Peng, A. Petrone, T. Henderson, D.

Ranasinghe, V. G. Zakrzewski, J. Gao, N. Rega, G. Zheng, W. Liang, M. Hada, M. Ehara, K. Toyota, R. Fukuda, J. Hasegawa, M. Ishida, T. Nakajima, Y. Honda, O. Kitao, H. Nakai, T. Vreven, K. Throssell, J. A. Montgomery, Jr., J. E. Peralta, F. Ogliaro, M. J. Bearpark, J. J. Heyd, E. N. Brothers, K. N. Kudin, V. N. Staroverov, T. A. Keith, R. Kobayashi, J. Normand, K. Raghavachari, A. P. Rendell, J. C. Burant, S. S. Iyengar, J. Tomasi, M. Cossi, J. M. Millam, M. Klene, C. Adamo, R. Cammi, J. W. Ochterski, R. L. Martin, K. Morokuma, O. Farkas, J. B. Foresman, and D. J. Fox, Gaussian, Inc.: Wallingford CT, USA (2016).

[17] Z. Zhang, and R. He, Effect of heterocyclic spacer on property of hole-transporting materials with silafluorene core for perovskite solar cells, Computational and Theoretical Chemistry 1161, 10–17 (2019). https://doi.org/10.1016/j.comptc.2019.06.002

[18] J. Deng, W. Hu, W. Shen, M. Li, and R. He, Exploring the electrochemical properties of hole transporting materials from first-principles calculations: an efficient strategy to improve the performance of perovskite solar cells, Phys.Chem.Chem.Phys. 21, 1235-1241 (2019). https://doi.org/10.1039/C8CP06693K

[19] J. Tomasi, B. Mennucci, and R. Cammi, Quantum Mechanical Continuum Solvation Models, Chem. Rev. 105, 2999−3093 (2005). https://doi.org/10.1021/cr9904009

[20] J. M. Soler, E. Artacho, J. D. Gale, A. García, J. Junquera, P. Ordejón, and D. Sánchez-Portal, The SIESTA method for ab initio order-N materials simulation, Journal of Physics: Condensed Matter 14, 2745-2779 (2002). https://doi.org/10.1088/0953-8984/14/11/302

[21] J. Junquera, O. Paz, D. Sánchez-Portal, and E. Artacho, Numerical atomic orbitals for linear-scaling calculations, Phys. Rev. B 64, 235111 (2001). https://doi.org/10.1103/PhysRevB.64.235111

[22] N. Troullier, and J. L. Martins, Efficient pseudopotentials for plane-wave calculations, Phys. Rev. B 43, 1993–2006 (1991). https://doi.org/10.1103/PhysRevB.43.1993

[23] J. Simokaitiene, M. Cekaviciute, K. Baucyte, D. Volyniuk, R. Durgaryan, D. Molina, B. Yang, J. Suo, Y.J. Kim, D. A. da Silva Filho, A. Hagfeldt, G.Sini, and J. V. Grazulevicius, Interfacial versus Bulk Properties of Hole-Transporting Materials for Perovskite Solar Cells: Isomeric Triphenylamine-Based Enamines versus Spiro-OMeTAD, ACS Appl. Mater. Interfaces 13, 21320−21330 (2021). https://doi.org/10.1021/acsami.1c03000

[24] R.A. Marcus, Electron transfer reactions in chemistry. Theory and experiment, Rev. Mod. Phys. 65, 599-610 (1993). https://doi.org/10.1103/RevModPhys.65.599

[25] W.-J. Chi, Q.-S. Li, and Z.-S. Li, Exploring the electrochemical properties of hole transport materials with spiro-cores for efficient perovskite solar cells from first-principles, Nanoscale 8, 6146-6154 (2016). https://doi.org/10.1039/C6NR00235H

[26] Y. Li, H. Li, C. Zhong, G. Sini, and J.-L. Brédas, Characterization of intrinsic hole transport in single-crystal spiro-OMeTAD, npj Flex Electron 1, 1-8 (2017). https://doi.org/10.1038/s41528-017-0002-0

[27] J. Urieta-Mora, I. García-Benito, A. Molina-Ontoria, and N. Martín, Hole transporting materials for perovskite solar cells: a chemical approach, Chem. Soc. Rev. 47, 8541-8571 (2018). https://doi.org/10.1039/C8CS00262B

[28] D. Wang, S. Huang, C. Wang, Y. Yue, and Q. Zhang, Computational prediction for oxidation and reduction potentials of organic molecules used in organic light-emitting diodes, Organic Electronics 64, 216-222 (2019). https://doi.org/10.1016/j.orgel.2018.10.038

[29] F. F. Targhi, Y. S. Jalili, and F. Kanjouri, $MAPbI_3$ and $FAPbI_3$ perovskites as solar cells: Case study on structural, electrical and optical properties, Results in Physics 10, 616–627 (2018). https://doi.org/10.1016/j.rinp.2018.07.007

[30] Y. Li, Y. Zhang, J. Zhang, J. Li, W. Wu, and L. Wang, Constructive effects of the interfacial properties: A strategy to design hole transport materials for high performance perovskite solar cells, Organic Electronics 62, 591–597 (2018). https://doi.org/10.1016/j.orgel.2018.06.035

[31] H.D. Pham, T.C.J. Yang, S.M. Jain, G.J. Wilson, and P. Sonar, Development of Dopant-Free Organic Hole Transporting Materials for Perovskite Solar Cells, Adv. Energy Mater. 10, 1903326 (2020). https://doi.org/10.1002/aenm.201903326

[32] E. Sheibani, L. Yang, and J. Zhang, Recent Advances in Organic Hole Transporting Materials for Perovskite Solar Cells, Sol. RRL. 4, 1–16 (2020). https://doi.org/10.1002/solr.202000461

4.3. Manuscript 3: "Synthesis and Characterization of New Organic Dyes Containing the Indigo Core"

Authors: D. Franchi, M. Calamante, C. Coppola, A. Mordini, G. Reginato, A. Sinicropi, and L. Zani.

In this work, a new series of symmetrical D-A-D dyes and one unsymmetrical D-A-π-A dye containing the indigo core have been designed, synthetized and fully characterized. Concerning the symmetrical D-A-D dyes, they have been endowed with different donor groups and it has been evaluated how their structure influences the interaction with light, as well as the energy and the nature of their electronic transitions. Additionally, the indigo scaffold has been evaluated as auxiliary acceptor unit when inserted in a D-A-π-A structure, combined to a triarylamine donor group and a cyanoacrylate acceptor group. Thus, the possibility of obtaining green colored D-A-π-A organic sensitizers bearing the indigo scaffold has been investigated for DSSCs application. As predicted from the computational investigation, the spectroscopic and the electrochemical characterization of the indigo-based D-A-π-A dye (**DF90**) confirmed its suitability for such application. The PhD candidate's contribution refers to the application of DFT and TDDFT methods for the prediction of the main optoelectronic properties of all the tautomeric forms of the indigo-based dyes. In particular, the ground-state geometries, the energy and the shape of FMOs and the excited-state properties have been calculated for the keto–keto (KK), keto–enol (KE) and enol–enol (EE) tautomers of the considered dyes. Solvent effects have been included by PCM. Additionally, the PhD candidate gave her contribution to the writing of the manuscript.

Article

Synthesis and Characterization of New Organic Dyes Containing the Indigo Core

Daniele Franchi [1,2,3] [iD], **Massimo Calamante** [1,2] [iD], **Carmen Coppola** [4,5], **Alessandro Mordini** [1,2,*], **Gianna Reginato** [2,*], **Adalgisa Sinicropi** [2,4,5] [iD] and **Lorenzo Zani** [2] [iD]

1   Dipartimento di Chimica "Ugo Schiff", Università degli Studi di Firenze, Via della Lastruccia, 13, 50019 Sesto Fiorentino, Italy; daniele.franchi87@gmail.com (D.F.); mcalamante@iccom.cnr.it (M.C.)
2   CNR-Istituto di Chimica dei Composti Organometallici (CNR-ICCOM), Via Madonna del Piano, 10, 50019 Sesto Fiorentino, Italy; adalgisa.sinicropi@unisi.it (A.S.); lorenzo.zani@iccom.cnr.it (L.Z.)
3   Department of Chemistry, KTH, Teknikringen 30, 10044 Stockholm, Sweden
4   R2ES Lab, Dipartimento di Biotecnologie, Chimica e Farmacia, Università degli Studi di Siena, Via A. Moro, 2, 53100 Siena, Italy; carmen.coppola@student.unisi.it
5   CSGI, Consorzio per lo Sviluppo dei Sistemi a Grande Interfase, Via della Lastruccia, 3, 50019 Sesto Fiorentino, Italy
*   Correspondence: alessandro.mordini@iccom.cnr.it (A.M.); gianna.reginato@iccom.cnr.it (G.R.)

Abstract: A new series of symmetrical organic dyes containing an indigo central core decorated with different electron donor groups have been prepared, starting from Tyrian Purple and using the Pd-catalyzed Stille-Migita coupling process. The effect of substituents on the spectroscopic properties of the dyes has been investigated theoretically and experimentally. In general, all dyes presented intense light absorption bands, both in the blue and red regions of the visible spectrum, conferring them a bright green color in solution. Using the same approach, an asymmetrically substituted D–A–π–A green dye, bearing a triarylamine electron donor and the cyanoacrylate acceptor/anchoring group, has been synthesized for the first time and fully characterized, confirming that spectroscopic and electrochemical properties are consistent with a possible application in dye-sensitized solar cells (DSSC).

Keywords: indigo dyes; DSSC; synthesis; cross coupling; spectroscopy

1. Introduction

Indigo (also known as C.I. Vat Blue 1) is a naturally occurring blue dye, originally obtained by extraction of indican from plants. Acid-hydrolysis and mild oxidation produce the dye (Figure 1), which has been known since ancient times and in different civilizations. Since the beginning, due to the shortage of natural blue dyes, indigo has played an important role in the economies of many countries, being mainly used for textile dyeing and printing and, indeed, it is still used in the fabric industry today, where it has probably the largest application in denim [1].
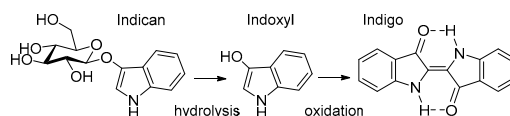

Figure 1. Biosynthesis of Indigo from Indican.

The first synthesis of indigo was reported by Adolf von Baeyer in 1882 [2] and its chemical structure was elucidated one year later [3]. Shortly after, a practical manufacturing process was developed and since 1897 natural indigo has almost been replaced by the synthetic molecule, which is probably the most produced dye in the world [4]. Concerning the spectroscopic properties of indigo [5–9], several studies have been reported, showing how the absorption spectrum of the dye is dependent on the environment, ranging from red (540 nm) in the gas phase, to violet (588 nm) in tetrachloromethane, to blue (606 nm) in polar solvents such as ethanol [8]. Moreover, indigo has extremely low solubility in water and in common organic solvents, a high melting point (390–392 °C), and gives highly-crystalline thin films upon evaporation. This behaviour is mainly due to the possibility to form inter- and intramolecular hydrogen bonds as well as strong intermolecular π-interactions, which are also responsible for providing very good charge transporting properties. Accordingly, indigo is an intrinsically ambipolar organic semiconductor with a bandgap of 1.7 eV, high and well-balanced electron and hole mobilities (approx. 1×10^{-2} cm^2/V·s) and good stability against degradation in air [10]. For these reasons, the dye has been recently exploited for the application in the field of natural and sustainable semiconductors, aiming to tackle the problem of electronic waste by using naturally occurring, low toxic and biodegradable materials [11]. For instance, indigo and its derivatives have found application as semiconductors in field-effect transistors [4,10,11], sensors [12,13], electrodes for ion batteries [14,15] and liquid crystals [16,17]. Moreover, the natural dye extracted from *Indigofera tinctorial* [18] has been used to prepare dye-sensitized solar cells (DSSC), a novel class of photovoltaics which represent a promising alternative to traditional silicon-containing devices [19,20]. The working principle of a DSSC is inspired by natural photosynthesis, as the light harvest is carried out by a dye, which is absorbed on a thin layer of a mesoporous semiconductor (usually TiO$_2$). For such an application some natural dyes have been used for titania sensitization, although low photocurrent conversion efficiencies (PCE) have been generally observed so far [21]. On the contrary, when specially designed molecules have been tested, better results were found, with record efficiency up to 13.6% [22]. In particular, donor-π-bridge-acceptor (D-π-A) structures [23–25] are conventionally used in the design of organic photosensitizers and, frequently, triphenylamine (TPA) and cyanoacrylic acid have been established to be optimal electron donor and electron acceptor substituents for obtaining efficient devices. Concerning the π-bridge, a large number of different heterocycles have been screened leading to several classes of sensitizers successfully used in DSSC. The vast majority of them, however, absorb light only in the blue and green regions of the spectrum (400–600 nm), giving rise to orange/red-colored devices, with the exception of those containing specific chromophores such as, for example, squaraines [26–30]. Blue and green dyes [31,32], on the other hand, have a high commercial interest due to both their lovely colours and their capability to absorb the incident photons also in the red and near-infrared region (NIR) of the spectrum (600–800 nm), maximizing solar light harvesting. A possible strategy to design this kind of sensitizers is that of introducing an additional acceptor unit between the donor and the conjugated bridge, modifying D-π-A structures into D-A-π-A ones. In this way, it is possible to affect the energy levels of the sensitizers, and maybe also improve their photostability [33,34]. Following this approach, the indigo unit can be considered a very interesting auxiliary acceptor to be inserted into a D-A-π-A structure with the aim of extending the absorption range and obtaining blue-green coloured organic sensitizers. However, despite theoretical design supported the possibility to use indigo derivatives as DSSC sensitizers [35,36]. D-A-π-A indigo-based dyes have never been prepared and tested for such an application. From the synthetic point of view, the modification of the pristine indigo to a more extended conjugated structure is not an easy task, due to its low solubility. As a matter of fact, the first indigo derivatives with conjugated aromatic substituents to be reported were obtained by modification of the precursors of the indigo core [16,17,37,38]. Procedures for the modification of preformed indigo are more recent and take advantage mainly of cross-coupling reactions of the 6-6' dibromo derivative Tyrian Purple (C.I. Natural Violet) with electrophiles (Figure 2) [38–41]. Spectroscopic characterization of such derivatives pointed out that it is possible to affect the energy levels of indigoids by chemical design and that the

effect of substituents can be qualitatively predicted by DFT calculations. Moreover, derivatization can drastically enhance the solubility in organic solvents, especially for functionalization in 4-4′ and 7-7′ position, resulting in twisting and buckling with respect to the central double bond [16].

In this paper, we report the preparation and the full spectroscopic characterization of some new indigo-based dyes (Figure 2). In particular, some symmetrical D-A-D dyes featuring an extended conjugation have been obtained, using a synthetic approach based on the Pd-catalyzed Stille-Migita coupling, which was performed in very mild conditions. The new dyes have been spectroscopically characterized and their optical properties compared with the results of computational investigations, in order to understand how their structure influences the interaction with light and evaluate the nature and energy of their electronic transitions. Based on these studies, an unsymmetrically substituted indigo-based D-A-π-A dye was then designed, synthesized, and fully characterized, to assess the possibility of using this scaffold to prepare blue-green dyes for DSSC application.
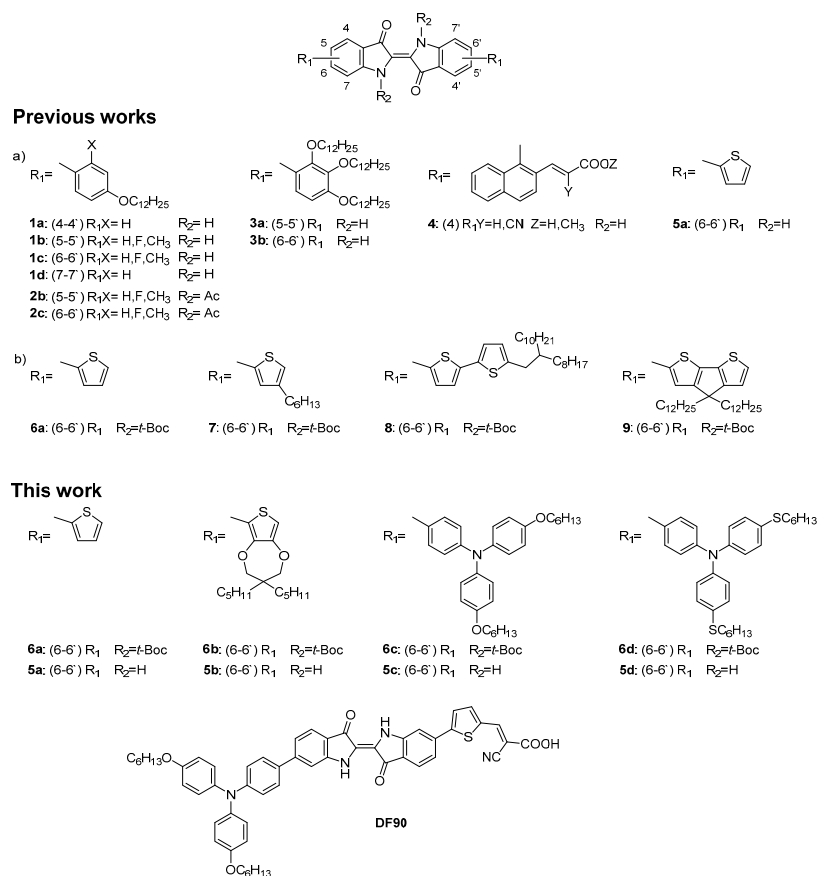
Figure 2. Conjugated indigo derivatives reported in the literature and dyes developed in this study. (**a**) non *t*-Boc-protected compounds; (**b**) *t*-Boc-protected compounds.

2. Results and Discussion

2.1. Computational Investigation

To extend the conjugation of the indigo scaffold we decided to exploit the effect of triarylamine- and thienyl groups, as they are very frequently used in the design of organic semiconductor materials as well as DSSC sensitizers. In particular, we considered four symmetrical dyes **5a–d** and a typical D-A-π-A structure such as **DF90** (Figure 2), where the cyanoacrylate moiety is essential not only as an acceptor group (facilitating electron injection in the conduction band of TiO_2) but also to ensure the anchoring of the dye to the semiconductor surface.

The B3LYP/6-31G** optimized geometries, both in vacuo and in DCM, of keto–keto (KK), keto–enol (KE) and enol–enol (EE) tautomers of compounds **5a**, **5b**, **5c**, **5d**, and **DF90** display a planar structure in the central indigo scaffold (dihedral angles ≤0.2°), whereas a more pronounced torsion is observed for the bonds with R_1 moieties (dihedral angles between 17° and 34°) (see Supporting Information Figures S1–S4, for **5d** only the KK tautomer is considered). No significant differences between the *in vacuo* and in DCM optimized geometrical parameters and relative energies are found for all investigated compounds (see Supporting Information Table S1). On the basis of the Boltzmann equation, the room temperature ΔG values, computed on two representative molecules **5a** and **DF90,** clearly indicate that the only species that would be present in solution is the KK tautomer (see Supporting Information Table S2). For such reason, in the following, we present and discuss only the results obtained for the KK tautomers. The complete set of data including KE and EE tautomers is reported in the Supporting Information.

The absorption maximum (λ^a_{max}), vertical excitation energy (E_{exc}) and oscillator strengths (f) computed in DCM on the minimized structures of KK tautomer of compounds **5a**, **5b**, **5c**, **5d**, and **DF90** are shown in Table 1. The DFT frontier molecular orbitals (FMOs) of the transitions are shown in Figure 3.

Orbital plots are similar for compounds **5a** and **5b**: the HOMO and LUMO, i.e., the FMOs involved in the lowest energy transition predicted at 604–610 nm, are localized over the indigo moiety and have a π and π^* character, respectively. This charge distribution is the same found for indigo and its derivatives in previous literature papers [9,38,42,43].

Table 1. TD-DFT (B3LYP/6-311++G**) absorption maxima (λ^amax), excitation energies (E_{exc}), oscillator strengths (f) and contribution (%) to the transition in DCM for the lowest excited states having a non-negligible oscillator strength of KK tautomer of compounds **5a**, **5b**, **5c**, **5d** and **DF90**.

Molecule	Excited States	λ^amax (nm)	E_{exc} (eV)	f	Contribution (%)
5a	1	604	2.05	0.54	100% H→L
5b	1	610	2.03	0.58	100% H→L
5c	1	760	1.63	0.86	99% H→L
	3	594	2.08	0.32	99% H-2→L
5d	1	746	1.62	0.76	99% H→L
	3	596	2.08	0.36	99% H-2→L
DF90	1	857	1.44	0.32	99% H→L
	2	645	1.92	0.41	97% H-1→L
DF90 [#]	1	543	2.28	0.66	80% H-1→L

[#] computed at the CAM-B3LYP/6-311++G** level of theory.

Similar localized orbitals correspond also to the HOMO-2 and LUMO of molecules **5c** and **5d**. Indeed, the absorption predicted at about 594–596 nm for **5c** and **5d** is due to the HOMO-2→LUMO transition. Likewise, the HOMO-1→LUMO transition of the asymmetric compound **DF90**, which corresponds to the absorption maximum at about 645 nm, is characterized by the same ground-state electron density delocalization on the Indigo part of the molecule. In this last case, the limited spatial separation between these frontier molecular orbitals suggests a consequent limited intramolecular charge separation upon photoexcitation of the dyes. The DFT FMOs energies obtained in DCM for tautomer KK of **5a**, **5b**, **5c**, **5d**, and **DF90** are reported in the Supporting Information (Figure S5).
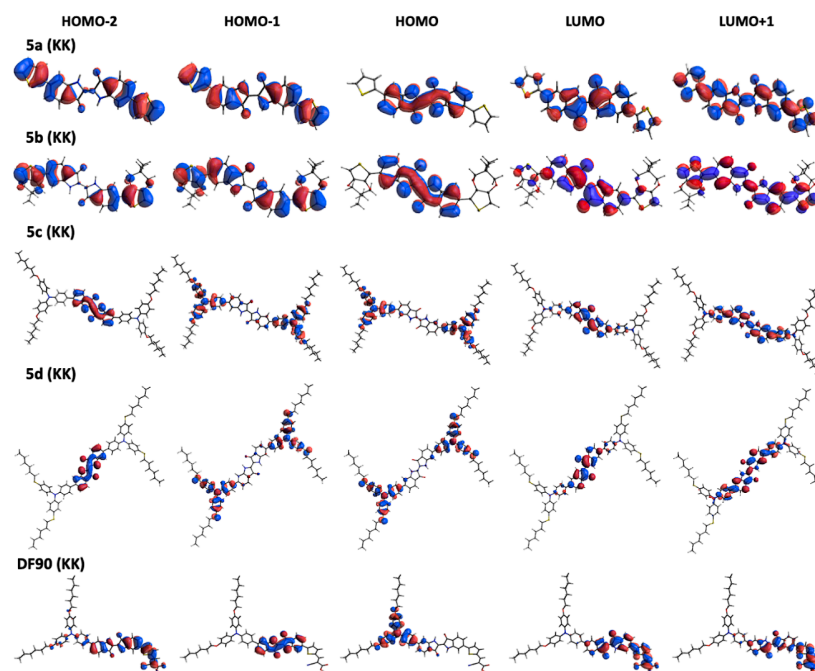
Figure 3. B3LYP/6-31G** ground-state electron density distributions in DCM of KK tautomer of compounds **5a**, **5b**, **5c**, **5d** and **DF90**.

2.2. Synthesis of Dyes

To prepare the symmetrical dyes **5a–d** we used an approach (Scheme 1) similar to that already described for the synthesis of 6,6'-dithienylindigo [38]. Tyrian Purple (**10**) was obtained as a purple powder in 71% yield, using the classical indigo-forming protocol [2]. To increase its solubility and simplify its chemical manipulation and processing, Tyrian Purple was protected using (*t*-Boc)₂O and DMAP in DMF solution, and the soluble deep red product **11** was obtained in 92% yield. In order to preserve the required but thermolabile *t*-Boc protection, the introduction of the side groups should occur under very mild and chemoselective conditions. For these reasons we decided to take advantage of the mild conditions usually applied in the Stille-Migita cross-coupling, and thus to react intermediate **11** with stannanes **12a–d** (Scheme 1).
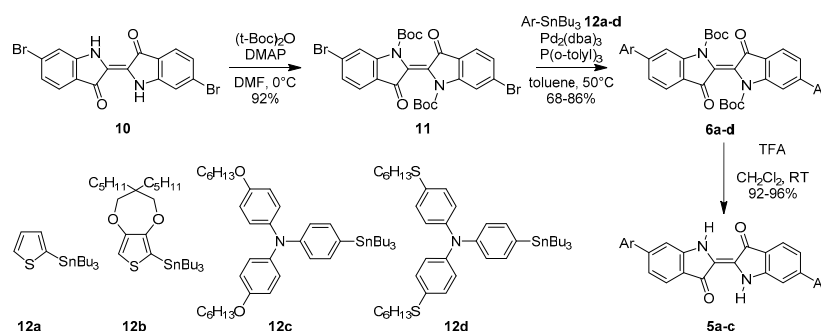
Scheme 1. Stille-Migita cross-coupling of t-Boc-protected Tyrian Purple (**10**) with thienyl- and triarylamino-stannanes 8a–d.

We optimized the reaction conditions using commercially available stannane **12a** and found that Pd$_2$(dba)$_3$ and the electron-rich tri(*o*-tolyl)phosphine was the best combination to generate the active catalytic species able to perform the cross-coupling at 50 °C. In this way, deprotection of the *t*-Boc group, which might occur when temperatures higher than 90 °C are used [44,45] and the consequent precipitation of unprotected starting material was prevented. Thus, using toluene as solvent and two equivalents of stannane **12a**, symmetric indigo derivative **6a** was obtained in good yield in 5 h. The reaction was then repeated using the more electron-rich thienylstannane **12b**, and two triarylamine-containing stannanes **12c** and **12d**, which were prepared as previously reported. [44,46] In all cases, the corresponding coupling compounds **6b–d** were recovered with high yields after purification. Unfortunately, compound **6d** appeared unstable in solution ad could not be fully characterized nor used for further deprotection. However, we were able to identify it by ESI/MS and to record UV/visible spectra. Finally, reaction of **6a–c** with TFA occurred smoothly at room temperature to give compounds **5a–c**, which were soluble in the most common organic solvents.

To prepare dye **DF90** a modification of the above-described synthetic approach was necessary in order to obtain a non-symmetrical molecule. Again we used the *t*-Boc protected Tyrian Purple (**11**) as starting material and decided to install the acceptor moiety first (Scheme 2).

To this end, we prepared stannane **12e** [44] carrying a formyl group, which was essential to later establish the required cyanoacrylic moiety (Scheme 2). Desymmetrization of compound **11** with stannane **12e** needed to be carried out using a large excess (five-fold) of the starting material, which, opportunely, could be easily recovered at the end of reaction by precipitation from ethyl acetate/hexane mixture. Evaporation of the solvent gave intermediate **13** which was obtained in 84% yield (based on **12e**) after column chromatography. The second coupling, required to introduce the donor group, was performed in essentially the same conditions, albeit using one equivalent of stannane **12c**: pure *t*-Boc protected aldehyde **14** was thus obtained in 79% yield after purification. Knoevenagel condensation of aldehyde **14** with cyanoacetic acid and piperidine in acetonitrile allowed introduction of the desired cyanoacrylate together with the simultaneous deprotection of *t*-Boc groups, affording dye **DF90** in 55% yield.
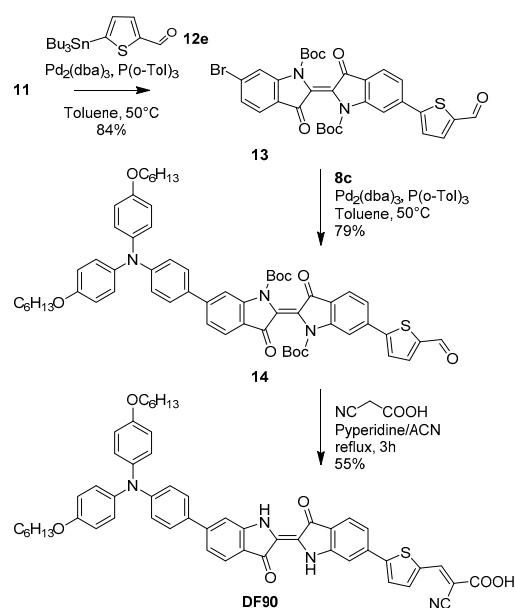
Scheme 2. Synthesis of dye **DF90**.

2.3. Optical and Electrochemical Properties

The optical properties of all the new dyes were studied and compared with those of the parent compound indigo (Figure 4). It must be considered, however, that when Indigo was suspended in CHCl$_3$ in the reported conditions (0.17 g/mL corresponding to 6.5×10^{-5} M), it was not possible to obtain a completely clear solution, thus the resulting molar extinction coefficient must be taken only as an approximate value.
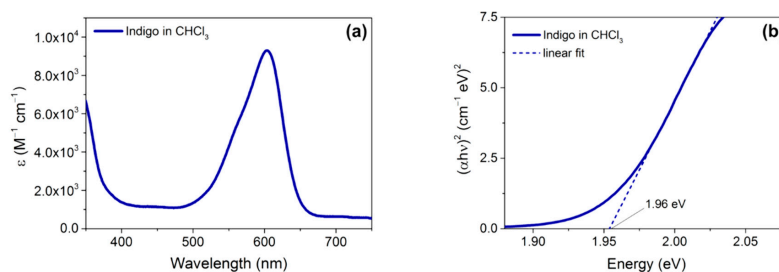
Figure 4. UV-Vis absorption spectrum of indigo dissolved in CHCl$_3$ (**a**) and corresponding Tauc plot (**b**).

In good agreement with previous literature reports [47], we observed a relatively intense transition at 604 nm, corresponding to an E_{0-0} of 1.96 eV, due to the so-called "*H*-chromophore" [8,38,48] corresponding to a cross-conjugated donor-acceptor system held together by intramolecular hydrogen bonds (see Figure 1). Computational studies revealed that the H-chromophore absorption is due to a

HOMO-LUMO transition with π-π* character, corresponding to a net electron transfer from the N–H group (acting as a donor) to the C=O group (acting as an acceptor) [9]. The UV-vis spectra of dyes **5a–c** were recorded in CH$_2$Cl$_2$ and EtOH solution. Spectra are reported in Figure 4 and compared with those of the corresponding *t*-Boc protected compounds **6a–d**. Due to its low solubility in EtOH, the spectrum of compound **6b** could be recorded only in CH$_2$Cl$_2$. All relevant spectroscopic data have been summarized in Table 2.

Table 2. Optical properties of dyes **5a–d** and **6a–c** compared with those of parent indigo compound.

Dye	λ_{max} CH$_2$Cl$_2$ [nm]	ε CH$_2$Cl$_2$ [× 10^4 M^{-1} cm^{-1}]	E_{0-0} CH$_2$Cl$_2$ [eV] [a]	λ_{max} EtOH [nm]	ε EtOH [× 10^4 M^{-1} cm^{-1}]	E_{0-0} EtOH [eV] [a]
Indigo	604 [b]	0.93 [b]	1.96 [b]	-	-	-
6a	324	1.75		323	1.74	
	406	2.04	2.14	411	1.94	2.14
	546	0.41		545	0.3	
5a	333	1.14		333	0.52	
	415	1.01	1.95	414	0.44	1.85
	610	1		620	0.38	
6b	328	2.4				
	426	1.7	2.11	- [c]	- [c]	- [c]
	548	0.9				
5b	335	3.05		335	3.06	
	445	2.77	1.94	441	2.56	1.87
	614	2.88		626	2.57	
6c	290	5.5		296	4.52	
	346	5.15	2.06	347	5.2	2.03
	554	2.9		556	2.88	
5c	293	4.7		293	3.2	
	355	4.55	1.93	351	2.89	1.82
	610	4.06		608	1.93	
6d	324	6.4	2.1	325	6.89	2.09
	548	1.11		549	1.09	

[a] E_{0-0} of the lowest energy transition, estimated by means of the corresponding Tauc plot (see Figure S6). [b] Spectrum recorded in CHCl$_3$. [c] The UV-Vis absorption spectrum of this compound could not be recorded in EtOH due to insufficient solubility.

The absorption maxima for the lowest energy band of **5a–5c** and **DF90** (see below) were well predicted by the results of the computational investigation. Indeed, the differences between DFT and experimental vertical excitation energies (E_{exc}) were 0.05 eV at most. In absence of the experimental values for **5d**, we computed the geometry, orbital energies, and UV-Vis properties for compound **6d** (see Supporting Information, Figure S4, Tables S4 and S6). The presence of the *t*-Boc group causes a slight deviation from the planarity of the central C–C bond of the indigo moiety (dihedral angle changes from 0° to 5°) which in turns lead to a blue-shift of the lowest energy band.

Significant differences were observed between the *N*-*t*-Boc protected and free N–H species (Figure 5). Considering the *t*-Boc-protected compounds **6a–d**, while the first two peaks (marked as a,b) can be assigned to localized π-π* transitions involving different parts of the molecules, the lower energy band is likely due to a charge transfer (ct) transition between the lateral donor groups and the central acceptor unit: this hypothesis is supported by the fact that such band is most red-shifted and intense in the case of compound **6c**, featuring the strongly electron-donating hexyloxy-TPA side groups. As a consequence of the particular absorption profile of the dyes, the corresponding solutions appeared red to purple in color.
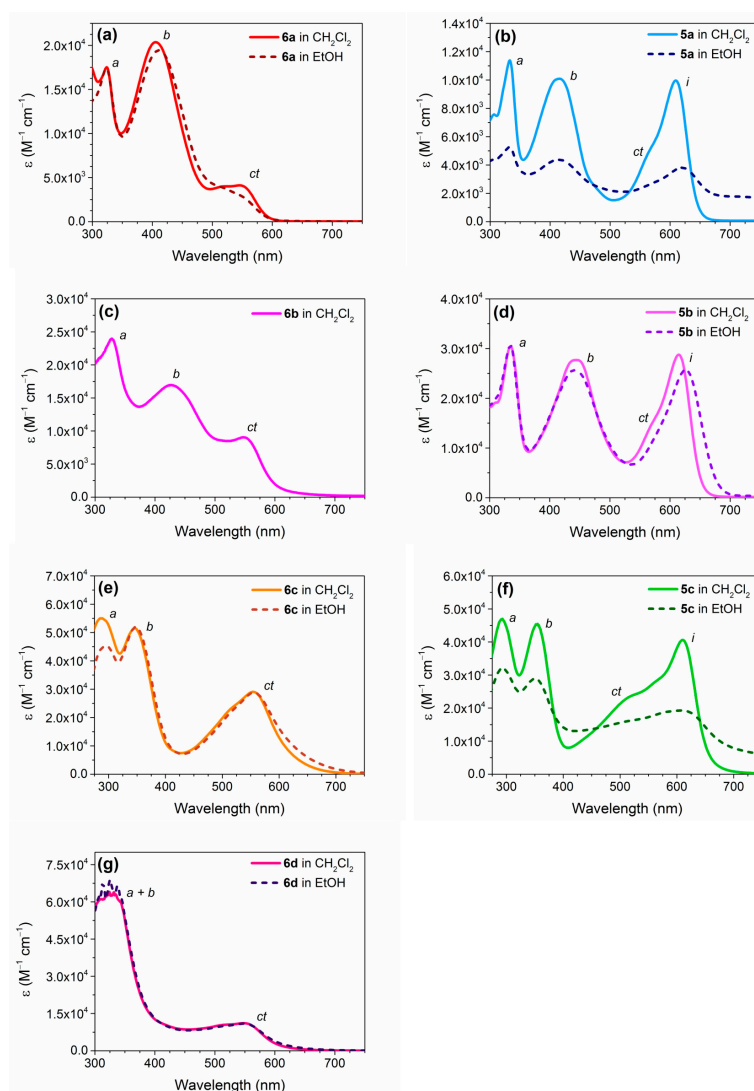
Figure 5. UV-Vis absorption spectra of dyes **6a–d** (panels (**a**), (**c**), (**e**), (**g**), respectively) and **5a–c** (panels (**b**), (**d**), (**f**), respectively).

No significant difference was observed when passing from CH_2Cl_2 to EtOH, with all compounds displaying essentially the same spectra, highlighting also their good solubility in the more polar and protic solvent (except for **6b**). Moving from *N*-Boc protected compounds **6a–d** to free *N*–H compounds **5a–c** the main change observed in the absorption spectra was the activation of the "*H*-chromophore" transition (indicated as *i*). In analogy with the parent indigo compound, such transition, in CH_2Cl_2

solution, appeared as an intense peak in the 610–614 nm range, corresponding to E_{0-0} values of 1.93–1.95 eV. The original *ct* band already observed for compounds **6a–d** was still present in the spectra of compounds **5a–c**, but appeared only as a shoulder of the more intense indigo transition. Furthermore, in analogy to its precursor **6c**, derivative **5c** had a relatively strong *ct* band, which together with the *i* transition gave rise to an intense panchromatic absorption in the 400–650 nm range.

In EtOH, unprotected dyes (especially compounds **5a** and **5c**) featured a much less intense and broadened spectrum, with a long tail extending in the near-IR region above 750 nm: this was attributed to their reduced solubility in that solvent, leading to the formation of aggregates and observation of light scattering effects. In addition, for most of the compounds, the lowest energy absorption peak was red-shifted in the more polar solvent, and in all cases, smaller E_{0-0} values were recorded (1.82–1.87 eV): this bathochromic shift when the dielectric constant of the solvent is increased is well-known also for the parent indigo compound [47] and has been attributed to increased stability of charged-separated structures (for instance, C^+–O^-) in the excited state rather than in the ground state [9]. As a result of their light absorption profiles, compounds **5a–c** gave bright green to dark green-coloured solutions (Figure 6), which were different from the typical blue colour of indigo, demonstrating that the placement of donor moieties on 6,6′-positions of the main chromophore could significantly alter the optical properties of the resulting substances.
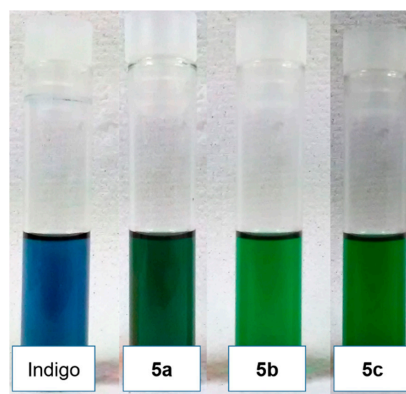
Figure 6. Solutions of dyes **5a** (2.3×10^{-4} M), **5b** (3.5×10^{-4} M) and **5c** (7.8×10^{-5} M) in CH$_2$Cl$_2$, in comparison with indigo suspension in CHCl$_3$ (0,17 mg/mL $\approx 6.5 \times 10^{-4}$ M).

The fluorescence behavior of the new dyes was complicated by the possible occurrence of several different emissive transitions, as illustrated by the emission spectra obtained for compound **5a** at three different excitation wavelengths (Figure 7, top). After excitation at 333 nm (corresponding to an S$_0$–S$_3$ transition), three different fluorescence peaks were observed at 380, 481 and 647 nm, respectively (the latter was partially covered by a peak at 666 nm due to second-order diffraction of the incident radiation). While the first of them was due to the opposite S$_3$–S$_0$ transition, the other two likely originate from S$_2$–S$_0$ and S$_1$–S$_0$ transitions, demonstrating the possibility of non-radiative decay from the S$_3$ state to the lower excited states of the dye. This was confirmed by the fact that irradiating at 415 nm only the peaks at 481 and 647 nm were observed, while only the latter was visible when irradiating at the wavelength of the indigo transition (610 nm).
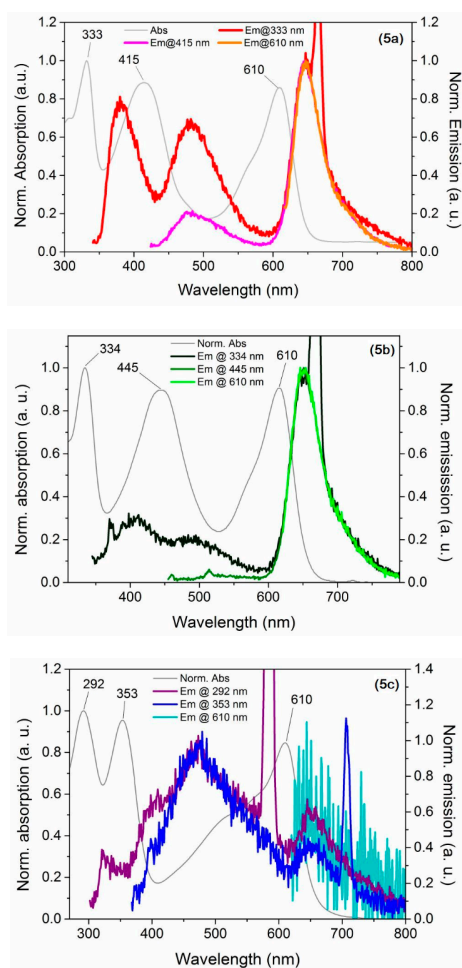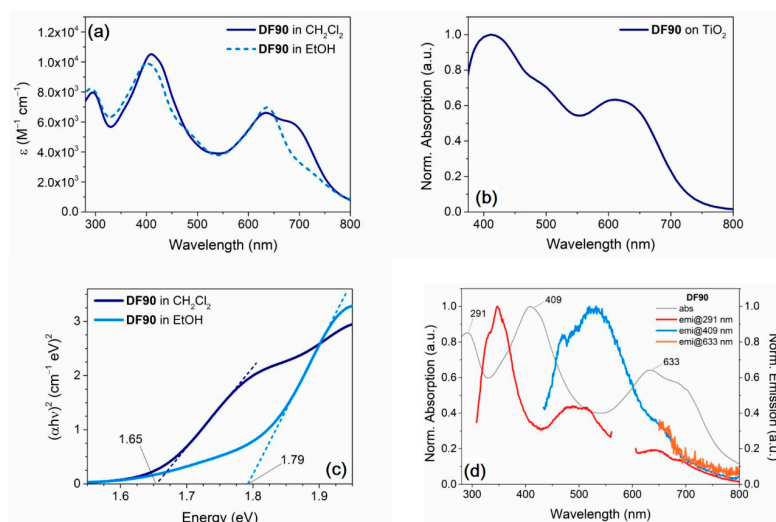
Figure 7. UV–Vis absorption and fluorescence emission spectra of compounds **5a–c** in CH$_2$Cl$_2$ solution. (**5a**): in the emission trace after excitation at 333 nm (red line) the peak visible at 666 nm is due to the second-order diffraction of the incident light. (**5b**): in the emission trace after excitation at 334 nm (dark green line) the sharp peak visible at 668 nm is due to the second-order diffraction of the incident light. (**5c**): in the emission traces after excitation at 292 nm (purple line) and 353 nm (blue line), the sharp peaks visible at 584 nm and 706 nm are due to the second-order diffraction of the incident light.

In the case of compounds **5b** (Figure 7, middle) the situation was slightly different. Irradiating a solution of **5b** at 334 nm (thus populating the S$_3$ state) induced only weak emissions at 411 and 493 nm, respectively, while a much more intense peak was observed at 646 nm, indicating that for this compound non-radiative decay to the S$_1$ state was the preferred mean of energy dissipation when excited with higher energy radiation (also in this case a sharp peak at 668 nm was observed due to second-order diffraction of the incident radiation). This supposition was confirmed by the experiments

conducted with irradiation at 445 and 610 nm, for which the lowest energy emission band at 646 was the only one observed.

The opposite behaviour was displayed by compound **5c** (Figure 7, bottom). In this instance, irradiation at 292 and 353 nm (whose absorption peaks should correspond to localized $\pi\rightarrow\pi^*$ transitions within the triarylamine moiety) caused a fluorescence of moderate intensity centered at 474 nm, while only a very weak peak was seen at 645 nm. When irradiating at 610 nm, the fluorescence was only barely detectable, as shown by the very noisy normalized spectrum in Figure 7 indicating the prevalence of non-radiative decay from the lowest excited state S_1 or the occurrence of extensive reabsorption by the dye.

Finally, the spectra of the unsymmetrical D-A-π-A dye **DF90** (Figure 8) were registered. In solution, the dye exhibited absorption spectra similar to those of the symmetrical compounds, with a significantly red-shifted low energy transition (633–635 nm in CH_2Cl_2 and EtOH, respectively), whose molar extinction coefficient was however only moderate (0.65–0.70×10^4 M^{-1} cm^{-1}). The spectrum in CH_2Cl_2 also presented a shoulder at longer wavelengths relative to the indigo H-chromophore transition, which was attributed to the low solubility of **DF90** with the consequent formation of J (head to tail)-aggregates [49]. Accordingly, Tauc plots for both spectra resulted in estimated E_{0-0} values of 1.65–1.79 eV, which were smaller than those calculated for indigo and its symmetrical derivatives. When adsorbed on TiO_2, **DF90** gave a very broad UV-Vis spectrum with the main peaks at 411 nm (shoulder at 495 nm) and 612 nm, and onset around 720–730 nm. The blue-shift of the spectrum compared to the one in solution could be due both to the formation of H (parallel)-aggregates as well as the deprotonation of the carboxylic function upon anchoring onto the semiconductor [50,51].

Figure 8. UV−vis absorption spectra of dye **DF90** in CH_2Cl_2 and EtOH solution (**a**), and adsorbed on TiO_2 (**b**); Tauc plots corresponding to the absorption spectra in solution (**c**); fluorescence emission spectra in CH_2Cl_2 solution after excitation at different wavelengths (**d**); in the latter scheme, a peak at 582 nm deriving from second-order diffraction of incident light was deleted for clarity (red trace).

Due to the absorption minimum centered at about 550 nm, also in the case of **DF90** the resulting solutions as well as the semiconductor surface assumed a bright green coloration.

The emission behaviour of **DF90** in CH_2Cl_2 was qualitatively similar to that already observed for the symmetrical compound **5c**, with relatively strong fluorescence peaks corresponding to the S_3-S_0

and S_2-S_0 transitions, while the emission peak at approx. 650 nm was very weak (or even visible only as a shoulder of the more intense peak at 530 nm), perhaps due to extensive reabsorption by the wide absorption band between 600 and 750 nm. This is not surprising considering that both **5c** and **DF90** share the same donor group.

Finally, the ground-state oxidation potential ($E_{S+/S}$) of **DF90** was measured by means of cyclic voltammetry (CV), which was carried out in THF and is reported in Figure 9.
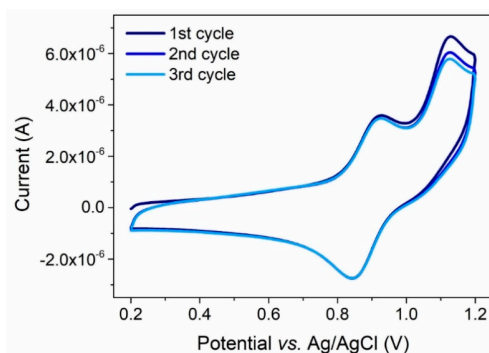
Figure 9. Cyclic Voltammetry plot relative to compound **DF90** in CH_2Cl_2 solution.

The observed curve indicated a reversible oxidation process and the observed potential (0.89 V vs. Ag/AgCl/satd. KCl, corresponding to 0.69 V vs. NHE) was more positive than the redox potential of the iodide/triiodide couple (0.35 V vs NHE), ref. [52] suggesting that regeneration of the sensitizer during operation of a solar cell was possible.

After a small current drop following the first cycle (perhaps due to the consumption of the dye physisorbed on the glassy carbon surface), the current/voltage curve remained practically identical in the following two cycles, indicating that the dye was sufficiently stable upon repeated oxidation/reduction processes. The $E_{S+/S}$ and E_{0-0} values in the same solvent were then used to calculate the excited state oxidation potential (E_{S+/S^*}) by means of the equation $E_{S+/S^*} = E_{S+/S} - E_{0-0}$. E_{S+/S^*} was found to be around -0.96 V vs. NHE, thereby more negative than the conduction band edge of the semiconductor (-0.5 V vs NHE) [53] and therefore appropriate to allow electron injection from the excited state dye to titania.

3. Experimental Section

3.1. General Information

Unless otherwise stated, all reagents were purchased from commercial suppliers and used without purification. *t*-Boc-protected 6-6′-dibromoindigo (**11**) [38] and stannanes **12c** [46], **12d** and **12e** [44] were prepared as previously reported. All air-sensitive reactions were performed using Schlenk techniques. Solvents used in cross-coupling reactions were previously degassed by means of the "freeze-pump-thaw" method. Tetrahydrofuran (THF) was freshly distilled immediately prior to use from sodium/benzophenone. CH_2Cl_2, toluene, and acetonitrile were dried on a resin exchange Solvent Purification System. Petroleum ether, unless specified, is the 40–70 °C boiling fraction. Organic phases derived from aqueous work-up were dried over Na_2SO_4. Reactions were monitored by TLC on SiO_2 plates, the detection was made using a $KMnO_4$ basic solution or UV lamp. Flash column chromatography was performed using glass columns (10–50 mm wide) and SiO_2 (230–400 mesh). ^{1}H-NMR spectra were recorded at 200, 300, or 400 MHz and ^{13}C-NMR spectra at 50.0, 75.5, or 100.6 MHz, respectively. Chemical shifts were referenced to the residual solvent peak ($CDCl_3$, δ 7.26 ppm for

^{1}H-NMR and δ 77.16 ppm for ^{13}C-NMR; THF-*d*[8] δ 3.58 and 1.72 ppm for ^{1}H-NMR, δ 67.21 and 25.31 ppm for ^{13}C-NMR; CD[2]Cl[2,] δ 5.32 ppm for ^{1}H-NMR, δ 53.84 ppm for ^{13}C-NMR). Coupling constants (*J*) are reported in Hz. ESI-MS were recorded with LCQ-Fleet Ion-Trap Mass Spectrometer. HR-MS were performed using an LTQ Orbitrap FT-MS Spectrometer. FT-IR spectra were recorded with a Perkin-Elmer Spectrum BX instrument in the range 4000–400 cm^{-1} with a 2 cm^{-1} resolution. UV-Vis spectra were recorded with a Varian Cary 400 spectrometer and a Shimadzu 2600 series spectrometer, and fluorescence spectra were recorded with a Varian Eclipse instrument, irradiating the sample at the wavelength corresponding to maximum absorption in the UV spectrum. UV-Vis spectra in different solvents were recorded on diluted solutions of the analyte (approximately 10^{-5} M) with a Shimadzu UV2600 spectrometer. UV-vis absorption or transmittance spectra of the compounds adsorbed on TiO$_2$ were recorded in transmission mode after the sensitization of thin, transparent semiconductor films (thickness approximately 5 μm).

Cyclic voltammetry experiments were conducted in chloroform solutions with a PARSTAT 2273 electrochemical workstation (Princeton Applied Research) employing a three-electrode cell having a 3 mm glassy carbon working electrode, a platinum counter electrode and an aqueous Ag/AgCl (sat. KCl) reference electrode and using ferrocene as a standard. The supporting electrolyte was electrochemical-grade 0.1 M [*N*(Bu)$_4$]PF$_6$; the dye concentration was approximately 10^{-3} M. Under these experimental conditions, the one-electron oxidation of ferrocene occurs at E$^{0'}$ = 0.55 V.

3.2. Computational Details

Molecular and electronic properties of keto–keto (KK), keto–enol (KE) and enol-enol (EE) tautomers of compounds **5a**, **5b**, **5c**, **5d**, **6d** and **DF90** have been computed via DFT [54–56] and time-dependent DFT (TD-DFT) [57,58] methods, using the Gaussian 16, Revision B.01 suite of programs [59]. Geometry optimizations have been carried out *in vacuo* and in solvent (DCM) using the polarizable continuum model (PCM) [60] to take into account solvent effects, at the B3LYP/6-31G** level of theory [61,62], according to a previous work of Amat et al. [9]. For molecule **5b**, methyl groups have been used in place of the alkyl chains attached to the ProDOT moiety in order to reduce the computational cost. Frequency calculations on the optimized structures have been performed at the same level to check that the stationary points were true energy minima. The ground-state electron density delocalization and the energy of DFT frontier molecular orbitals have been calculated at the same level of theory in DCM. The UV-Vis spectroscopic properties of the analyzed compounds, including absorption maximum (λ$^a_{max}$), vertical excitation energy (E$_{exc}$) and oscillator strengths (*f*) have been calculated in DCM on the minimized structures by means of TD-DFT at the B3LYP/6-311++G** and CAM-B3LYP/6-311++G** levels of theory [63].

3.3. Synthesis

3.3.1. Synthesis of Tributyl(3,3-dipentyl-3,4-dihydro-2H-thieno[3,4-b][1,4]dioxepin-6-yl)-stannane (**12b**)

3,3-Dipentyl-3,4-dihydro-2*H*-thieno[3,4-b][1,4]dioxepine (ProDOT, 1.35 g, 4.56 mmol, 1.0 eq.) was dissolved in dry THF (14 mL). The solution was cooled to −78 °C, and *n*-BuLi (1.6 M solution in hexanes, 3.2 mL, 5.5 mmol, 1.2 eq.) was slowly added. The reaction mixture was allowed to warm up to −20 °C while stirring, then cooled down again to −78 °C. Tributyltin chloride (Bu$_3$SnCl, 1.78 g, 5.5 mmol, 1.2 eq.) was added and the solution was allowed to warm up to room temperature and left under stirring overnight. The mixture was diluted with Et$_2$O (20 mL) and washed with a cold saturated solution of NH$_4$Cl (2 × 30 mL). The solvent was removed under reduced pressure to yield crude product **12b** (1.74 g, 3.0 mmol, 66% yield), which was used without further purification. ^{1}H-NMR (200 MHz, CDCl$_3$) δH = δH = 6.67 (1H, s), 3.75–3.87 (10H, m), 1.19–1.74 (24H, m), 0.76–1.03 (15H, m) ppm; ^{13}C-NMR {[1]H} (50 MHz, CDCl$_3$) δC = 155.7, 114.8, 111.0, 77.6, 43.8, 43.7, 32.7, 32.2, 29.0, 27.9, 27.2, 22.5, 14.0, 13.7, 10.7 ppm.

3.3.2. General Procedure for Preparation of Compounds **6a–d**

Pd$_2$(dba)$_3$ (10 mg, 0.011 mmol, 0.05 eq.) and P(o-Tol)$_3$ (7 mg, 0.022 mmol, 0.1 eq.) were dissolved in toluene (4 mL) and the solution was left at room temperature, under stirring for 15 min. *t*-Boc-protected 6-6′ dibromoindigo (**11**, 93 mg, 0.22 mmol, 1.0 eq.) was then added and the mixture stirred at room temperature for additional 15 min. The required stannane (0.46 mmol, 2.1 eq.) was dissolved in dry toluene (4 mL), and added to the reaction mixture, that was then warmed up to 50 °C, left under stirring and monitored by TLC. After 5 h, the mixture was cooled to room temperature, the solvent was removed by rotatory evaporation, and the crude was purified by flash column chromatography.

(E)-(1,1′-di-tert-butyl 3,3′-dioxo-6,6′-bis(thiophen-2-yl)-1H,1′H,3H,3′H-[2,2′-biindolylidene-1,1′-dicarboxylate) (**6a**). Compound **11** (92.5 mg, 0.22 mmol, 1.0 eq.) was reacted with tributyl(thiophen-2-yl)stannane **12a** (173 mg, 0.46 mmol, 2.1 eq.). Purification (petroleum ether:EtOAc gradient from 50:1 to 10:1) gave **6a** (119 mg, 0.19 mmol) as a purple red solid. Yield 86 %. Spectroscopic data were in agreement with those already reported.[45] ^{1}H-NMR (400 MHz, CDCl$_3$) δH = 8.32 (2H, s), 7.77 (2H, d, *J* = 7.9 Hz), 7.52 (2H, d, *J* = 3.5 Hz), 7.48 (2H, dd, *J*$_1$ = 7.9Hz, *J*$_2$ = 0.8Hz), 7.43 (2H, d, *J* = 5.0 Hz), 7.17–7.13 (m, 2H), 1.69 (18H, s). ^{13}C-NMR{[1]H} (100 MHz, CDCl$_3$) δC = 182.8, 150.0, 149.7, 143.6, 141.8, 128.7, 127.2, 125.6, 124.8, 122.0, 121,8, 114.0, 113.6, 84.8, 28.4. FT-IR (neat): ν = 3006 (w), 2956 (m), 2924 (m), 2854 (m), 1743 (s), 1670 (s), 1603 (s), 1579 (m) cm^{-1}. MS (ESI) *m/z* 627.1 [M + 1]$^+$.

(E)-(1,1′-di-tert-butyl 6,6′-bis({3,3-dipentyl-2H,3H,4H-thieno[3,4-b][1,4]dioxepin-6-yl})-3,3′- dioxo-1H, 1′H,3H,3′H-[2,2′-biindolylidene]-1,1′-dicarboxylate) (**6b**). Compound **11** (92.5 mg, 0.22 mmol, 1.0 eq.) was reacted with stannane **12b** (271 mg, 0.46 mmol, 2.1 eq.). Purification (CH$_2$Cl$_2$: petroleum ether = 50:1) gave **6b** (155 mg, 0.15 mmol) as a purple red solid. Yield 67%. 8.29 (2 H, br. s), 7.72 (2H, d, J = 8.2 Hz)), 7.61 (2 H, d, J = 8.2 Hz), 6.53 (2H, s), 4.02 (4H, s), 3.93 (4H, s), 1.67 (18H, s), 1.46–1.39 (8H, m), 1.38–1.25 (26H, m), 0. 91(12H, t, J = 6.9 Hz) ppm. ^{13}C-NMR{[1]H} (100 MHz, CDCl$_3$) δC =182.4, 150.5, 149.3, 147.9, 141.0, 129.0, 128.4, 125.4, 125.0, 121.1, 113.8, 104.9, 84.3, 77.7(2C), 43.7, 32.6, 32.0, 28.2, 28.0, 22.5, 14.0. FT-IR (neat): ν = 2926 (w), 2857 (w), 1605 (s), 1439 (s), 1374 (w) cm^{-1}. HRMS (ESI) m/z calculated for C$_{60}$H$_{79}$N$_2$O$_{10}$S$_2$: 1051.5170. Found: 1051.5177 [M + 1]$^+$.

(E)-(1,1′-di-tert-butyl 6,6′-bis(4-{bis[4-(hexyloxy)phenyl]amino}phenyl)-3,3′-dioxo-1H,1′H, 3H,3′H-[2,2′- biindolylidene]-1,1′-dicarboxylate) (**6c**). Compound **11** (130 mg, 0.2 mmol, 1.0 eq.) was reacted with stannane **12c** (308 mg, 0.42 mmol, 2.1 eq). Purification (petroleum ether: EtOAc gradient from 50:1 to 10:1) gave **6c** (210 mg, 0.16 mmol) as a purple solid. Yield 78 %. ^{1}H-NMR (200 MHz, CDCl$_3$) δH = 8.29 (2H, s), 7.62–7.91 (6H, m), 7.53 (4H, d, J = 8.8 Hz), 7.36–7.47 (6H, m), 7.13 (8H, d, J = 8.8 Hz), 7.00 (4H, d, J = 8.8 Hz), 6.88 (8H, d, J = 8.8 Hz), 3.96 (8H, t, J = 6.4 Hz), 1.72–1.79 (8H, m), 1.65 (18H, s), 1.56–1.30 (24H, s), 0.88–0.97 (12H, m) ppm. ^{13}C-NMR{[1]H} (50 MHz, CDCl$_3$) δC 182.9, 156.0, 149.9, 149.6, 148.7 143.4, 140.1, 131.1, 130.5, 129.0, 128.4, 128.1, 127.2, 125.5, 124.4, 119.7, 115.5, 84.2, 68.4, 31.7, 29.4, 28.2, 25.8, 22.6, 14.1. FT-IR (neat): ν = 2940 (m), 2929 (m), 2856 (m), 1733 (m), 1673 (s), 1589 (s), 1507 (s) cm^{-1}. HRMS (ESI) m/z calculated for C$_{86}$H$_{100}$N$_4$O$_{10}$: 1348.7434. Found: 1348.7455 [M]$^+$.

(E)-(1,1′-di-tert-butyl 6,6′-bis(4-{bis[4-(hexylsulfanyl)phenyl]amino}phenyl)-3,3′-dioxo-1H, 1′H,3H,3′H-[2,2′-biindolylidene]-1,1′- dicarboxylate) (**6d**). Compound **11** (93 mg, 0.22 mmol, 1.0 eq.) was reacted with stannane **12c** (353 mg, 0.46 mmol, 2.1 eq). Purification (petroleum ether:EtOAc gradient from 50:1 to 10:1) gave **6d** (235 mg, 0.15 mmol) as a purple red solid (yield 68%). Due to rapid decomposition, compound 6d, could not be fully characterized. MS (ESI) m/z 1576.0

3.3.3. General Procedure for the Preparation of Compounds **5a–c**

Compounds **6a–c** were dissolved in a 1:1 mixture of CH$_2$Cl$_2$ and TFA (5 mL) and the solution was left under stirring for 4 h at room temperature. The solvent was removed by rotatory evaporation, and the crude was purified by washing with petroleum ether or by flash column chromatography.

(E)-6,6′-bis(thiophen-2-yl)-1H,1′H,3H,3′H-[2,2′-biindolylidene]-3,3′-dione (**5a**) [45]. Deprotection of compound **6a** (70 mg, 0.11 mmol), after crystallization from petroleum ether, gave **5a** (44 mg, 0.10 mmol) as a green amorphous solid. Yield 93%. Spectroscopic data were in agreement with those already reported. [45] ^{1}H-NMR (400 MHz, THF-*d*$_8$) δH = 9.95 (2H, s), 7.64 (2H, d, J = 8.0 Hz), 7.55 (2H, dd,

J_1 = 3.6 Hz, J_2 = 1.0 Hz), 7.52 (2H, d, *J* = 0.7), 7.49 (2H, d, *J* = 4.7), 7.27 (2H, dd, J_1 = 8.0Hz, J_2 = 1.4Hz), 7.12 (2H, dd, J_1 = 5.0Hz, J_2 = 3.6 Hz). ^{13}C-NMR{^{1}H} (100 MHz, THF-d_8) δC 187.7, 154.0, 144.4, 141.9, 129.0, 127.4, 125.7, 124.9, 122.4, 119.7, 118.4, 109.7. FT-IR (neat): ν = 3344 (m), 3302 (m), 2954 (w), 2920 (m), 2850 (m), 1631 (s), 1610 (s), 1582 (s) cm^{-1}. MS (ESI) *m/z* 427, 2 [M + H]$^+$.

(E)-6,6′-bis({3,3-dipentyl-2H,3H,4H-thieno[3,4-b][1,4]dioxepin-6-yl})-1H,1′H,3H,3′H-[2,2′-bis-indolylidene]-3,3′-dione (**5b**). After purification (petroleum ether:EtOAc gradient from 35:1 to 10:1, then pure EtOAc), deprotection of compound **6b** (105 mg, 0.10 mmol) gave **5b** (82 mg, 0.96 mmol) as a green amorphous solid. Yield 96%. ^{1}H-NMR (200 MHz, CDCl$_3$) δH = 9.17 (2H, br. s.), 7.61 (2H, d, *J* = 8.1 Hz), 7.48 (2H, s), 7.12 (2H, d, *J* = 8.1 Hz), 6.45 (2H, s), 3.95 (4H, s), 3.88 (4H, s), 1.17–1.43 (32H, m), 0.81–0.98 (12H, m) ppm. ^{13}C-NMR{^{1}H} (50 MHz, CDCl$_3$) δC = 187.4, 152.2, 150.5, 147.9, 141.0, 124.4, 122.2, 120.6, 118.5,118.1, 109.3, 104.6, 77.5(2C), 65.8, 43.8, 32.7, 32.1, 22.5, 14.0 ppm. FT-IR (neat): ν = 3385 (w), 2954 (m), 2926 (m), 2857 (m), 1624 (m), 1604 (s), 1572 (m), 1438 (s) cm^{-1}. HRMS (ESI) *m/z* calculated for C$_{50}$H$_{62}$N$_2$O$_6$S$_2$: 851.4122. Found: 851.4145 [M + 1]$^+$.

(E)-6,6′-bis(4-{bis[4-(hexyloxy)phenyl]amino}phenyl)-1H,1′H,3H,3′H-[2,2′-biindolylidene]-3,3′-dione (**5c**). After purification (petroleum ether:EtOAc gradient from 35:1 to 10:1, then pure EtOAc), deprotection of compound **6c** (60 mg, 0.045 mmol), gave **5c** (52 mg, 0.044 mmol) as a green amorphous solid. Yield 92%. ^{1}H-NMR (200 MHz, CDCl$_3$) δH = 9.03 (2H, br. s.), 7.68 (2 H, d, *J*= 8.2 Hz), 7.41 (4 H, d, *J* = 8.8Hz), 7.10–7.17 (4H, m), 7.07 (8H, d, *J* = 9.3 Hz), 6.94 (4H, d, *J* = 8.2 Hz), 6.84 (8H, d, *J* = 9.3), 3.94 (8H, t, *J* = 6.3Hz), 1.74–1.83 (8H, m), 1.43–1.52 (8H, m), 1.32–1.37 (16H, m), 0.90–0.94 (12H, m); ^{13}C-NMR{^{1}H} (50 MHz, CDCl$_3$) δC = 187.9, 155.9, 152.5, 149.4, 148.7, 140.0, 130.8, 127.8, 127.1, 124.7, 122.2, 119.5, 118.2, 117.1, 115.35, 109.2, 68.2, 31.6, 29.3, 25.7, 22.6, 14.0. FT-IR (neat): ν = 3368 (w), 2952 (w), 2927 (m), 2857 (m), 1627 (m), 1594 (s), 1503 (s), 1444 (s) cm^{-1}. HRMS (ESI) *m/z* calculated for C$_{76}$H$_{84}$N$_4$O$_6$: 1148.6391. Found: 1148.6415 [M]$^+$.

3.3.4. Synthesis of Dye **DF90**

Synthesis of (E)-(1,1′-di-tert-butyl 6-bromo-6′-(5-formylthiophen-2-yl)-3,3′-dioxo-1H,1′H, 3H,3′H-[2,2′-biindolylidene]-1,1′-dicarboxylate) (**13**). Pd$_2$(dba)$_3$·CHCl$_3$ (86.0 mg, 0.08 mmol, 0.2 eq.) and P(o-Tol)$_3$ (100.0 mg, 0.32 mmol, 0.7 eq.) were dissolved in toluene (150 mL) and the solution was left under stirring for 15 min. t-Boc-protected 6-6′-dibromoindigo (**11**, 1.50 g, 2.4 mmol, 5.0 eq.) was then added and the mixture stirred at room temperature for additional 15 min. A solution of 5-(tributylstannyl)thiophene-2-carbaldehyde 12e (190 mg, 0.48 mmol, 1.0 eq.) in toluene (10 mL) was added and the mixture warmed to 50 °C overnight. The solvent was then removed by rotatory evaporation and a mixture of EtOAc:hexane = 1:20 (100 mL) was added to the residue. The insoluble fraction was washed several times with the same mixture, allowing to recover starting material **11**. The organic phase, after evaporation, gave a crude solid which was purified by flash chromatography (CH$_2$Cl$_2$ then CH$_2$Cl$_2$:EtOAc 50:1) to afford aldehyde **13** (310 mg, 0.48 mmol) as a red amorphous solid. Yield 79%. ^{1}H-NMR (200 MHz, CDCl$_3$) δH = 9.95 (1H, s), 8.39 (1H, d, J = 1.5 Hz), 8.27 (1H, d, J = 1.5 Hz), 7.79–7.85 (2H, m), 7.57–7.65 (2H, m), 7.54 (1H, dd, J_1 = 7.9, J_2 = 1.5), 7.38 (1H, dd, J_1 = 8.1, J_2 = 1.5). 1.72 (9H, s), 1.69 (9H, s). ^{13}C-NMR{^{1}H} (50 MHz, CDCl$_3$) δC = 182.7, 182.4, 182.3, 152.3, 149.6, 149.5, 149.4, 144.0, 140.1, 137.1, 131.0, 127.7, 126.1, 126.0, 125.0, 124.9, 124.8, 123.0, 122.5, 122.4, 121.7, 120.2, 114.4, 85.2, 85.1, 28.1, 28.0; MS (ESI) m/z 673.0 [M + Na]$^+$.

Synthesis of di-tert-butyl (E)-6-(4-(bis(4-(hexyloxy)phenyl)amino)phenyl)-6′-(5-formylthiophen-2-yl)-3,3′-dioxo-[2,2′-biindolinylidene]-1,1′-dicarboxylate (**14**). Pd$_2$(dba)$_3$·CHCl$_3$ (6.0 mg, 0.02 mmol, 0.2 eq.) and P(o-Tol)$_3$ (31.0 mg, 0.10 mmol, 0.7 eq.) were dissolved in THF (4 mL) and the solution was left under stirring for 15 min. Bromoaldehyde **13** (100.0 mg, 0.15 mmol, 1.0 eq.) was then added and the mixture stirred at room temperature for an additional 15 min. A solution of stannane **12c** (220.0 mg, 0.30 mmol, 2.0 eq) in THF (1 mL) was added to the mixture and warmed to 55 °C. After 7 h the solvent was removed by rotatory evaporation, the crude residue was dissolved with EtOAc (10 mL) and washed with an aqueous saturated KF solution, then with brine. The organic phase was dried, then removed under vacuum to give a crude product which was purified by flash chromatography (CH$_2$Cl$_2$: Petroleum

94

ether = 1:1 then CH_2Cl_2: Ethyl acetate 20:1) to obtain **14** (93 mg, 0.15 mmol) as a red amorphous solid. Yield 61%. ^{1}H-NMR (400 MHz, CD_2Cl_2) δH 9.95 (1H, s), 8.42 (1H, s), 8.24 (1H, s), 7.83–7.74 (m, 3H), 7.63 (1H, d, J = 3.9Hz) 7.58–7.53 (3H, m), 7.53–7.47 (m, 3H), 7.46 (1H, dd, J_1 = 7.8Hz, J_2 = 1.5Hz m), 7.12 (4H, d, J = 9.0Hz), 6.98 (2H, d, J = 9.0Hz), 6.89 (4H, d, J = 9.0Hz), 3.97 (4H, d, J = 6.4Hz), 1.82–1.75 (4H, m), 1.66 (9H, s), 1.63 (9H, s), 1.55–1.45 (4H, m), 1.40–1.32 (8H, m), 0.92 (6H, t, J = 5.9 Hz); ^{13}C-NMR{[1]H} (100 MHz, CD_2Cl_2) δC = 182.8, 182.7, 182.3, 152.1, 149.9, 149.8, 149.7, 149.3, 148.7, 144.0, 139.8, 139.7, 137.2, 130.4, 127.9, 127.3, 126.2, 126.1, 124.7, 124.6, 124.3, 123.2, 122.2, 122.1, 120.8, 119.2, 115.3, 114.1, 113.5, 84.7, 84.4, 68.3, 31.6, 29.3, 27.8, 25.7, 22.6, 13.8; MS (ESI) Found: m/z 1015.25 [M]$^+$.

Synthesis of (2E,Z)-3-{5-[(E)-6'-(4-{bis[4-(hexyloxy)phenyl]amino}phenyl)-3,3'-dioxo-1H,1'H, 3H,3'H-[2,2'-biindolyliden]-6-yl]thiophen-2-yl}-2-cyanoprop-2-enoic acid (**DF90**).To a solution of aldehyde **14** (95 mg, 0.093 mmol, 1 eq) in a mixture of acetonitrile/CH_2Cl_2 (1:1, 4 mL, dried on molecular sieves) were added cyanoacetic acid (10 mg, 0.12 mmol, 1.3 eq) and dry piperidine (84 mg, 0.99 mmol, 8 eq). The mixture was refluxed for 1 h, then it was cooled and the solvent removed under vacuum. The crude was dissolved in CH_2Cl_2 (10 mL) and washed with NaOH 0.1M and finally with HCl 0.1M. The organic phase was dried on Na_2SO_4, then the solvent was removed under vacuum. The crude product was recrystallized from CH_2Cl_2/ethyl acetate (2:1) to obtain **DF90** (45 mg, 0.093 mmol) as a green solid. Yield 55%. ^{1}H-NMR (400 MHz, THF-d_8) δH = 9.99 (2H, br s), 8.39 (1H, s), 7.89 (1H, d, J = 3.9 Hz), 7.70–7.62 (4H, m), 7.52 (2H, d, J = 9.0 Hz), 7.42 (1H, s), 7.38 (1H, d, J = 8.2 Hz), 7.20 (1H, d, J = 8.6 Hz), 7.08–7.05 (4H, m), 6.93 (2H, d, J = 9.0 Hz), 6.88-6.85 (4H, m), 3.95, (4H, t, J = 6.4 Hz), 1.81–1.74 (4H, m), 1.53–1.46 (4H, m), 1.39–1.35 (8H, m), 0.93 (6H, t, J = 7.0 Hz); ^{13}C-NMR{[1]H} (100 MHz, $CDCl_3$) δC= 188.2, 187.6, 163.4, 157.2, 154.5, 153.8, 153.3, 150.6, 149.2, 146.5, 141.2, 139.9, 137.5, 132.2, 128.5, 128.0, 126.8, 125.2, 124.9, 123.3, 122.2, 121.2, 120.4, 119.5, 119.1, 118.6, 116.5, 116.1, 111.5, 111.1, 110.9, 110.4, 68.8, 32.6, 30.4, 26.8, 23.6, 14.4; FT-IR (neat): ν = 2923 (w), 2853 (m), 1704 (m), 1586 (s), 1505 (s), 1445 (s) cm^{-1}. HRMS (ESI) m/z calculated for $C_{54}H_{50}N_4O_6S$: 882,3451. Found: 882.3435 [M]$^+$.

4. Conclusions

In this paper, a mild synthetic approach to prepare indigo based dyes is reported. Tyrian Purple is used as starting material to be coupled, after *t*-Boc protection, with different stannanes under Stille-Migita conditions. Three new symmetrical D-A-D dyes featuring an extended conjugation have been prepared and spectroscopically characterized and their optical properties compared with the results of theoretical calculations. Furthermore, non-symmetrical indigo-based D-A-π-A dye has been designed, synthesized and fully characterized both spectroscopically and electrochemically, assessing the possibility of using the indigo scaffold to prepare green dyes for DSSC application

Author Contributions: D.F. and M.C. carried out the synthesis and characterization of the new compounds; D.F. and L.Z. carried out the spectroscopic and electrochemical studies of the dyes and prepared the corresponding figures; A.S. and C.C. carried out the DFT computational studies. A.M. and G.R. supervised and coordinated the research work. All authors have read and agreed to the published version of the manuscript.

Conflicts of Interest: The authors declare no conflict of interest.

References

1. Editorial: Chemists go green to make better blue jeans. *Nature* **2018**, *553*, 128. [CrossRef] [PubMed]
2. Baeyer, A.; Drewsen, V. Darstellung von Indigblau aus Orthonitrobenzaldehyd. *Berichte der Dtsch. Chem. Gesellschaft* **1882**, *15*, 2856–2864. [CrossRef]

3.   Baeyer, A. Ueber die Verbindungen der Indigogruppe. *Berichte der Dtsch. Chem. Gesellschaft* **1883**, *16*, 2188–2204. [CrossRef]

4.   Głowacki, E.D.; Voss, G.; Sariciftci, N.S. 25th Anniversary Article: Progress in Chemistry and Applications of Functional Indigos for Organic Electronics. *Adv. Mater.* **2013**, *25*, 6783–6800. [CrossRef] [PubMed]

5.   Jacquemin, D.; Perpète, E.A.; Scuseria, G.E.; Ciofini, I.; Adamo, C. TD-DFT Performance for the Visible Absorption Spectra of Organic Dyes: Conventional versus Long-Range Hybrids. *J. Chem. Theory Comput.* **2008**, *4*, 123–135. [CrossRef] [PubMed]

6.   Tatsch, E.; Schrader, B. Near-infrared fourier transform Raman spectroscopy of indigoids. *J. Raman Spectrosc.* **1995**, *26*, 467–473. [CrossRef]

7.   Konarev, D.V.; Zorina, L.V.; Batov, M.S.; Khasanov, S.S.; Otsuka, A.; Yamochi, H.; Kitagawa, H.; Lyubovskaya, R.N. Optical and magnetic properties of trans -indigo˙−radical anions. Magnetic coupling between trans-indigo˙-(S = 1/2) mediated by intermolecular hydrogen N–H···O=C bonds. *New J. Chem.* **2019**, *43*, 7350–7354. [CrossRef]

8.   Serrano-Andrés, L.; Roos, B.O. A Theoretical Study of the Indigoid Dyes and Their Chromophore. *Chem.-A Eur. J.* **1997**, *3*, 717–725. [CrossRef]

9.   Amat, A.; Rosi, F.; Miliani, C.; Sgamellotti, A.; Fantacci, S. Theoretical and experimental investigation on the spectroscopic properties of indigo dye. *J. Mol. Struct.* **2011**, *993*, 43–51. [CrossRef]

10.   Irimia-Vladu, M.; Głowacki, E.D.; Troshin, P.A.; Schwabegger, G.; Leonat, L.; Susarova, D.K.; Krystal, O.; Ullah, M.; Kanbur, Y.; Bodea, M.A.; et al. Indigo - A Natural Pigment for High Performance Ambipolar Organic Field Effect Transistors and Circuits. *Adv. Mater.* **2012**, *24*, 375–380. [CrossRef]

11.   Klimovich, I.V.; Leshanskaya, L.I.; Troyanov, S.I.; Anokhin, D.V.; Novikov, D.V.; Piryazev, A.A.; Ivanov, D.A.; Dremova, N.N.; Troshin, P.A. Design of indigo derivatives as environment-friendly organic semiconductors for sustainable organic electronics. *J. Mater. Chem. C* **2014**, *2*, 7621–7631. [CrossRef]

12.   Alexy, M.; Voss, G.; Heinze, J. Optochemical sensor for determining ozone based on novel soluble indigo dyes immobilised in a highly permeable polymeric film. *Anal. Bioanal. Chem.* **2005**, *382*, 1628–1641. [CrossRef] [PubMed]

13.   Brunet, J.; Spinelle, L.; Ndiaye, A.; Dubois, M.; Monier, G.; Varenne, C.; Pauly, A.; Lauron, B.; Guerin, K.; Hamwi, A. Physical and chemical characterizations of nanometric indigo layers as efficient ozone filter for gas sensor devices. *Thin Solid Films* **2011**, *520*, 971–977. [CrossRef]

14.   Yao, M.; Kuratani, K.; Kojima, T.; Takeichi, N.; Senoh, H.; Kiyobayashi, T. Indigo carmine: An organic crystal as a positive-electrode material for rechargeable sodium batteries. *Sci. Rep.* **2015**, *4*, 3650. [CrossRef] [PubMed]

15.   Yao, M.; Araki, M.; Senoh, H.; Yamazaki, S.; Sakai, T.; Yasuda, K. Indigo Dye as a Positive-electrode Material for Rechargeable Lithium Batteries. *Chem. Lett.* **2010**, *39*, 950–952. [CrossRef]

16.   Porada, J.H.; Neudörfl, J.-M.; Blunk, D. Planar and distorted indigo as the core motif in novel chromophoric liquid crystals. *New J. Chem.* **2015**, *39*, 8291–8301. [CrossRef]

17.   Porada, J.H.; Blunk, D. Phasmidic indigoid liquid crystals. *J. Mater. Chem.* **2010**, *20*, 2956–2958. [CrossRef]

18.   Rajan, A.K.; Cindrella, L. Studies on new natural dye sensitizers from Indigofera tinctoria in dye-sensitized solar cells. *Opt. Mater. (Amst).* **2019**, *88*, 39–47. [CrossRef]

19.   Kalyanasundaram, K. *Dye-sensitized Solar Cells*; EFPL Press: Lausanne, Switzerland, 2010; ISBN 9781439808665.

20.   O'Regan, B.; Grätzel, M. A low-cost, high-efficiency solar cell based on dye-sensitized colloidal TiO$_2$ films. *Nature* **1991**, *353*, 737–740. [CrossRef]

21.   Calogero, G.; Bartolotta, A.; Di Marco, G.; Di Carlo, A.; Bonaccorso, F. Vegetable-based dye-sensitized solar cells. *Chem. Soc. Rev.* **2015**, *44*, 3244–3294. [CrossRef]

22.   Zhang, L.; Yang, X.; Wang, W.; Gurzadyan, G.G.; Li, J.; Li, X.; An, J.; Yu, Z.; Wang, H.; Cai, B.; et al. 13.6% Efficient Organic Dye-Sensitized Solar Cells by Minimizing Energy Losses of the Excited State. *ACS Energy Lett.* **2019**, *4*, 943–951. [CrossRef]

23.   Mishra, A.; Fischer, M.K.R.; Bäuerle, P. Metal-Free Organic Dyes for Dye-Sensitized Solar Cells: From Structure: Property Relationships to Design Rules. *Angew. Chemie Int. Ed.* **2009**, *48*, 2474–2499. [CrossRef]

24.   Ooyama, Y.; Harima, Y. Molecular Designs and Syntheses of Organic Dyes for Dye-Sensitized Solar Cells. *European J. Org. Chem.* **2009**, *2009*, 2903–2934. [CrossRef]

25.   Obotowo, I.N.; Obot, I.B.; Ekpe, U.J. Organic sensitizers for dye-sensitized solar cell (DSSC): Properties from computation, progress and future perspectives. *J. Mol. Struct.* **2016**, *1122*, 80–87. [CrossRef]

26. Brogdon, P.; Cheema, H.; Delcamp, J.H. Near-Infrared-Absorbing Metal-Free Organic, Porphyrin, and Phthalocyanine Sensitizers for Panchromatic Dye-Sensitized Solar Cells. *ChemSusChem* **2018**, *11*, 86–103. [CrossRef] [PubMed]

27. Burke, A.; Schmidt-Mende, L.; Ito, S.; Grätzel, M. A novel blue dye for near-IR 'dye-sensitised' solar cell applications. *Chem. Commun.* **2007**, 234–236. [CrossRef]

28. Paek, S.; Choi, H.; Kim, C.; Cho, N.; So, S.; Song, K.; Nazeeruddin, M.K.; Ko, J. Efficient and stable panchromatic squaraine dyes for dye-sensitized solar cells. *Chem. Commun.* **2011**, *47*, 2874. [CrossRef]

29. Shi, Y.; Hill, R.B.M.; Yum, J.-H.; Dualeh, A.; Barlow, S.; Grätzel, M.; Marder, S.R.; Nazeeruddin, M.K. A High-Efficiency Panchromatic Squaraine Sensitizer for Dye-Sensitized Solar Cells. *Angew. Chem. Int. Ed.* **2011**, *50*, 6619–6621. [CrossRef]

30. Jradi, F.M.; Kang, X.; O'Neil, D.; Pajares, G.; Getmanenko, Y.A.; Szymanski, P.; Parker, T.C.; El-Sayed, M.A.; Marder, S.R. Near-Infrared Asymmetrical Squaraine Sensitizers for Highly Efficient Dye Sensitized Solar Cells: The Effect of π-Bridges and Anchoring Groups on Solar Cell Performance. *Chem. Mater.* **2015**, *27*, 2480–2487. [CrossRef]

31. Yum, J.-H.; Holcombe, T.W.; Kim, Y.; Rakstys, K.; Moehl, T.; Teuscher, J.; Delcamp, J.H.; Nazeeruddin, M.K.; Grätzel, M. Blue-Coloured Highly Efficient Dye-Sensitized Solar Cells by Implementing the Diketopyrrolopyrrole Chromophore. *Sci. Rep.* **2013**, *3*, 2446. [CrossRef]

32. Liyanage, N.P.; Yella, A.; Nazeeruddin, M.; Grätzel, M.; Delcamp, J.H. Thieno[3,4- b]pyrazine as an Electron Deficient π-Bridge in D–A−π– A DSCs. *ACS Appl. Mater. Interfaces* **2016**, *8*, 5376–5384. [CrossRef] [PubMed]

33. Wu, Y.; Zhu, W.-H.; Zakeeruddin, S.M.; Grätzel, M. Insight into D–A−π–A Structured Sensitizers: A Promising Route to Highly Efficient and Stable Dye-Sensitized Solar Cells. *ACS Appl. Mater. Interfaces* **2015**, *7*, 9307–9318. [CrossRef] [PubMed]

34. Dessì, A.; Sinicropi, A.; Mohammadpourasl, S.; Basosi, R.; Taddei, M.; Fabrizi de Biani, F.; Calamante, M.; Zani, L.; Mordini, A.; Bracq, P.; et al. New Blue Donor–Acceptor Pechmann Dyes: Synthesis, Spectroscopic, Electrochemical, and Computational Studies. *ACS Omega* **2019**, *4*, 7614–7627. [CrossRef]

35. Abdullah, M.I.; Janjua, M.R.S.A.; Mahmood, A.; Ali, S.; Ali, M. Quantum Chemical Designing of Efficient Sensitizers for Dye Sensitized Solar Cells. *Bull. Korean Chem. Soc.* **2013**, *34*, 2093–2098. [CrossRef]

36. Cervantes-Navarro, F.; Glossman-Mitnik, D. Density functional theory study of indigo and its derivatives as photosensitizers for dye-sensitized solar cells. *J. Photochem. Photobiol. A Chem.* **2013**, *255*, 24–26. [CrossRef]

37. Hosseinnezhad, M.; Moradian, S.; Gharanjig, K. Synthesis and Characterization of Two New Organic Dyes for Dye-Sensitized Solar Cells. *Synth. Commun.* **2014**, *44*, 779–787. [CrossRef]

38. Głowacki, E.D.; Apaydin, D.H.; Bozkurt, Z.; Monkowius, U.; Demirak, K.; Tordin, E.; Himmelsbach, M.; Schwarzinger, C.; Burian, M.; Lechner, R.T.; et al. Air-stable organic semiconductors based on 6,6′-dithienylindigo and polymers thereof. *J. Mater. Chem. C* **2014**, *2*, 8089–8097. [CrossRef]

39. Pina, J.; Alnady, M.; Eckert, A.; Scherf, U.; Seixas de Melo, J.S. Alternating donor–acceptor indigo-cyclopentadithiophene copolymers: Competition between excited state conformational relaxation, energy transfer and excited state proton transfer. *Mater. Chem. Front.* **2018**, *2*, 281–290. [CrossRef]

40. Liu, C.; Xu, W.; Xue, Q.; Cai, P.; Ying, L.; Huang, F.; Cao, Y. Nanowires of indigo and isoindigo-based molecules with thermally removable groups. *Dye. Pigment.* **2016**, *125*, 54–63. [CrossRef]

41. Liu, C.; Dong, S.; Cai, P.; Liu, P.; Liu, S.; Chen, J.; Liu, F.; Ying, L.; Russell, T.P.; Huang, F.; et al. Donor–Acceptor Copolymers Based on Thermally Cleavable Indigo, Isoindigo, and DPP Units: Synthesis, Field Effect Transistors, and Polymer Solar Cells. *ACS Appl. Mater. Interfaces* **2015**, *7*, 9038–9051. [CrossRef]

42. Ma, C.; Li, H.; Yang, Y.; Li, D.; Liu, Y. TD-DFT study on electron transfer mobility and intramolecular hydrogen bond of substituted indigo derivatives. *Chem. Phys. Lett.* **2015**, *638*, 72–77. [CrossRef]

43. Pina, J.; Sarmento, D.; Accoto, M.; Gentili, P.L.; Vaccaro, L.; Adelino, G.; Seixas De Melo, J.S. Excited-State Proton Transfer in Indigo. *J. Phys. Chem. B* **2017**, *121*, 2308–2318. [CrossRef]

44. Dessì, A.; Bartolini, M.; Calamante, M.; Zani, L.; Mordini, A.; Reginato, G. Extending the Conjugation of Pechmann Lactone Thienyl Derivatives: A New Class of Small Molecules for Organic Electronics Application. *Synthesis (Sttutgart)* **2018**, *50*, 1284–1292. [CrossRef]

45. Baran, P.S.; Shenvi, R.A. Total Synthesis of (±)-Chartelline C. *J. Am. Chem. Soc.* **2006**, *128*, 14028–14029. [CrossRef]

46. Gao, P.; Tsao, H.N.; Grätzel, M.; Nazeeruddin, M.K. Fine-tuning the Electronic Structure of Organic Dyes for Dye-Sensitized Solar Cells. *Org. Lett.* **2012**, *14*, 4330–4333. [CrossRef] [PubMed]

47. Jacquemin, D.; Preat, J.; Wathelet, V.; Perpète, E.A. Substitution and chemical environment effects on the absorption spectrum of indigo. *J. Chem. Phys.* **2006**, *124*, 074104. [CrossRef] [PubMed]
48. Dähne, S.; Leupold, D. Coupling Principles in Organic Dyes. *Angew. Chem. Int. Ed. Eng.* **1966**, *5*, 984–993. [CrossRef]
49. Shimizu, M.; Hiyama, T. Organic Fluorophores Exhibiting Highly Efficient Photoluminescence in the Solid State. *Chem. Asian J.* **2010**, *5*, 1516–1531. [CrossRef]
50. Zhang, L.; Cole, J.M. Dye aggregation in dye-sensitized solar cells. *J. Mater. Chem. A* **2017**, *5*, 19541–19559. [CrossRef]
51. Chang, Y.J.; Chow, T.J. Highly efficient triarylene conjugated dyes for sensitized solar cells. *J. Mater. Chem.* **2011**, *21*, 9523. [CrossRef]
52. Boschloo, G.; Hagfeldt, A. Characteristics of the Iodide/Triiodide Redox Mediator in Dye-Sensitized Solar Cells. *Acc. Chem. Res.* **2009**, *42*, 1819–1826. [CrossRef] [PubMed]
53. Hagfeldt, A.; Boschloo, G.; Sun, L.; Kloo, L.; Pettersson, H. Dye-Sensitized Solar Cells. *Chem. Rev.* **2010**, *110*, 6595–6663. [CrossRef] [PubMed]
54. Honenberg, P.; Kohn, W. Inhomogeneous Electron Gas. *Phys. Rev. B* **1964**, *136*, 864–871. [CrossRef]
55. Kohn, W.; Sham, L.J. Self-Consistent Equations Including Exchange and Correlation Effects. *Phys. Rev.* **1965**, *140*, 1134–1138. [CrossRef]
56. Parr, R.G.; Yang, W. *Density-Functional Theory of Atoms and Molecules*; Oxford University Press: New York, NY, USA, 1989.
57. Adamo, C.; Jacquemin, D. The calculations of excited-state properties with Time-Dependent Density Functional Theory. *Chem. Soc. Rev.* **2013**, *42*, 845–856. [CrossRef] [PubMed]
58. Laurent, A.D.; Adamo, C.; Jacquemin, D. Dye chemistry with time-dependent density functional theory. *Phys. Chem. Chem. Phys.* **2014**, *16*, 14334–14356. [CrossRef] [PubMed]
59. Frisch, M.J.; Trucks, G.W.; Schlegel, H.B.; Scuseria, G.E.; Robb, M.A.; Cheeseman, J.R.; Scalmani, G.; Barone, V.; Petersson, G.A.; Nakatsuji, H.; et al. *Gaussian 09, Revision D.01*; Gaussian, Inc.: Wallingford, CT, USA, 2016.
60. Tomasi, J.; Mennucci, B.; Cammi, R. Quantum Mechanical Continuum Solvation Models. *Chem. Rev.* **2005**, *105*, 2999–3094. [CrossRef]
61. Becke, A.D. Density-functional thermochemistry. III. The role of exact exchange. *J. Chem. Phys.* **1993**, *98*, 5648–5652. [CrossRef]
62. Lee, C.; Yang, W.; Parr, R.G. Development of the Colle-Salvetti correlation-energy formula into a functional of the electron density. *Phys. Rev. B* **1988**, *37*, 785–789. [CrossRef]
63. Yanai, T.; Tew, D.P.; Handy, N.C. A new hybrid exchange–correlation functional using the Coulomb-attenuating method (CAM-B3LYP). *Chem. Phys. Lett.* **2004**, *393*, 51–57. [CrossRef]

Sample Availability: Samples of the compounds **5a–c** and **6a–c** available from the authors.

4.4. Manuscript 4: "Ground-State Redox Potentials Calculations of D-π-A and D-A-π-A Organic Dyes for DSSC and Visible-Light-Driven Hydrogen Production"

In this work, the ground-state redox potentials of 16 D-π-A and D-A-π-A dyes, having medium to large size of the conjugated scaffold, have been predicted by DFT and TDDFT methods at MPW1K/6-31+G* level of theory, in terms of Gibbs free energy differences between the neutral and oxidized state. The results have been compared with the experimental available data, demonstrating that the employed strategy is very accurate and consent to identify the most promising dyes to be used in DSSCs application. Indeed, one of the main parameters that influence the overall DSSCs performances is a correct energy levels alignment between the dye and the redox couple, hence the ground-state redox potential is a measure of the dye regeneration driving force.

The PhD candidate's contribution refers to the application of DFT and TDDFT methods for the investigation of the orbital relaxation. In particular, the HOMO of each neutral dye has been compared with the calculated spin-density surface of its cation in gas-phase and dichloromethane, showing that they have very similar shape and space distribution. Hence, orbital relaxation is minimal, and Koopmans' theorem has been demonstrated to be valid in gas-phase and in dichloromethane. The spin density of cation species has been calculated at MPW1K/6-31+G* level of theory in *vacuo* and in dichloromethane, including the solvent effects by PCM.

Article

Ground-State Redox Potentials Calculations of D-π-A and D-A-π-A Organic Dyes for DSSC and Visible-Light-Driven Hydrogen Production

Sanaz Mohammadpourasl [1], **Fabrizia Fabrizi de Biani** [2], **Carmen Coppola** [1,3],
Maria Laura Parisi [1,3,4], **Lorenzo Zani** [4], **Alessio Dessì** [4], **Massimo Calamante** [4],
Gianna Reginato [4], **Riccardo Basosi** [1,3,4] and **Adalgisa Sinicropi** [1,3,4,*]

[1] R²ES Lab, Department of Biotechnology, Chemistry and Pharmacy, University of Siena, 53100 Siena, Italy;
sanaz.mohammadpourasl@unifi.it (S.M.); carmen.coppola@student.unisi.it (C.C.);
marialaura.parisi@unisi.it (M.L.P.); riccardo.basosi@unisi.it (R.B.)

[2] Department of Biotechnology, Chemistry and Pharmacy, University of Siena, 53100 Siena, Italy;
fabrizia.fabrizi@unisi.it

[3] Center for Colloid and Surface Science (CSGI), 50019 Sesto Fiorentino, Italy

[4] National Research Council, Institute for the Chemistry of OrganoMetallic Compounds (CNR-ICCOM),
50019 Sesto Fiorentino, Italy; lorenzo.zani@iccom.cnr.it (L.Z.); a.dessi@iccom.cnr.it (A.D.);
mcalamante@iccom.cnr.it (M.C.); gianna.reginato@iccom.cnr.it (G.R.)

* Correspondence: adalgisa.sinicropi@unisi.it

Abstract: The prediction of ground-state redox potentials by quantum chemical methods has a prominent role in the rational design of novel organic photosensitizers both for dye-sensitized solar cells (DSSCs) and photocatalytic systems for the production of H_2. Indeed, the ground-state redox potential of the photosensitizers is one of the key parameters to identify the most promising candidates for such applications. Here, the ground-state redox potentials of 16 organic donor-π-acceptor D-π-A and donor-acceptor-π-acceptor D-A-π-A dyes having a medium to large size of the conjugated scaffold are evaluated, using the methods of the Density Functional Theory (DFT), in terms of free energy differences between their neutral and oxidized ground-state forms. These results are compared to the available experimental data and to the computed highest occupied molecular orbital energy $-\varepsilon(HOMO)$ values as an approximation of ground-state redox potentials according to Koopmans' theorem. Using the MPW1K functional in combination with the 6-31+G* basis set, the strategy based on the free energy cycle, including solvent effects, reproduces with a good level of accuracy the observed values (mean absolute error (MAE) < 0.2 eV) and trend of redox potentials within related families of dyes. On the other hand, the $-\varepsilon(HOMO)$ values are only able to capture the experimental trends in redox potential values.

Keywords: dye-sensitized solar cells; first principle modelling; ground-state oxidation potentials; solar energy devices; solar fuel devices; organic sensitizers; photocatalytic hydrogen production

---

1. Introduction

Organic dyes having a donor-π-acceptor (D-π-A) or donor-acceptor-π-acceptor (D-A-π-A) architecture have been extensively used as photosensitizers in dye-sensitized solar cells (DSSCs) [1–3] and, more recently, as sensitizers in photocatalytic systems for the production of H_2 [4–7]. In both devices, visible-light absorbing dyes are employed to enhance light harvesting of semiconductor nanoparticles of TiO_2.

The use of synthetic organic push-pull dyes is becoming increasingly popular [6]. In particular, donor–acceptor D-π-A architectures, have been found able to establish an efficient charge separation: indeed, due to the wide diversity of suitable D, A and π fragments a huge number of different sensitizers can be accessed, allowing a fine-tuning of their chemical, optical, energetic, and stability properties. In addition, recently, the use of sensitizers based on the D−A−π−A architecture has been investigated, finding that the additional acceptor is useful for modulating the energy levels, extending the light harvesting ability, as well as improving photovoltaic performances and photostability. Indeed, the additional electron acceptor unit can enhance the intramolecular electronic push−pull effect, thus significantly affecting the energy levels and absorption properties of sensitizers [8].

In DSSCs, the dye absorbs light and, upon excitation, it transfers an electron to the conduction band of the semiconductor, which carries it to a glass electrode (transparent conducting oxide layer); at the same time, the resulting hole is transferred from the dye/sensitizer to the redox mediator (usually an I^-/I_3^- redox couple) which, through an oxidation-reduction interchange, carries it to the counter-electrode, thereby closing the circuit and generating a current (See Figure 1a).

The photocatalytic systems, on the other hand, are dye-sensitized Pt/TiO_2 photocatalysts in which the dye, as in DSSCs, harvests visible light and injects the electron in the TiO_2 conduction band (See Figure 1b). Electrons are then transferred to Pt^0 nanoparticles, which are adsorbed on the TiO_2 surface and here protons are reduced to H_2. The regeneration of the oxidized dye occurs by using a sacrificial electron donor (SED) agent. Triethanolamine (TEOA), ethylenediaminetetraacetic acid (EDTA), ascorbic acid (AA) and, more recently, ethanol, have been employed as SEDs [4].
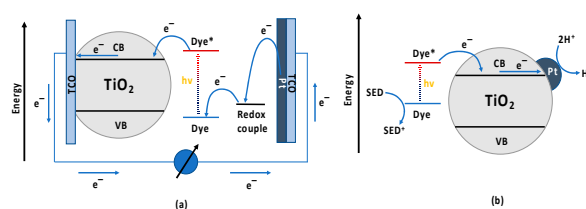
Figure 1. Energy levels and working mechanisms of: (**a**) dye-sensitized solar cells and (**b**) dye-sensitized Pt/TiO_2 photocatalysts.

Among other requirements, the correct alignment of the relative energy levels of the dye and the redox couple in DSSCs or the SED in the Pt/TiO_2 photocatalysts is a key issue that affects the overall efficiency of both dye-sensitized systems. Indeed, the effective regeneration of the oxidized dye is pivotal for both devices to obtain good performances in terms of efficiency. Thus, a key parameter for an efficient dye to be employed is the ground-state redox potential (GSRP) since this value, especially when compared to the redox couple or SED energy levels, is a measure of the dye regeneration driving force.

The prediction of GSRP by quantum chemical methods is of outstanding importance for the rational design of novel organic sensitizers and greatly contributes to the development of more efficient devices. Indeed, the calculations of these photoelectrochemical properties along with the modeling of other key parameters such as the excited state redox potential, the vertical excitation and emission energies, the charge transfer nature of the excitation process and the electronic coupling between the dye and the semiconductor, would indicate the most promising dye candidates for solar energy and fuel (H_2) devices. This strategy has been intensely applied in literature for the molecular engineering of the organic sensitizer for DSSC [9–14], mostly using the methods of the density functional theory (DFT) and its time-dependent extension (TDDFT).

The accurate evaluation of GSRP is hard to achieve, especially because it has been shown that the accuracy deteriorates as the conjugation length of the molecule increases [15]. In the present study,

the GSRP of 16 organic dyes having a medium to large conjugation length (see molecules in Figure 2) have been computed using DFT, and in particular the MPW1K functional [16,17], which has been shown to give the best accuracy before [15], and a polarizable continuum model (PCM) [18] to take into account solvent effects. To the best of our knowledge, this is the first work dealing with the calculations of GSRP of a relatively large set of organic dyes having a medium to large size of the conjugated scaffold. The DFT predicted values had been compared to the available experimental data showing that the employed strategy allows reproducing the GSRP with a mean absolute error <0.2 eV.
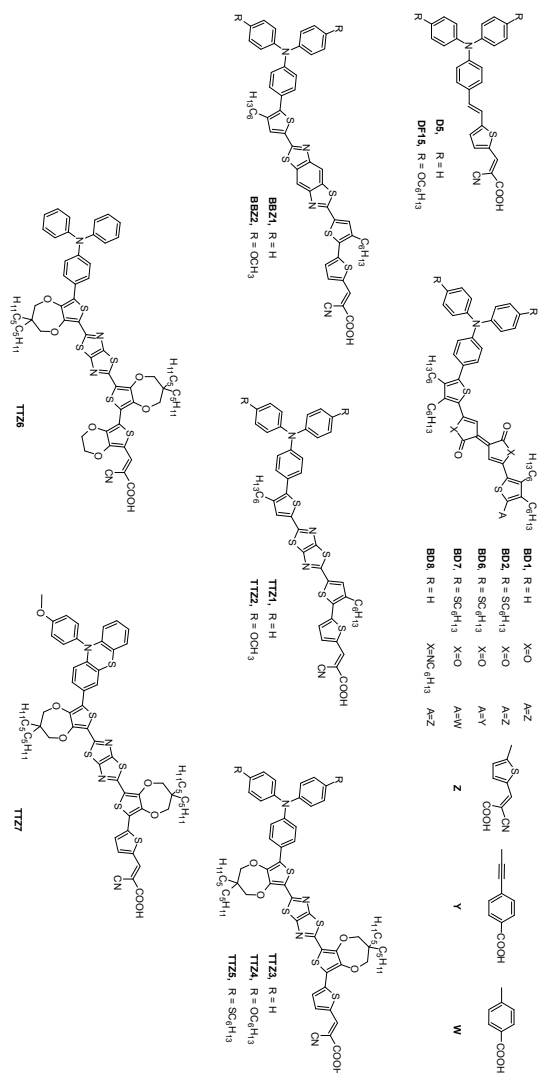

Figure 2. Investigated set of molecules.

2. Methods

All quantum mechanical(QM) calculations were performed using density functional theory (DFT) and time-dependent DFT (TDDFT) [19] using the G09 program package [20]. The ground-state redox potential was computed at the MPW1K/6-31+G* level of theory as free energy differences between the neutral and oxidized state of these dyes following the procedure described by Pastore et al. [15].

More specifically, $GSRP = \left(G^0 - G^+\right)solv$ where both G^0_{solv} and G^+_{solv} are obtained by adding the solvent effect to the free energies of the gas-phase optimized molecules: $G^0_{solv} = G^0_{vac} + \Delta G^0_{solv}$ and $G^+_{solv} = G^+_{vac} + \Delta G^+_{solv}$. G^0_{vac} and G^+_{vac} are obtained by performing a single point calculation at the optimized geometry in vacuo, followed by frequency calculations. The free energies of solvation ΔG^0_{solv} and ΔG^+_{solv} are estimated as the free energy difference between the system in solution and in gas-phase, calculated at the geometry optimized in solution.

Neutral and oxidized ground-state geometries of all dyes were computed using the MPW1K [16,17] functional in combination with 6-31G* and 6-31+G* basis set both in gas-phase and in the presence of dichloromethane (DCM) as a solvent. The MPW1K functional choice was made as it was shown to be the method providing results closer to the experimental values when used for the calculations of GSRPs in smaller but related D-π-A dyes [15]. Solvent effects were added via PCM [18]. DCM is the solvent experimentally employed for the electrochemical measurements. Indeed, a rigorous way to obtain the ground state redox potential needs to consider in the calculation energy terms including geometry relaxation energy connected with changes of electronic structure and changes of the solvation energies.

Initial structures for the ground-state geometry optimization were built starting from their B3LYP/6-31G* optimized geometries, for which the most stable among the possible conformers had been identified in our previous papers (see References [10,12,21–23]).

DFT frontier molecular orbitals and spin densities of the cation species were computed at MPW1K/6-31+G* level both in vacuo and using PCM.

Minus the value of the highest occupied molecular orbital (HOMO) energies, $-\varepsilon$(HOMO), were evaluated both in gas-phase and in DCM, for the neutral state of all dyes at their optimized geometry in DCM.

Vertical excitation energies (E_{exc}), absorption maxima (λ_{max}), and oscillator strengths (*f*) were computed at the time-dependent DFT (MPW1K/6-31+G*) level on all the optimized structures. Again, the PCM was used to include the effect of the solvent. These results are shown in the Supplementary Materials.

Electrochemical experiments were conducted on N_2-saturated solutions of the compound under study in freshly distilled dichloromethane, in the presence of electrochemical grade $[Bu_4N]$ $[PF_6]$ (0.1 M) as supporting electrolyte (Merck). Cyclic voltammetry was performed in a three-electrode cell using a glassy carbon working electrode, a platinum counter electrode, and an AgCl/Ag (NaCl 3 M) reference electrode. A Bioanalytical Systems (BAS) 100 W electrochemical analyzer was used as polarizing unit. $E_{S+/S}$ values were obtained as standard potentials by averaging the values of the anodic and cathodic peaks and using the ferrocenium/ferrocene couple as an external standard. All the potential values were then referred to normal hydrogen electrode (NHE) by using a value of +0.63 V for ferrocene *vs.* NHE [24]. Typical analyte concentration was approx. 10^{-3} M.

3. Results and Discussion

All the investigated dyes (see Figure 2) were based on fully conjugated D-π-A or D-A-π-A structures, the latter having an auxiliary acceptor group in the central part of the molecule. D5 and DF15 were triarylamine-thiophene derivatives bearing cyanoacrylic acid as anchoring group. The heterocyclic benzobisthiazole- and thiazolothiazole-systems constituted the central π scaffold of BBZ1,2 and TTZ1-7 sensitizers, respectively. The last group of molecules (BD1,2,6,7,8) contained an electron-poor *bis*-lactone moiety (Pechmann lactone) connected to thiophenes decorated with various donor and acceptor groups. With the only exception of compound D5 [25], the investigated dyes were selected based on reliable experimental data available, having been designed, characterized and synthetized in our laboratories, as described in our previous works [4,10,21–23].

The neutral ground-state geometries of these dyes, computed at the MPW1K/6-31+G* level, are shown in Figure S1 (see Supplementary Materials). All the dyes assumed a largely planar structure along most of the conjugated system with a deviation from coplanarity (ranging from 27° to 49°) between the triarylamine and the linked thiophene. To assess the quality of the MPW1K/6-31+G* optimized structures, their vertical excitation energies were computed at the TDDFT level and the comparison between these results and experimental values is shown in Table S1 of the Supplementary Materials. The mean absolute error was about 0.06 eV, which clearly indicates the accuracy of the optimized structures and the high degree of accuracy of MPW1K functional in dealing with the excited states of the analyzed D-π-A or D-A-π-A dyes. Table S1 (see Supplementary Materials) also shows that the main electronic transition was, in all cases, a HOMO→LUMO transition with a smaller contribution of a HOMO−1→LUMO transition. From the plot of the corresponding DFT frontier molecular orbitals collected in Table S2 of the Supplementary Materials, it is clear that the HOMO and LUMO were mostly localized on the donor and acceptor unit, respectively, albeit still with a sizable contribution of the conjugated scaffold.

Given the good performance of the MPW1K functional in reproducing the vertical excitation energies (this work) and in computing excited state geometries and vertical emission energies [12], the choice of MPW1K functional appears appropriate also to compute GSRP. Additionally, in a previous paper, the MPW1K has been demonstrated to be by far the method that provided computed GSRP values closer to the experimental ones [15].

The results of GSRP computed *vs* experimental $E_{S^+/S}$ values on all the investigated dyes are shown in Figure 3. The graph is built from raw data of Table S3 (GSRP[b-d]). The analysis of the computed values leads to some interesting considerations. At first glance, it is straightforward to observe that data covered two distinct regions of the graph: GSRP values calculated in the gas-phase overestimated the experimental value (black circles in the region above the diagonal, where $y = x$, i.e., calculated (y) = experimental (x)), while GSRP values calculated in the presence of the solvent slightly underestimated the experimental value (red and blue circles, below the diagonal). The use of high-quality basis sets in the geometry calculation visibly improved the agreement between the calculated GSRP and experimental potential values (red circles). From the quantitative point of view, the highest level of theory employed, i.e., computing frequencies at the MPW1K/6-31+G* on neutral and oxidized state geometries optimized at the same level (MPW1K/6-31+G*//MPW1K/6-31+G*) was the one that provided the most accurate values with a mean absolute error (MAE) of 0.18 eV (red circles). Higher deviations from experiments were found applying the MPW1K/6-31+G* combination on neutral and oxidized state geometries computed at the MPW1K/6-31G* level (MPW1K/6-31+G*//MPW1K/6-31G*). Indeed, the MAE was about 0.32 eV (blue circles). The highest deviations from experiments were provided by the GSRP calculations in terms of free energies using the MPW1K/6-31+G*//MPW1K/6-31+G* level in gas-phase (black circles). Thus, we may conclude that the difference of the free energy values allows, at least, to correctly reproduce the redox potential qualitative trend, while calculations using the use of the MPW1K/6-31+G*//MPW1K/6-31+G* level in the presence of the solvent is crucial to correctly reproduce the quantitative trend.

According to Koopmans' theorem [26], related to the closed-shell Hartree-Fock theory and extended to Kohn-Sham orbital energies within the DFT [27,28], the negative of the HOMO energy is equal to the first ionization energy of a system, which is the minimum energy required to remove an electron from the HOMO of a molecule. The first ionization energy of a system can be related to the energy involved in the oxidation (loss of electrons) of a molecule and therefore to $E_{S+/S}$.

Thus, $-\varepsilon$(HOMO) values were also computed both in gas-phase (Figure 3, grey triangles and Figure 5, blue circles) and in DCM (Figure 3, grey asterisks and Figure 5, brown circles)) giving a MAE of 0.50 and 0.56 eV, respectively. The data provided by the computation of $-\varepsilon$(HOMO) values in gas-phase were slightly closer to the experimental values than the $-\varepsilon$(HOMO) values computed in solution. This evidence could be related to the fact that, for the investigated molecules in the gas-phase, the orbitals of the charged and neutral species are nearly identical and orbital relaxation is not expected.

104
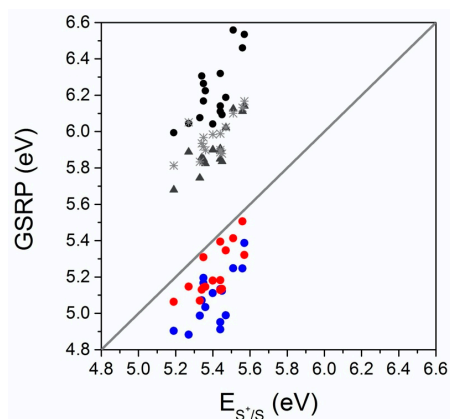
Figure 3. Computed ground state redox potential (GSRP) values (GSRP[b-d] in Table S3) vs. experimental $E_S{}^+{}_{/S}$ values. The $y = x$ diagonal is reported as a reference. Black circles: MPW1K/6-31+G*//MPW1K/6-31+G* values in gas-phase; blue circles: MPW1K/6-31+G*//MPW1K/6-31G* values in DCM; red circles MPW1K/6-31+G*//MPW1K/6-31+G* values in dichloromethane (DCM); grey triangles: minus the value of the highest occupied molecular orbital energies, $-\varepsilon$(HOMO) in gas-phase; grey asterisks: $-\varepsilon$(HOMO) in DCM.

Since the difference $\Delta\varepsilon = \varepsilon$ (HOMO)$_{vac} - \varepsilon$(HOMO)$_{solv}$ broadly varies from ~ 0 to a few hundreds of meV, we further investigated three of the dyes, namely TTZ7 (a large molecule with the largest $\Delta\varepsilon$), BD2 (a large molecule with $\Delta\varepsilon \approx 0$) and D5 (a small molecule with $\Delta\varepsilon \approx 0$). To probe the extent of the orbital relaxation, the HOMO of each neutral dye was compared with the spin-density surface calculated for its cation; orbital relaxation should produce visible differences in the space localization of these two surfaces. Figure 4 shows how, for D5 and BD2, the HOMO of the neutral dye and the spin density of its cation had a very similar shape and space distribution, both in the gas-phase and in DCM. Therefore, in this case, the orbital relaxation was minimal and Koopmans' theorem was expected to be valid, either in gas phase or in solution. On the other hand, the HOMO of TTZ7 and the spin density of TTZ7$^+$ had a similar shape and space distribution in the gas-phase. In contrast, in solution, the spin density was much more localized on the donor region as an effect of the orbital rearrangement. Localization of the charge on a more restricted region was possible because of the stabilizing interaction with the solvent. In this case, there were not favorable conditions to apply Koopmans' theorem. In general, charge localization is driven by the presence of electron-withdrawing groups, facilitated by the larger size of the molecule and made possible by the presence of the solvent. At the same time, charge delocalization is favored by the relief of the interelectronic repulsion and made possible by the presence of an efficient conjugation path. Considering all these aspects, after having analyzed the conformation, the dimensions and the presence of electron-withdrawing groups, it has not been possible to univocally identify the reason why a more marked charge localization is observed only in some cases. Reasonably this interesting aspect will require a dedicated study and may be the subject of subsequent work, but we will have to settle for this further caveat against the uncritical use of Koopmans' theorem.
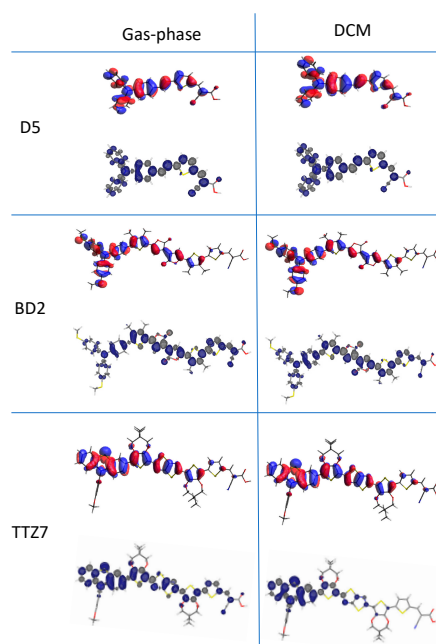
Figure 4. HOMO of the neutral species (top) and the spin density of its cation (bottom) in gas-phase (left) and DCM (right) for D5, BD2 and TTZ7 dyes computed at the MPW1K/6-31+G* level and plotted using Avogadro [29,30] and Chemcraft [31] softwares, respectively.

Inspection of Figure 5, which collects the computed GSRP vs. dyes, reveals that, considering closely related compounds with similar scaffolds, computed GSRPs and $-\varepsilon$(HOMO) reproduced the same trends found for the experimental values. For example, GSRP and $-\varepsilon$(HOMO) values of DF15 were lower in energy than those of D5, due to the presence of a stronger hexyloxy-substituted donor group in DF15. Both dyes had more positive values than the redox potential of the conventionally and commonly used redox couple in DSSC, i.e., the iodide/triiodide redox couple (4.77 eV) [32], as well some Co-based redox systems (4.85–5.04 eV) [33] suggesting that regeneration of the sensitizer is feasible. Similar considerations apply to the Pechmann lactone containing molecules (BD1,2,6,7,8) and to the benzobisthiazole- (BBZ1,2) and thiazolothiazole-systems (TTZ1-7). In particular, and again in agreement with the experimental values, the introduction of a stronger donor group in BD2 compared to the one present in BD1, and the substitution of the lactone moiety of BD1 with the less electron-withdrawing lactam in BD8, determined the lowering of the GSRP. Moreover, the substitution of the cyanoacrylic acid with a less electron-withdrawing acceptor (BD6 and BD7 vs. BD2) provided experimental ground-state oxidation potentials similar to BD2. While the computed GSRP and $-\varepsilon$(HOMO) values for BD6 and $-\varepsilon$(HOMO) value for BD7 are in line with this observation, GSRPs of BD7 were instead predicted to be higher in energy although closer to the experimental values. Concerning the benzobisthiazole- (BBZ1,2) and thiazolothiazole-systems (TTZ1-7), the introduction of electron-rich methoxy-substituents on TTZ2 and BBZ2 led to a decrease in the ground-state oxidation potentials compared to TTZ1 and BBZ1, respectively, which is also evident in the computational results. In the series TTZ3-7, in line with experiments, the introduction of the electron-donating alkoxy groups on the triarylamine portion in TTZ4 and the presence of the terminal phenothiazine unit in TTZ7

resulted in lowering ground-state oxidation potential values. However, all BBZs and TTZs dyes had ground-state oxidation potentials more positive than that of the iodide/triiodide couple, thus assuring dye regeneration. The present results are consistent with the following final observations: (i) the frontier orbital approximations, according to Koopmans' theorem, might be used to reproduce the trend of standard potentials in closely related families of compounds but cannot be used as a method to predict quantitative values; (ii) to obtain GSRPs with a certain degree of accuracy sufficient to be comparable with experimental standard potentials, free energy differences computations including solvent effects need to be taken into account.
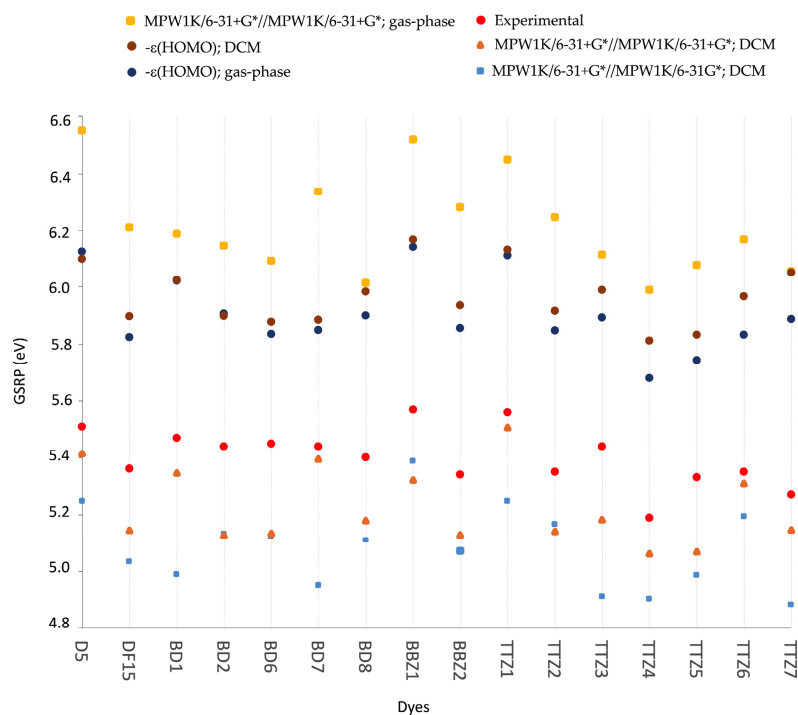
Figure 5. Experimental, computed GSRP and $-\varepsilon$(HOMO) of dye sensitizers.

4. Conclusions

The present study shows that, using the MPW1K functional in combination with an appropriate basis set, the prediction of GSRP of a relatively large set of D-π-A/D-A-π-A dyes having a medium to large size of the conjugated scaffold can be obtained with a good level of accuracy. Moreover, the experimental trends in GSRP values of closely related compounds with similar scaffolds are well reproduced. Thus, the employed strategy should help researchers to identify sensitizers that can efficiently be used in DSSCs or in photocatalytic systems for the production of H_2, allowing them to concentrate precious time and resources only on the preparation of the most promising candidates.

given in brackets. Table S2: DFT frontier molecular orbitals for all dyes obtained at MPW1K/6-31 + G* level in vacuo. Table S3: Experimental ($E_{S+/S}$), computed GSRP (eV) and - ε(HOMO) of all investigated dyes. Cartesian Coordinated of all the investigated dyes in gas-phase and in solvent, Figure S1. MPW1K/6-31+G* optimized geometries of all dyes computed in vacuo and in DCM (in brackets). Dihedral angles are given in degrees.

References

1. Hagfeldt, A.; Boschloo, G.; Sun, L.; Kloo, L.; Pettersson, H. Dye-Sensitized Solar Cells. *Chem. Rev.* **2013**, *110*, 159–184.

2. Lee, C.P.; Li, C.T.; Ho, K.C. Use of organic materials in dye-sensitized solar cells. *Mater. Today* **2017**, *20*, 267–283. [CrossRef]

3. Gong, J.; Sumathy, K.; Qiao, Q.; Zhou, Z. Review on dye-sensitized solar cells (DSSCs): Advanced techniques and research trends. *Renew. Sustain. Energy Rev.* **2017**, *68*, 234–246. [CrossRef]

4. Dessì, A.; Monai, M.; Bessi, M.; Montini, T.; Calamante, M.; Mordini, A.; Reginato, G.; Trono, C.; Fornasiero, P.; Zani, L. Towards Sustainable H2 Production: Rational Design of Hydrophobic Triphenylamine-based Dyes for Sensitized Ethanol Photoreforming. *ChemSusChem* **2018**, *11*, 793–805. [CrossRef] [PubMed]

5. Zhang, X.; Peng, T.; Shuaishuai, S. Recent advances in dye-sensitized semiconductor systems for photocatalytic hydrogen production. *J. Mater. Chem. A Mater. Energy Sustain.* **2016**, *4*, 2365–2402. [CrossRef]

6. Cecconi, B.; Manfredi, N.; Montini, T.; Fornasiero, P.; Abbotto, A. Dye-Sensitized Solar Hydrogen Production: The Emerging Role of Metal-Free Organic Sensitizers. *Eur. J. Org. Chem.* **2016**, *2016*, 5194–5215. [CrossRef]

7. Watanabe, M. Dye-sensitized photocatalyst for effective water splitting catalyst. *Sci. Technol. Adv. Mater.* **2017**, *18*, 705–723. [CrossRef]

8. Wu, Y.; Zhu, W.H.; Zakeeruddin, S.M.; Grätzel, M. Insight into D−A−π−A Structured Sensitizers: A Promising Route to Highly Efficient and Stable Dye-Sensitized Solar Cells. *ACS Appl. Mater. Interfaces* **2015**, *7*, 9307–9318. [CrossRef]

9. De Angelis, F.; Fantacci, S.; Selloni, A. Alignment of the dye's molecular levels with the TiO2band edges in dye-sensitized solar cells: A DFT-TDDFT study. *Nanotechnology* **2008**, *19*, 15–17. [CrossRef]

10. Dessì, A.; Calamante, M.; Mordini, A.; Peruzzini, M.; Sinicropi, A.; Basosi, R.; Fabrizi de Biani, F.; Taddei, M.; Colonna, D.; Di Carlo, A.; et al. Organic dyes with intense light absorption especially suitable for application in thin-layer. *Chem. Commun.* **2014**, *50*, 13952–13955. [CrossRef]

11. Pastore, M.; Fantacci, S.; De Angelis, F. Modeling Excited States and Alignment of Energy Levels in Dye-Sensitized Solar Cells: Successes, Failures, and Challenges. *J. Phys. Chem. C* **2013**, *117*, 3685–3700. [CrossRef]

12. Bernini, C.; Zani, L.; Calamante, M.; Reginato, G.; Mordini, A.; Taddei, M.; Basosi, R.; Sinicropi, A. Excited state geometries and vertical emission energies of solvated dyes for DSSC: A PCM/TD-DFT benchmark study. *J. Chem. Theory Comput.* **2014**, *10*, 3925–3933. [CrossRef]

13. Fantacci, S.; De Angelis, F. Ab Initio Modeling of Solar Cell Dye Sensitizers: The Hunt for Red Photons Continues. *Eur. J. Inorg. Chem.* **2019**, *2019*, 743–750. [CrossRef]

14. Chiu, C.C.; Sheng, Y.C.; Lin, W.J.; Juwita, R.; Tan, C.J.; Gavin Tsai, H.H. Effects of internal electron-withdrawing moieties in d−a−π−a organic sensitizers on photophysical properties for DSSCs: A computational study. *ACS Omega* **2018**, *3*, 433–445. [CrossRef] [PubMed]

15. Pastore, M.; Fantacci, S.; De Angelis, F. Ab Initio Determination of Ground and Excited State Oxidation Potentials of Organic Chromophores for Dye-Sensitized Solar Cells. *J. Phys. Chem. C* **2010**, 22742–22750. [CrossRef]

16. Lynch, B.J.; Fast, P.L.; Harris, M.; Truhlar, D.G. Adiabatic Connection for Kinetics. *J. Phys. Chem. A* **2000**, *104*, 4811–4815. [CrossRef]

17. Zhao, J.; Lynch, B.J.; Truhlar, D.G. Development and Assessment of a New Hybrid Density Functional Model for Thermochemical Kinetics. *J. Phys. Chem. A* **2004**, *108*, 2715–2719. [CrossRef]

18. Tomasi, J.; Mennucci, B.; Cammi, R. Quantum Mechanical Continuum Solvation Models. *Chem. Rev.* **2005**, *105*, 2999–3094. [CrossRef]

19. Lecture Notes in Physics. In *Fundamentals of Time-Dependent Density Functional Theory*; Marques, M.A.L.; Maitra, N.T.; Nogueira, F.M.S.; Gross, E.K.U.; Rubio, A. (Eds.) Springer: Berlin/Heidelberg, Germany, 2012; Volume 837, ISBN 978-3-642-23517-7.

20. Frisch, M.J.; Trucks, G.W.; Schlegel, H.B.; Scuseria, G.E.; Robb, M.A.; Cheeseman, J.R.; Scalmani, G.; Barone, V.; Mennucci, B.; Petersson, G.A.; et al. *Gaussian 09, Revision C.01*; Gaussian, Inc.: Wallingford, CT, USA, 2010.

21. Dessì, A.; Calamante, M.; Mordini, A.; Peruzzini, M.; Sinicropi, A.; Basosi, R.; De Biani, F.F.; Taddei, M.; Colonna, D.; Di Carlo, A.; et al. Thiazolo[5,4-d]thiazole-based organic sensitizers with strong visible light absorption for transparent, efficient and stable dye-sensitized solar cells. *RSC Adv.* **2015**, *5*, 32657–32668. [CrossRef]

22. Dessì, A.; Consiglio, B.; Calamante, M.; Reginato, G.; Mordini, A.; Peruzzini, M.; Taddei, M.; Sinicropi, A.; Parisi, L.; de Biani, F.F.; et al. Organic Chromophores Based on a Fused Bis-Thiazole Core and Their Application in Dye-Sensitized Solar Cells. *Eur. J. Org. Chem.* **2013**, *2013*, 1916–1928. [CrossRef]

23. Dessì, A.; Sinicropi, A.; Mohammadpourasl, S.; Basosi, R.; Taddei, M.; de Biani, F.F.; Calamante, M.; Zani, L.; Mordini, A.; Bracq, P.; et al. New Blue Donor—Acceptor Pechmann Dyes: Synthesis, Spectroscopic, Electrochemical, and Computational Studies. *ACS Omega* **2019**, *4*, 7614–7627. [CrossRef] [PubMed]

24. Pavlishchuk, V.V.; Addison, A.W. Conversion constants for redox potentials measured versus different reference electrodes in acetonitrile solutions at 25 °C. *Inorg. Chim. Acta* **2000**, *298*, 97–102. [CrossRef]

25. Hagberg, D.P.; Edvinsson, T.; Marinado, T.; Boschloo, G.; Hagfeldt, A.; Sun, L. A novel organic chromophore for dye-sensitized nanostructured solar cells. *Chem. Commun.* **2006**, *21*, 2245–2247. [CrossRef] [PubMed]

26. Koopmans, T. Über die Zuordnung von Wellenfunktionen und Eigenwerten zu den einzelnen Elektronen eines Atoms. *Physica* **1934**, *1*, 104–113. [CrossRef]

27. Koopmans, T. Proof that $\frac{\partial E}{\partial n_i} = \varepsilon$ in density-functional theory. *Phys. Rev. B* **1978**, *18*, 7165. [CrossRef]

28. Conradie, J. A Frontier orbital energy approach to redox potentials. *J. Phys. Conf. Ser.* **2015**, *633*, 012045. [CrossRef]

29. Hanwell, M.D.; Curtis, D.E.; Lonie, D.C.; Vandermeersch, T.; Zurek, E.; Hutchison, G.R. Avogadro: An advanced semantic chemical editor, visualization, and analysis platform. *J. Cheminform.* **2012**, *4*, 17. [CrossRef] [PubMed]

30. Avogadro: An Open-Source Molecular Builder and Visualization Tool. Version 1.1.1. Available online: http://avogadro.cc/ (accessed on 19 April 2020).

31. Chemcraft—Graphical Software for Visualization of Quantum Chemistry Computations. Available online: https://www.chemcraftprog.comtle (accessed on 19 April 2020).

32. Boschloo, G.; Hagfeldt, A. Characteristics of the Iodide/Triiodide Redox Mediator in Dye-Sensitized Solar Cells. *Acc. Chem. Res.* **2009**, *42*, 1819–1826. [CrossRef] [PubMed]

33. Feldt, S.M.; Gibson, E.A.; Gabrielsson, E.; Sun, L. Design of Organic Dyes and Cobalt Polypyridine Redox Mediators for High-Efficiency Dye-Sensitized Solar Cells. *J. Am. Chem. Soc.* **2010**, *132*, 16714–16724. [CrossRef] [PubMed]

4.5. Manuscript 5: "*In silico* investigation of catechol-based sensitizers for type II dye sensitized solar cells (DSSCs)"

Authors: C. Coppola, A. D'Ettorre, M. L. Parisi, L. Zani, G. Reginato, M. Calamante, A. Mordini, M. Taddei, R. Basosi, and A. Sinicropi.

In this work, 15 catechol-based sensitizers, **Cat-I** to **Cat-XV**, have been designed for a possible application in type-II DSSCs. They have been endowed with strong or moderated electron-donating and electron-withdrawing substituents directly linked to the catechol unit or through an ethylene π spacer. *State-of-the-art* DFT and TDDFT methods have been employed to calculate the electronic structures and the excited-state properties of free and $(TiO_2)_9$-bound **Cat-I-XV** dyes, to investigate the effect of the substituents and the π spacer relatively to the dye-to-TiO_2 charge transfer (DTCT) properties and to the direct (type-II) electron injection mechanism. The computed properties suggest that fully conjugated molecules, regardless of the kind of substituent, have more red-shifted DTCT bands, formed by the interaction of d orbitals of Ti and p orbitals of catechol oxygens. This aspect promotes a strong electron coupling which fosters the direct electron injection mechanism. Hence, dyes possessing these features could perform better in type-II DSSCs. As first author of the manuscript, the PhD candidate's contribution refers to the application of computational methodologies to investigate the Cat-dyes properties, as well as the writing of the original draft.
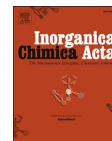
Research paper

In silico investigation of catechol-based sensitizers for type II dye sensitized solar cells (DSSCs)

Carmen Coppola [a,b], Alessio D'Ettorre [a], Maria Laura Parisi [a,b,c,e], Lorenzo Zani [c], Gianna Reginato [c], Massimo Calamante [c,d], Alessandro Mordini [c,d], Maurizio Taddei [c,e], Riccardo Basosi [a,b,c], Adalgisa Sinicropi [a,b,c,e,*]

[a] *Università di Siena, R²ES Lab, Dipartimento di Biotecnologie, Chimica e Farmacia, Via Aldo Moro 2, 53100 Siena, Italy*
[b] *CSGI, Consorzio per lo Sviluppo dei Sistemi a Grande Interfase, Via della Lastruccia 3, 50019 Sesto Fiorentino, Italy*
[c] *CNR – Istituto di Chimica dei Composti Organometallici (CNR-ICCOM), Via Madonna del Piano 10, 50019 Sesto Fiorentino, Italy*
[d] *University of Florence, Department of Chemistry "U. Schiff", Via della Lastruccia 13, 50019 Sesto Fiorentino, Italy*
[e] *Università di Siena, Dipartimento di Biotecnologie, Chimica e Farmacia, Via Aldo Moro 2, 53100 Siena, Italy*

ARTICLE INFO	ABSTRACT
	A series of catechol-based sensitizers, **Cat-I** to **Cat-XV**, for a possible application in type II DSSCs is presented. The electronic structures and excited state properties of free and bound to (TiO₂)₉ dyes have been analysed and compared by means of Density Functional Theory (DFT) and Time Dependent DFT (TDDFT) methods. In particular, the effect of introducing electron-donating and electron-withdrawing substituents, as well as the effect of introducing an ethylene spacer as π bridge between the substituents and the catechol unit to increase the conjugation has been investigated. Moreover, key aspects that could strongly influence the direct (type II) electron injection mechanism are analyzed and discussed. The results of the calculations suggest that the introduction of the π bridge contributes to enhance the dye-to-TiO₂ charge transfer (DTCT) efficiency regardless of the presence of electron-donating or electron-withdrawing substituents.

1. Introduction

In the last two decades many organic molecules, mainly based on $D_{(Donor)}$-$\pi_{(spacer)}$-$A_{(Acceptor/Anchoring)}$ structures, have been designed and tested as photosensitizers for Dye Sensitized Solar Cells (DSSCs) [1-4]. These dyes, most of which featuring a carboxylic acid group as anchor, are characterized by large visible light absorption coefficients associated to intramolecular charge transfer transitions (ICT) from the donor to the acceptor moiety of the dye. They are considered sensitizers for type I DSSCs, where the electron injection pathway is "two-step" or "indirect", i.e. the electron injection into the conduction band (CB) of the semiconductor oxide (generally TiO₂) follows the excitation of the dye [5] (Fig. 1, (a)).

Catechol-based (Cat-) dyes, such as dopamine [6], fluorone [7] and some natural pigments (e.g. Bromopyrogallol Red [8,9] and anthocyanins [10-12]) have attracted much attention for their capability, upon binding to TiO₂ surfaces, to exhibit broad light absorption bands in the

longer wavelength region, corresponding to DTCT (dye-to-TiO₂ charge transfer) processes. Accordingly, Cat-dyes of this kind are light-harvesting molecules for type II DSSCs, where the electron injection pathway is "one-step" or "direct", i.e. the electron is injected from the dye to the CB of TiO₂ by photoexcitation of the DTCT bands [5,13] (Fig. 1, (b)).

In addition to the efficient light-harvesting capabilities, the direct mechanism is faster (<100 fs) and it overcomes the restriction regarding the energy of the lowest unoccupied molecular orbital (LUMO) of the sensitizer, that in type I DSSCs should be higher than the CB of the oxide [13,14]. Indeed, the efficiency of type I DSSCs depends on the dyes energy gaps and on the interfacial level alignment between the dye LUMO and the conduction band minimum (CBM) of the surface, while the efficiency of type II DSSCs depends on the interfacial level alignment between the dye HOMO and the CBM of the surface [15-17].

Unfortunately, the back-electron transfer (BET) of type II DSSCs is faster than in the "two-step" mechanism too, as a result of a lower degree
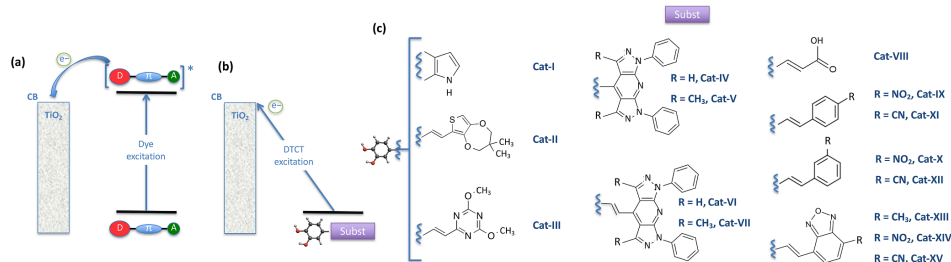
111

Fig. 1. (a): Type I DSSCs electron injection pathway scheme; (b): Type II DSSCs electron injection pathway scheme; (c): designed **Cat-I-XV** dyes scheme.

of charge separation following electron injection. Consequently, up to now, Cat-type II DSSCs have shown very low efficiency, up to about 2.5% [18], compared to that of type I DSSCs, which instead have shown certified efficiency exceeding 12% [19,20]. Nevertheless, only few efforts have been made to develop more efficient Cat-dyes for type II DSSCs and increase our knowledge about the above-mentioned direct mechanism [18,21–27]. With this aim, we embarked in the *in silico* investigation of Cat-dyes for type II DSSCs using the methods of Density Functional Theory (DFT), being aware from previous studies that: (i) D-π-Cat sensitizers with strongly electron-donating groups or D-Cat sensitizers with strong electron-donating substituents directly bound to the Cat unit can enhance the electron injection mechanism of type II DSSCs by improving the DTCT features; (ii) the BET could be fostered by strong electron-withdrawing groups directly linked to Cat unit, leading to a decrease in DTCT characteristics; (iii) moderately electron-withdrawing groups, such as acetyl and cyano groups, can enhance the DTCT efficiency and delay the BET [5,18,21,24–26]. Nevertheless, a study of Ooyama et al. [18] has demonstrated that also the introduction of the nitro group, and its interaction with I⁻ ions of the electrolyte, can increase the DTCT efficiency and retard the BET.

In addition to a new broad DTCT band further into the visible range, efficient dyes for direct (type II) mechanism should fulfil the following requirements once bound to TiO₂ semiconductor: the LUMOs of the dye-TiO₂ complexes should be localized on d orbitals of Ti; the DTCT excitations should be governed by transitions from the highest occupied molecular orbitals of the sensitizer (HOMOs) to several Ti-localized unoccupied orbitals interacting with p orbitals of catechol oxygens; moreover, a strong coupling between the HOMO of the dyes and the CB of TiO₂ is required to slower the BET from reduced TiO₂ to the oxidized dye [23,28].

Thus, in this work, a series of Cat-sensitizers (**Cat-I** to **Cat-XV**) with electron-donating and electron-withdrawing moieties is computationally investigated. We explored the effect of substituents in different positions, as well as the effect of enhancing the conjugation by introducing an ethylene spacer as π bridge between the substituents and the catechol unit (Fig. 1(c)), knowing that type II character can also increase by expanding the π conjugation in the anchoring group [27].

In particular, **Cat-I** is the 5,6-dihydroxyindole, generally known as DHI, where the pyrrole is considered as the electron-donating moiety; **Cat-II** and **Cat-III** contain the 3,4-(2,2-dimethylpropylenedioxy)thiophene and the 2,4-dimethoxy-1,3,5-triazine as electron-donating substituents, respectively, both linked to the Cat unit through the π spacer. **Cat-IV** to **Cat-VII** dyes have 1,7-diphenyl-1,7-dihydrodipyrazolo[3,4-*b*:4′,3′-*e*]pyridine directly linked to the Cat unit in **Cat-IV** and **Cat-V**, or through the π spacer in **Cat-VI** and **Cat-VII**. The pyrazolo[3,4-*b*]pyridine moiety was selected due to its easy synthetic access [29]. Moreover, its versatile scaffold can accommodate different substituents in various positions and serve to modulate the dye light absorption properties as well.

From **Cat-VIII** to **Cat-XII**, the molecules have been endowed with strong and moderately electron-withdrawing substituents: a carboxylic group in **Cat-VIII** (3-(3,4-dihydroxyphenyl)-2-propenoic acid or caffeic acid), *para* and *meta* nitro-substituted benzene rings in **Cat-IX** and **Cat-X**, respectively, and *para* and *meta* cyano-substituted benzene rings in **Cat-XI** and **Cat-XII**. Additionally, **Cat-VIII** to **Cat-XII** have the electron-withdrawing moiety linked to the Cat unit through the ethylene π spacer. The last three dyes, **Cat-XIII**, **Cat-XIV** and **Cat-XV**, bear a benzo[1,2,5]oxadiazole ring carrying a methyl, a nitro and a cyano group in 4-position with respect to the ethylene spacer, respectively. These substituents give to benzo[1,2,5]oxadiazole moderately electron-donating features (–CH₃) or electron-withdrawing features (–NO₂ and –CN).

In order to test if **Cat-I-XV** can be considered suitable candidates as sensitizers for efficient type II DSSCs, DFT and Time Dependent DFT (TDDFT) methods are applied to compute the electronic structures and excited state properties of free and bound to (TiO₂)₉ **Cat-I-XV** dyes. The results of such in silico investigation are presented below.

2. Computational details

All QM calculations have been performed using Gaussian 09, Revision C.01 suite of programs [30]. Geometry optimizations of free and adsorbed **Cat-I-XV** have been obtained by DFT calculations [31,32] using the Perdew-Wang (PW91) exchange–correlation functional [33,34] in combination with the standard 6-31G* basis set. Absorption maxima (λ_{max}^a), vertical excitation energies (E_{exc}) and oscillator strengths (*f*) have been calculated in *vacuo* via TDDFT [35] at the PW91/TZVP level on PW91/6-31G* optimized structures. Over 400 singlet transitions have been computed. The partial and the total density of states (PDOS and DOS) have been calculated at the same level of theory. The employed functional has been selected on the basis of previous benchmark studies. Indeed, Duncan et al. [36] reported that the PW91 exchange–correlation functional with TDDFT could reproduce adequately the major features in the UV absorption spectrum of catechol. Moreover, as recently reported by Ronchi et al., the use of more costly range-separated hybrid functionals, i.e. CAM-B3LYP, did not significantly improve the main physics of Cat-based molecules bound to TiO₂, in particular the type of mechanism of charge transfer [37].

The starting geometry for the (TiO₂)₉ cluster was taken from the literature [38,39]. The (TiO₂)₉ cluster has been proved to be a good compromise between efficiency and computational costs in reproducing electronic absorption spectra of the dye-TiO₂ systems [22,23,28,40].

The dyes have been adsorbed to (TiO₂)₉ using a bidentate chelating mode as reported in Sanchez-de-Armas et al. [23].

UV–Vis spectra, PDOS and DOS of the designed sensitizers have been simulated with GaussSum [41] considering a Gaussian distribution and an arbitrary line width of 0.03 eV.
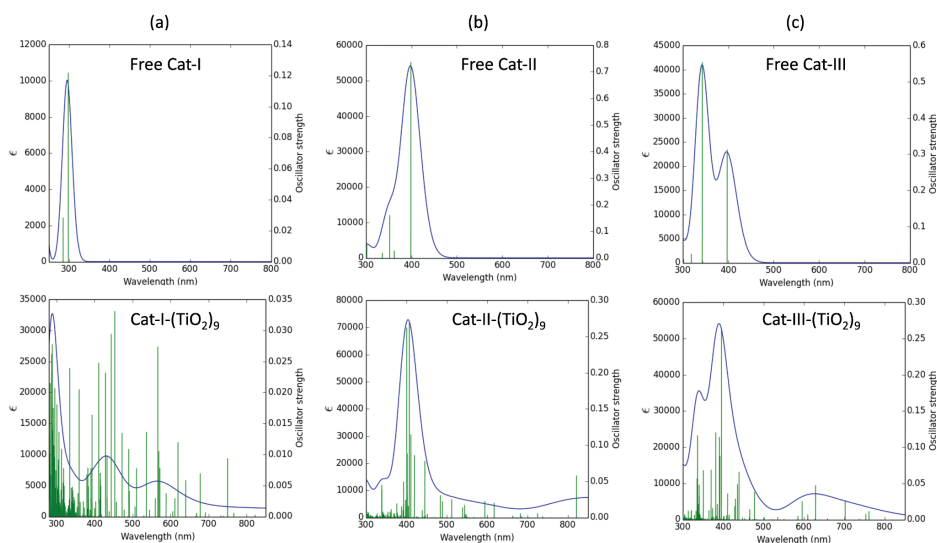
Fig. 2. Simulated TDDFT UV–Vis absorption spectra of: (a) free **Cat-I** (top) and **Cat-I-(TiO₂)₉** (bottom); (b) free **Cat-II** (top) and **Cat-II-(TiO₂)₉** (bottom); (c) free **Cat-III** (top) and **Cat-III-(TiO₂)₉** (bottom).

3. Results and discussion

The analysis of electronic structures and excited state properties of free and adsorbed dyes is reported by grouping them on the basis of their substituents in the following subsections. PW91/6-31G* optimized geometries of **Cat-I-XV** dyes bound to (TiO₂)₉ are shown in Fig. S1 of the Supporting Information. TD-PW91/TZVP absorption maxima (λ^a_{max}), vertical excitation energies (E_{exc}) and oscillator strengths (f) of free and adsorbed dyes, computed in *vacuo* on PW91/6-31G* minimized structures, are reported in Table S1 and Table S2 of the Supporting Information, respectively. The DFT frontier molecular orbitals (FMOs) energies of free and adsorbed dyes are reported in Table S3 of the Supporting Information.

3.1. Cat-I to Cat-VII

Simulated UV–Vis spectra of free and adsorbed **Cat-I**, **Cat-II** and **Cat-III** are shown in Fig. 2 and the involved molecular orbitals are shown in Fig. 3.

Free **Cat-I**, **Cat-II** and **Cat-III** present the lowest energy transitions at 297, 398 and 397 nm (4.17, 3.11 and 3.12 eV), respectively, which correspond to $\pi \rightarrow \pi^*$ transitions involving HOMO → LUMO orbitals (Table S1). Once adsorbed on the (TiO₂)₉ cluster, these transitions are still present but are accompanied by new DTCT red-shifted bands at 452, 820 and 702 nm (2.74, 1.51 and 1.77 eV) for **Cat-I-(TiO₂)₉**, **Cat-II-(TiO₂)₉** and **Cat-III-(TiO₂)₉**, respectively, corresponding to HOMO-1 → LUMO + 20, HOMO → LUMO + 12 and HOMO → LUMO + 8 orbital transitions (see also Table S2). As expected, the presence of a conjugated spacer between the Cat unit and the electron-donating substituents in **Cat-II** and **Cat-III** resulted in a significant bathochromic shift of the first DTCT band with respect to **Cat-I**.

The inspection of the wavefunction plots (Fig. 3) reveals that the HOMOs of the three bound dyes are localized on the chromophores, while LUMO + 20, LUMO + 12 and LUMO + 8, involved in DTCT bands, are mainly localized on (TiO₂)₉ cluster, with an important contribution from p orbitals of catechol oxygens. Indeed, when the DTCT band is involved, a strong interaction among d orbitals of the Ti atoms closest to the catechol moiety and p orbitals of catechol oxygens is present. On the contrary, the LUMO orbital of complexes is completely localized on the TiO₂ surface, with no contribution from the dyes, as it has been previously reported for catechol [22,23].

Moreover, the HOMO levels of these complexes are only slightly lower in energy compared to those of the free dyes (by at most 0.63 eV), while the LUMO energies resulted to be highly stabilized (Table S3). Indeed, as already reported in previous works [21,24,26], the red-shifted DTCT absorption bands can be considered as a consequence of LUMO levels stabilization when the dyes are bound to the TiO₂ cluster. Additionally, the LUMOs of free **Cat-I**, **Cat-II** and **Cat-III** have energy similar to LUMO + 41, LUMO + 29 and LUMO + 23 of **Cat-I-(TiO₂)₉**, **Cat-II-(TiO₂)₉** and **Cat-III-(TiO₂)₉**, respectively, that lie high in energy within the CB. LUMO + 41, LUMO + 29 and LUMO + 23 are delocalized both on dyes and TiO₂ cluster (Fig. 3).

To investigate the presence of a possibly strong electron coupling between the HOMO of the dyes and the CB of the TiO₂, the PDOS and DOS have been computed and analyzed (Fig. 4).

From the comparison between the free and adsorbed dyes graphs, it is evident that when the dyes are adsorbed on the TiO₂ cluster, the bandgaps become smaller, the highest occupied state is mainly composed by the dye molecule and it lies within the bandgap. The very first virtual states are completely localized on TiO₂ surface, as it occurs in the case of adsorbed catechol [22,23], while the virtual states higher in energy, until the first unoccupied state completely localized on the dye, show an important contribution from the dye molecules. This is particularly evident in **Cat-II** and **Cat-III**. In fact, all these acceptor states are the ones responsible for the direct electron injection mechanism (type II), making **Cat-I-III** suitable candidates as type II dyes. In particular, among the three dyes, **Cat-II** and **Cat-III** have more red-shifted DTCT bands and a more pronounced interaction of d orbitals of Ti and p orbitals of catechol oxygen in acceptor states, leading to a strong electron coupling which fosters the direct (type II) mechanism.
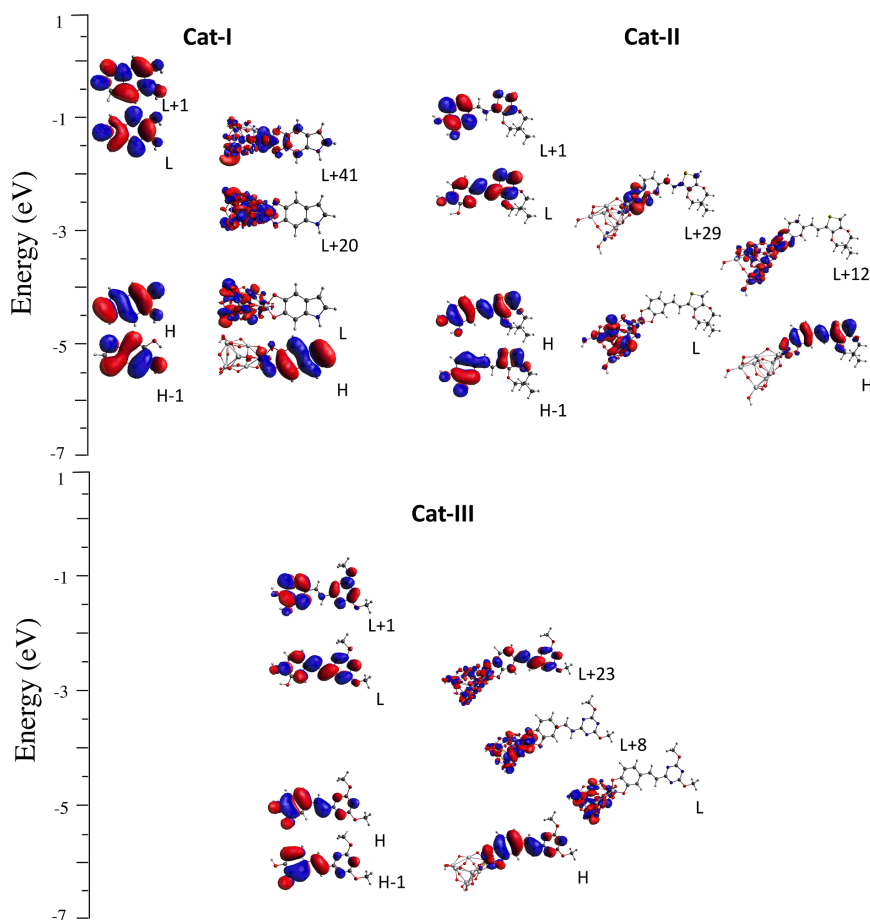
Fig. 3. DFT FMOs plots of free and selected occupied and virtual MOs of adsorbed on $(TiO_2)_9$ **Cat-I-III dyes.**

The simulated UV–Vis spectra of **Cat-IV-VII** (Fig. 5) show the lowest energy absorption maxima at 490, 478, 577 and 574 nm (2.53, 2.59, 2.15 and 2.16 eV), for **Cat-IV, Cat-V, Cat-VI** and **Cat-VII**, respectively, which are governed by $\pi \rightarrow \pi^*$ transitions involving HOMO → LUMO orbitals. For all these sensitizers, many other bands with f > 0.03, corresponding to higher energy excitations over the third excited state, are present and are governed by HOMOs → LUMOs transitions (Table S1). When the dyes are adsorbed on the TiO$_2$ cluster, the $\pi \rightarrow \pi^*$ transitions are still present. Nevertheless, **Cat-IV-(TiO$_2$)$_9$** is the only compound that presents a slight red-shifted DTCT band, with non-negligible oscillator strength at 542 nm (2.29 eV), governed by HOMO-2 → LUMO + 10 and HOMO-6 → LUMO + 3 orbital transitions, while in **Cat-V-(TiO$_2$)$_9$** the first dye-on-TiO$_2$ transition with non-negligible oscillator strength corresponds to a HOMO → LUMO + 23 orbital transition and it is very similar in energy to the HOMO → LUMO transition of the free dye. In this connection, LUMO + 23 orbital corresponds to the LUMO of the free dye. The presence of the red-shifted DTCT band in **Cat-IV-(TiO$_2$)$_9$** can be

ascribed to a better degree of conjugation, due to higher planarity, in this dye with respect to **Cat-V-(TiO$_2$)$_9$.**

Cat-VI-(TiO$_2$)$_9$ and **Cat-VII-(TiO$_2$)$_9$** show the first red-shifted DTCT band at 723 and 688 nm (1.71 and 1.80 eV), dominated by HOMO-1 → LUMO + 6 and HOMO-2 → LUMO + 8 orbital transitions, respectively. Nevertheless, they have very low intensity as their oscillator strengths are lower than 0.03 (Table S2), and thus appear only as long tailings of the main absorption bands just below 600 nm in the simulated spectra.

The analysis of the MOs energies and plots, Table S3 and Fig. 6, reveals that the HOMOs of the **Cat-IV-VII** dyes bound to $(TiO_2)_9$ are localized on the chromophores. However, for **Cat-V-(TiO$_2$)$_9$** only, the electron density of HOMO does not involve the catechol moiety which leads to a weak electron coupling between the sensitizer and the $(TiO_2)_9$ cluster.

The HOMO of **Cat-IV-VII** dyes bound to $(TiO_2)_9$ have almost the same energies of those of free dyes (they are lower in energy by at most 0.20 eV), while the LUMOs are mainly localized on $(TiO_2)_9$ cluster, with
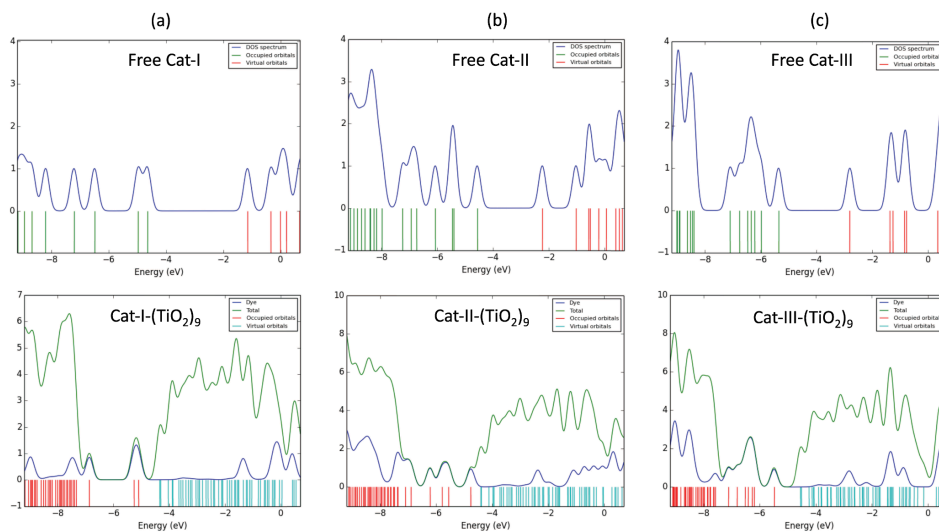
Fig. 4. PDOS and DOS of: (a) free **Cat-I** (top) and **Cat-I-(TiO$_2$)$_9$** (bottom); (b) free **Cat-II** (top) and **Cat-II-(TiO$_2$)$_9$** (bottom); (c) free **Cat-III** (top) and **Cat-III-(TiO$_2$)$_9$** (bottom).
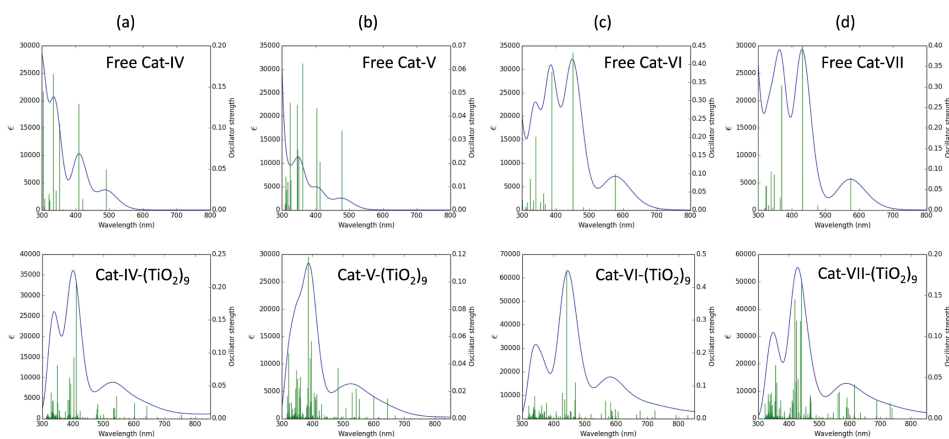

Fig. 5. Simulated TDDFT UV–Vis absorption spectra of: (a) free **Cat-IV** (top) and **Cat-IV-(TiO$_2$)$_9$** (bottom); (b) free **Cat-V** (top) and **Cat-V-(TiO$_2$)$_9$** (bottom); (c) free **Cat-VI** (top) and **Cat-VI-(TiO$_2$)$_9$** (bottom); (d) free **Cat-VII** (top) and **Cat-VII-(TiO$_2$)$_9$** (bottom).

a contribution from p orbitals of catechol oxygens.

Moreover, LUMO energies are more stabilized than those of HOMOs. Additionally LUMO + 21, LUMO + 23, LUMO + 19 and LUMO + 20 of **Cat-IV, Cat-V, Cat-VI** and **Cat-VII** dyes bound to TiO$_2$, respectively, have the same energy of the LUMOs of the corresponding free dyes, and their electron density distributions are prevalently localized on the dyes, with a contribution from the cluster.

The PDOS and DOS of free and adsorbed **Cat-IV-VII** dyes are showed in Fig. 7. As for **Cat-I-III**, when these dyes are adsorbed on the cluster, the bandgaps become very small, close to 0. The highest occupied state is

mainly composed by the dye molecule and it lies within the bandgap. The very first virtual states are completely localized on TiO$_2$ surface, while virtual states higher in energy, until the first unoccupied state totally localized on the dye, show an important contribution from the dye molecules. Therefore, even in these molecules, the electron-coupling between the HOMO of the dyes and the CB of TiO$_2$ seems to be present.

Nevertheless, **Cat-IV-VII** do not satisfy all the requirements that make them suitable candidates as type II dyes. Indeed, there is not a clear evidence of red-shifted DTCT bands, with the only exception of **Cat-IV**. Therefore, it is possible to suppose that these sensitizers could

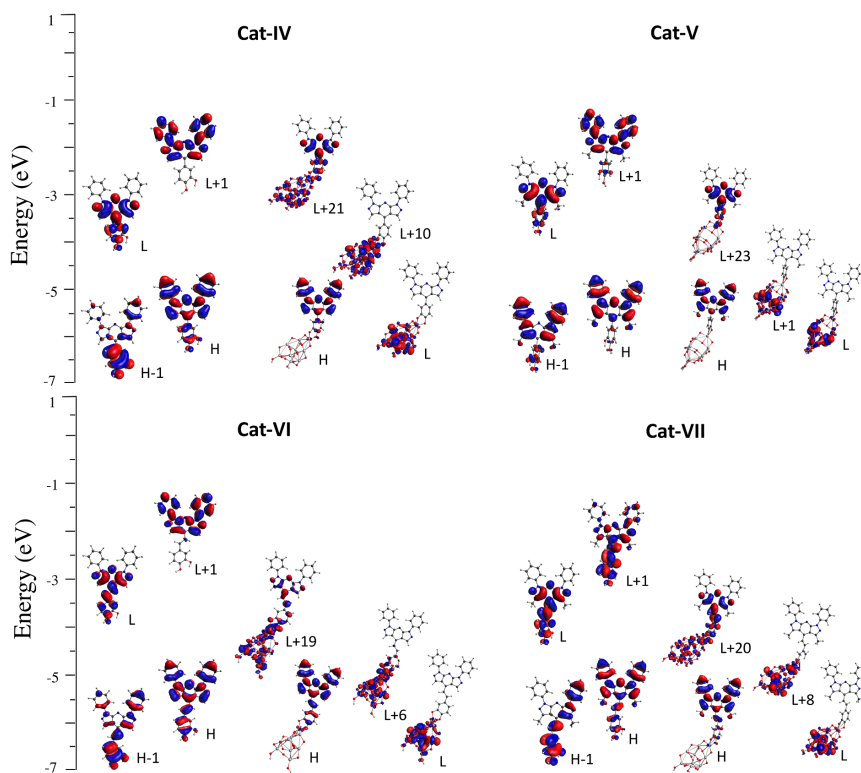**Fig. 6.** DFT FMOs plots of free and selected occupied and virtual MOs of adsorbed on $(TiO_2)_9$ **Cat-IV-VII dyes**.
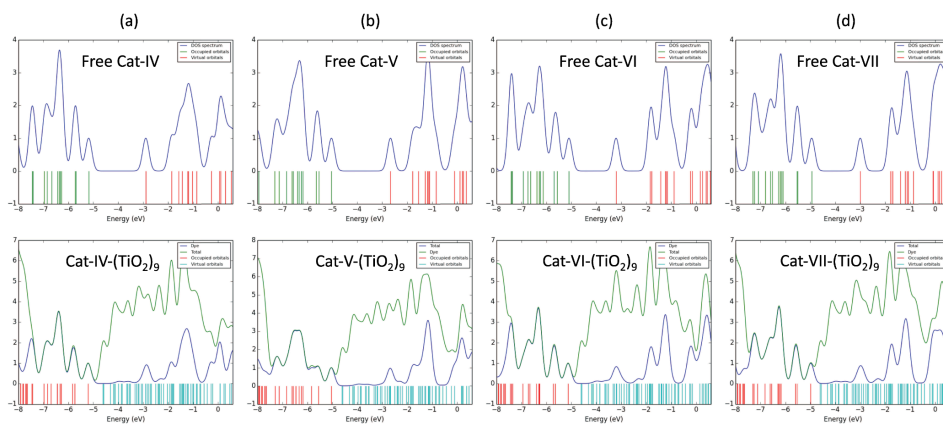
Fig. 7. PDOS and DOS of: (a) free **Cat-IV** (top) and **Cat-IV-(TiO$_2$)$_9$** (bottom); (b) free **Cat-V** (top) and **Cat-V-(TiO$_2$)$_9$** (bottom); (c) free **Cat-VI** (top) and **Cat-VI-(TiO$_2$)$_9$** (bottom); (d) free **Cat-VII** (top) and **Cat-VII-(TiO$_2$)$_9$** (bottom).
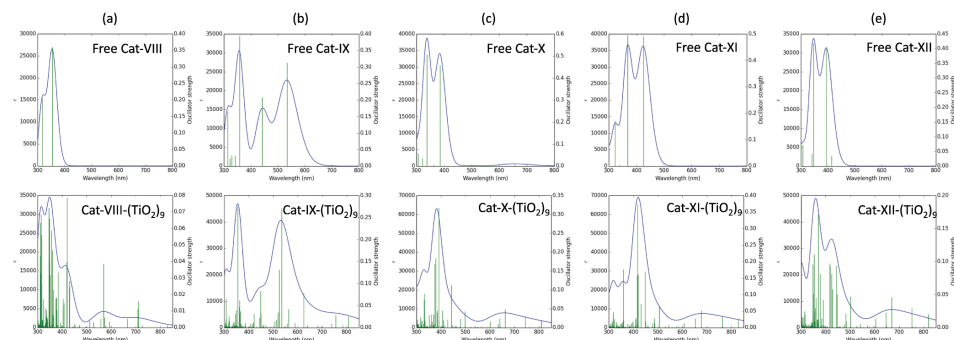
6

Fig. 8. Simulated TDDFT UV–Vis absorption spectra of: (a) free **Cat-VIII** (top) and **Cat-VIII-(TiO$_2$)$_9$** (bottom); (b) free **Cat-IX** (top) and **Cat-IX-(TiO$_2$)$_9$** (bottom); (c) free **Cat-X** (top) and **Cat-X-(TiO$_2$)$_9$** (bottom); (d) free **Cat-X** (top) and **Cat-XI-(TiO$_2$)$_9$** (bottom); (e) free **Cat-XII** (top) and **Cat-XII-(TiO$_2$)$_9$** (bottom).

Table 1
Main DFT and TDDFT results obtained on **Cat-I-XV** sensitizers.

Sensitizers	λ^a_{max} of free Cat	λ^a_{max} of DTCT band	Orbital interactions$^\%$	Virtual states$^\$$
Cat-I	297 nm$^\&$	452 nm	present	present
Cat-II	398 nm$^\&$	820 nm	present	present
Cat-III	397 nm$^\&$	702 nm	present	present
Cat-IV	490 nm	542 nm	present	present
Cat-V	478 nm$^\&$	not present	#	present
Cat-VI	577 nm$^\&$	723 nm*	present	present
Cat-VII	574 nm$^\&$	688 nm*	present	present
Cat-VIII	354 nm$^\&$	569 nm	present	present
Cat-IX	534 nm	755 nm	present	present
Cat-X	386 nm$^\&$	744 nm	present	present
Cat-XI	425 nm$^\&$	763 nm	present	present
Cat-XII	414 nm$^\&$	752 nm	present	present
Cat-XIII	593 nm$^\&$	733 nm	present	§
Cat-XIV	631 nm$^\&$	765 nm	present	§
Cat-XV	617 nm$^\&$	794 nm	present	§

$^\%$ Interaction between p orbitals of sensitizers and d orbitals of TiO$_2$.
$^\$$ Virtual states formed by the interaction between HOMO of free-Cat and CB of TiO$_2$.
$^\&$ The wavelength of the transition remains unchanged upon binding to TiO$_2$.
$^\#$ Weaker interaction with respect to other sensitizers.
* Negligible intensity (f < 0.03).
§ Less acceptor virtual states are present.

follow an intermediate regime between the direct (type II) and the indirect (type I) electron injection mechanisms [22,23].

3.2. Cat-VIII to Cat-XII

Simulated UV–Vis spectra of free and adsorbed **Cat-VIII** to **Cat-XII** are showed in Fig. 8.

Free **Cat-VIII** to **Cat-XII** show the lowest energy absorption maxima (considering transitions with f > 0.03) in the range of 354–534 nm corresponding to $\pi \rightarrow \pi^*$ transitions dominated by HOMOs → LUMOs orbitals (Table 1).

The $\pi \rightarrow \pi^*$ transitions of the free dyes are present at the same wavelengths when they are adsorbed on (TiO$_2$)$_9$ cluster, together with new red-shifted DTCT bands (Fig. 8, Table S2), visible at 569, 755, 744, 763 and 752 nm (2.17, 1.64, 1.67, 1.62 and 1.65 eV) for **Cat-VIII-XII-(TiO$_2$)$_9$**, respectively, and governed by HOMO → LUMO + 11 in **Cat-VIII-(TiO$_2$)$_9$** and HOMO → LUMO + 8 transitions in **Cat-IX-(TiO$_2$)$_9$**, **Cat-X-(TiO$_2$)$_9$**, **Cat-XI-(TiO$_2$)$_9$** and **Cat-XII-(TiO$_2$)$_9$** (Table S2).

The DTCT bands of **Cat-XI** and **Cat-XII**, bearing –CN are more red-

shifted with respect to their analogue substituted with –NO$_2$ (**Cat-IX** and **Cat-X**), confirming the merit of moderately electron-withdrawing substituents in increasing the DTCT efficiency. All the DTCT bands correspond to a photoexcitation from states fully localized on the dyes to states mainly localized on the cluster but with appreciable catechol contribution (Fig. 9), similar to what previously observed for dyes **Cat-I-III-(TiO$_2$)$_9$**. On the contrary, the LUMOs of dye-TiO$_2$ complexes are completely localized on the TiO$_2$ surface, with no contribution from the dyes, as in catechol [22,23].

As expected, the analysis of the computed Kohn-Sham orbital energies (Table S3) reveals that the LUMO energies of free **Cat-IX** and **Cat-X**, which have –NO$_2$ as strong electron-withdrawing substituent, are lower in energy with respect to those of free **Cat-VIII**, **Cat-XI** and **Cat-XII**, which have –CO$_2$H and –CN as moderately electron-withdrawing substituents. However, when the dyes are adsorbed on (TiO$_2$)$_9$ cluster, their LUMO energies are all stabilized and differences become much smaller, while HOMO energies are almost at the same level as those of the free dyes (they are lower in energy by at most 0.40 eV). Additionally, the LUMOs energies of free dyes corresponding to the LUMO + 22, LUMO + 15, LUMO + 24, LUMO + 20 and LUMO + 23 levels of **Cat-VIII-(TiO$_2$)$_9$**, **Cat-IX-(TiO$_2$)$_9$**, **Cat-X-(TiO$_2$)$_9$**, **Cat-XI-(TiO$_2$)$_9$** and **Cat-XII-(TiO$_2$)$_9$**, respectively, are well inside the CB and are delocalized both on the dyes and on the titanium dioxide cluster (Fig. 9).

To complete the analysis, the PDOS and DOS of free and adsorbed **Cat-VIII-XII** dyes are showed in Fig. 10. Similar to the other molecules previously discussed, the highest occupied state is mainly composed by the dye molecule and lies near the CB edge, while the LUMO levels of the free dyes are well shifted toward the CB. The very first virtual states are completely localized on TiO$_2$ surface, as it occurs in catechol [22,23], while virtual states higher in energy, until the first unoccupied state localized on the dye, show an important contribution from the dye molecules. Therefore, a good electron coupling between the HOMO of the dyes and the CB of TiO$_2$ exists and the direct (type II) mechanism is promoted. In conclusion, even if the analyzed **Cat-VIII-XII** dyes have electron-withdrawing substituents, they fulfill all type II dyes requirements, showing red-shifted DTCT bands and a consistent interaction between the HOMO of the dyes and the CB of TiO$_2$, comparable to those of dyes bringing electron-donating substituents.

3.3. Cat-XIII to Cat-XV

As already mentioned in the introduction, the substitution with –CH$_3$ gives moderate electron-donating features, while the substitution with –NO$_2$ and –CN makes the benzo[1,3,5]oxadiazole an electron-withdrawing group. This is evident looking at the simulated UV–Vis

Fig. 9. DFT FMOs plots of free and selected occupied and virtual MOs of adsorbed on $(TiO_2)_9$ **Cat-VIII-XII dyes**.
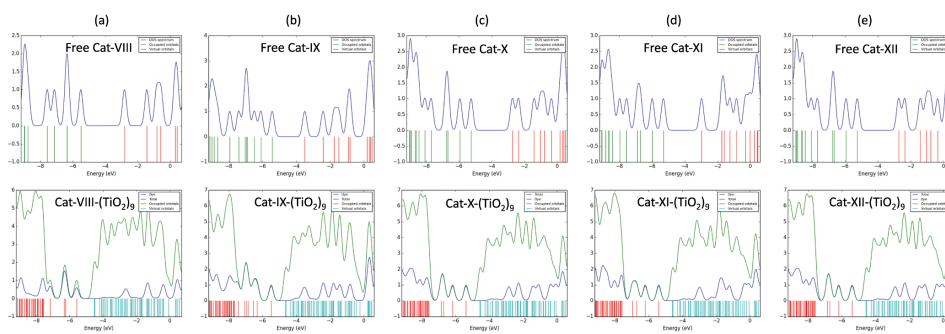
Fig. 10. PDOS and DOS of: (a) free **Cat-VIII** on the top and **Cat-VIII-(TiO₂)₉** on the bottom; (b) free **Cat-IX** on the top and **Cat-IX-(TiO₂)₉** on the bottom; (c) free **Cat-X** on the top and **Cat-X-(TiO₂)₉** on the bottom; (d) free **Cat-XI** on the top and **Cat-XI-(TiO₂)₉** on the bottom; (e) free **Cat-XII** on the top and **Cat-XII-(TiO₂)₉** on the bottom.
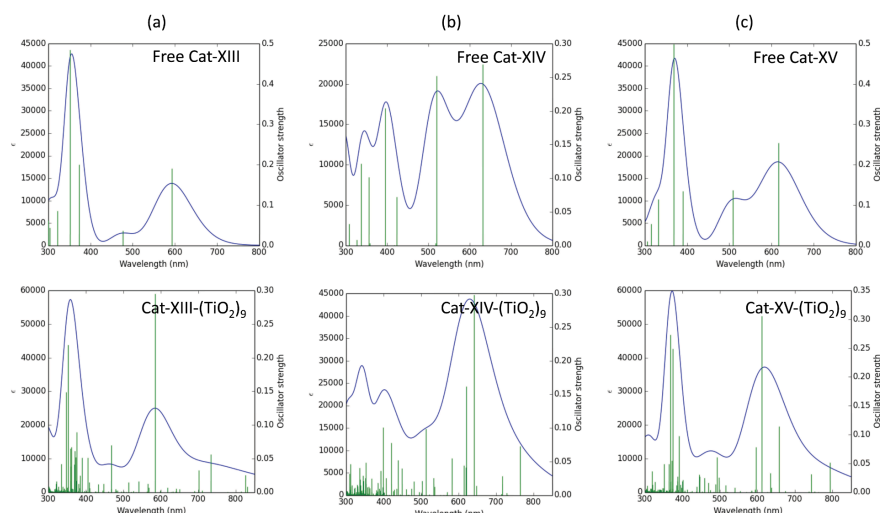
Fig. 11. Simulated TDDFT UV–Vis absorption spectra of: (a) free **Cat-XIII** (top) and **Cat-XIII-(TiO₂)₉** (bottom); (b) free **Cat-XIV** (top) and **Cat-XIV-(TiO₂)₉** (bottom); (c) free **Cat-XV** (top) and **Cat-XV-(TiO₂)₉** (bottom).

spectra of the dyes (Fig. 11). Indeed, the benzo[1,3,5]oxadiazole substituted with electron-withdrawing groups (**Cat-XIV** and **Cat-XV**) shows red-shifted absorptions in comparison to **Cat-XIII**. More specifically, free **Cat-XIII, Cat-XIV** and **Cat-XV** present the lowest energy absorption maxima at 593, 631 and 617 nm (2.09, 1.96 and 2.01 eV), respectively, which are assigned to $\pi \rightarrow \pi^*$ transitions dominated by HOMO $\rightarrow$ LUMO orbital transitions (Table S1). Additionally, the LUMO energy levels of free **Cat-XIV** and **Cat-XV** are clearly lower than that of **Cat-XIII** (Table S3).

Also in this case, the $\pi \rightarrow \pi^*$ transitions of free dyes are still present when the molecules are adsorbed on (TiO₂)₉ cluster and new red-shifted DTCT bands also appear at 733, 765 and 794 nm (1.69, 1.62 and 1.56 eV), corresponding to HOMO $\rightarrow$ LUMO + 10, HOMO $\rightarrow$ LUMO + 7 and HOMO $\rightarrow$ LUMO + 6 orbital transitions of **Cat-XIII-(TiO₂)₉**, **Cat-XIV-(TiO₂)₉** and **Cat-XV-(TiO₂)₉**, respectively. It is noteworthy that the –CN substituted benzo[1,3,5]oxadiazole, **Cat-XV-(TiO₂)₉**, has the most red-shifted DTCT band in comparison to **Cat-XIII-(TiO₂)₉ and Cat-XIV-(TiO₂)₉**, confirming the effect of moderately electron-withdrawing substituents, as previously stressed out also in **Cat-XI** and **Cat-XII** (Table S2) [21]. The inspection of the wavefunction plots involved in DTCT bands (Fig. 12) reveals that the HOMOs of all the three bound dyes are fully localized on the catechol systems, while the LUMOs are prevalently localized on d orbitals of Ti, with a contribution from the groups anchored to the chromophore (p orbitals of cathecol oxygens). Additionally, LUMO + 7 in **Cat-XIV-(TiO₂)₉** and LUMO + 6 in **Cat-XV-(TiO₂)** also show a strong contribution from dye. The HOMO energy levels of bound dyes are almost at the same energies of those of free dyes (they are lower by at most 0.43 eV), while all the LUMO energy levels resulted to be stabilized (Table S3). The LUMO energies of free dyes correspond to LUMO + 14, LUMO + 9 and LUMO + 9 energies of **Cat-XIII-(TiO₂)₉**, **Cat-XIV-(TiO₂)₉** and **Cat-XV-(TiO₂)**, respectively, and they are delocalized both on the dye and on the cluster.

Finally, the analysis of PDOS and DOS of free and bound to TiO₂ **Cat-XIII-XV** is presented (Fig. 13). The bandgaps of the three compounds are small, with those **of Cat-XIV** and **Cat-XV** slightly bigger than that of **Cat-XIII**. The highest occupied state of all three dyes has a large component

coming from the dye molecule and lies near the CB edge. All the first virtual states are completely localized on TiO₂ surface, with no contribution from the dyes [22,23]. Moreover, the first unoccupied states totally localized on the dyes are very close to the CB edge and therefore there are less acceptor virtual states formed by the interaction between the HOMOs of these dyes and the CB of TiO₂ with respect to the previously analyzed compounds. Thus, on the basis of discussed properties, **Cat-XIII-XV** can potentially follow an intermediate regime between the pure direct (type II) and the pure indirect (type I) injection mechanisms [22,23]. Indeed, even if they have red-shifted DTCT bands, the electron coupling between the HOMOs of these dyes and the CB of TiO₂ is not strong enough to indicate **Cat-XIII-XV** as efficient type II dyes.

4. Conclusions

In this work, 15 catechol-based sensitizers, **Cat-I** to **Cat-XV**, bringing different electron-donating and electron-withdrawing groups, have been investigated. The electronic structures and excited state properties of free and bound to TiO₂-dyes have been analyzed and compared by means of DFT and TDDFT methods. The main results are summarized in Table 1.

The computed properties suggest that, among the studied sensitizers, fully conjugated molecules, such as **Cat-II**, **Cat-III**, **Cat-VIII**, **Cat-IX**, **Cat-X**, **Cat-XI** and **Cat-XII** could perform better as type II dyes. Indeed, they show red-shifted DTCT bands with a large number of acceptor orbitals formed by the interaction of d orbitals of Ti and p orbitals of catechol oxygens, leading to a strong electron coupling which fosters the direct (type II) mechanisms. The above-mentioned molecules are linked to the Cat unit through a π spacer and they have both electron-donating and electron-withdrawing substituents. Therefore, a good degree of conjugation should be taken into account in the design of type II dyes as it contributes to enhance the DTCT efficiency. These results are in very good agreement with a previous experimental work in which different Cat derivatives were successfully used to sensitize the TiO₂ powder for photocatalytic H₂ production and photocathode assembly. Among the Cat derivatives, the Caffeic Acid (**Cat-VIII** of this work) showed the

9

Cat-XIII

Cat-XIV

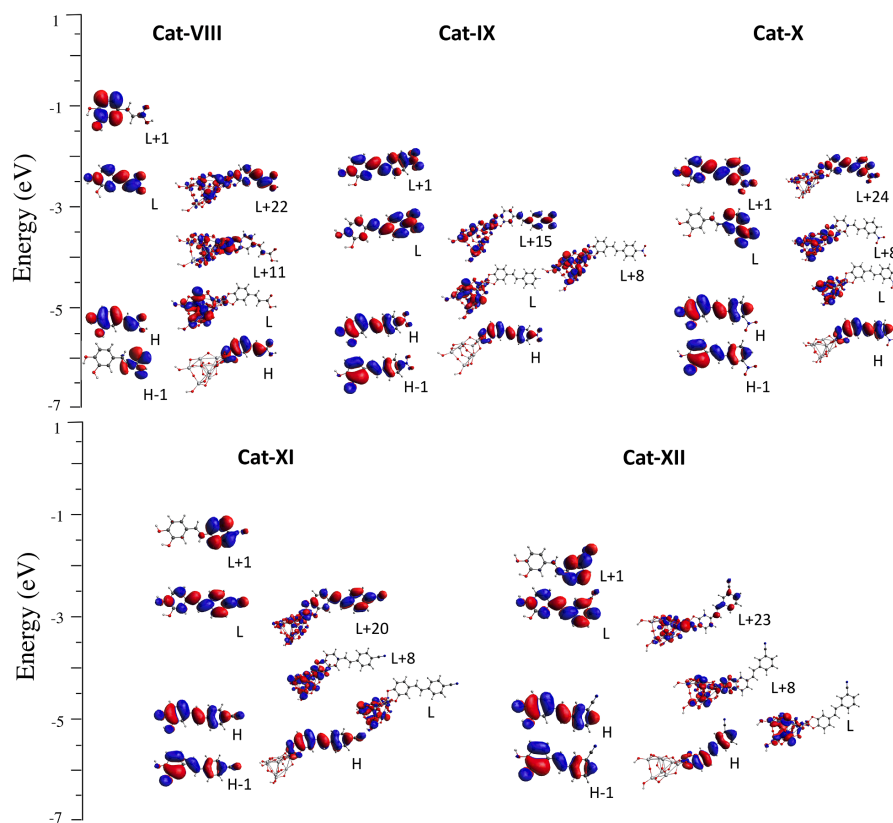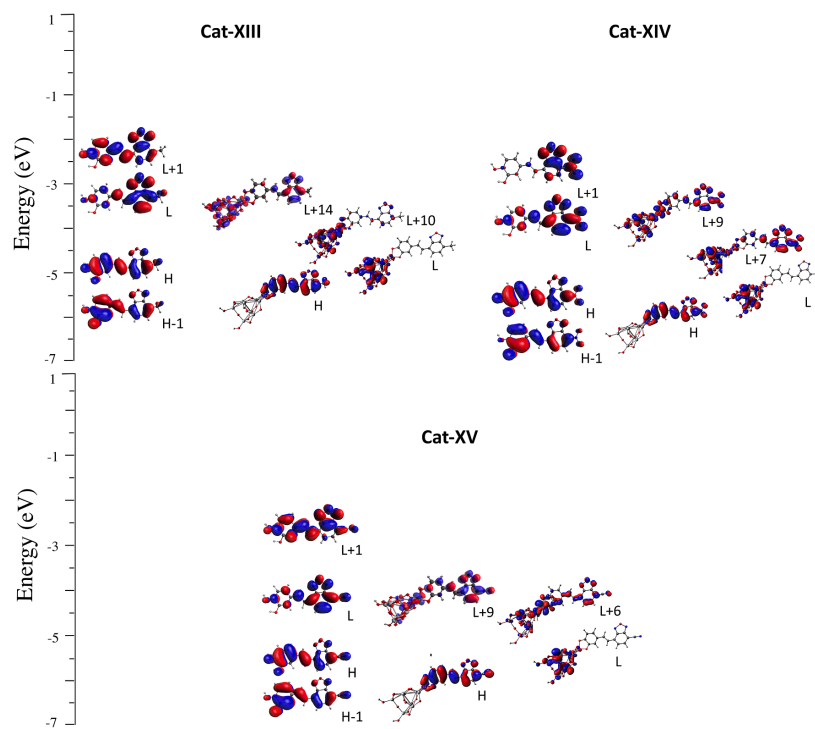Energy (eV)

Cat-XV

Energy (eV)

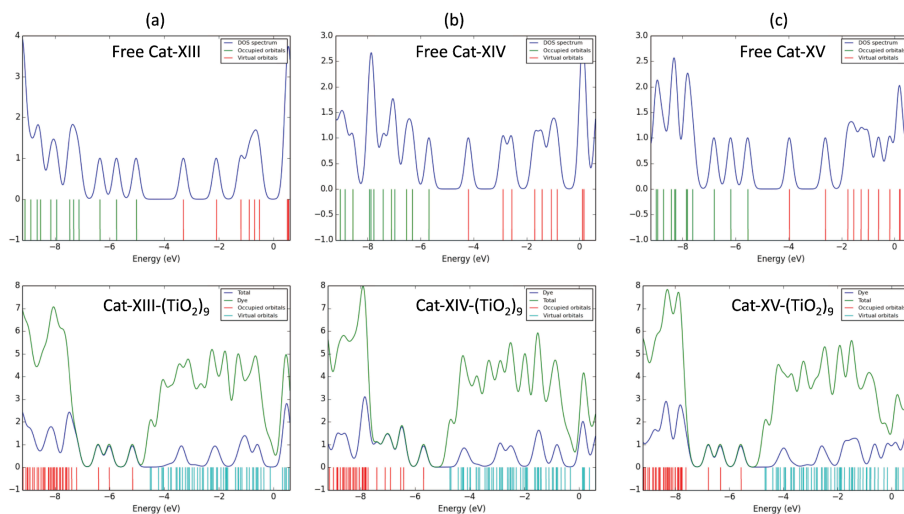**Fig. 12.** DFT FMOs plots of free and selected occupied and virtual MOs of adsorbed on $(TiO_2)_9$ **Cat-XIII-XV dyes**.

10

120

Fig. 13. PDOS and DOS of: (a) free **Cat-XIII** (top) and **Cat-XIII-(TiO$_2$)$_9$** (bottom); (b) free **Cat-XIV** (top) and **Cat-XIV-(TiO$_2$)$_9$** (bottom); (c) free **Cat-XV** (top) and **Cat-XV-(TiO$_2$)$_9$** (bottom).

highest activity in comparison to the unconjugated analogue 3,4-dihydroxyhydrocinnamic acid demonstrating that a greater conjugation increases both the catechol binding constant and the electron injection efficiency [42].

Additionally, **Cat-II**, **Cat-III**, **Cat-VIII**, **Cat-IX**, **Cat-X**, **Cat-XI** and **Cat-XII** sensitizers perform better than **Cat-I** which has an electron-donating substituent directly linked to Cat unit. Besides and related to the conjugation issue, another aspect to consider is the molecules' planarity: less planar molecules, such as **Cat-IV-VII,** perform generally worse and, if present, their DTCT bands have low intensity. Lastly, **Cat-XIII**, **Cat-IV** and **Cat-XV** show that even if the DTCT bands are present, this is not enough to promote a direct electron injection mechanism, as this process is strongly influenced by the contribution of the dye in the virtual states of dye-TiO$_2$ complexes.

CRediT authorship contribution statement

Carmen Coppola: Investigation, Writing - original draft, Writing - review & editing. **Alessio D'Ettorre:** Investigation, Writing - original draft. **Maria Laura Parisi:** Writing - original draft, Writing - review & editing. **Lorenzo Zani:** Writing - original draft, Writing - review & editing. **Gianna Reginato:** Conceptualization, Writing - review & editing. **Massimo Calamante:** Writing - review & editing. **Alessandro Mordini:** Writing - review & editing. **Maurizio Taddei:** Conceptualization, Writing - review & editing. **Riccardo Basosi:** Funding acquisition, Writing - review & editing. **Adalgisa Sinicropi:** Conceptualization, Writing - original draft, Writing - review & editing, Supervision.

Declaration of Competing Interest

The authors declare that they have no known competing financial interests or personal relationships that could have appeared to influence the work reported in this paper.

Appendix A. Supplementary data

Supplementary data to this article can be found online at https://doi.org/10.1016/j.ica.2020.120233.

References

[1] A. Hagfeldt, G. Boschloo, L. Sun, L. Kloo, H. Pettersson, Dye-sensitized solar cells, Chem. Rev. 110 (11) (2010) 6595–6663, https://doi.org/10.1021/cr900356p.
[2] C.-P. Lee, C.-T. Li, K-C. Ho, Use of organic materials in dye-sensitized solar cells, Mater. Today 20 (5) (2017) 267–283, https://doi.org/10.1016/j.mattod.2017.01.012.
[3] J. Gong, K. Sumathy, Q. Qiao, Z. Zhou, Review on dye-sensitized solar cells (DSSCs): advanced techniques and research trends, Renew. Sustain. Energy Rev. 68 (2017) 234–246, https://doi.org/10.1016/j.rser.2016.09.097.
[4] A. Dessì, M. Calamante, A. Mordini, M. Peruzzini, A. Sinicropi, R. Basosi, F. Fabrizi de Biani, M. Taddei, D. Colonna, A. Di Carlo, G. Reginato, L. Zani, Organic dyes with intense light absorption especially suitable for application in thin-layer dye-sensitized solar cells, Chem. Commun. 50 (90) (2014) 13952–13955, https://doi.org/10.1039/C4CC06160H.
[5] Y. Ooyama, Y. Harima, Photophysical and electrochemical properties, and molecular structures of organic dyes for dye-sensitized solar cells, ChemPhysChem 13 (18) (2012) 4032–4080, https://doi.org/10.1002/cphc.201200218.
[6] N.M. Dimitrijevic, Z.V. Saponjic, D.M. Bartels, M.C. Thurnauer, D.M. Tiede, T. Rajh, Revealing the nature of trapping sites in nanocrystalline titanium dioxide by selective surface modification, J. Phys. Chem. B 107 (30) (2003) 7368–7375, https://doi.org/10.1021/jp034064i.
[7] H. Frei, D.J. Fitzmaurice, M. Graetzel, Surface chelation of semiconductors and interfacial electron transfer, Langmuir 6 (1) (1990) 198–206, https://doi.org/10.1021/la00091a032.
[8] P.M. Jayaweera, A.R. Kumarasinghe, K. Tennakone, Nano-porous TiO$_2$ photovoltaic cells sensitized with metallochromic triphenylmethane dyes: [n-TiO$_2$/triphenylmethane dye/p-I$^-$/I$_3^-$ (or CuI)], J. Photochem. Photobiol., A 126 (1–3) (1999) 111–115, https://doi.org/10.1016/S1010-6030(99)00121-5.
[9] G. Ramakrishna, H.N. Ghosh, A.K. Singh, D.K. Palit, J.P. Mittal, Dynamics of back-electron transfer processes of strongly coupled triphenyl methane dyes adsorbed on

TiO$_2$ nanoparticle surface as studied by fast and ultrafast visible spectroscopy, J. Phys. Chem. B 105 (51) (2001) 12786–12796, https://doi.org/10.1021/jp011078k.

[10] C.G. Garcia, A.S. Polo, N.Y. Murakami Iha, Fruit extracts and ruthenium polypyridinic dyes for sensitization of TiO2 in photoelectrochemical solar cells, J. Photochem. Photobiol., A 160 (1-2) (2003) 87–91, https://doi.org/10.1016/S1010-6030(03)00225-9.

[11] Q. Dai, J. Rabani, Unusually efficient photosensitization of nanocrystalline TiO$_2$ films by pomegranate pigments in aqueous medium, New J. Chem. 26 (2002) 421–426, https://doi.org/10.1039/b108390b.

[12] Q. Dai, J. Rabani, Photosensitization of nanocrystalline TiO$_2$ films by pomegranate pigments with unusually high efficiency in aqueous medium, Chem. Commun. 20 (2001) 2142–2143, https://doi.org/10.1039/b106197f.

[13] E.L. Tae, S.H. Lee, J.K. Lee, S.S. Yoo, E.J. Kang, K.B. Yoon, A strategy to increase the efficiency of the dye-sensitized TiO$_2$ solar cells operated by photoexcitation of dye-to-TiO$_2$ charge-transfer bands, J. Phys. Chem. B 109 (47) (2005) 22513–22522, https://doi.org/10.1021/jp0537411.

[14] B.-K. An, W. Hu, P.L. Burn, P. Meredith, New type II catechol-thiophene sensitizers for dye-sensitized solar cells, J. Phys. Chem. C 114 (41) (2010) 17964–17974, https://doi.org/10.1021/jp105687z.

[15] P. Persson, R. Bergström, S. Lunell, Quantum chemical study of photoinjection processes in dye-sensitized TiO$_2$ nanoparticles, J. Phys. Chem. B 104 (44) (2000) 10348–10351, https://doi.org/10.1021/jp002550p.

[16] L. Lasser, E. Ronca, M. Pastore, F. De Angelis, J. Cornil, R. Lazzaroni, D. Beljonne, Energy level alignment at titanium oxide–dye interfaces: implications for electron injection and light harvesting, J. Phys. Chem. C 119 (18) (2015) 9899–9909, https://doi.org/10.1021/acs.jpcc.5b01267.

[17] D.J. Mowbray, A. Migani, Optical absorption spectra and excitons of dye-substrate interfaces: catechol on TiO$_2$(110), J. Chem. Theory Comput. 12 (6) (2016) 2843–2852, https://doi.org/10.1021/acs.jctc.6b00217.s001.

[18] Y. Ooyama, K. Yamaji, J. Ohshita, Photovoltaic performances of type-II dye-sensitized solar cells based on catechol dye sensitizers: retardation of back-electron transfer by PET (photo-induced electron transfer), Mater. Chem. Front. 1 (11) (2017) 2243–2255, https://doi.org/10.1039/C7QM00211D.

[19] 17. best-research-cell-efficiencies.20200803.pdf, (n.d.). www.nrel.gov/pv/cell-efficiency (accessed October 3, 2020).

[20] L. Zhang, X. Yang, W. Wang, G.G. Gurzadyan, J. Li, X. Li, J. An, Z. Yu, H. Wang, B. Cai, A. Hagfeldt, L. Sun, 13.6% efficient organic dye-sensitized solar cells by minimizing energy losses of the excited state, ACS Energy Lett. 4 (4) (2019) 943–951, https://doi.org/10.1021/acsenergylett.9b00141.s001.

[21] Y. Ooyama, M. Kanda, K. Uenaka, J. Ohshita, Effect of substituents in catechol dye sensitizers on photovoltaic performance of type II dye-sensitized solar cells, ChemPhysChem 16 (14) (2015) 3049–3057, https://doi.org/10.1002/cphc.201500419.

[22] R. Sánchez-de-Armas, M.A. San-Miguel, J. Oviedo, J.F. Sanz, Direct vs. indirect mechanisms for electron injection in DSSC: catechol and alizarin, Comput. Theor. Chem. 975 (1-3) (2011) 99–105, https://doi.org/10.1016/j.comptc.2011.01.010.

[23] R. Sánchez-de-Armas, J. Oviedo, M.Á. San Miguel, J.F. Sanz, Direct vs indirect mechanisms for electron injection in dye-sensitized solar cells, J. Phys. Chem. C 115 (22) (2011) 11293–11301, https://doi.org/10.1021/jp201233y.

[24] Y. Ooyama, T. Yamada, T. Fujita, Y. Harima, J. Ohshita, Development of D–π–Cat fluorescent dyes with a catechol group for dye-sensitized solar cells based on dye-to-TiO$_2$ charge transfer, J. Mater. Chem. A 2 (22) (2014) 8500, https://doi.org/10.1039/c4ta01286k.

[25] Y.-C. Chen, J.T. Lin, Multi-anchored sensitizers for dye-sensitized solar cells, Sustainable Energy Fuels 1 (5) (2017) 969–985, https://doi.org/10.1039/C7SE00141J.

[26] Y. Ooyama, K. Furue, T. Enoki, M. Kanda, Y. Adachi, J. Ohshita, Development of type-I/type-II hybrid dye sensitizer with both pyridyl group and catechol unit as anchoring group for type-I/type-II dye-sensitized solar cell, Phys. Chem. Chem. Phys. 18 (44) (2016) 30662–30676, https://doi.org/10.1039/C6CP06513A.

[27] F. De Angelis, Direct vs. indirect injection mechanisms in perylene dye-sensitized solar cells: a DFT/TDDFT investigation, Chem. Phys. Lett. 493 (4-6) (2010) 323–327, https://doi.org/10.1016/j.cplett.2010.05.064.

[28] R. Sánchez-de-Armas, M.A. San-Miguel, J. Oviedo, A. Márquez, J.F. Sanz, Electronic structure and optical spectra of catechol on TiO$_2$ nanoparticles from real time TD-DFT simulations, Phys. Chem. Chem. Phys. 13 (4) (2011) 1506–1514, https://doi.org/10.1039/C0CP00906G.

[29] R. Qiu, S. Qiao, B. Peng, J. Long, G. Yin, A mild method for the synthesis of bis-pyrazolo[3,4-b:4′,3′-e]pyridine derivatives, Tetrahedron Lett. 59 (43) (2018) 3884–3888, https://doi.org/10.1016/j.tetlet.2018.09.033.

[30] Gaussian 09, Revision C.01, M.J. Frisch, G.W. Trucks, H.B. Schlegel, G.E. Scuseria, M.A. Robb, J.R. Cheeseman, G. Scalmani, V. Barone, B. Mennucci, G.A. Petersson, H. Nakatsuji, M. Caricato, X. Li, H.P. Hratchian, A.F. Izmaylov, J. Bloino, G. Zheng, J.L. Sonnenberg, M. Hada, M. Ehara, K. Toyota, R. Fukuda, J. Hasegawa, M. Ishida, T. Nakajima, Y. Honda, O. Kitao, H. Nakai, T. Vreven, J. A. Montgomery, Jr., J.E. Peralta, F. Ogliaro, M. Bearpark, J.J. Heyd, E. Brothers, K.N. Kudin, V. N. Staroverov, T. Keith, R. Kobayashi, J. Normand, K. Raghavachari, A. Rendell, J.C. Burant, S.S. Iyengar, J. Tomasi, M. Cossi, N. Rega, J.M. Millam, M. Klene, J.E. Knox, J.B. Cross, V. Bakken, C. Adamo, J. Jaramillo, R. Gomperts, R.E. Stratmann, O. Yazyev, A.J. Austin, R. Cammi, C. Pomelli, J.W. Ochterski, R.L. Martin, K. Morokuma, V.G. Zakrzewski, G.A. Voth, P. Salvador, J.J. Dannenberg, S. Dapprich, A.D. Daniels, O. Farkas, J.B. Foresman, J.V. Ortiz, J. Cioslowski, D.J. Fox, Gaussian, Inc.: Wallingford, CT, USA (2010).

[31] P. Hohenberg, W. Kohn, Inhomogeneous Electron Gas, Phys. Rev. 136 (3B) (1964) B864–B871, https://doi.org/10.1103/PhysRev.136.B864.

[32] W. Kohn, L.J. Sham, Self-consisten equations including exchange and correlation effects, Phys. Rev. 140 (1965) A1134–A1138, https://doi.org/10.1103/PhysRev.140.A1133.

[33] J.P. Perdew. Electronic Structure of Solids '91, Eschrig (Akademie Verlag), Berlin, 1991, p. 11.

[34] K. Burke, J.P. Perdew, Y. Wang, Derivation of a Generalized Gradient Approximation: The PW91 Density Functional, in: Electron. Density Funct. Theory, Springer US, Boston, MA, 1998, pp. 81–111, https://doi.org/10.1007/978-1-4899-0316-7_7.

[35] A.D. Laurent, C. Adamo, D. Jacquemin, Dye chemistry with time-dependent density functional theory, Phys. Chem. Chem. Phys. 16 (28) (2014) 14334–14356, https://doi.org/10.1039/C3CP55336A.

[36] W.R. Duncan, O.V. Prezhdo, Electronic structure and spectra of catechol and alizarin in the gas phase and attached to titanium, J. Phys. Chem. B 109 (1) (2005) 365–373, https://doi.org/10.1021/jp046342z.

[37] C. Ronchi, F.A. Soria, L. Ferraro, S. Botti, C. Di Valentin, Absorption mechanism of dopamine/DOPAC-modified TiO$_2$ nanoparticles by time-dependent density functional theory calculations, Mater. Today Energy 19 (2021) 100571, https://doi.org/10.1016/j.mtener.2020.100571.

[38] Z.-w. Qu, G.-J. Kroes, Theoretical study of the electronic structure and stability of titanium dioxide clusters (TiO$_2$)$_n$ with n=1−9, J. Phys. Chem. B 110 (18) (2006) 8998–9007, https://doi.org/10.1021/jp056607p.

[39] S. Hamad, C.R.A. Catlow, S.M. Woodley, S. Lago, J.A. Mejías, Structure and Stability of Small TiO$_2$ Nanoparticles, J. Phys. Chem. B. 109 (2005) 15741–15748, https://doi.org/10.1021/jp0521914.

[40] R. Sánchez-de-Armas, J. Oviedo López, M. A. San-Miguel, J.F. Sanz, P. Ordejón, M. Pruneda, Real-Time TD-DFT Simulations in Dye Sensitized Solar Cells: The Electronic Absorption Spectrum of Alizarin Supported on TiO$_2$ Nanoclusters, J. Chem. Theory Comput. 6 (9) (2010) 2856–2865, https://doi.org/10.1021/ct100289t.

[41] N.M. O'boyle, A.L. Tenderholt, K.M. Langner, cclib: A library for package-independent computational chemistry algorithms, J. Comput. Chem. 29 (5) (2008) 839–845, https://doi.org/10.1002/jcc.20823.

[42] K.L. Orchard, D. Hojo, K.P. Sokol, M.-J. Chan, N. Asao, T. Adschiri, E. Reisner, Catechol–TiO$_2$ hybrids for photocatalytic H$_2$ production and photocathode assembly, Chem. Commun. 53 (94) (2017) 12638–12641, https://doi.org/10.1039/C7CC05094A.

4.6. Manuscript 6: "Benzo[1,2-*d*:4,5-*d'*]bisthiazole fluorophores for luminescent solar concentrators: synthesis, optical properties and effect of the polymer matrix on the device performances"

In this work, three novel molecules, **BBT2-4**, have been designed and synthetized for a possible application as fluorophores in LSCs, investigating their properties on different polymer matrices. Additionally, LSCs devices with the designed molecules have been built and characterized in comparison with a LSC employing the *state-of-the-art* LR305. **BBT2-4** possess the peculiar D-A-D structure, and they carry the common benzo[1,2-*d*:4,5-*d'*] bisthiazole (BBT) acceptor core (A) together with different donor groups (D). From the computational investigation and the experimental characterization, it emerged that the three molecules have intense emission properties, overlapping the light-absorption spectrum of Si-based cells. Moreover, they present Stokes shifts larger than the LR305, hence minimal self-absorption phenomena, suggesting that they could perform well as fluorophores in LSCs devices. LSCs devices built with **BBT2-4** show good transparency and light yellow to orange colors. In particular, the optical efficiency obtained employing **BBT4** dispersed in PMMA, PCMA and PBzMA matrices resulted to be very similar to the best data obtained employing LR305.

The PhD candidate's contribution refers to the application of DFT and TDDFT methods for the prediction of the relevant electronic and excited-state properties of the designed fluorophores. In particular, the vertical absorption and the emission energies of **BBT2-4** have been computed in solvent and in PMMA, by using PCM, to evaluate if their Stokes Shifts values would be suitable for a possible application in LSCs devices. Additionally, the PhD candidate contributed to the writing of the manuscript.
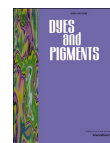
Benzo[1,2-*d*:4,5-*d*′]bisthiazole fluorophores for luminescent solar concentrators: synthesis, optical properties and effect of the polymer matrix on the device performances

Costanza Papucci [a,b,c], Alessio Dessì [a], Carmen Coppola [b,d], Adalgisa Sinicropi [a,b,d], Greta Santi [e], Mariangela Di Donato [a,f], Maria Taddei [f], Paolo Foggi [f,g,h], Lorenzo Zani [a], Gianna Reginato [a], Andrea Pucci [e,**], Massimo Calamante [a,c,*], Alessandro Mordini [a,c]

[a] *Institute of Chemistry of Organometallic Compounds (CNR-ICCOM), Via Madonna del Piano 10, 50019, Sesto Fiorentino, Italy*
[b] *Department of Biotechnology, Chemistry and Pharmacy, University of Siena, Via A. Moro 2, 53100, Siena, Italy*
[c] *Department of Chemistry "U. Schiff", University of Florence, Via della Lastruccia 13, 50019, Sesto Fiorentino, Italy*
[d] *CSGI, Consorzio per lo Sviluppo dei Sistemi a Grande Interfase, Via della Lastruccia 3, Sesto Fiorentino, 50019, Italy*
[e] *Department of Chemistry and Industrial Chemistry, University of Pisa, Via Giuseppe Moruzzi 13, 56124, Pisa, Italy*
[f] *LENS, European Laboratory for Non-Linear Spectroscopy, via N. Carrara 1, Sesto Fiorentino, 50019, Italy*
[g] *Department of Chemistry, Biology and Biotechnology, University of Perugia, via Elce di Sotto 8, 06123, Perugia, Italy*
[h] *INRIM (Istituto Nazionale di Scienza Metrologica), Strada delle Cacce 91, 10135, Torino, Italy*

ARTICLE INFO

ABSTRACT

Three new fluorophores (**BBT2-4**) with a D-A-D structure, characterised by the common benzo[1,2-*d*:4,5-*d*′] bisthiazole (BBT) as acceptor core (A) and different donor groups (D), were designed and synthesised for use in thin-film luminescent solar concentrators (LSC). The optical and spectroscopic properties of the new dyes were analysed both in solution (toluene) and in polymeric films, using static and time-resolved techniques. All the prepared molecules showed intense emissions between 460 and 550 nm with large Stokes shift (>50 nm), moderate-to-good fluorescence quantum yields (Φ_f) both in toluene solution (18–73%) and in poly(methyl methacrylate) (PMMA) films (10–52%) and good optical efficiencies (5.8–7.5%) as LSC. Transient absorption spectroscopy (TAS) studies highlighted that higher Φ_f were related to long excited-state lifetimes and that such properties were critically dependent on the polarity of the surrounding environment. Notably, homogeneous **BBT4** dispersions into the less polar poly(benzyl methacrylate) (PBzMA) and poly(cyclohexyl methacrylate) (PCMA) polymeric matrices showed higher Φ_f (52.6% and 65.6%, respectively) than those gathered from PMMA films. Accordingly, **BBT4**/PCMA films revealed significant optical efficiency of 9.0% as LSC, which was comparable to that provided by the state-of-art fluorophore Lumogen Red 305 (10.1%).

1. Introduction

Silicon-based solar cells are still the main photovoltaic (PV) devices used worldwide to exploit renewable energy sources in an effort to reduce fossil fuels consumption. Due to their high efficiency and light-harvesting capability, such cells are indeed the most used devices for the conversion of solar energy into electricity. Nonetheless, in search of more flexible and efficient options, several alternative technologies have been developed in the last 30 years, such as thin-film solar cells [1,2], DSSCs [3,4] and perovskite solar cells [5,6]. In addition, luminescent

solar concentrator (LSC) technology has recently received considerable attention. According to the first definition of Weber and Lambe [7], a LSC consists of a polymeric panel doped with a high optical efficiency fluorophore, which can absorb sunlight and emit it in a specific spectral range. Due to the different refraction index of the polymeric material and air[8], most of the emitted light is concentrated at the edges of the panel, where a PV cell can be located. Being the light concentrated, the surface of the PV cell can be very small, allowing to use materials different from silicon. Moreover, the final device is coloured and not opaque, thus allowing easy integration in buildings, e. g. in windows and

---

onto rooftops. Despite these advantages, the LSC technology still presents some drawbacks limiting its photovoltaic efficiency. A key point to performance increase is to develop new emitters and in particular, to design suitable fluorophores having a wide absorption range (between 450 and 700 nm, areas of maximum intensity of solar radiation reaching the earth), a high fluorescence quantum yield, a large Stokes displacement, with limited overlap between absorption and emission spectra, good solubility in the host matrix and long-term stability.

Various materials have been developed as emitters, such as quantum dots [9–11], inorganic fluorophores (rare earths complexes [12]), and small organic molecules like perylene diimides [13], BODIPY oligomers [14], benzothiadiazoles [15–17] and diketopyrrolopyrroles dyes [18].

Recently, we proposed new fluorophores for LSC applications based on the benzo[1,2-*d*:4,5-*d′*]bisthiazole (BBT) heterocyclic core and characterised by a donor-acceptor-donor (D-A-D) structure [19] (Fig. 1). In particular, dye **BBT1** was decorated with triphenylamines as donor groups, and thiophene rings were added between the core and the donor groups to increase the conjugation, inducing a red-shift of the absorption and emission spectra. Such a dye, when integrated into poly(methyl methacrylate) (PMMA) films at different concentrations, gave a maximum optical efficiency of 6.4%, close to the value of 7.2% measured, in the same conditions, for the reference standard Lumogen Red 305 (**LR 305**).

An important feature of the new fluorophore **BBT1** was its large Stokes shift of 94 nm in ethanol (0.48 eV), ensuring a small overlap between the absorption and the emission bands, thus minimising the self-absorption phenomena. This could enable the use of this type of luminophore in devices with a large surface area without a great loss in optical efficiency, which instead occurs when **LR 305** is employed [20].

Starting from the above-mentioned results, we decided to extend our study to a new series of BBT-derivatives still having a D-A-D design but carrying different donor groups. The aim was to obtain new fluorophores with absorption and emission in different spectral ranges, to tune the colour of the resulting poly(methyl methacrylate) (PMMA) films and, at the same time, to increase or, at least, maintain the optical characteristics suitable for LSC application (i.e., quantum yield, Stokes shift, optical efficiency). In addition, expanding our previous studies, we wanted to combine the computational characterisation of the dyes with appropriate transient absorption spectroscopy (TAS) studies, with the aim to investigate the dynamics of light absorption and emission processes, both in solution and in the solid state, and correlate them with the optical performances of the devices.

The new dyes have been synthesised and completely characterised both in solution and as dispersion in three different polymeric matrices, namely PMMA, poly(benzyl methacrylate) (PBzMA) and poly(cyclohexyl methacrylate) (PCMA) with the aim also to test the effect of the less polar lateral substituent (i.e. benzyl and cyclohexyl compared to the traditional methyl ester group in PMMA) on the optical features of the derived films.

Their computational characterisation and TAS investigation have been carried out, and the prepared thin-film LSC devices were eventually characterised in terms of their photovoltaic performances.

2. Experimental Section

2.1. General remarks

All commercially available compounds were purchased from Merck KgaA, Fluorochem Ltd. and T.C.I. Co. Ltd., and were used without further purification unless stated otherwise. Anhydrous toluene and *N,N*-dimethylformamide (*N,N*-DMF) were obtained after drying with a PureSolv Micro apparatus (Inert). Tetrahydrofuran was dried by distillation on metallic sodium using benzophenone as indicator until the characteristic blue colour of in situ-generated sodium diphenyl-ketyl radical was found to persist. Diisopropylamine was distilled under inert atmosphere and kept over KOH. Poly(methyl methacrylate) (PMMA, Aldrich, Mw = 350,000 g/mol, T_g = 105 °C), Poly(benzyl methacrylate) (PBzMA, Aldrich, Mw = 100,000 g/mol, T_g = 54 °C) and Poly(cyclohexyl methacrylate) (PCMA, Aldrich, Mw = 65,000 g/mol, T_g = 104 °C) were used as received. Organometallic reactions were carried out under dry nitrogen using Schlenk techniques. Solvent degassing was carried out according to the "freeze-pump-thaw" method. The temperature of −78 °C was obtained with a liquid N_2/acetone cooling bath. Reactions were monitored by TLC on Kieselgel 60 F254 (Merck) aluminium sheets, and the products were visualised by exposing the plate to UV light or by staining it with KMnO$_4$ solution. Flash column chromatography [21] was performed using Merck Kieselgel 60 (300–400 mesh) as the stationary phase. ^{1}H NMR spectra were recorded at 200–400 MHz, and ^{13}C NMR spectra were recorded at 50.3–100.6 MHz, respectively, on Varian Gemini/Mercury/INOVA series instruments. Chemical shifts (δ) are reported in parts per million (ppm) and are referred to the residual solvent peak (CDCl$_3$, δ = 7.26 ppm for ^{1}H NMR and δ = 77.0 ppm for ^{13}C NMR; CD$_2$Cl$_2$ δ = 5.32 ppm for ^{1}H NMR and δ = 53.84 ppm for ^{13}C NMR; THF-*d8* δ = 3.58, 1.73 ppm for ^{1}H NMR and δ = 67.57, 25.37 ppm for ^{13}C NMR), while coupling constants (*J*) are reported in Hz. GC/MS analyses of species with MW lower than 400 g/mol were performed using a Shimadzu QP505A gas-chromatograph. ESI-MS spectra were obtained by direct injection of the sample solution using a Thermo Scientific LCQ-FLEET instrument, while HRMS spectra were measured using a Thermo Scientific LTQ Orbitrap (FT-MS) instrument (carried out at the Interdepartmental Center for Mass Spectroscopy of the University of Florence, CISM); both are reported in the form *m/z*. UV/Vis spectra in solution were recorded with a Varian Cary 4000 spectrometer, and fluorescence spectra in solution were recorded with a Varian Eclipse instrument, irradiating the sample at the wavelength corresponding to maximum absorption in the UV spectrum.

UV–Vis absorption spectroscopy on polymer films was performed at room temperature by using an Agilent Cary 5000 spectrophotometer. Fluorescence spectra on polymer films were measured at room temperature with a Horiba Jobin–Yvon Fluorolog®-3 spectrofluorometer equipped with a 450 W Xenon arc lamp and double-grating excitation and single-grating emission monochromators. The emission quantum yields (Φ_f) were determined by using a 152 mm diameter "Quanta-φ" integrating sphere, coated with Spectralon® and following the procedures reported earlier[22–24]. The optical microscope analysis was
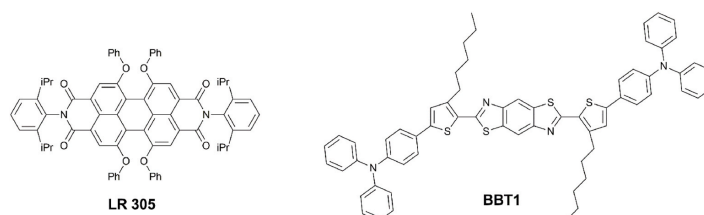

Fig. 1. *Structures of LR 305 and BBT1.*

accomplished on a SMZ-168-BLED Motic microscope and the images collected by a 12 MP digital camera with a ƒ/1.8 aperture. The concentration factors and the optical efficiencies of the LSC were obtained by using a solar simulator (ORIEL® LCS-100 solar simulator 94011A S/N: 322, AM1.5G std filter: 69 mW/cm^{-2} at 254 mm) and a PV cell (IXYS SLMD121H08L mono solar cell 86 × 14 mm, V_{oc} = 5.04 V, I_{sc} = 50.0 mA, FF > 70%, η = 22%) [25–28] connected to a precision source/measure unit (Keysight Technologies B2900 Series). The PV cell is masked with black tape to match LSC edge (50 mm × 3 mm)and therefore limit the stray light to negligible levels. Silicon was used to grease the LSC edge. The other three edges of the LSC were covered with a reflective aluminium tape.

The optical efficiency η$_{opt}$ was determined from the concentration factor (C), i.e. the ratio between the maximum power measured for the cell over the LSC edge (P$_{LSC}$) and that of the bare cell when perpendicular to the light source (P$_{SC}$):

$$\eta_{opt} = \frac{P_{LSC}}{P_{SC} \cdot G} \qquad (1)$$

where G is the geometrical factor (G = 16.6) that is the ratio between the area exposed to the solar simulator and the collecting area by the PV cell. A white backscattering layer (ERGA TAPES Srl Microcellular MCPET reflective sheet) was placed beneath the LSC with an air gap of about 2.5 mm during the P$_{LSC}$ measurements. The reported η$_{opt}$ values were calculated as the average of three distinct measurements on identical LSC samples.

2.2. Synthesis

2.2.1. Synthesis of 3-hexyl-2-thiophenecarboxaldehyde (**2**)

In a Schlenk tube, under an inert atmosphere of N$_2$, to a suspension of Mg° (370 mg, 15.2 mmol, 2.5 eq, preactivated in a solution of HCl 1 M) in dry THF (12 mL), one drop of 1,2-dibromoethane and then 2-bromo-3-hexylthiophene **1** (1.5 g, 6.1 mmol, 1.0 eq) were added. The mixture was stirred under reflux for 2 h. Then the mixture was cooled first to room temperature, then to −78 °C. *N,N*-DMF (2.36 mL, 30.5 mmol, 5.0 eq) was added dropwise to the solution. The mixture was warmed slowly until it reached room temperature and stirred for 12 h, then a saturated aqueous solution of NH$_4$Cl (10 mL) was added under vigorous stirring and the mixture was extracted with diethyl ether (2 × 15 mL). The organic phase was washed with H$_2$O (12 mL) and brine (12 mL) and dried on Na$_2$SO$_4$. The crude product (1.090 g, 91%) was directly used in the next step without further purification. Spectroscopic data are in agreement with those reported in the literature [19]. ^{1}H NMR (400 MHz, CDCl$_3$): δ = 10.04 (d, *J* = 0.9 Hz, 1H), 7.64 (dd, *J$_1$* = 5.0 Hz, *J$_2$* = 0.9 Hz, 1H), 7.00 (d, *J* = 5.0 Hz, 1H), 2.96 (t, *J* = 7.4 Hz, 2H), 1.68–1.62 (m, 2H), 1.40–1.27 (m, 6H), 0.88 (t, *J* = 8.0 Hz, 3H) ppm. ^{13}C NMR (100 MHz, CDCl$_3$): δ = 182.2, 152.9, 137.6, 134.4, 130.7, 31.5, 31.4, 28.9, 28.5, 22.5, 14.0 ppm.

2.2.2. 2,6-Bis(3-hexylthiophen-2-yl)benzobisthiazole (**4**)

In a Schlenk tube, aldehyde **2** (1.09 g, 5.55 mmol, 2.5 eq) was dissolved in *N,N*-DMF (32 mL). 2,5-diamino-1,4-benzenedithiol dihydrochloride **3** (544 mg, 2.22 mmol, 1.0 eq) and ZnCl$_2$ (15 mg, 0.11 mmol, 0.05 eq) were added to the solution. The mixture was stirred in air at room temperature for 16 h obtaining a yellow solid that was recovered by filtration and washed twice with a mixture of petrolium ether and EtOAc (2 × 15 mL) to give product **4** with a yield of 53% (617 mg). Spectroscopic data are in agreement with those reported in literature [19]. ^{1}H NMR (400 MHz, CDCl$_3$): δ = 8.58 (s, 2H), 7.48 (d, *J* = 5.0 Hz, 2H), 7.06 (d, *J* = 5.0 Hz, 2H), 3.07 (t, *J* = 4.0 Hz, 4H), 1.81–1.69 (m, 4H), 1.30–1.54 (m, 12H), 0.80–0.95 (m, 6H) ppm. ^{13}C NMR (100 MHz, CDCl$_3$): δ = 162.1, 149.4, 146.0, 134.1, 131.1, 130.4, 129.4, 114.3, 31.6, 30.3, 30.2, 29.3, 22.6, 14.1 ppm. ESI-MS: *m/z* = 525.3 [M + H]$^+$.

2.2.3. 2,6-Bis(5-bromo-3-hexylthiophen-2-yl)benzobisthiazole (**5**)

In a round-bottom flask, compound **4** (930 mg, 1.77 mmol, 1.0 eq) was dissolved in a mixture of CHCl$_3$ and acetic acid (2:1 v/v) (40 mL). The solution was cooled at 0 °C and NBS (1.263 g, 7.09 mmol, 4.0 eq) was added. The mixture was stirred at room temperature in the dark for 72 h. Then water (30 mL) was added and the organic phase was extracted with CHCl$_3$ (2 × 30 mL). The organic phase was washed with water (20 mL) and brine (20 mL) and dried on Na$_2$SO$_4$. The solvent was evaporated and the residue recrystalized from ethyl acetate to give compound **5** as a yellow solid with a yield of 98% (1.16 g). ^{1}H NMR (400 MHz, CDCl$_3$ + 10% v/v TFA-d): δ = 8.81 (s, 2H), 7.28 (s, 2H), 3.00 (t, *J* = 7.9 Hz, 4H), 1.75–1.85 (m, 4H), 1.44–1.54 (m, 4H), 1.30–1.39 (m, 8H), 0.91 (t, *J* = 6.9 Hz, 6H) ppm. ^{13}C NMR (100 MHz, CDCl$_3$ + 10% v/v TFA-d): δ = 165.8, 155.6, 140.1, 135.7, 131.7, 127.4, 124.7, 112.6, 31.4, 31.2, 29.4, 29.1, 22.4, 13.8 ppm. ESI-MS: *m/z* = 685.3, 683.2, 681.2 (1:2:1) [M + H]$^+$.

2.2.4. Synthesis of BBT2

In a microwave tube, Pd$_2$(dba)$_3$·CHCl$_3$ (7.6 mg, 0.007 mmol, 0.05 eq) was mixed with XantPhos (17.5 mg, 0.015 mmol, 0.1 eq) under stirring for 20 min in dry toluene (3 mL). In a Schlenk tube, 9*H*-carbazole **6** (149 mg, 0.3 mmol, 2.0 eq) and ^{t}BuONa (42 mg, 0.44 mmol, 3.0 eq) were dissolved in MeOH (0.5 mL). The resulting solution was transferred in the microwave tube and compound **5** (100 mg, 0.15 mmol, 1.0 eq) was then added. The mixture was stirred for 30 min at room temperature and then heated in the MW reactor at 70 °C, for 35 min. The mixture was cooled to room temperature obtaining a yellow solid precipitate. The solid was recovered by filtration and washed with cold toluene (10 mL), water (2 × 10mL) and then dried under vacuum, giving **BBT2** as yellow amorphous solid (150 mg, yield >99%). ^{1}H NMR (400 MHz, THF-*d8*): δ = 8.62 (s, 2H), 8.16 (d, *J* = 8.0 Hz, 4H), 7.71 (d, *J* = 8.2 Hz, 4H), 7.47 (dt, *J$_1$* = 7.0, *J$_2$* = 1.2, 4H), 7.36 (s, 2H), 7.34–7.29 (m, 4H), 3.28–3.22 (m, 4H), 1.96–1.87 (m, 4H), 1.65–1.56 (m, 4H), 1.50–1.35 (m, 8H), 0.95 (t, *J* = 7.0, 6H) ppm. ^{13}C NMR (100 MHz, THF-*d8*): δ = 152.1, 145.5, 142.3, 142.2, 135.8, 129.9, 128.6, 127.4, 125.1, 122.1, 121.2, 115.9, 115.8, 111.3, 32.8, 31.5, 31.3, 30.8, 23.7, 14.6 ppm. HRMS: calculated for C$_{52}$H$_{47}$N$_4$S$_4$: 855.2683. Found: 855.2703 [M+H]$^+$.

2.2.5. Synthesis BBT3

In a microwave tube, Pd$_2$(dba)$_3$·CHCl$_3$ (4.0 mg, 0.0038 mmol, 0.05 eq) was mixed with XantPhos (4.4 mg, 0.0075 mmol, 0.1 eq) under stirring for 20 min in dry toluene (3 mL). In a Schlenk tube, boronic ester **7** (59 mg, 0.15 mmol, 2.0 eq) and KF (13 mg, 0.225 mmol, 3 eq) were dissolved in MeOH (0.5 mL). The resulting solution was transferred in the microwave tube and compound **5** (50 mg, 0.075 mmol, 1.0 eq) was then added. The mixture was stirred for 30 min at room temperature and then heated in the MW reactor at 70 °C, for 35 min. After cooling to room temperature the solvent was evaporated and the crude was purified by flash column chromatography (SiO$_2$, petroleum ether/DCM/tol 6:2:1) to give compound **BBT3** (33.4 mg, 43%) as a pale orange solid. ^{1}H NMR (400 MHz, THF-*d8*): δ = 8.58 (s, 2H), 8.14 (d, *J* = 7.8 Hz, 4H), 7.97 (d, *J* = 7.8 Hz, 4H), 7.64 (s, 2H), 7.56 (d, *J* = 8.6 Hz, 4H), 7.46–7.40 (m, 4H), 7.23 (t, *J* = 7.4 Hz, 4H), 6.83 (d, *J* = 8.6 Hz, 4H), 3.21–3.18 (m, 4H), 1.60–1.30 (m, 16H), 0.94 (t, *J* = 8.0 Hz, 6H) ppm. ^{13}C NMR (100 MHz, THF-*d8*): δ = 152.2, 147.2, 146.1, 145.1, 140.7, 139.9, 135.7, 133.1, 132.8, 132.5, 129.8, 129.3, 127.9, 125.4, 123.8, 122.9, 118.1, 115.8, 32.9, 31.4, 31.3, 30.5, 23.7, 14.6 ppm. HRMS: *m/z* calculated for C$_{64}$H$_{54}$N$_4$S$_6$: 1070.2673. Found: 1070.2672 [M·]$^+$.

2.2.6. Synthesis of BBT4

In a microwave tube, Pd$_2$(dba)$_3$·CHCl$_3$ (4.0 mg, 0.0038 mmol, 0.05 eq) was mixed with XantPhos (4.4 mg, 0.0075 mmol, 0.1 eq) under stirring for 20 min in dry toluene (3 mL). In a Schlenk tube, boronic ester **8** [60] (63 mg, 0.15 mmol, 2.0 eq) and KF (13 mg, 0.225 mmol, 3 eq) were dissolved in MeOH (0.5 mL). The resulting solution was transferred in the microwave tube and compound **5** (50 mg, 0.075 mmol, 1.0 eq)

was then added. The mixture was stirred for 30 min at room temperature and then heated in the MW reactor at 70 °C, for 35 min. After cooling to room temperature, the solvent was evaporated and the crude was purified by flash column chromatography (SiO₂, petroleum ether/DCM 3:1), to give compound **BBT4** (57.6 mg, 69%) as an orange solid. ^{1}H NMR (400 MHz, THF-*d8*): δ = 8.49 (s, 2H), 7.37 (d, *J* = 2.1 Hz, 2H), 7.34 (d, *J* = 8.8 Hz, 4H), 7.29 (s, 2H), 7.21 (d, *J₁* = 8.8 Hz, 4H), 6.98 (dd, *J₁* = 7.2 Hz, *J₂* = 2.0 Hz, 2H), 6.85–6.77 (m, 4H), 6.21 (d, *J₁* = 8.2, 2H), 6.18 (dd, *J₁* = 7.2 Hz, *J₂* = 2.0, 2H), 3.89 (s, 6H), 3.12–3.08 (m, 4H), 1.56–1.51 (m, 4H), 1.42–1.36 (m, 4H), 1.28–1.27 (m, 8H), 0.89 (t, *J* = 8.1 Hz, 6H) ppm. ^{13}C NMR (100 MHz, THF-*d8*): δ = 161.5, 160.9, 152.2, 147.1, 145.8, 145.1, 135.5, 134.0, 133.1, 128.9, 127.9, 127.4, 127.1, 125.3, 124.3, 123.5, 120.1, 117.1, 116.9, 116.8, 56.0, 32.8, 32.7, 31.3, 30.6, 23.7, 14.6 ppm. (Some quaternary carbon signal missing due to low solubility). HRMS: *m/z* calculated for C₆₆H₅₉N₄O₂S₆: 1131.2962. Found: 1131.2989 [M+H][+].

2.3. Transient absorption spectroscopy

Ultrafast transient absorption spectra of all samples have been measured on a system consisting of a home-built Ti:sapphire laser oscillator and regenerative amplifier system (Amplitude Pulsar) which produced 80 fs pulses at 810 nm with an average output power of 450–500 mW. Excitation pulses at 400 nm were obtained by the second harmonic generation of the fundamental laser output in a 2 mm thick BBO crystal. For all measurements, the pump beam polarization was set at the magic angle with respect to the probe beam by rotating a λ/2 plate to exclude rotational contributions to the transient signal [29,30].

The excitation powers were on the order of 50–100 nJ. The probe pulses were generated by focusing a portion of the 800 nm radiation beam on a 3 mm thick CaF₂ window. The time delay between pump and probe pulses was introduced by sending the portion of 800 nm light used for probe generation through a motorised stage. After passing through the sample, the white light probe was sent to a flat field monochromator coupled to a home-made CCD detector. For samples in solution measurements were performed in a quartz cell (2 mm thick) mounted on a movable stage in order to refresh the solution and avoid undesired photochemical degradation of the sample. In the case of samples dispersed in PMMA, the polymeric films were directly mounted on the same motorised stage used for liquid samples.

Analysis of the transient data was performed applying Singular Value Decomposition (SVD) [31] and global analysis [32], using the software GLOTARAN [33]. Global analysis allows the simultaneous fit at all the measured wavelengths with a combination of exponential decay functions and retrieves the kinetic constants describing the dynamic evolution of the system and the corresponding spectral component, called Evolution Associated Difference Spectra (EADS). A linear decay kinetic scheme was employed for data analysis.

2.4. Computational details

Molecular and electronic properties of compounds **BBT2**, **BBT3** and **BBT4** have been computed *via* DFT [34–36] and time-dependent DFT (TD-DFT) [37,38] methods, using Gaussian 09, Revision C.01 suite of programs[39]. The S₀ optimised geometries of compounds **BBT2-4** were obtained at B3LYP [40,41]/6-31G* level of theory in vacuum, as well as the ground-state electron density delocalisation and the energy of FMOs in solvent (toluene), while the S₁ optimised geometries were computed at TD-CAM-B3LYP [42]/6-31G* level of theory. The UV–Vis spectroscopic properties of the analysed compounds, including absorption (λ_{max}^{abs}) and emission maxima (λ_{max}^{emi}), vertical excitation (E$_{exc}$) and emission (E$_{emi}$) energies, oscillator strengths (*f*) and composition (%) in terms of molecular orbitals for the lowest singlet-singlet excitations and the singlet-singlet emissions, S₀→S₁ and S₁→S₀ respectively, in toluene and PMMA, have been computed on the minimised structures at

TD-MPW1K [43]/6-311 + G(2d,p) level of theory. Solvent effects have been included by using the polarisable continuum model (PCM) and, in the case of the emission maxima, using the Linear-Response implementation (LR-PCM)[44].

2.5. LSC preparation

Polymer thin films containing the selected fluorophore were prepared by pouring 1.5 mL of toluene (Sigma-Aldrich, HPLC Plus, for HPLC, GC, and residue analysis, ≥99.9%) solution containing about 60 mg of the polymer and different concentrations (0.2–1.8 wt%) of the fluorophore on a 50 × 50 × 3 mm optically pure glass substrate (Edmund Optics Ltd BOROFLOAT window 50 × 50 TS). The amount of fluorophore was taken from a mother solution at a concentration of 1.5 mg/mL. The glass slides were cleaned with chloroform and immersed in 6 M HCl for at least 12 h and then dried according to previously reported procedures [24,25,28,46–48]. Fluorophore-doped polymer thin films with a thickness of 25 ± 5 μm (Starrett micrometer) were obtained after complete evaporation of toluene at room temperature under a saturated atmosphere of chloroform (Sigma Aldrich, ACS reagent, ≥99.8%). For absorption and emission spectroscopic characterisation, the polymer films were carefully detached from the glass surface by immersing the LSC in water and then stored in a desiccator.

3. Results and discussion

We designed three new luminophores characterised by the same BBT heterocyclic core employed in the past [19], but symmetrically decorated with 9*H*-carbazole (**BBT2**), 10-phenyl-10*H*-phenothiazine (**BBT3**) and 10-(4-methoxyphenyl)-10*H*-phenothiazine (**BBT4**) as donors (Fig. 2).

In particular, the different electron-donor groups were introduced to shift the maximum absorption peaks by affecting the HOMO energy levels, aiming to obtain three materials with different colours. Besides, the more rigid donor groups compared to the triphenylamine present in **BBT1** were expected to decrease the energy dissipation through internal conversion and vibrational motions[49], which should result in a higher fluorescence quantum yield. Finally, alkyl chains were introduced to increase the solubility and possibly favour the fluorophore miscibility into the polymer matrices.

3.1. Computational investigation

A computational investigation based on Density Functional Theory (DFT) and time-dependent DFT (TD-DFT) methods was carried out to rationalise the structural, electronic and photophysical properties of compounds **BBT2-4**.

The ground (S₀) and excited states (S₁) optimised geometries of **BBT2-4** are shown in Fig. 3. S₀ geometries of all the luminophores present a planar central scaffold consisting of the BBT core and thiophene rings (dihedral angles ≤ 1°), while a pronounced torsion is found between the donor groups and the thiophene rings (dihedral angles between 24° and 57°). On the other hand, calculated geometries for S₁ have smaller torsional angles, thus increasing the overall planarity of the molecules (Fig. 3).

TD-MPW1K/6-311 + G(2d,p) absorption (λ_{max}^{abs}) and emission (λ_{max}^{emi}) maxima, vertical excitation (E$_{exc}$) and emission (E$_{emi}$) energies, oscillator strengths (*f*) and composition (%) in terms of molecular orbitals for the lowest singlet-singlet excitations (S₀→S₁) and the singlet-singlet emissions (S₁→S₀) in toluene and PMMA of compounds **BBT2**, **BBT3** and **BBT4** are shown in Table 1 and Table 2 respectively. The three fluorophores show absorption maxima between 404 and 441 nm (corresponding to 3.06–2.81 eV), both in toluene and PMMA.

Looking at the DFT orbitals (see Figure S1 and S2, Supporting Information) and, in particular at the frontier molecular orbitals involved
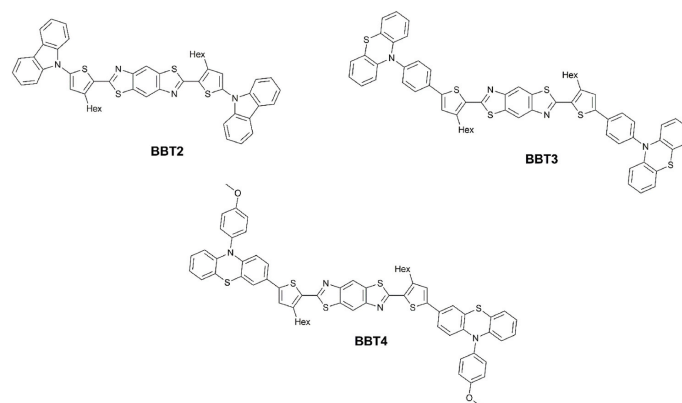
Fig. 2. *Structures of the new fluorophores* **BBT2**, **BBT3** *and* **BBT4**.
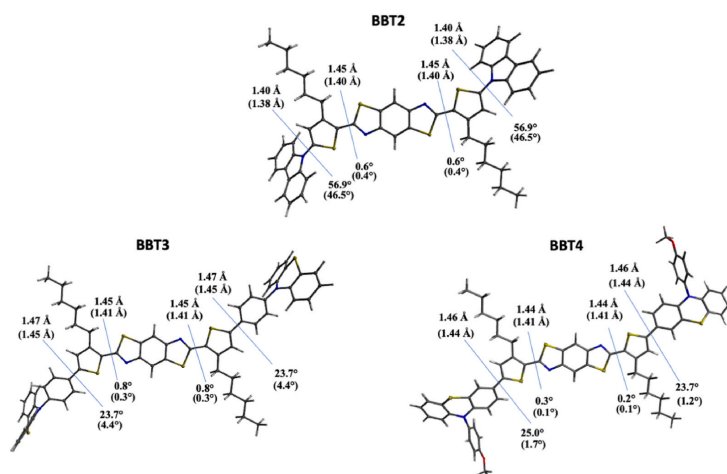
Fig. 3. Bond lengths (Å) and dihedral angles (degrees) of S_0 and S_1 (in brackets) optimised geometries of **BBT2, BBT3 and BBT4**.

Table 1

TD-DFT (MPW1K/6-311+G(2d,p)) absorption maxima (λ_{max}^{abs} in nm), excitation energies (E_{exc} in eV), oscillator strengths (f) and contributions (%) to the $S_0 \to S_1$ transition in toluene and in PMMA for **BBT2, BBT3** and **BBT4** compounds.

Cmpd.	Medium	λ_{max}^{abs} [nm]	E_{exc}	f	Transition (%)
BBT2	toluene	404	3.06	2.20	87 (H→L)
	PMMA	404	3.06	2.20	87 (H→L)
BBT3	toluene	419	2.95	2.78	89 (H-2→L)
	PMMA	419	2.96	2.78	89 (H-2→L)
BBT4	toluene	440	2.81	3.02	79 (H→L)
	PMMA	441	2.81	3.02	78 (H→L)

Table 2

TDDFT (MPW1K/6-311+G(2d,p)) emission maxima (λ_{max}^{emi} in nm), emission energies (E_{emi} in eV), oscillator strengths (f) and contributions (%) to the transition $S_1 \to S_0$ in toluene and in PMMA for **BBT2, BBT3** and **BBT4** compounds.

Cmpd.	Medium	λ_{max}^{emi} [nm]	E_{exc}	f	Transition L→H (%)
BBT2	toluene	477	2.59	2.40	92
	PMMA	477	2.60	2.40	93
BBT3	toluene	504	2.46	2.82	93
	PMMA	504	2.45	2.82	93
BBT4	toluene	521	2.38	3.18	88
	PMMA	523	2.37	3.18	88

in the lowest energy transition (HOMO and LUMO for **BBT2** and **BBT4**, HOMO-2 and LUMO for **BBT3**), it is evident that the $S_0 \to S_1$ excitation is characterised by an intramolecular charge transfer from the donor to the

acceptor group.

BBT2 shows the most blue-shifted computed absorption maximum

due to the lower donor character of the carbazole group compared to the phenothiazine group, and its lower conjugation in comparison with **BBT3-4**. Indeed, a wider angle of approx. 57° between the carbazole group and the thiophene ring is computed. Thanks to the introduction of an additional phenyl ring between the thiophene ring and the phenothiazine donor group, which increases its conjugation (angle of approx. 24°), **BBT3** λ_{max}^{abs} is predicted to be red-shifted by 15 nm in comparison to **BBT2**. Finally, **BBT4** shows the most red-shifted absorption maximum, due to the higher donor strenght of the methoxyphenylphenothiazine (Fig. 3).

The LR-PCM computed emission maxima (Table 2) fall in the 477–523 nm range, almost coincident both in toluene and PMMA. The computed Stokes shifts (0.47, 0.49 and 0.44 eV for **BBT2**, **BBT3** and **BBT4**, respectively) look very promising for a potential successful implementation of **BBT2**, **BBT3** and **BBT4** in the LSC field.

3.2. Synthesis of compounds BBT2-4

The preparation of the three dyes was carried out by applying an easy and flexible synthetic approach, essential to reduce the number and complexity of synthetic operations. To this end, the previously reported synthesis [19] of **BBT1** was modified to increase the yields and simplify the purification steps, keeping 2,6-bis(3-hexylthiophen-2-yl)benzo[1,2-*d*:4,5-*d'*]bis(thiazole) (**4**) as the common intermediate for the synthesis of the new fluorophores **BBT2-4**. The new synthetic strategy (Scheme 1) started with the quantitative conversion of commercial bromide **1** into the corresponding aldehyde **2**, using a modified Grignard procedure [50].

Aldehyde **2** was then reacted with commercially available 2,5-diaminobenzene-1,4-dithiol *bis*-hydrochloride (**3**) to obtain the BBT tricycle **4**. Following a previously reported procedure [19] the reaction was performed using *N,N*-DMF as solvent under air, at room temperature, and in the presence of ZnCl₂ as a Lewis acid, smoothly giving product **4** in 53% yield after crystallisation. Then, dibromo-intermediate **5** was obtained through electrophilic bromination of **4**, using a large excess of *N*-bromosuccinimide (NBS). The reaction was complete after three days at room temperature. The desired compound precipitated from the reaction mixture and was quantitatively recovered by simple filtration,

avoiding complex chromatographic purification and recrystallisation. Finally, dibromide **5** was reacted with carbazole **6**, using Buchwald-Hartwig conditions, with XantPhos as ligand and *t*BuONa as base, thus obtaining **BBT2** in almost quantitative yield. Otherwise, compounds **BBT3** and **BBT4** were prepared by performing a Suzuki-Miyaura cross-coupling using boronic esters **7** or **8**, respectively, SPhos as the ligand and KF as the base. A lab-scale microwave activation protocol was developed and applied to all cross-coupling reactions, resulting in a significant reduction of the reaction times, if compared to thermal heating, and in a limitation of side-products, with consequent simplification of the following chromatographic purifications. For all coupling reactions, toluene/MeOH (6/1) was the best solvents mixture to ensure a proper dissolution of the starting materials and to absorb microwaves efficiently; Pd₂(dba)₃ was used as catalyst precursor.

The thermal stability of the dyes was assessed through a thermogravimetric analysis which showed a maintenance of 90–94% of the sample weight up to 200 °C and 87–89% up to 300 °C. **BBT2** shows slightly faster weight loss than **BBT3-4** (Figure S8).

3.3. Spectroscopic characterisation in solution

The optical properties of **BBT2-4** were studied in solution by UV–Vis absorption and fluorescence emission spectroscopies. The solvent used was toluene because it could effectively dissolve all compounds and its refractive index (1.496) is similar to that of PMMA (1.491). Relevant data are presented in Table 3 and Fig. 4.

The experimental absorption maxima for **BBT2-4** (Fig. 4a) are in

Table 3

Spectroscopic properties of compounds BBT2, BBT3 and BBT4 in toluene solution.

Cmpd.	λ_{abs} [nm]	ε [M⁻¹ cm⁻¹]	λ_{emi} [nm (eV)]	SS [nm (eV)]	Φ_f	$E_{0,0}$ [eV]
BBT2	409	33700	463 (0.13)[a]	54 (0.35)	18%	2.78
BBT3	420	7800	491 (0.16)[a]	71 (0.43)	18%	2.67
BBT4	456	18600	527	71 (0.37)	73%	2.45

[a] In parenthesis the interval between the two vibronic peaks in the emission spectra (in eV).
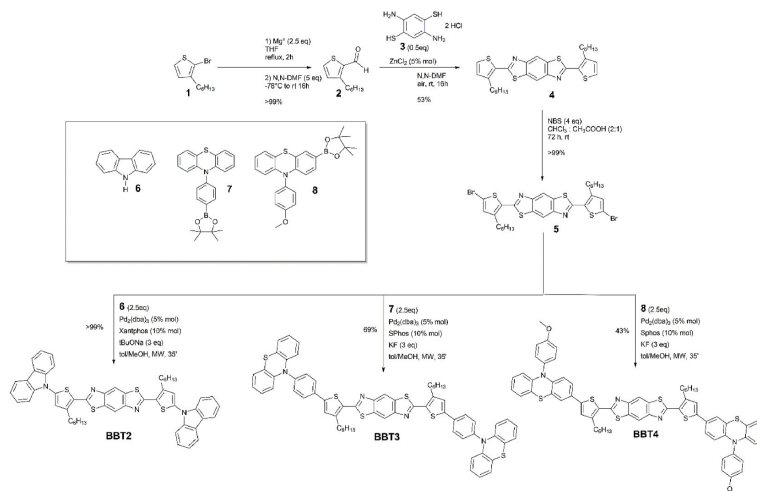
Scheme 1. *Synthesis of BBT derivatives.*

6
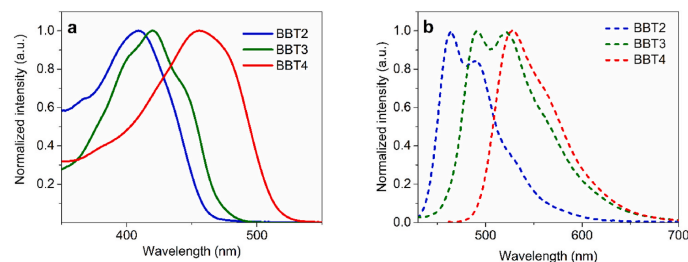
Fig. 4. (a) *BBT2*, *BBT3* and *BBT4* absorbance in toluene (0.01 mM); (b) *BBT2*, *BBT3* and *BBT4* emission in toluene (0.01 mM) respectively at 409, 420 and 456 nm excitation wavelength.

good agreement with the computed values (see Table 1), with differences of ca. 0.1 eV. Moreover, the computational analysis reproduced the red-shift of the lowest energy transition going from **BBT2** to **BBT4**. By changing the concentration, the ratio between the absorbance value taken at two different wavelengths (**BBT2**: 409 nm and 390 nm; **BBT3**: 400 nm and 420 nm; **BBT4**: 456 nm and 400 nm) remained constant for all tested molecules, showing that aggregation phenomena in solution were negligible (Figure S3).

All molecules had intense emissions between 400 and 650 nm. Computations also estimated the vertical $S_1 \rightarrow S_0$ emission energies with a high level of accuracy, with an energy difference of less than 0.1 eV, as well as the Stokes shifts (Table 2). **BBT2** and **BBT3** had similar emission spectra (Fig. 4b), showing a marked vibronic progression on their emission band. The shape of the emission spectrum remained unchanged regardless of the concentration, ruling out any aggregation effect for concentrations up to 0.01 mM (Figure S4). The presence of the vibronic structure indicates the occurrence of an important structural rearrangement upon excitation [49]. Unfortunately, this phenomenon led to a decrease in the fluorescence quantum yield (Φ_f), which was therefore relatively low for **BBT2** and **BBT3** ($\Phi_f = 0.18$). However, both molecules displayed a large Stokes shift (Table 3), thus meaning a poor overlap between the absorption and emission spectra and a modest self-absorption, that is a very important feature for the possible use in LSC [20].

In case of **BBT4** the vibronic structure of the fluorescence band, peaked at 527 nm in toluene, is less evident, and only a weak shoulder at lower energy is visible. Remarkably, a large Stokes shift of 71 nm (0.37 eV) was found. The fluorescence quantum yield was 0.73, therefore much higher than **BBT2** and **BBT3**. This increase in fluorescence quantum yield might be due to a greater conjugation between the donor and acceptor groups and to a decreased rotational freedom of their connecting bond, resulting in a smaller structural rearrangement of the excited molecule. The reduced vibrational structure of the emission band confirmed this hypothesis.

3.4. Spectroscopic characterisation in polymeric films

Given the promising spectroscopic properties of **BBT2-4** compounds in solution, in particular Stokes shifts and Φ_f, the behaviour of the new molecules was also investigated within polymer matrices. Experiments were performed in poly(methyl methacrylate) (PMMA), which is the most used polymer matrix for LSC devices. The fluorophores were dispersed in PMMA at different concentrations (from 0.2 to 1.8% by weight) obtaining films with a 25 μm ± 5 thickness. The films were light yellow for **BBT2**, yellow-green for **BBT3** and orange-yellow for **BBT4** (Figure S6). They are transparent and homogeneous for samples containing **BBT3** and **BBT4** in all the investigated range of concentration (Fig. 5).
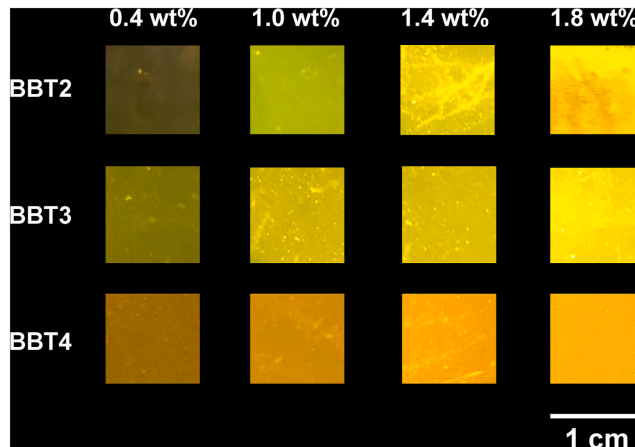

Fig. 5. *PMMA film doped with BBT2-4 at different concentration under the illumination of a Dark Reader Transilluminator at 450 nm.*

Conversely, **BBT2** appeared incompatible with PMMA at concentrations higher than 1.4 wt% with phase separation clearly visible at the macroscopic level (Fig. 5) and confirmed by optical microscope analysis (Fig. 6). Notably, PMMA films doped with **BBT2** displayed the formation of microscopic fluorophore aggregates, appearing mostly phase-separated from the PMMA matrix. Instead, **BBT3** and **BBT4** resulted quite compatible with PMMA also at the highest fluorophore content of 1.8 wt%, with no clear evidence of microscale phase separation.

The absorbance of **BBT2**/PMMA linearly increased with the concentration for values up to 1.0 wt%. Beyond this concentration value, a drastic reduction in absorption occurred due to the formation of aggregates and phase separation. Other experimental data demonstrated the formation of **BBT2** aggregates in the polymer phase, that is (*i*) the progressive red-shift of both the absorption and emission maxima (Fig. 7) with modification of the spectra in films at 1.4 wt% and 1.8 wt% contents and (*ii*) the decrease of the Φ_f with **BBT2** concentration, a phenomenon associated with the ACQ (Aggregation-Caused Quenching) behaviour of the fluorophore [51].

BBT3 and **BBT4** showed better compatibility with PMMA and the absorbance intensity of the derived films regularly increased with fluorophores concentration, keeping the maximum position almost unchanged (Fig. 7). For all molecules, the vibronic structure is no longer visible in the emission spectrum in PMMA, whose maximum overlaps with the lowest energy vibronic peak of the emission spectrum in solution. This can be attributed to the limited rotational freedom experienced by the fluorophores within the solid matrix and to the higher polarity of the latter compared to toluene, favouring less planar conformations with greater charge separation character[51–53], thus provoking larger Stokes shift in comparison to the toluene solution.

For all molecules, the fluorescence quantum yield decreased with increasing concentration, due to the rising self-absorption caused by a partial overlap between the absorption and emission spectrum [28,54]. Notably, while Φ_f values of about 10–15% showed by **BBT2** in PMMA were considered too low for practical applications in LSC, for all concentrations **BBT3** showed consistently higher values than that recorded in solution, in the range of 29–33%, due to the above-mentioned confinement effect.

Two alternative polymeric matrices, poly(cyclohexyl methacrylate) (PCMA) and poly(benzyl methacrylate) (PBzMA) were also investigated, to evaluate the effect of the less polar lateral substituent (*i.e.*, benzyl and cyclohexyl, compared to the traditional methyl ester group in PMMA) on the optical features of the derived films. PBzMA and PCMA are 100% amorphous, transparent and commercially available, features that make them suitable for LSC application. **BBT2** and **BBT3** presented poor compatibility with the new matrices, showing marked segregation of the fluorophore and formation of macroscopic aggregates (Figure S7). On the contrary, **BBT4** was well dispersible within the new matrices

(Fig. 8), even at the highest concentration of 1.8 wt%, thus providing well homogeneous films. For the three concentrations examined (1.0 wt %, 1.4 wt% and 1.8 wt%) in the two new matrices, the maximum absorption wavelength remained constant and similar to PMMA (around 450–460 nm, Fig. 9). The emission peak changed its shape as concentration increases, possibly because of the formation of intermolecular interactions among fluorophore molecules.

The broadening of the emission band observed at higher concentrations could be possibly attributed to the formation of small size aggregates that, however, did not adversely affect the phase dispersion into the polymer. Moreover, the Stokes shifts of **BBT4** remained high in PBzMA and PCMA films, with values of about 0.50 eV.

The quantum yield rose to 52.6% for **BBT4**/PBzMA (1.0 wt%) and 65.6% for **BBT4**/PCMA (1.4 wt%) in comparison with 41.5% previously registered for **BBT4**/PMMA (1.0 wt%). Such an increase can be attributed to the greater hydrophobicity of PBzMA and PCMA matrices compared to PMMA, possibly inducing a smaller stabilisation of the charge separation state of the excited fluorophore, in turn reducing the weight of non-radiative recombination channels [55].

3.5. Transient absorption spectroscopy

To further characterise the excited states of **BBT2-4** chromophores and investigate the dynamics of relaxation after light absorption, femtosecond transient absorption spectra have been recorded both in solution and PMMA matrix. The samples were excited at 400 nm, at the blue edge of absorption of the BBT core, and their transient spectra were recorded in the 0.1 ps-1.5 ns time interval.

The results were analysed by simultaneously fitting all the kinetic traces with a combination of exponential functions (global analysis), and using a kinetic scheme based on a sequential decay. Beside kinetic constants, global analysis also retrieves the correspondent spectral components, indicated as Evolution Associated Difference Spectra (EADS). The transient absorption spectra of **BBT2** and **BBT4** recorded in toluene are reported in Fig. 10a and b, with the correspondent EADS obtained from global analysis (Fig. 10c and d).

The transient spectra of **BBT2** present a negative band peaked at about 500 nm, in the wavelength interval where fluorescence is observed, thus associated to the stimulated emission of the sample, and a broad positive band spanning from about 570 nm to >750 nm, assigned as an excited state absorption (ESA). The transient spectra of **BBT4** are qualitatively similar, but being the absorption profile of this sample red shifted in comparison to **BBT2**, a ground state bleaching band is also visible, peaking at about 500 nm. Analysis of the EADS reported in panels c and d of Fig. 10 allows to follow the spectral changes associated to the excited state decay of the samples and the correspondent time-scale. The initial spectral component (black line, Fig. 11c and d)
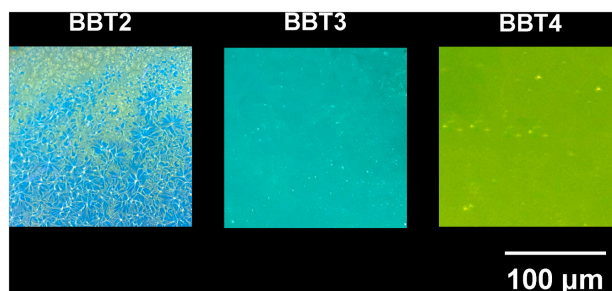

Fig. 6. *Optical microscopy images of PMMA film doped with **BBT2**, **BBT3** and **BBT4** at the concentration of 1.8 wt% under the illumination with a long-range UV lamp at 366 nm.*

Fig. 8. *Optical microscopy images of* **BBT4**/*PBzMA film (left) and* **BBT4**/*PCMA film (right) at a concentration of 1.8 wt% under the illumination with a long-range UV lamp at 366 nm.*

represents the transient spectrum of the Franck-Condon state, reached immediately after excitation. In <1 ps an evolution is observed, most probably associated to a fast electronic relaxation of the system. In case of **BBT2** the relaxation is spectrally manifested with an intensity

increase and red shift of the stimulated emission signal, while for **BBT4** we observe a partial recovery of the sharp bleaching band and a broadening and red shift of the stimulated emission (evolution from black to red line). On the following timescale (7.6 ps for **BBT2**, 5.6 ps for **BBT4**) the stimulated emission band becomes more structured. This is particularly evident for **BBT2**, where a double peak structure with maxima at about 495 nm and 535 nm appears. This evolution is most probably associated with a structural relaxation occurring in the excited state because of solvent rearrangement and, as suggested from the computed geometrical changes between ground and excited state, mostly involves a planarization of the molecule due to the rotation of the donor groups. The signal intensity then mostly decays on the following 415 ps timescale for **BBT2** (772 ps for **BBT4**) leaving a small residual component, whose lifetime is longer than the maximum pump-probe delay accessed within our measurement (1.5 ns). It is worth noticing that the evolution of the ESA band in both samples is quite limited, suggesting that the electronic distribution in the excited state does not significantly change in the investigated time interval, and no intermediate dark states are involved in the relaxation of the systems towards the ground state. Excitation at 400 nm thus brings the molecules in their S$_1$ state, which is a charge transfer state because of the D-A-D structure

Fig. 9. *(a) UV–Vis absorption spectra of **BBT4**/PBzMA films as a function of fluorophore concentration (wt.%); (b) fluorescence spectra of the same **BBT4**/PBzMA films with an excitation wavelength of 456 nm (Φ_f values are reported in parentheses); (c) UV–Vis absorption spectra of **BBT4**/PCM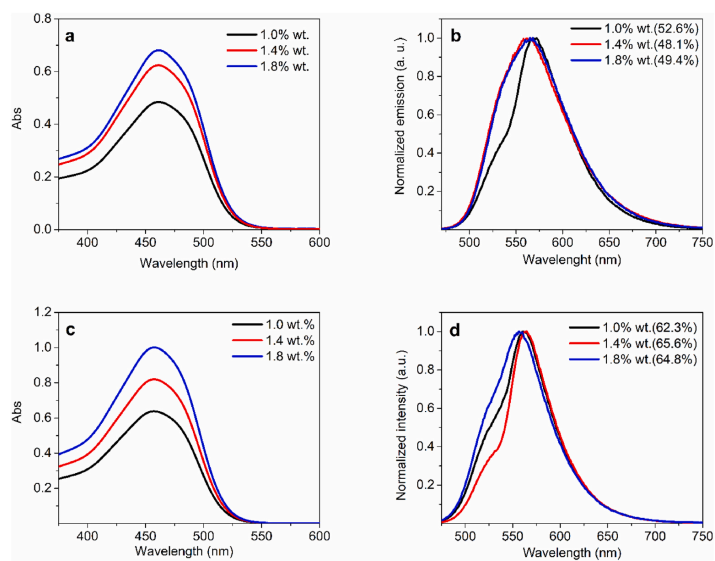A films as a function of fluorophore concentration (wt.%); (d) fluorescence spectra of the same **BBT4**/PCMA films with an excitation wavelength of 456 nm (Φ_f values are reported in parentheses).*
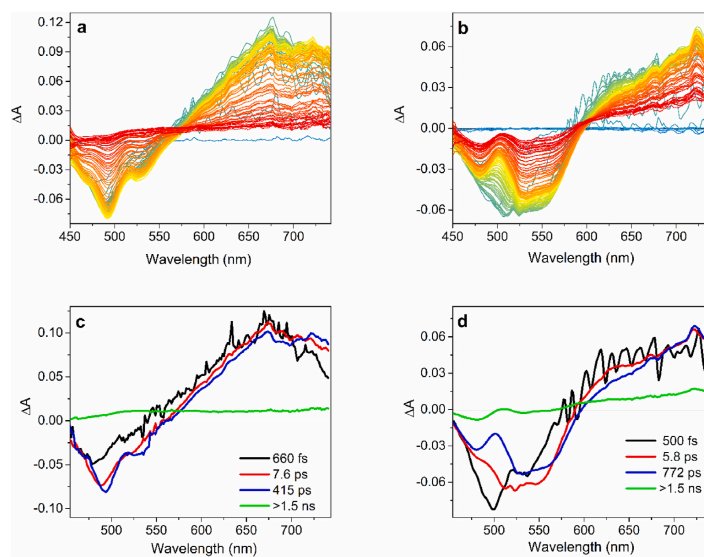
Fig. 10. *Transient absorption spectra recorded for a) **BBT2** and b) **BBT4** in toluene with excitation at 400 nm. Panels c) and d) reports the corresponding Evolution Associated Difference Spectra and lifetimes obtained from Global Analysis of the transient data.*
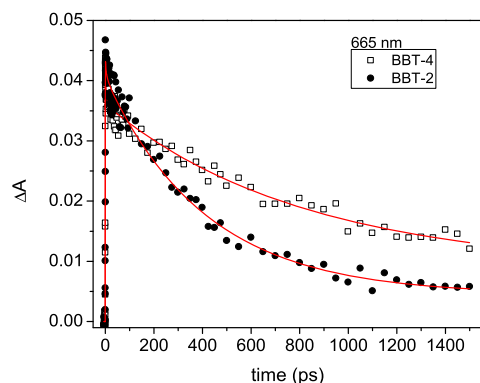
Fig. 11. *Comparison between the kinetic traces at 665 nm (ESA band) of **BBT2** (closed symbols) and **BBT4** (open symbols) in toluene. Continuous lines represent the fit obtained from global analysis.*

of the samples, and the large Stokes shift observed (see also the DFT orbitals in Figure S2), from which they decay directly to the ground state.

The comparison of the kinetic traces registered for the two samples on the ESA band, at 665 nm (Fig. 11) shows that **BBT2** decays faster than **BBT4**, also presenting a minor residual signal on the long timescale. This result agrees with the lower measured fluorescence quantum yield of **BBT2** compared to **BBT4**.

To complete the excited state characterisation of the samples, transient spectra were also measured for the dyes dispersed in PMMA films. For all samples, the transient spectra recorded in PMMA are qualitatively similar to those recorded in solution. As visible in Fig. 12a, reporting the EADS obtained from global analysis of the transient data measured for a 1.0 wt% dispersion of **BBT4** in PMMA (spectra and EADS of the other samples are reported in SI), a negative bleaching/stimulated emission signal and a broad ESA band are also observed in this case. The negative band however appears less structured and presents a less extended band shape evolution in time if compared to the solution. This is readily explained through the prevention of vibrational and structural relaxation in the polymer matrix. The comparison of the kinetic traces measured at 665 nm for **BBT4** in toluene and PMMA, reported in Fig. 12b, shows that the signal recovery is faster in the matrix and that the residual observed on the long timescale has lower intensity. This observation points to an increased radiationless relaxation in PMMA compared to the solution, which agrees with the decreased fluorescence QY measured for a 1.0 wt% dispersion of **BBT4** in PMMA compared to

toluene. This could be due to the possibility that the geometry adopted by this compound in the matrix is more twisted compared to the solution, stabilising charge separation and lowering the energy gap between the excited and ground state, which in turn would decrease the excited state lifetime and decrease the fluorescence quantum yield.

3.6. Optical efficiencies

The performances of the fluorophore/polymer films as LSC were determined according to the procedure reported in the experimental part. Notably, the power generated by the photovoltaic cell was measured when directly exposed to the lighting of the AM1.5 solar simulator (P_{SC}) and when combined with the LSC (P_{LSC}). The P_{LSC}/P_{SC} ratio is the concentration factor (C), linked to the optical efficiency (η_{opt}) through the LSC geometric factor (G), which is the ratio between the area exposed to the light source and the collecting area (i.e., 16.6 in our case, see equation (1), Experimental Section). The results obtained with the derived **BBTs** were compared with those collected from the reference dye Lumogen Red 305 (**LR305**, Table 4) under the same conditions. Notably, it appears quite evident how the optical efficiency of the different fluorophore/polymer matrix is connected to the respective fluorescence quantum yield (Fig. 13). Nevertheless, Φ_f is not the only parameter that affects optical efficiency. The large Stokes shift showed by **BBT2-4** contributed in limiting the losses in efficiency, despite the poor compatibility with the polymeric matrix and the low fluorescence quantum yield. Indeed, **BBT2**/PMMA showed optical efficiencies of 5–6%, whereas, notwithstanding its $\Phi_f > 90\%$, **LR305** in PMMA did not exceed optical efficiencies of 10%, due to an evident overlap between the absorption and emission spectrum[56].

The combination of large Stokes shift and Φ_f values around 30% increased the optical efficiency of PMMA films containing **BBT3** and **BBT4** fluorophore up to about 6 and 7%, respectively (Fig. 13). The observed different performances of these two fluorophores can be possibly ascribed to the evident red-shift of about 50 nm of both the maximum absorption and emission of **BBT4** in PMMA (Fig. 7). In fact,

Table 4
Best optical efficiency (η_{opt}) and concentration factor (C) obtained for fluorophore/polymer **BBTs** series in comparison with **LR305**.

Fluorophore	Polymer	Concentration (wt%)	η_{opt} (%)[a]	C[a]
BBT2	PMMA	1.0	5.8	0.97
BBT3	PMMA	1.0	6.5	1.08
BBT4	PMMA	1.4	7.5	1.25
BBT4	PBzMA	1.0	8.5	1.42
BBT4	PCMA	1.4	9.0	1.50
LR305	PMMA	1.4	10.1	1.68
LR305	PCMA	1.0	9.1	1.52

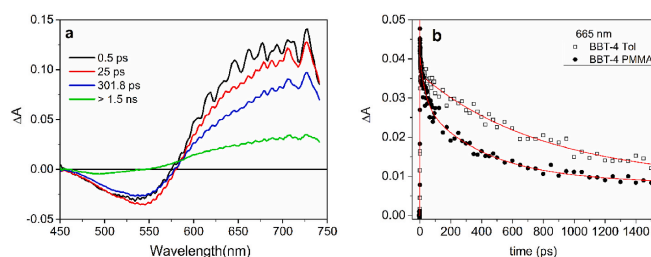[a] η_{opt} and C data were characterised by standard deviations of 0.5 and 0.1, respectively.

Fig. 12. a) Evolution Associated Difference Spectra obtained from global analysis of the transient absorption data measured for **BBT4**/PMMA upon excitation at 400 nm; b) Comparison between the kinetic traces at 665 nm (ESA band) of **BBT4** in toluene (open symbols) and PMMA film 1 wt% (closed symbols) with fit (red lines).
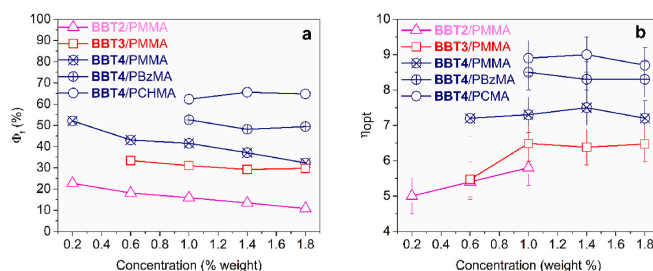
11

134

Fig. 13. *(a) Φ_f values (%) and (b) optical efficiencies (η_{opt}) of the fluorophores tested in films at different concentration.*

while approaching the zone of maximum intensity of the solar spectrum in absorption provides better solar harvesting features, shifting the emission towards the best operation window of the silicon-based cell increases the efficiency of the light-current process, that in turn boosts the LSC overall performances.[23].

In the case of **BBT4**, the use of alternative polymer matrices promoted a considerable increase in fluorescence quantum yield (Fig. 9) and greater optical efficiencies were measured both in PBzMA (8.5% at 1 wt% concentration) and in PCMA (9.0% at 1.4% concentration). Remarkably, for these types of fluorophores, the decrease in the polarity of the matrix favored not only a better dispersion of the fluorophore but also increased the relaxation of the excited state through radiative channels. The optimal concentrations of the fluorophore were found to be 1.0 and 1.4 wt%, respectively, while beyond these values no increase in efficiencies was recorded. The values obtained were very close to those measured with the **LR305** reference fluorophore that did not apparently benefit from the PCMA matrix in the range of concentration investigated. The importance of the LSC devices based on the **BBT3-4** fluorophores resulted even more evident when considering the concentration factor C that for practical applications must be higher than 1. To our knowledge, there are a few examples of small area devices (25 cm^2 or less) based on organic emitters that reported C factor greater than 1 [57] and only two greater than 1.50 [58,59], i.e. the maximum value gathered in this work for the **BTT4**/PCMA system.

4. Conclusions

In summary, we obtained a series of three new **BBT**-based fluorescent molecules with a very straightforward synthesis and with good yields that are essential to promote their use in the LSC technology. The absorption wavelength was tuned adequately by changing the donor moiety bound to the **BBT** acceptor core. All the three molecules showed an intense emission spectrum between 460 and 550 nm, overlapping the light-absorption spectrum of a Si-based photovoltaic cell, and down-converting the blue part of the solar spectrum where the efficiency of Si-cells is usually low. Furthermore, Stokes shifts were large enough to minimise the self-absorption effects of the fluorophores.

Computational analysis showed that the major transition involves a charge separation process that causes a planarization of the molecule in the excited state. **BBT2** and **BBT3** behave very similarly and exhibit a relatively low fluorescence quantum yield, which can be ascribed to non-radiative relaxation phenomena. Φ_f values up to 73% were recorded for **BBT4** in toluene and with an emission depending on the environment polarity. The TAS studies, showed that the excited state absorption of **BBT4** decayed more rapidly in PMMA than in toluene, and it was characterised by a lower residual intensity. This phenomenon appeared mitigated by the dispersion in less polar matrices such as PBzMA and PCMA, in agreement with an increase of Φ_f.

The LSC devices built with BBT dyes were characterised by good

transparency and different colours ranging from light yellow to orange. **BBT2** and **BBT3** showed relatively low Φ_f in PMMA (approx. 16% and 31%, respectively), and optical efficiencies of 5.8% and 6.5%, respectively, that were favourably affected by the large Stokes shift that, in turn, limited the efficiency losses within the waveguide. Notably, **BBT4** gave LSCs C factor >1 for all polymeric matrices and with maximum optical efficiencies of 9.0% in the less polar PCMA matrix, in agreement with the computational and TAS investigations. This performance is very similar to the best data obtained by **LR305** in PMMA. Nevertheless, the larger Stokes shifts and the consequent lower self-absorption than **LR305** suggest that the **BBT**-series fluorophores could possibly attain better optical efficiencies in large surface area LSC devices.

Declaration of competing interest

The authors declare that they have no known competing financial interests or personal relationships that could have appeared to influence the work reported in this paper.

Appendix A. Supplementary data

Supplementary data to this article can be found online at https://doi.org/10.1016/j.dyepig.2021.109207.

References

[1] Lee TD, Ebong AU. A review of thin film solar cell technologies and challenges. Renew Sustain Energy Rev 2017;70:1286–97. https://doi.org/10.1016/j.rser.2016.12.028.

[2] Le Donne A, Scaccabarozzi A, Tombolato S, Marchionna S, Garattini P, Vodopivec B, et al. State of the art and Perspectives of inorganic photovoltaics. ISRN Renew Energy 2013;2013:1–8. https://doi.org/10.1155/2013/830731.

[3] Gong J, Sumathy K, Qiao Q, Zhou Z. Review on dye-sensitized solar cells (DSSCs): Advanced techniques and research trends. Renew Sustain Energy Rev 2017;68: 234–46. https://doi.org/10.1016/j.rser.2016.09.097.

[4] Hagfeldt A, Boschloo G, Sun L, Kloo L, Pettersson H. Dye-sensitized solar cells. Chem Rev 2010;110:6595–663. https://doi.org/10.1021/cr900356p.

[5] Roy P, Kumar Sinha N, Tiwari S, Khare A. A review on perovskite solar cells: evolution of architecture, fabrication techniques, commercialization issues and status. Sol Energy 2020;198:665–88. https://doi.org/10.1016/j.solener.2020.01.080.

[6] Correa-Baena JP, Abate A, Saliba M, Tress W, Jesper Jacobsson T, Grätzel M, et al. The rapid evolution of highly efficient perovskite solar cells. Energy Environ Sci 2017;10:710–27. https://doi.org/10.1039/c6ee03397k.

[7] Weber WH, Lambe J. Luminescent greenhouse collector for solar radiation. Appl Optic 1976;15:2299. https://doi.org/10.1364/ao.15.002299.

12

[8] Batchelder JS, Zewai AH, Cole T. Luminescent solar concentrators 1: theory of operation and techniques for performance evaluation. Appl Optic 1979;18:3090. https://doi.org/10.1364/AO.18.003090.

[9] Meinardi F, Colombo A, Velizhanin KA, Simonutti R, Lorenzon M, Beverina L, et al. Large-area luminescent solar concentrators based on 'Stokes-shift-engineered' nanocrystals in a mass-polymerized PMMA matrix. Nat Photon 2014;8:392–9. https://doi.org/10.1038/nphoton.2014.54.

[10] Coropceanu I, Bawendi MG. Core/shell quantum dot based luminescent solar concentrators with reduced reabsorption and enhanced efficiency. Nano Lett 2014; 14:4097–101. https://doi.org/10.1021/nl501627e.

[11] Meinardi F, Bruni F, Brovelli S. Luminescent solar concentrators for building-integrated photovoltaics. Nat Rev Mater 2017;2:17072. https://doi.org/10.1038/natrevmats.2017.72.

[12] Bünzli J-CG, Chauvin A-S. Lanthanides in solar energy conversion. Handb Phys Chem Rare Earths 2014:169–281. https://doi.org/10.1016/B978-0-444-62711-7.00261-9.

[13] McKenna B, Evans RC. Towards efficient spectral Converters through materials design for luminescent solar devices. Adv Mater 2017;29:1606491. https://doi.org/10.1002/adma.201606491.

[14] Davis NJLK, Macqueen RW, Jones STE, Orofino-Pena C, Cortizo-Lacalle D, Taylor RGD, et al. Star-shaped fluorene-BODIPY oligomers: versatile donor-acceptor systems for luminescent solar concentrators. J Mater Chem C 1952;5: 1952. https://doi.org/10.1039/c6tc05298c.

[15] Lee WWH, Zhao Z, Cai Y, Xu Z, Yu Y, Xiong Y, et al. Facile access to deep red/near-infrared emissive AIEgens for efficient non-doped OLEDs. Chem Sci 2018;9: 6118–25. https://doi.org/10.1039/c8sc01377b.

[16] Iagatti A, Patrizi B, Basagni A, Marcelli A, Alessi A, Zanardi S, et al. Photophysical properties and excited state dynamics of 4,7-dithien-2-yl-2,1,3-benzothiadiazole. Phys Chem Chem Phys 2017;19:13604. https://doi.org/10.1039/c6cp08721c.

[17] Patrizi B, Iagatti A, Abbondanza L, Bussotti L, Zanardi S, Salvalaggio M, et al. Ultrafast intramolecular and solvation dynamics in 4,7-bis (4,5-dibutylbenzo[1,2-b:4,3-b']bisthiophene[1,2-b:4,3-b']bisthiophen-2-yl)-2,1,3-benzothiadiazole. J Phys Chem C 2019;123(10):5840–52. https://doi.org/10.1021/acs.jpcc.8b11191.

[18] Lucarelli J, Lessi M, Manzini C, Minei P, Bellina F, Pucci A. N-alkyl diketopyrrolopyrrole-based fluorophores for luminescent solar concentrators: effect of the alkyl chain on dye efficiency. Dyes Pigments 2016;135:154–62. https://doi.org/10.1016/j.dyepig.2016.03.036.

[19] Papucci C, Geervliet TA, Franchi D, Bettucci O, Mordini A, Reginato G, et al. Green/yellow-emitting conjugated heterocyclic fluorophores for luminescent solar concentrators. Eur J Org Chem 2018;2018:2657–66. https://doi.org/10.1002/ejoc.201800242.

[20] Della Sala P, Buccheri N, Sanzone A, Sassi M, Neri P, Talotta C, et al. First demonstration of the use of very large Stokes shift cycloparaphenylenes as promising organic luminophores for transparent luminescent solar concentrators. Chem Commun 2019;55:3160. https://doi.org/10.1039/c8cc09859j.

[21] Still WC, Kahn M, Mitra A. Rapid chromatographic technique for preparative separations with moderate resolution. J Org Chem 1978;43:2923–5. https://doi.org/10.1021/jo00408a041.

[22] Albano G, Colli T, Nucci L, Charaf R, Biver T, Pucci A, et al. Synthesis of new bis[1-(thiophenyl)propynones] as potential organic dyes for colorless luminescent solar concentrators (LSCs). Dyes Pigments 2020;174:108100. https://doi.org/10.1016/j.dyepig.2019.108100.

[23] Albano G, Colli T, Biver T, Aronica LA, Pucci A. Photophysical properties of new p-phenylene- and benzodithiophene-based fluorophores for luminescent solar concentrators (LSCs). Dyes Pigments 2020;178:108368. https://doi.org/10.1016/j.dyepig.2020.108368.

[24] Geervliet TA, Gavrila I, Iasilli G, Picchioni F, Pucci A. Luminescent solar concentrators based on renewable polyester matrices. Chem Asian J 2019;14: 877–83. https://doi.org/10.1002/asia.201801690.

[25] Mori R, Iasilli G, Lessi M, Belén Muñoz-García A, Pavone M, Bellina F, et al. Polymer Chemistry rsc.li/polymers Luminescent solar concentrators based on PMMA films obtained from a red-emitting ATRP initiator †. Polym Chem 2018;9: 1168. https://doi.org/10.1039/c7py01933e.

[26] Sottile M, Tomei G, Borsacchi S, Martini F, Geppi M, Ruggeri G, et al. Epoxy resin doped with Coumarin 6: Example of accessible luminescent collectors. Eur Polym J 2017;89:23–33. https://doi.org/10.1016/j.eurpolymj.2017.02.003.

[27] Gianfaldoni F, De Nisi F, Iasilli G, Panniello A, Fanizza E, Striccoli M, et al. A push-pull silafluorene fluorophore for highly efficient luminescent solar concentrators. RSC Adv 2017;7:37302–9. https://doi.org/10.1039/c7ra08022k.

[28] Lucarelli J, Lessi M, Manzini C, Minei P, Bellina F, Pucci A. "N-alkyl diketopyrrolopyrrole-based fluorophores for luminescent solar concentrators: effect of the alkyl chain on dye efficiency". Dyes Pigments 2016;135:154–62. https://doi.org/10.1016/j.dyepig.2016.03.036.

[29] Gentili PL, Mugnai M, Bussotti L, Righini R, Foggi P, Cicchi S, et al. The ultrafast energy transfer process in Naphtole - Nitrobenzofurazan bichromophoric molecular systems. A study by femtosecond UV-VIS pump-probe spectroscopy. J Photochem Photobiol A: Chem 2007;187:209–21. https://doi.org/10.1016/j.jphotochem.2006.10.020.

[30] Di Donato M, Iagatti A, Lapini A, Foggi P, Cicchi S, Lascialfari L, et al. Combined experimental and theoretical study of efficient and ultrafast energy transfer in a molecular dyad. J Phys Chem C 2014;118:23476–86. https://doi.org/10.1021/jp505957q.

[31] Henry ER. The use of matrix methods in the modeling of spectroscopic data sets. Biophys J 1997;72:652–73.

[32] Van Stokkum IHM, Larsen DS, Van Grondelle R. Global and target analysis of time-resolved spectra. Biochim Biophys Acta Bioenerg 2004;1657:82–104. https://doi.org/10.1016/j.bbabio.2004.04.011.

[33] Snellenburg JJ, Laptenok S, Seger R, Mullen KM, van Stokkum IHM. Glotaran: a Java-based graphical user interface for the R package TIMP. J Stat Software 2012; 49:1–22. https://doi.org/10.18637/jss.v049.i03.

[34] Hohenberg P, Kohn W. Inhomogeneous electron gas. Phys Rev 1964;136:864–71.

[35] Kohn W, Sham LJ. Self-consistent equations including exchange and correlation effects. Phys Rev 1965;140:A1133–8. https://doi.org/10.1103/PhysRev.140.A1133.

[36] Parr RG, Yang W. Density-functional theory of atoms and molecules. New York, Oxford: Oxford Uni; 1989.

[37] Adamo C, Jacquemin D. The calculations of excited-state properties with time-dependent density functional theory. Chem Soc Rev 2013;42:845–56. https://doi.org/10.1039/c2cs35394f.

[38] Laurent AD, Adamo C, Jacquemin D. Dye chemistry with time-dependent density functional theory. Phys Chem Chem Phys 2014;16:14334–56. https://doi.org/10.1039/c3cp55336a.

[39] Gaussian 09, Revision C.01, M.J. Frisch, G.W. Trucks, H.B. Schlegel, G.E. Scuseria, M.A. Robb, J.R. Cheeseman, G. Scalmani, V. Barone, B. Mennucci, G.A. Petersson, H. Nakatsuji, M. Caricato, X. Li, H.P. Hratchian, A.F. Izmaylov, J. Bloino, G. Zheng, J.L. Sonnenberg, M. Hada, M. Ehara, K. Toyota, R. Fukuda, J. Hasegawa, M. Ishida, T. Nakajima, Y. Honda, O. Kitao, H. Nakai, T. Vreven, J.A. Montgomery, Jr., J.E. Peralta, F. Ogliaro, M. Bearpark, J.J. Heyd, E. Brothers, K.N. Kudin, V.N. Staroverov, T. Keith, R. Kobayashi, J. Normand, K. Raghavachari, A. Rendell, J.C. Burant, S.S. Iyengar, J. Tomasi, M. Cossi, N. Rega, J.M. Millam, M. Klene, J.E. Knox, J.B. Cross, V. Bakken, C. Adamo, J. Jaramillo, R. Gomperts, R.E. Stratmann, O. Yazyev, A.J. Austin, R. Cammi, C. Pomelli, J.W. Ochterski, R.L. Martin, K. Morokuma, V.G. Zakrzewski, G.A. Voth, P. Salvador, J.J. Dannenberg, S. Dapprich, A.D. Daniels, O. Farkas, J.B. Foresman, J.V. Ortiz, J. Cioslowski, D.J. Fox, Gaussian, Inc.: Wallingford, CT, USA (2010).

[40] Becke AD. Density-functional thermochemistry. III. The role of exact exchange. J Chem Phys 1993;98:5648–52. https://doi.org/10.1063/1.464913.

[41] Lee C, Yang W, Parr RG. Development of the Colle-Salvetti correlation-energy formula into a functional of the electron density. Phys Rev B 1988;37:785–9. https://doi.org/10.1103/PhysRevB.37.785.

[42] Yanai T, Tew DP, Handy NC. A new hybrid exchange–correlation functional using the Coulomb-attenuating method (CAM-B3LYP). Chem Phys Lett 2004;393:51–7. https://doi.org/10.1016/j.cplett.2004.06.011.

[43] Lynch BJ, Fast PL, Harris M, Truhlar DG. Adiabatic connection for kinetics. J Phys Chem 2000;104:4811–5. https://doi.org/10.1021/jp000497z.

[44] Tomasi J, Mennucci B, Cammi R. Quantum mechanical continuum solvation models. Chem Rev 2005;105:2999–3094. https://doi.org/10.1021/cr9904009.

[46] Iasilli G, Francischello R, Lova P, Silvano S, Surace A, Pesce G, et al. Luminescent solar concentrators: boosted optical efficiency by polymer dielectric mirrors. Mater Chem Front 2019;3:429. https://doi.org/10.1039/c8qm00595h.

[47] De Nisi F, Francischello R, Battisti A, Panniello A, Fanizza E, Striccoli M, et al. Red-emitting AIEgen for luminescent solar concentrators. Mat Chem Front 2017;1: 1406. https://doi.org/10.1039/c7qm00008a.

[48] Carlotti M, Fanizza E, Panniello A, Pucci A. A fast and effective procedure for the optical efficiency determination of luminescent solar concentrators. Sol Energy 2015;119:452–60. https://doi.org/10.1016/j.solener.2015.05.031.

[49] Omary MA, Patterson HH. Luminescence, theory. Encycl. Spectrosc. Spectrom. Elsevier Inc.; 2017. p. 636–53. https://doi.org/10.1016/B978-0-12-803224-4.00193-X.

[50] Zhou W, Zhao B, Shen P, Jiang S, Huang H, Deng L, et al. Multi-alkylthienyl appended porphyrins for efficient dye-sensitized solar cells. Dyes Pigments 2011; 91:404–12. https://doi.org/10.1016/j.dyepig.2011.05.017.

[51] Mei J, Hong Y, Lam JWY, Qin A, Tang Y, Tang BZ. Aggregation-induced emission: the whole is more brilliant than the parts. Adv Mater 2014;26:5429–79. https://doi.org/10.1002/adma.201401356.

[52] Sasaki S, Drummen GPC, Konishi GI. Recent advances in twisted intramolecular charge transfer (TICT) fluorescence and related phenomena in materials chemistry. J Mater Chem C 2016;4:2731–43. https://doi.org/10.1039/c5tc03933a.

[53] Valeur B, Berberan-Santos MN. Molecular fluorescence. Weinheim, Germany: Wiley-VCH Verlag GmbH & Co. KGaA; 2012. https://doi.org/10.1002/9783527650002.

[54] Donati F, Pucci A, Cappelli C, Mennucci B, Ruggeri G. Modulation of the optical Response of Polyethylene films containing luminescent perylene chromophores. J Phys Chem B 2008;112:3668–79. https://doi.org/10.1021/jp711193u.

[55] Clarke TM, Gordon KC, Kwok WM, Phillips DL, Officer DL. Tuning from π,π* to charge-transfer excited states in styryl-substituted Terthiophenes: an ultrafast and steady-state emission study. J Phys Chem 2006;110:7696–702. https://doi.org/10.1021/jp0600312.

[56] Green AP, Buckley AR. Solid state concentration quenching of organic fluorophores in PMMA. Phys Chem Chem Phys 2015;17:1435. https://doi.org/10.1039/c4cp05244g.

[57] Roncali J. Luminescent solar collectors: Quo Vadis? Adv Energy Mater 2020;10: 2001907. https://doi.org/10.1002/aenm.202001907.

[58] Bomm J, Büchtemann A, Chatten AJ, Bose R, Farrell DJ, Chan NLA, et al. Fabrication and full characterization of state-of-the-art quantum dot luminescent

solar concentrators. Sol Energy Mater Sol Cells 2011;95:2087–94. https://doi.org/10.1016/j.solmat.2011.02.027.

[59] Mateen F, Ali M, Lee SY, Jeong SH, Ko MJ, Hong SK. Tandem structured luminescent solar concentrator based on inorganic carbon quantum dots and organic dyes. Sol Energy 2019;190:488–94. https://doi.org/10.1016/j.solener.2019.08.045.

[60] Dessì A, Calamante M, Mordini A, Peruzzini M, Sinicropi A, et al. Thiazolo[5,4-d]thiazole-based organic sensitizers with strong visible light absorption for transparent, efficient and stable dye-sensitized solar cells. RSC Adv 2015;5:32657–68. https://doi.org/10.1039/C5RA03530A.

137

4.7. Manuscript 7: "Luminescent solar concentrators with outstanding optical properties by employment of D–A–D quinoxaline fluorophores"

In this work, five novel molecules, **DQ1-5**, have been designed and synthetized for a possible application as fluorophores in LSCs, investigating their properties in solution and after dispersion on PMMA and PCMA matrices. Additionally, the optical properties of LSCs devices built with the designed molecules have been evaluated and compared with those reported for the *state-of-the-art* LR305 [1]. **DQ1-5** possess the peculiar D-A-D structure, and they carry the quinoxaline acceptor core (A) substituted in 5,8 positions with different donor groups (D). Additionally, alkyl chains have been inserted on the central core and on the donor groups to explore their compatibility with the two matrices. The results of this study show that these fluorophores possess excited states with a high degree of intramolecular charge transfer, intense emission properties and large Stokes shifts that minimize the auto-absorption phenomena, while the long alkyl chains contribute to tune their dispersibility in polymer films. In particular, devices built with **DQ1** have excellent optical properties, better than those of LR305.

The PhD candidate's contribution concerns the application of DFT methods for the calculation of the FMOs, including solvent effects (toluene) by PCM, in order to add knowledge with respect to the possible mechanism upon excitation of the designed fluorophores.

Additionally, compounds **DQ1-5** have been subjected to a further in-depth computational investigation. These results (see Section 4.7.1) have not been reported in the present manuscript and they will be the subject of a future publication.

Journal of Materials Chemistry C

Check for updates

Luminescent solar concentrators with outstanding optical properties by employment of D–A–D quinoxaline fluorophores†

Costanza Papucci,[abc] Rima Charaf,[d] Carmen Coppola, [ID][ce] Adalgisa Sinicropi, [ID][ace] Mariangela di Donato, [ID][af] Maria Taddei,[af] Paolo Foggi, [ID][fgh] Antonella Battisti, [ID][i] Bastiaan de Jong,[cj] Lorenzo Zani, [ID][a] Alessandro Mordini, [ID][ab] Andrea Pucci, [ID]★[ad] Massimo Calamante [ID]★[ab] and Gianna Reginato [ID]★[a]

Luminescent solar concentrators (LSCs) are devices designed to efficiently collect both direct and diffuse solar radiation and concentrate it on photovoltaic cells to foster their use in building-integrated photovoltaics (BIPV). The optimization of LSC performances involves the adjustment of both the fluorophore and the guest polymer matrix. On this account, we investigated a series of high quantum yield, donor–acceptor–donor (D–A–D) photostable fluorophores (DQ1–5), presenting a central quinoxalinic acceptor core, not previously employed in LSCs, and triarylamines or phenothiazine as donor groups. The molecules were also decorated with alkyl chains on the central core and/or the donor groups, to explore their compatibility with the poly(methyl methacrylate) (PMMA) and poly(cyclohexyl methacrylate) (PCMA) matrices utilized in this study. The PMMA and PCMA films (25 μm thick), containing 0.2–2.2 wt% of DQ1–5, absorbed in the 370–550 nm range and presented emission maxima at 550–600 nm, with fluorescence quantum yields higher than 40% even at the highest doping contents. Notably, the DQ1/PMMA thin-films showed enhanced phase compatibility and excellent quantum yields, i.e., >95%. Accordingly, they were designed to obtain 25 cm² area LSCs with remarkable internal (η_{int}) and external (η_{ext}) photon efficiencies of 42.9% and 6.2%, respectively, higher than those observed from state-of-the-art devices based on the Lumogen Red 305 (LR305) as the reference fluorophore. Overall, these were the best results ever achieved in our laboratory for thin-film LSCs built with organic fluorescent emitters.

[a] Institute of Chemistry of Organometallic Compounds (CNR-ICCOM), Via Madonna del Piano 10, 50019 Sesto Fiorentino, Italy

[b] Department of Chemistry "U. Schiff", University of Florence, Via della Lastruccia 13, 50019 Sesto Fiorentino, Italy

[c] Department of Biotechnology, Chemistry and Pharmacy, University of Siena, Via A. Moro 2, 53100 Siena, Italy

[d] Department of Chemistry and Industrial Chemistry, University of Pisa, Via G. Moruzzi 13, 56124 Pisa, Italy

[e] CSGI, Consorzio per lo Sviluppo dei Sistemi a Grande Interfase, 50019 Sesto Fiorentino, Italy

[f] LENS, European Laboratory for Non-Linear Spectroscopy, via N. Carrara 1, 50019 Sesto Fiorentino, Italy

[g] Department of Chemistry, Biology and Biotechnology, University of Perugia, via Elce di Sotto 8, 06123 Perugia, Italy

[h] INRIM (Istituto Nazionale di Scienza Metrologica), Strada delle Cacce 91, 10135 Torino, Italy

[i] Nanoscience Institute, CNR and NEST, Scuola Normale Superiore, P.zza S. Silvestro 12, 56127 Pisa, Italy

[j] Cicci Research s.r.l., Via Giordania 227, 58100 Grosseto, Italy

† Electronic supplementary information (ESI) available. See DOI: 10.1039/d1tc02923a

1. Introduction

In the past few decades, the need to reduce CO_2 emissions generated by human activities has prompted the scientific community to study new and efficient methods to utilize renewable energy sources, such as sunlight, for power generation, aiming to progressively replace the use of fossil fuels.[1] Among the currently available technologies, silicon photovoltaics (Si-PVs) have been the subject of continuous development efforts, which ultimately led to the reduction in the production prices of the modules at an actual electricity cost of about 0.2 $ per Watt peak (Wp)[2] without detrimenting performances.

Nevertheless, Si-PV panels provide the maximum efficiency only under direct light irradiation and require an efficient dissipation of the excess heat due to the unconverted energy. Luminescent solar concentrators (LSCs) rely on a technology studied since the 1970s[3,4] and were developed with the aim of obtaining large-area, semi-transparent and cheap photovoltaic devices capable of concentrating both direct and diffuse solar

radiation on small solar cells at their edges. Specifically, they consist of a panel of a common plastic material (*e.g.*, poly(methyl methacrylate), PMMA) containing a fluorescent dopant capable of absorbing direct and indirect sunlight and emitting it at longer wavelengths. Commonly used fluorescent compounds can be quantum dots, perovskites, rare-earth complexes and organic molecules.[5] The emitted radiation is mainly concentrated, *via* total internal reflection, at the edge of the panel (where the solar cells are placed) thanks to the different refractive indexes of air and the plastic material. This, together with the aesthetic characteristics of LSCs (color and shape tunability), supports their use in building-integrated photovoltaics (BIPVs).[6]

In order to obtain high-performance LSC devices, a careful study of the materials used for their assembly must be performed, concerning both the selection of the fluorophore and the plastic material in which it is dispersed.[5] Regarding the fluorophore, the most critical parameters influencing the final properties of the device are its fluorescence quantum yield (Φ_f) and Stokes shift (SS) which, together with the match between its emission spectrum and the electronic band-gap of the PV cell, govern the efficiency of the solar collector.

These properties, particularly Φ_f, can depend on the polarity of the medium (solution or polymer) in which the fluorophore is dispersed. For the polymer matrix, the main factor to be considered is its ability to disperse large amounts of fluorophores to promote solar harvesting, without activating fluorescence quenching phenomena due to aggregation[7,8] (aggregation caused quenching – ACQ). Furthermore, a good matrix might be able to affect the stability of the fluorophore excited state and thus enhance its fluorescence quantum yield. Clearly, a smart selection of the polymer, specifically tailored to fit the fluorophore properties, is an important factor for improving the device performance.

Among the different kinds of fluorophores applicable in LSCs, small organic molecules with a donor–acceptor type (D–A) structure, whose excitation determines the formation of a charge-transfer state with a significant dipole moment,[9] appear particularly interesting. We recently investigated the properties of a series of organic fluorophores with donor–acceptor–donor (D–A–D) structures, presenting a benzo[1,2-*d*:4,5-*d'*]bisthiazole acceptor core, dispersed in three methacrylic polymer matrices of different polarity.[10] Notably, we found that by decreasing the polarity of the matrix by passing from PMMA to poly(cyclohexyl methacrylate) (PCMA, Fig. 1), the Φ_f of the molecules increased due to the decreased stabilization of the charge-transfer excited state, resulting in a superior optical efficiency of the corresponding LSCs.

To further explore the interactions between organic emitters and polymer matrices of varying polarity and assess their effects on the performances of the corresponding LSCs, we decided to investigate a different series of luminophores, still presenting the same D–A–D architecture. We focused on quinoxaline, a molecular scaffold which is quite easy to functionalize and is characterized by good light harvesting ability, high Φ_f and large SS.[11–18]

Owing to their photophysical properties, quinoxalines are good candidates for application in LSCs but, although they have been extensively applied in organic optoelectronics,[19] their use in such devices has not yet been reported. Therefore, starting from a previously reported compound, **DQ1**,[20,21] a series of symmetrical derivatives were designed and synthesized by modifying both the donor groups at the 5,8 positions and the substituents at the 2,3 positions (Fig. 1).

The optical properties of the new molecules were investigated in solution and after dispersion in the PMMA and PCMA matrices to determine their absorption and emission features as well as their Φ_f. Furthermore, transient absorption spectroscopy (TAS) and fluorescence lifetime studies were also carried out to monitor the excited state evolution and correlate the device characteristics with the dynamic optical properties of the fluorophores. Due to the outstanding performances of these emitters also when dispersed into polymers, LSCs presented excellent optical properties, even superior to those found using the commercial reference fluorophore Lumogen Red 305 (**LR305**).[5,8,10]
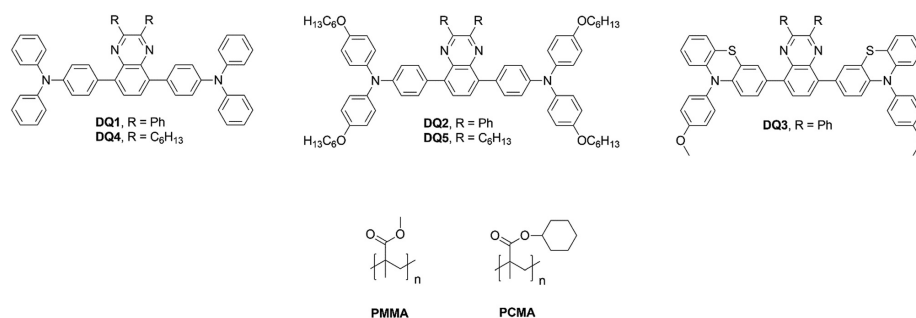

Fig. 1 Chemical structure of fluorophores based on 2,3-diphenyl-quinoxaline (**DQ1-3**) or 2,3-dihexyl-quinoxaline (**DQ4-5**) acceptor cores and of the used polymer matrices.

Journal of Materials Chemistry C

2. Experimental

2.1 General remarks

All commercially available compounds were purchased from Merck KgaA, Fluorochem Ltd and T.C.I. Co. Ltd, and were used without further purification unless stated otherwise. Anhydrous toluene was obtained after drying with a PureSolv Micro apparatus (Inert). Organometallic reactions were carried out under dry nitrogen using Schlenk techniques. Solvent degassing was carried out according to the ''freeze–pump–thaw'' method. Reactions were monitored by TLC on Kieselgel 60 F254 (Merck) aluminium sheets and the products were visualized by exposing the plate to UV light or by staining it with $KMnO_4$ solution. Flash column chromatography was performed using a Merck Kieselgel 60 (300–400 mesh) as the stationary phase. ^{1}H-NMR spectra were recorded at 200–400 MHz, and ^{13}C-NMR spectra were recorded at 50.3–100.6 MHz, using Varian Gemini/Mercury/INOVA series instruments. Chemical shifts (δ) are reported in parts per million (ppm) and are referenced to the residual solvent peak (CDCl$_3$, δ = 7.26 ppm for ^{1}H-NMR and δ = 77.0 ppm for ^{13}C-NMR; CD$_2$Cl$_2$, δ = 5.32 ppm for ^{1}H-NMR and δ = 53.84 ppm for ^{13}C-NMR), while coupling constants (J) are reported in Hz. ESI-MS spectra were obtained by direct injection of the sample solution using a Thermo Scientific LCQ-FLEET instrument, while HRMS spectra were measured using a Thermo Scientific LTQ Orbitrap (FT-MS) instrument (carried out at the Interdepartmental Centre for Mass Spectrometry of the University of Florence, CISM); main peaks for both are reported in the form m/z.

2.2 Spectroscopic analysis in solution

UV-vis absorption spectra were recorded with a Shimadzu 2600 series spectrometer, and fluorescence spectra were recorded with a JASCO FP-8300 spectrofluorometer, irradiating the sample at the wavelength corresponding to maximum absorption in the UV-vis spectrum. Absolute fluorescence quantum yields (Φ_f) in toluene solution were determined at room temperature using an integration sphere.

2.3 LSC film preparation

Polymer thin films containing the selected fluorophore were prepared by pouring 1.5 mL of toluene (Sigma-Aldrich, HPLC Plus, ≥99.9%) solution containing about 60 mg of the polymer and different concentrations (0.2–2.2 wt%) of the fluorophore on a 50 × 50 × 3 mm optically pure glass substrate (Edmund Optics Ltd BOROFLOAT window 50 × 50 TS). The amount of fluorophore was taken from a mother solution at a concentration of 1.5 mg mL^{-1}. The glass slides were cleaned with chloroform and immersed in 6M HCl for at least 12 h and then dried according to previously reported procedures.[22–27] Fluorophore-doped polymer thin films with a thickness of 25 ± 5 µm (Starrett micrometer) were obtained after complete evaporation of toluene at room temperature under a saturated atmosphere of chloroform (Merck, ACS reagent, ≥99.8%). After LSC characterization, the polymer films were carefully detached from the glass surface by immersing the LSC in water, stored in a desiccator and then analysed by means of absorption and emission spectroscopies.

2.4 Spectroscopic analysis of polymer films

UV-vis absorption spectroscopy on polymer films was performed at room temperature by using an Agilent Cary 5000 spectrophotometer. Fluorescence spectra on polymer films were recorded at room temperature with a Horiba Jobin-Yvon Fluorolog$^{\circledR}$-3 spectrofluorometer equipped with a 450 W xenon arc lamp and double-grating excitation and single-grating emission monochromators. Fluorescence quantum yields (Φ_f) in the solid state were determined using a 152-mm-diameter ''Quanta-φ'' integrating sphere, coated with Spectralon$^{\circledR}$ and following the procedures reported earlier.[22,28,29] Epifluorescence microscopy was accomplished using a LED epifluorescence microscope (Schaefer South-East Europe S.r.l., Rovigo, Italy) equipped with a LED blue and green 5W light source and a DeltaPix Invenio 2EIII microscope camera (DeltaPix, Smorum, Denmark).

2.5 Transient absorption spectroscopy and fluorescence lifetime imaging (FLIM)

Ultrafast transient absorption spectra of all samples have been recorded on a system consisting of a home-built Ti:sapphire laser oscillator and regenerative amplifier system (Amplitude Pulsar) which produced 80 femtoseconds pulses at 810 nm with an average output power of 450–500 mW. Excitation pulses at 400 nm were obtained by the second harmonic generation of the fundamental laser output in a *2 mm-thick β-barium borate (BBO)* crystal. For all measurements, the pump beam polarization was set at the magic angle with respect to the probe beam by rotating a $\lambda/2$ plate to exclude rotational contributions to the transient signal.[30,31] The excitation powers were on the order of 50–100 nJ. The probe pulses were generated by focusing a portion of the 800 nm radiation beam on a *3 mm-thick CaF$_2$* window. The time delay between the pump and probe pulses was introduced by sending the portion of 800 nm light used for probe generation through a motorised stage. After passing through the sample, the white light probe was sent to a flat field monochromator coupled to a home-made CCD detector. For samples in solution, measurements were performed in a quartz cell (2 mm thick) mounted on a movable stage in order to refresh the solution and avoid undesired photochemical degradation of the sample. In the case of samples dispersed in PMMA, the polymeric films were directly mounted on the same motorised stage used for liquid samples. Analysis of the transient data was performed applying singular value decomposition (SVD)[32] and global analysis,[33] using GLOTARAN software.[34] Global analysis allows the simultaneous fit of all the measured wavelengths with a combination of exponential decay functions and retrieves the kinetic constants describing the dynamic evolution of the system and the corresponding spectral component, called evolution associated difference spectra (EADS). A linear decay kinetic scheme was employed for data analysis.

Fluorescence lifetime imaging (FLIM) was carried out on PMMA films doped with fluorophores **DQ1–5** (1.0 wt%) using an inverted confocal microscope Leica TCS SP5 (Leica Microsystems, Wetzlar, GE) coupled with an external pulsed diode laser (λ_{ex} = 405 nm) and a TCSPC acquisition card (PicoHarp 300, PicoQuant,

Berlin, GE) connected to internal spectral detectors. The laser repetition rate was set to 20 or 40 Hz. The images (256 × 256 pixels) were usually acquired with a scan speed of 400 Hz (lines per second). The pinhole aperture was adjusted depending on the fluorescence intensity and films were imaged under a 40×/NA 0.60 dry objective (Leica Microsystems). Fluorescence emission was monitored in the 480 and 620 nm range using the built-in acousto-optical beam splitter detection system of the microscope. Acquisitions were stopped after the collection of about 100–200 photons per pixel, at a photon counting rate of about 200–300 kHz. The decay curves were obtained from the binned lifetime images and fitted using PicoQuant SymPhoTime software.

2.6 Determination of LSC optical properties

Internal (η_{int}) and external (η_{ext}) photon efficiencies were evaluated in agreement with recent protocols[35] (see the ESI† for additional discussion and pictures). All the measurements were performed using a commercially available system (Arkeo – Cicci research s.r.l.) containing a CMOS-based spectrometer with a symmetrical Czerny–Turner optical bench connected to an integrating sphere. A fiber-based tunable LED source was used to excite the center of the LSC device with a circular spot of 2 mm in diameter and at a distance of 0.5 mm. The platform includes a tunable LED source composed of 10 monochromatic diodes (from 360 to 960 nm) and 2 white diodes (warm and cold) used to match AM 1.5G (Fig. S22 and S23, ESI†). The use of LED source allowed the irradiation stability with time. An integrating sphere of 5 cm of diameter and 1 cm of aperture is placed along the edge of the glass plate, such that the aperture of the sphere is fully covered by the glass and one corner coincides with the edge of the aperture hole. The integrating sphere was moved along the side of the LSC until all the slab edges had been scanned. The spectrally resolved edge output photon count was collected from the CMOS-based spectrometer and calibrated into optical power (W) and then in irradiance. Aimed at limiting reflections of unabsorbed light, an absorbing matte black background was placed in contact with the LSC rear side. The fiber was kept close and perpendicular to the centre of the LSC front surface to minimize the diverge of the excitation beam and to avoid the direct illumination of the integrating sphere.[36] A series of 3–5 measurements were repeated in order to align the integration sphere to collect the maximum single-edge output power. For the auto-absorption experiments, the Arkeo platform included a motorised translation stage and was equipped with a 405 nm, 1 mW laser.

2.7 Synthesis of DQs

4,4′-(2,3-Diphenylquinoxaline-5,8-diyl)bis(N,N-diphenyl) aniline, DQ1. In a Schlenk tube, under an inert atmosphere of nitrogen, Pd(dppf)Cl$_2$ (18 mg, 0.023 mmol, 10 mol%) was added to a solution of 5,8-dibromo-2,3-diphenylquinoxaline 5 (100 mg, 0.23 mmol, 1.0 eq.) in toluene/MeOH 6 : 1 (4 mL). KF (39 mg, 0.68 mmol, 3.0 eq.) and boronic acid 7 (164 mg, 0.57 mmol, 2.5 eq.) were added to the mixture. The solution was heated at 80 °C for 18 h. The mixture was then cooled at room temperature and water (5 mL) was added. The mixture

was extracted with EtOAc (3 × 4 mL). The organic phase was washed with water and brine and then dried on anhydrous Na$_2$SO$_4$. Purification by flash column chromatography (SiO$_2$, petroleum ether/DCM 3 : 1) gave product **DQ1** as an orange solid (37 mg, 0.048 mmol, 21%). ^{1}H-NMR (400 MHz, CDCl$_3$): δ = 7.89 (s, 2H), 7.80 (d, J = 8.4 Hz, 4H), 7.63 (d, J = 7.6 Hz, 4H), 7.27–7.38 (m, 14H), 7.20–7.27 (m, 12H), 7.07 (dd, J = 7.6, 6.4 Hz, 4H) ppm. ^{13}C-NMR (100 MHz, CDCl$_3$): δ = 151.0, 147.7, 147.3, 139.1, 138.6, 138.4, 132.1, 131.7, 130.1, 129.4, 129.3, 128.8, 128.2, 124.7, 123.0, 122.7 ppm. HRMS: m/z calculated for C$_{56}$H$_{41}$N$_4$: 769.3326. Found: 769.3315 [M + H]$^+$.

General procedure for microwave-activated Suzuki–Miyaura cross coupling

In a microwave tube, Pd(dppf)Cl$_2$ (10 mol%) was added to a solution of appropriate dibromoquinoxaline (1.0 eq.) in toluene. Meanwhile, in a Schlenk tube, under a nitrogen atmosphere, boronic ester/acid (2.5 eq.) and KF (3.0 eq.) were dissolved in MeOH. After complete dissolution, the latter solution was added into the MW tube. The mixture was stirred for 30′ at room temperature and then heated under MW irradiation at 70 °C for 35′. The mixture was cooled at room temperature and the solvent was removed under a vacuum.

4,4′-(2,3-Diphenylquinoxaline-5,8-diyl)bis(N,N-bis(4-(hexyloxy)) phenyl)aniline, DQ2. 5,8-Dibromo-2,3-diphenylquinoxaline 5 (86 mg, 0.11 mmol, 1.0 eq.), Pd(dppf)Cl$_2$ (8.0 mg, 0.011 mmol, 10 mol%) in toluene (3 mL), boronic ester 8[37] (157 mg, 0.27 mmol, 2.5 eq.) and KF (19 mg, 0.33 mmol, 3.0 eq.) in MeOH (0.5 mL) were reacted following the above general procedure. The crude product was purified by flash column chromatography (SiO$_2$, petroleum ether/DCM 5 : 1 → 3 : 1) obtaining **DQ2** as an orange solid (28 mg, 0.024 mmol, 21%). ^{1}H-NMR (400 MHz, CDCl$_3$): δ = 7.86 (s, 2H), 7.69 (d, J = 9.0 Hz, 4H), 7.58 (d, J = 7.4 Hz, 4H), 7.37–7.29 (m, 6H), 7.15 (d, J = 9.0 Hz, 8H), 7.04 (d, J = 11.9 Hz, 4H), 6.88 (d, J = 9.1 Hz, 8H), 3.96 (t, J = 6.4 Hz, 8H), 1.83–1.74 (m, 8H), 1.52–1.44 (m, 8H), 1.40–1.33 (m, 16H), 0.93 (t, J = 6.6 Hz, 12H) ppm. ^{13}C-NMR (100 MHz, CDCl$_3$): δ = 155.8, 151.1, 148.4, 140.4, 139.2, 138.3, 131.3, 129.9, 129.8, 129.15, 128.6, 128.1, 127.0, 118.9, 115.2, 68.3, 31.6, 29.3, 25.7, 22.6, 13.8 ppm. HRMS: m/z calculated for C$_{80}$H$_{89}$O$_4$N$_4$: 1169.6878. Found: 1169.6864 [M + H]$^+$.

3,3′-(2,3-Diphenylquinoxaline-5,8-diyl)bis(10-(4-methoxyphenyl))- 10H-phenothiazine, DQ3. 5,8-Dibromo-2,3-diphenylquinoxaline 5 (174 mg, 0.23 mmol, 1.0 eq.), Pd(dppf)Cl$_2$ (16.8 mg, 0.023 mmol, 10 mol) in toluene (3 mL), boronic ester 9[10] (248 mg, 0.57 mmol, 2.5 eq.) and KF (40 mg, 0.69 mmol, 3.0 eq.) in MeOH (0.5 mL) were reacted following the above general procedure. The crude product was purified by flash column chromatography (SiO$_2$, petroleum ether/DCM 4 : 1 → 2 : 1) obtaining **DQ3** as a yellow solid (93 mg, 0.10 mmol, 46%). ^{1}H-NMR (400 MHz, CDCl$_3$): δ = 7.74 (s, 2H), 7.59 (dd, J = 6.0, 3.6 Hz, 6H), 7.36 (d, J = 6.0 Hz, 4H), 7.33–7.29 (m, 8H), 7.15 (dd, J = 7.6, 3.2 Hz, 4H), 7.03 (dd, J = 5.6, 1.6 Hz, 2H), 6.82 (ddd, J = 9.2, 4.0, 1.2 Hz, 4H), 6.30 (d, J = 8.8 Hz, 2H), 6.19 (dd, J = 4.0, 2.0 Hz, 2H), 3.92 (s, 6H) ppm. ^{13}C-NMR (100 MHz, CDCl$_3$): δ = 159.2, 151.1, 144.4, 144.0, 138.3, 137.5, 133.2, 132.3, 132.2, 130.1, 129.1, 128.8, 128.7, 128.2, 126.8, 126.6, 122.3, 119.5, 118.9, 115.9,

115.6, 115.2, 55.5 ppm. HRMS: m/z calculated for $C_{58}H_{57}N_4$: 889.2665. Found: 889.2652 $[M + H]^+$.

4,4′-(2,3-Dihexylquinoxaline-5,8-diyl)bis(N,N-diphenyl)aniline, DQ4. 5,8-Dibromo-2,3-dihexylquinoxaline **6** (66 mg, 0.14 mmol, 1.0 eq.), Pd(dppf)Cl$_2$ (10.2 mg, 0.014 mmol, 10 mol%) in toluene (3 mL), boronic acid **7** (101 mg, 0.35 mmol, 2.5 eq.) and KF (24.4 mg, 0.42 mmol, 3.0 eq.) in MeOH (0.5 mL) were reacted following the above general procedure. The crude product was purified by flash column chromatography (SiO$_2$, petroleum ether/DCM $4:1 \rightarrow 2:1 \rightarrow$ EtOAc) obtaining **DQ4** as a yellow solid (67 mg, 0.08 mmol, 55%). ^{1}H-NMR (400 MHz, CDCl$_3$): δ = 7.77 (s, 2H), 7.72 (d, J = 8.4 Hz, 4H), 7.29 (dd, J = 15.9, 8.0 Hz, 8H), 7.24–7.15 (m, 12H), 7.04 (m, 4H), 2.97 (t, J = 7.6 Hz, 4H), 1.91–1.81 (m, 4H), 1.46–1.37 (m, 4H), 1.36–1.21 (m, 6H), 0.86 (t, J = 6.0 Hz, 6H) ppm. ^{13}C-NMR (100 MHz, CDCl$_3$): δ = 155.1, 148.0, 147.1, 138.8, 138.3, 132.9, 131.8, 129.4, 128.5, 124.7, 123.0, 34.9, 32.0, 29.3, 27.3, 22.8, 14.2 ppm. HRMS: m/z calculated for $C_{56}H_{57}N_4$: 785.4577. Found: 785.4564 $[M + H]^+$.

4,4′-(2,3-Dihexylquinoxaline-5,8-diyl)bis(N,N-bis(4-(hexyloxy)phenyl)aniline), DQ5. In a Schlenk tube, under an inert atmosphere of nitrogen, Pd(PPh$_3$)$_4$ (13 mg, 0.011 mmol, 10 mol%) was added to a solution of 5,8-dibromo-2,3-dihexylquinoxaline **6** (50 mg, 0.11 mmol, 1.0 eq.) in toluene (4 mL). Cs$_2$CO$_3$ (116 mg, 0.33 mmol, 3.0 eq.) and appropriate boronic ester **8**[37] (132 mg, 0.23 mmol, 2.1 eq.) were added to the mixture. The solution was heated at 110 °C for 4 h. The mixture was cooled at room temperature, water (5 mL) was added and the resulting solution was extracted with EtOAc (3 × 4 mL). The organic phase was washed with water and brine and then dried on anhydrous Na$_2$SO$_4$. The crude product was purified by flash column chromatography (SiO$_2$, petroleum ether/DCM $3:1 \rightarrow 1:1$) obtaining **DQ5** as an orange solid (108 mg, 0.091 mmol, 83%). ^{1}H-NMR (400 MHz, CDCl$_3$): δ = 7.72 (s, 2H), 7.65 (d, J = 8.4 Hz, 4H), 7.13 (d, J = 9.2 Hz, 8H), 7.03 (d, J = 8.4 Hz, 4H), 6.84 (d, J = 9.0 Hz, 8H), 3.94 (t, J = 1.2 Hz, 8H), 2.96 (t, J = 1.2 Hz, 4H), 1.74–1.90 (m, 14H), 1.51–1.43 (m, 10H), 1.37–1.33 (m, 21H), 0.95–0.89 (m, 14H), 0.88–0.82 (m, 7H) ppm. ^{13}C-NMR (100 MHz, CDCl$_3$): δ = 155.4, 154.7, 147.9, 140.8, 138.7, 138.0, 131.4, 130.6, 128.1, 126.7, 119.6, 115.2, 68.2, 34.7, 31.8, 31.6, 29.3, 29.2, 27.3, 25.8, 22.6, 14.1, 14.0 ppm. HRMS: m/z calculated for $C_{80}H_{105}O_4N_4$: 1184.8058. Found: 1184.8042 $[M + H]^+$.

3. Results and Discussions

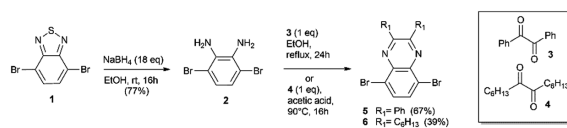## 3.1 Synthesis of chromophores DQ1–5

Compounds **DQ1–5** were rationally designed to modulate their relevant electronic and physico-chemical properties. By inserting different electron-donating groups at the 5,8 positions of the quinoxaline core, the HOMO–LUMO energy difference could be tuned, thus effectively modulating their absorption spectra.[38] In addition, the nature of the substituents at the 2,3 positions can affect the electron-accepting capacity of the quinoxaline unit, stabilizing the LUMO orbital.[21] Finally, the presence of alkyl chains on the acceptor and donor groups, other than modifying the electronic and optical properties, can also alter the dispersibility of the fluorophores in the polymer matrix, controlling the potential formation of non-emissive aggregates. Compounds **DQ1–5** (Fig. 1) were synthesized by means of an easy and flexible three-step route, making use of well-known Suzuki–Miyaura cross-coupling reactions as key steps. The two acceptor cores were prepared following a common strategy, shown in Scheme 1. Diamine **2** was synthesized in good yield by the reduction of commercially available 4,7-dibromo-2,1,3-benzothiadiazole (**1**) using a large excess of NaBH$_4$ in EtOH.[17] Compound **2** was used immediately, without purification, for the subsequent step involving a cyclization reaction using diketones **3** or **4**, under slightly different conditions, to obtain quinoxalines **5** and **6**, respectively. The latter were employed in the Suzuki–Miyaura cross-coupling reactions, whose conditions were individually optimized to enhance the yield of each product (Scheme 2).

In particular, compounds **DQ2–4** were synthesized by reacting quinoxalines **5** or **6** with the corresponding boronic acid/ester (**7–9**) in the presence of Pd(dppf)Cl$_2$ as the catalyst and KF as the base under microwave (MW) heating. Compared to conventional heating, MW irradiation allowed shortening the reaction time (approx. 35 minutes at 70 °C) and reducing the number of side-products. A mixture of toluene and MeOH (6/1) was identified as the best medium to absorb microwaves efficiently. However, the MW irradiation conditions were surprisingly ineffective in the synthesis of **DQ1** and **DQ5**. So, **DQ1** was obtained under similar conditions to **DQ2–4** (Scheme 2), but applying conventional heating for 18 h, while **DQ5** was prepared using a synthetic method reported by Kang *et al.* for a different compound.[20] This last reaction was run using Pd(PPh$_3$)$_4$ and Cs$_2$CO$_3$ as the catalyst and base, respectively, at a temperature of 100 °C for 4 hours.

3.2 Spectroscopic characterization in solution

Steady-state UV-vis absorption and fluorescence emission studies. The optical properties of compounds **DQ1–5** were studied in solution by UV-vis absorption and fluorescence emission spectroscopies. The solvent used was toluene because it effectively dissolved all compounds and its refractive index (1.496) is similar to that of PMMA (1.491). Relevant data are presented in Table 1 and Fig. 2. All compounds showed

Scheme 1 Synthesis of the quinoxaline cores.
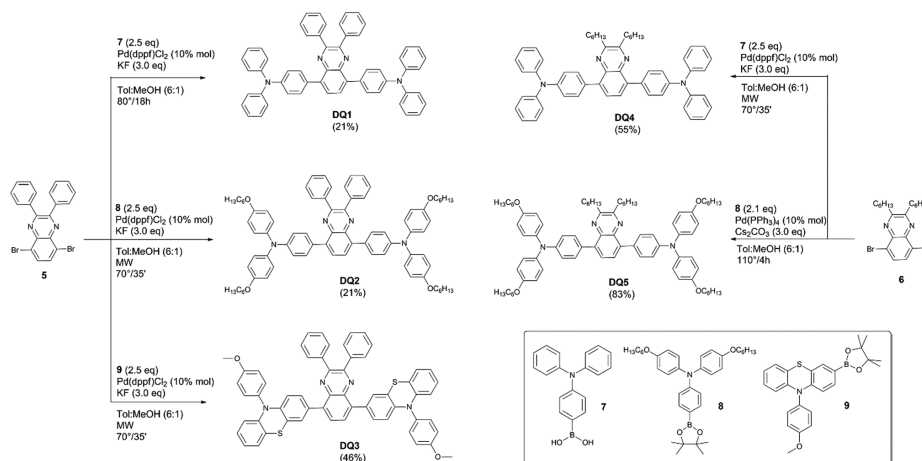
Scheme 2 Synthetic procedures for the preparation of **DQ** fluorophores.

Table 1 Spectroscopic properties of compounds **DQ1–5** in toluene solution

Compound	λ_{abs} (nm)	$\varepsilon \times 10^4$ (M^{-1} cm^{-1})	λ_{emi} (nm)	SS (nm [eV])	$\Phi_f{}^a$ (%)
DQ1	433	3.1	538	105 [0.56]	74
DQ2	457	3.3	567	110 [0.53]	66
DQ3	452	1.2	601	149 [0.68]	46
DQ4	398	1.2	512	117 [0.71]	44
DQ5	416	2.0	529	112 [0.62]	67

^{a} Absolute quantum yield of solutions.

maximum absorption wavelengths between 400 nm and 460 nm (Fig. 2, solid lines). Fluorophores **DQ1–3**, having a
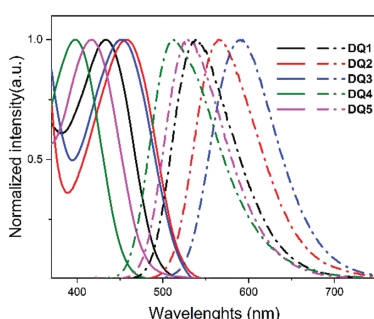
Fig. 2 Normalized absorption spectra (solid lines) and normalized fluorescence emission spectra (dash dot lines) of **DQ1–5** in toluene (0.01 mM) with λ_{exc} at 433, 457, 452, 398 and 416 nm, respectively.

2,3-diphenylquinoxaline acceptor core, showed a red-shifted absorption in comparison with the 2,3-dihexylquinoxalines **DQ4–5**. This is consistent with the more extended conjugation provided by the phenyl rings.[21] The maximum absorption wavelength increased from **DQ1** (433 nm) to **DQ3** (452 nm) and then **DQ2** (457 nm), in agreement with the increasing electron-donating characteristics of the lateral groups.[39] The same effect was also found for **DQ4** and **DQ5**.

In addition, all the absorption spectra featured broad peaks, maintaining a constant shape at different concentrations (see Fig. S2–S6, ESI†).

The ground-state frontier molecular orbitals of the **DQ** series were calculated using Gaussian 16,[40] Revision C.01 suite of programs, at the B3LYP[41,42]/6-31G* level of theory in toluene.

Solvent effects were included using the polarizable continuum model (PCM).[43] The inspection of the frontier molecular orbitals (see Fig. S1, ESI†) suggests that in all cases, the light absorption in the visible region could involve an internal charge-transfer (ICT) mechanism, as already observed in **DQ1** and similar molecules.[21,44] This is in agreement with the spectroscopic results.

The fluorescence spectra showed an intense emission band between 512 and 600 nm (Fig. 2, dash dot lines), relatively well-matched with the external quantum efficiency of a Si-based PV module. No vibronic structure was observed, and the constant shape of the emission band at different concentrations proved the absence of dye aggregation in toluene for all **DQs** in the explored concentration range (Fig. S2–S6, ESI†). Furthermore, in all cases, large Stokes shifts (0.53–0.71 eV, corresponding to >100 nm) with limited overlap between the absorption and emission spectra were observed, leading to minimal re-absorption phenomena (Table 1).

Transient absorption spectroscopy (TAS) studies. To further characterize the excited states of **DQ1–5** chromophores and

investigate the dynamics of their relaxation after light absorption in toluene solution, femtosecond transient absorption spectroscopy experiments were also carried out. The samples were excited at 400 nm, at the blue edge of absorption of the quinoxaline core, and their transient spectra were recorded in the 0.1 ps–1.5 ns time interval. The results were analysed by simultaneously fitting all the kinetic traces with a combination of exponential functions (global analysis), and using a kinetic scheme based on a sequential decay. Besides kinetic constants, global analysis also retrieves the corresponding spectral components, indicated as evolution associated difference spectra (EADS). The transient absorption spectra of **DQ1–5** recorded in toluene are reported in Fig. 3 and 4, respectively, with the correspondent EADS obtained from global analysis in the bottom panels.

2,3-Diphenyl-substituted compounds **DQ1–3** showed a broad positive excited state absorption (ESA) band, covering almost all the probed spectral interval (Fig. 3a–c). **DQ1** and **DQ2** showed very similar spectra, indicating a minor influence of the alkyl chains on the excited state dynamics, with a small negative band centred at about 440 nm, corresponding to the ground-state bleaching, and a more intense broad positive one, featuring a double-peaked structure because of an evident overlap with the negative stimulated emission (SE) band. In the corresponding EADS panels (Fig. 3d and e), the first component (black line) of both samples presents a broad positive band peaked at 600 nm, living about 2 ps in case of **DQ1** and 700 fs for **DQ2**.

In the following evolution (red lines in Fig. 3d and e), the ESA assumes a double-peaked shape, because of the increase in the positive signal in the 450–500 nm region and the super-position between the broad positive absorption band and the stimulated emission band (peaked at about 530 nm for **DQ1** and 550 nm for **DQ2**). This spectral evolution can be assigned

to a fast electronic relaxation of the molecule, as evidenced by a large red-shift of the stimulated emission signal.

According to the theoretical analysis (see Fig. S1, ESI†), the lowest excited state has a charge-transfer character. The positive band above 700 nm noticed in the second EADS could be interpreted in terms of the simultaneous localization of the negative charge on the quinoxaline unit and the positive charge on the triphenylamine donor, as evidenced in previous studies.[45,46] After 14.4 ps for **DQ1** (7.3 ps for **DQ2**), the red component evolves towards the blue EADS.

Although the spectral shape of the third EADS remains mostly unaffected, the stimulated emission signal partially recovers and red-shifts at about 30 nm reflecting a dynamic Stokes-shift due to solvent-induced excited state relaxation. On the same timescale, the band peaked at 600 nm narrows and slightly blue-shifts, as the effect of vibrational cooling occurring in the excited state. The narrowing at 600 nm is particularly evident for **DQ2**. Finally, the signal intensity slightly decreases on the following 448 ps timescale for **DQ1** (540 ps for **DQ2**). For both samples, the final spectral component (green EADS) lives beyond the time interval of the measurement (1.5 ns).

The transient spectrum of **DQ3** appears slightly different as compared to the previously described samples, reflecting the presence of the phenothiazine donor group (Fig. 3c and f), but the excited evolution can be interpreted in a similar way. Also in this case, after a fast electronic relaxation occurring in about 500 fs, a positive band peaked at about 500 nm is observed to increase, together with a broad absorption extending between 600 and >750 nm, and presenting a minimum at about 570 nm, due to the superposition with the stimulated emission band. The band peaked at 500 nm may reflect the localization of positive charge on the phenothiazine ring, while the signal in the red part of the spectrum (>600 nm) can be assigned to the
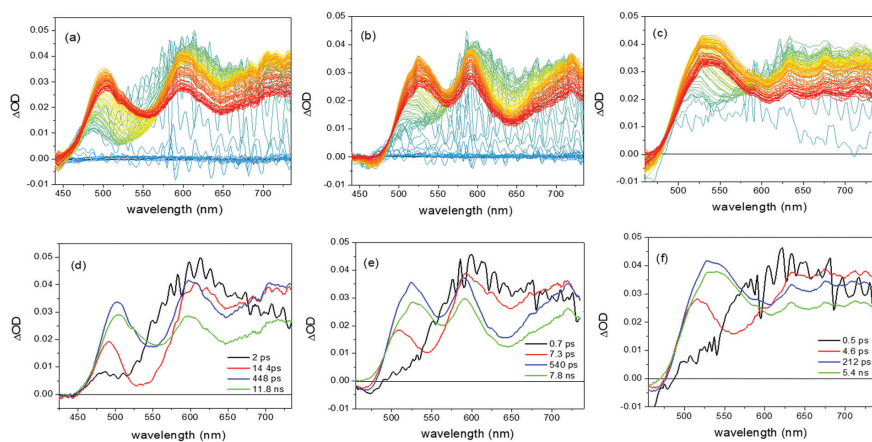

Fig. 3 Transient absorption spectra (a–c) and evolution associated difference spectra (EADS) (d–f) of **DQ1–3** (from left to right) in toluene solutions.

localization of the negative charge on the quinoxaline core, thus confirming the formation of a charge-transfer state also in this case. The spectral dynamics observed on the 5 ps timescale reflects a dynamic Stokes shift of the emission band. The intensity of the overall transient spectrum slightly decreases on the following 212 ps timescale and the final spectral component (green line, Fig. 3f) once again lives longer than the investigated timescale.

The transient absorption spectra and EADS of 2,3-di-*n*-hexylquinoxalines **DQ4** and **DQ5** are reported in Fig. 4. For both samples, a negative band, peaked at about 500 nm, is assigned as the SE signal, and a broad positive ESA band is noticed in the spectra. Opposite to the previous series of compounds, here the spectral evolution observed within the investigated timescale is quite limited. Inspection of the EADS shows a progressive red-shift of the SE band, ascribed to a solvent-induced excited state relaxation, occurring within 10 ps for both samples (evolution from the black to the red component and from the red to the blue one, Fig. 4c and d). The intensity of the ESA band partially decreases in about 325 ps for **DQ4** (about 430 ps for **DQ5**). Already in the second spectral component, a positive band at about 600 nm can be recognized, possibly related to the partial localization of the positive charge on the triphenylamine groups and therefore signalling the emergence of a charge-transfer state upon photoexcitation. Also for these samples, the final spectral component lives longer than the investigated timescale. Overall, the transient absorption

spectroscopy measurements of all the investigated compounds confirm the charge-transfer characteristic of the lowest energy excited state, furthermore indicating that no intermediate dark states are involved in its decay, suggesting that its main relaxation channel is of radiative nature, a very beneficial feature for compounds to be employed as LSC emitters.

3.3 Spectroscopic characterization in polymer matrices

DQ luminophores were characterized in polymer matrices by dispersing them in transparent and totally amorphous PMMA and PCMA, obtaining films with a 25 μm ± 5 μm thickness, at different concentrations (0.2–2.2 wt%). All molecules visually showed good dispersion in the polymer matrices, which appeared homogenous and with negligible macroscopic phase separation at the film surface even at the highest fluorophore content (Fig. 5).

Steady-state absorption and emission studies in PMMA. In PMMA films, all **DQs** exhibited broad absorption bands in the 370–550 nm interval (Fig. 6, solid lines and Table 2), with intensity regularly increasing with concentration and without evident differences in the spectral shape (Fig. S7–S11, ESI†). Moreover, no clear absorption bands attributed to the aggregates in polymer films were observed. Fluorescence bands encompassed the 500–700 nm spectral range (Fig. 6 dash dot lines), without evident vibronic contributions even at high doping (Fig. S7–S11, ESI†). The shape of the emission band remained unaltered at different fluorophore concentrations but showed a
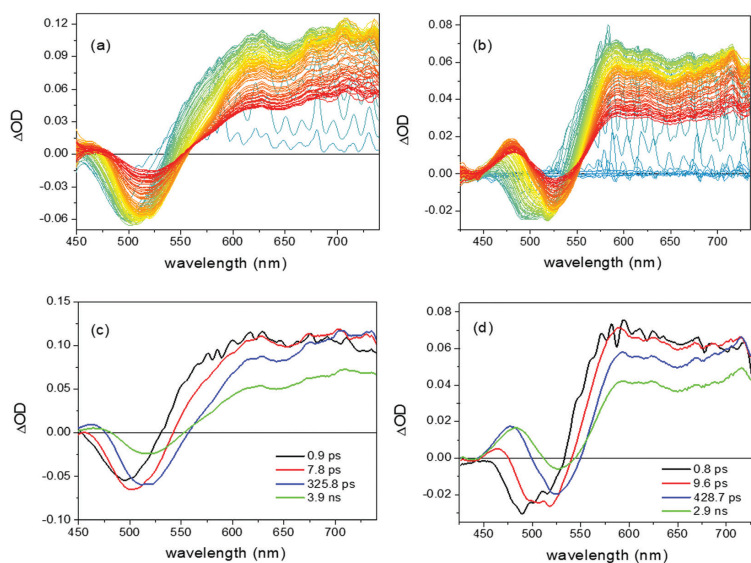

Fig. 4 Transient absorption spectra (a and b) and evolution associated difference spectra (EADS) (c and d) of **DQ4-5** (from left to right) in toluene solutions.
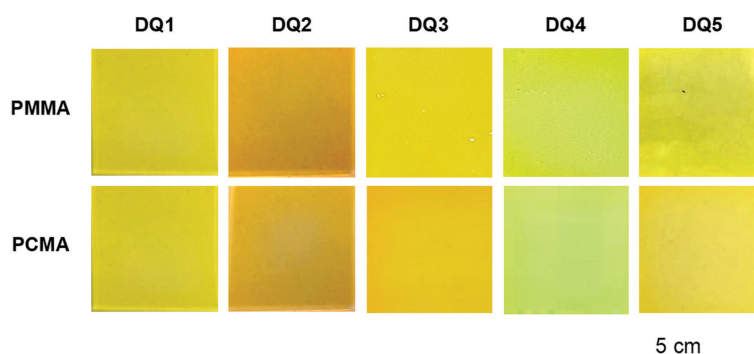
Fig. 5 PMMA and PCMA films doped with **DQ1–5** at 1.4 wt% concentration under visible light illumination.
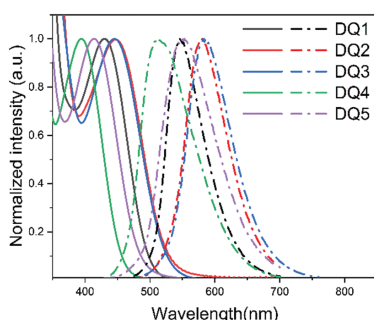

Fig. 6 Normalized absorption spectra (solid lines) and normalized fluorescence emission spectra (dash dot lines) of **DQ1–5** in PMMA (1.0 wt%) with λ_{exc} at 430, 454, 456, 400 and 415 nm, respectively. UV-vis absorption and emission spectra as a function of fluorophore concentration are reported in the ESI† (Fig. S7–S11).

progressive red-shift, possibly caused by moderate auto-absorption phenomena (*i.e.*, inner filter effects).[24,47] Notably, SS of more than 100 nm were observed for all **DQs**/PMMA films. It is worth noting that **DQ1** showed an outstanding fluorescence quantum yield in PMMA (90–97% as compared to 74% in

Table 2 Spectroscopic properties of compounds **DQ1–5** in PMMA and PCMA (1.0 wt%)

| Compound | PMMA | | | PCMA | | |
	λ_{abs} (nm)	λ_{emi} (nm)	SS (nm [eV])	λ_{abs} (nm)	λ_{emi} (nm)	SS (nm [eV])
DQ1	430	546	116 [0.61]	432	538	106 [0.56]
DQ2	447	580	133 [0.64]	459	569	110 [0.52]
DQ3	446	583	137 [0.65]	449	566	117 [0.57]
DQ4	406	513	107 [0.64]	404	493	89 [0.55]
DQ5	414	553	139 [0.75]	419	519	100 [0.57]

toluene) (Fig. S7, ESI†), seemingly due to the beneficial effect provided by the glassy polymer matrix. This is a typical trend, since entrapment of the fluorophore within the polymer chains can cause a decrease in its conformational freedom, resulting in an increased dissipation of the excited state energy through radiative channels.[48–51] Moreover, no quenching effects were observed up to a concentration of 1.8 wt%, thus suggesting also an excellent compatibility of the fluorophore with the polymer matrix.

This is confirmed by the inspection of epifluorescence microscopy images, revealing the presence of only a few micro-sized fluorophore aggregates with an average size of about 15 μm (Fig. 7), characterized by brilliant emission. Such behaviour appears very promising in obtaining solar collectors with improved optical performances.

Conversely, **DQ2**/PMMA films showed Φ_f values of 30–40% within the entire range of concentrations (Fig. S8, ESI†), lower than those recorded in solutions. No beneficial effect was exerted by the polymer matrix in this case, which can be attributed to the emersion of a large fraction of phase-separated microscopic fluorophore aggregates (Fig. 7). We can hypothesize that, in the initial toluene solution used for film preparation, **DQ2** molecules were well-dispersed. Upon the evaporation of the solvent, their local concentration increased, and thanks to the interaction of their long alkyl chains, they started to form small aggregates, which became progressively entrapped in the polymer matrix. This caused the size of the aggregates to increase, leading to the observed microscopic phase separation (Fig. 7).

The phase dispersion in PMMA also influenced the quantum efficiency of **DQ3**/PMMA and **DQ4**/PMMA films, since the values of 56% and 80% measured at the lowest fluorophore content (0.2 wt%) gradually collapsed with the increasing content to 33% and 58%, respectively (Fig. S9 and S10, ESI†). In these cases, the lower fluorophore compatibility with the PMMA matrix progressively gave rise to the emersion of micro-scale aggregates that, in turn, triggered the activation of the typical ACQ effect (Fig. 7).[52,53]
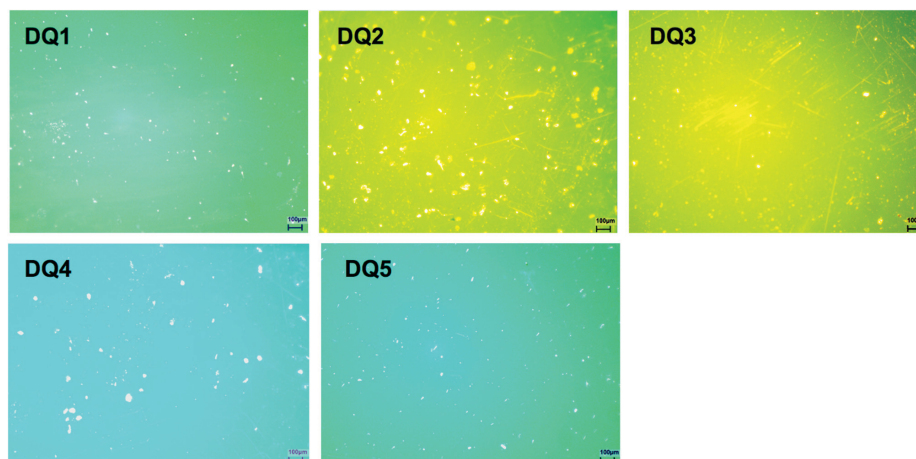
Fig. 7 Fluorescent microscopy images of 1.4 wt% **DQ1–5**/PMMA films. Scale bar = 100 μm.

This phenomenon appeared much less severe in the case of **DQ5**/PMMA films, whose fluorescence quantum yield remained constant at 50–60% in the entire range of investigated concentrations (Fig. S11, ESI†).

Steady-state absorption and emission studies in PCMA. All **DQ** fluorophores were also dispersed in PCMA, which is considered less polar than PMMA due to the stronger aliphatic contribution of the side-chain (Fig. 1).[10] In general, the spectra recorded in PCMA were comparable with those recorded in PMMA, with negligible differences between the peak maxima positions (Fig. 8 and Table 2). In particular, **DQ1–3** films showed absorption maxima increasing with concentration and all the emission bands were affected by red-shifts at high

fluorophore concentrations (Fig. S12–S14, ESI†). Significant SS at about 90–120 nm were observed for all molecules, similar to what found in PMMA.

The quantum yields of **DQ1–3** fluorophores appeared generally maintained or increased in the PCMA matrix compared to PMMA. Accordingly, **DQ1**/PCMA films confirmed high values of Φ_f of around 96–98% (Fig. S12, ESI†), whereas a striking increase from 40% to 71% and from 33% to 53% was recorded moving from PMMA to PCMA for **DQ2** (Fig. S13, ESI†) and **DQ3** (Fig. S14, ESI†), respectively, at the highest fluorophore content. This behaviour suggests that a less polar environment increases the phase compatibility between the fluorophores and the polymer matrix, as indicated by the images obtained by fluorescence microscopy of compound **DQ2** in PCMA films (Fig. 9, left). Clearly, a reduced number of smaller **DQ2** aggregates were present in PCMA with respect to the more phase-separated **DQ2**/PMMA system (Fig. 7).

Moving to **DQ4** and **DQ5** (Fig. S15 and S16, ESI†), the introduction of hexyl chains into their acceptor core resulted in a less evident quenching of fluorescence for concentrations higher than 1.4 wt% and in a less pronounced bathochromic shift of the emission maximum. Nevertheless, the alkyl

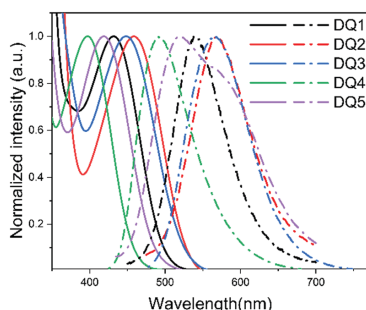**Fig. 8** Normalized absorption spectra (solid lines) and normalized emission spectra (dash dot lines) of **DQ1–5** in PCMA (1.0 wt%) with λ_{exc} at 430, 459, 447, 400, and 419 nm, respectively. UV-vis absorption and emission spectra as a function of fluorophore concentration are reported in the ESI† (Fig. S12–S16).
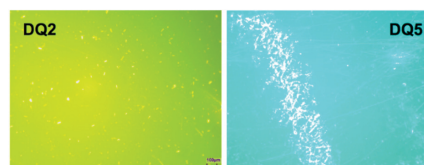

Fig. 9 Fluorescent microscopy images of a 1.4 wt% **DQ2,5**/PCMA film. Scale bar = 100 μm.

characteristic of **DQ4** and **DQ5** affected divergently the Φ_f variations with the fluorophore content. While **DQ4** showed a considerable increase of Φ_f with concentrations (*i.e.*, from 65% at 1.0 wt% to 90% at 1.8 wt%), the quantum yield of **DQ5** declined drastically from 80% at 0.2 wt% to around 53% at 1.8 wt%, *i.e.*, comparable to data gathered from PMMA films at the same content. Φ_f declining in **DQ5**/PCMA films was attributed to the formation of phase-separated aggregates triggering the formation of micro-cracks over the surface of the PCMA film as revealed by fluorescence microscopy (Fig. 9, right). Such hypothesis seems to be confirmed by the emission spectra of **DQ5**/PCMA (Fig. S16, ESI†), where a second emission at a longer wavelength appeared for high concentrations in agreement with the formation of emissive aggregates. Overall, the introduction of alkyl chains into the backbone of the fluorophores seems to promote better dispersion and compatibility with the less polar PCMA matrix, as especially evident in the case of compounds **DQ2** and **DQ4**. Notwithstanding this general observation, **DQ5**, featuring the highest number of alkyl chains of the series, diverges from such behaviour, requiring a more refined explanation.[54,55] Indeed, it must be considered that **DQ5**, despite the flexibility of the *n*-hexyloxy substituents, is the largest molecule among those examined, clearly larger than **DQ1**, but also than **DQ4**. Since the relative motions of the polymer film constituents are restricted, unlike what happens in solutions, it is possible that increasing the concentration of **DQ5** above a certain limit prevented the polymer chains to come sufficiently close due to steric reasons, decreasing the mechanical strength of the films. This caused the appearance of the observed micro-cracks, accompanied by a progressive phase-segregation of the emitter molecules, which was supported by the above-mentioned change in shape of the emission spectra (Fig. S16, ESI†).

Overall, **DQ1** displayed the highest quantum yields in both polymer matrices. Notably, compared to the other compounds studied in this work, **DQ1** does not present either any flexible alkyl substituent on its backbone or phenothiazine substituents, which can assume different conformations due

to the bending of the tricyclic system. Therefore, compared to the other compounds, it should be less prone to the non-radiative energy losses resulting from vibrational relaxation of the excited state. This is supported by its relatively low SS value, as can be seen in Table 1, indicative of a lower degree of structural reorganization in the excited state. Finally, from the TAS studies reported in Fig. 3 and 4, it can also be seen that the initial spectral evolution for **DQ1**, assigned to a fast electronic relaxation of the molecule, appears slower than that of the other emitters seem to indicate similar rate constants for all compounds. The variation of Φ_f values with concentrations for all compounds both in the PMMA and PCMA matrices is reported in Fig. 10. All the collected results possibly suggest that even PCMA could experience compatibility issues at the highest fluorophore content of 1.8–2 wt%, which often requires maximizing the solar harvesting features of the LSC collectors. An accessible solution to overcome such an issue would be using copolymers made from methyl methacrylate and cyclo-hexyl methacrylate to take advantage of both the film stability induced by the former and the effective fluorophore dispersion allowed by the latter. Research efforts aimed at developing these new aspects are currently being pursued in our labs.

Transient absorption spectroscopy studies in polymer matrices. All the transient absorption spectra of the samples dispersed in the polymer appeared very similar (Fig. S17 and S18, ESI†): an intense and broad positive excited state absorption band was observed soon after excitation, covering the most of the spectrum. The intensity of the signal gradually decreases in time, without significant spectral evolution.

The dynamic Stokes shift observed in solution is barely observed in the matrix, because of the lower vibrational freedom and more constrained geometry experienced by the molecules in such an environment. The intensity of the absorption signal decayed bi-exponentially in all **DQ** samples, with the excited state showing a relatively long lifetime of >1.5 ns. Overall, these measurements show that the excited state relaxation is dominated by the radiative channel also in the polymer, and that
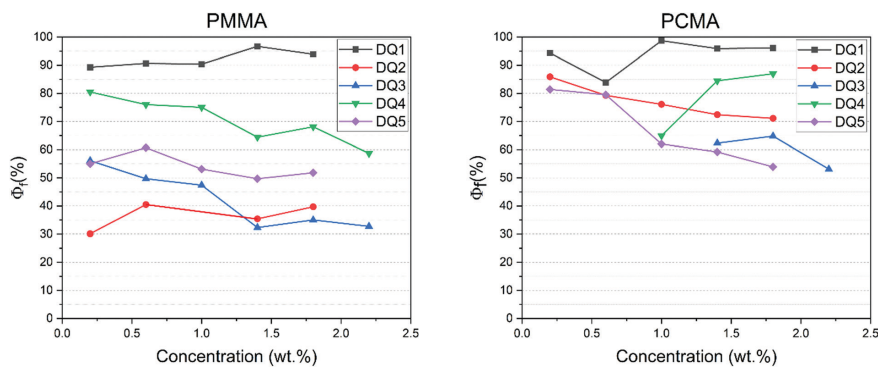

Fig. 10 Φ_f values (%) of the PMMA (left) and PCMA (right) films tested at different fluorophore concentrations.

Paper

the variation in Φ_f observed when moving from the solution to the solid phase can mainly be associated with both the more restricted conformation adopted by the different molecules in the polymer and the degree of dispersibility of the various compounds in the matrix. To demonstrate the effect of the matrix, which can also induce a decreased emission efficiency in the case of suboptimal compatibility, Fig. 11 reports the comparison of the kinetic traces measured at the maximum of the excited state absorption band (640 nm) for **DQ5** in toluene and in the two polymer matrices, PMMA and PCMA (1.0 wt%). It is evident that the fast decay component has a higher weight in the polymers compared to the solution, which affects the overall Φ_f observed in the different environments. This is most probably due to the lower conformational freedom experienced by the molecules in the polymer matrix, which reduces the degrees of structural rearrangement in the excited state, as also evidenced by the reduced dynamic Stokes shift of the stimulated emission band (see Fig. S17 and S18, ESI†). To complete the characterization of the films, fluorescence lifetime measurements have also been performed for all compounds dispersed in PMMA at 1.0 wt% concentration. The fluorescence decay rates are similar for all compounds, with lifetimes in the 4–8 ns time range, quite typical of organic fluorophores. Fluorescence lifetimes are slightly shorter for **DQ4** and **DQ5** if compared to the other molecules. We found that the best fitting results (with a χ^2 value of about 1) were obtained for a bi-exponential decay: this could reflect either the presence of small inhomogeneities in the chemical environment surrounding the fluorophore molecules or the formation of oligomers with slightly different decay rates. The fluorescence decay curves and lifetimes are reported in the ESI† (Fig. S19 and Table S1).

3.4 LSC performances

Before determining the photon efficiencies of the prepared thin-film LSCs, auto-absorption in the active film was analysed. The measurements were performed by irradiating the surface of the selected devices with a laser ($\lambda_{exc} = 405$ nm, 1 mW cm^{-2})
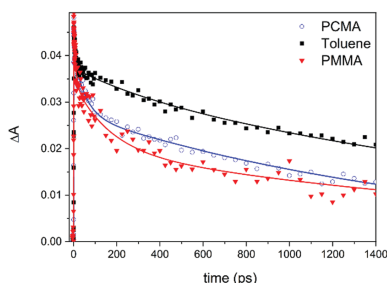

Fig. 11 Comparison of the kinetic trace at 640 nm measured for **DQ5** in toluene (black squares); PCMA (blue open circles); PMMA (red filled triangles). Continuous lines represent fit from global analysis. The associated time constants are reported in Fig. 4(d), Fig. S18.1(d) and S182(b) (ESI†).

and the edge-emitted power was recorded as a function of the optical pathlength distance between the excitation spot and the collecting edge (Fig. S21, ESI†). LSCs based on **LR305**, **DQ1** and **DQ4** were evaluated. **LR305** was selected to be as the state-of-the-art fluorophore in LSC, while **DQ1** and **DQ4** as fluorophores with top and intermediate fluorescence quantum efficiencies, as reported in Figure 10. Fluorophore content was selected in terms of the maximum absolute Φ_f, *i.e.*, 1.4 wt% for **DQ1** and **DQ4**. As far as **LR305** is concerned, the concentration of 1.0 wt% was selected in terms of the maximum LSC performance as determined in a previous study.[8]

Notably, as the optical pathlength distance increased, the edge-emitted power was found to progressively decrease in all cases (Fig. S21a, ESI†). This phenomenon appeared more evident for the LSC based on **LR305**, possibly due to the lowest SS of 36 nm[27] compared to 106 nm for **DQ1** and 89 nm for **DQ4**. Moreover, by comparing the collected emission spectra, an evident red-shift of about 20 nm in the emission maximum was observed in the case of **LR305**, thus supporting emission losses by the occurrence of reabsorption phenomena (Fig. S21b, ESI†).

The optical performances of LSC based on **LR305**, **DQ1** and **DQ4** were then evaluated in terms of the internal and external photon efficiency (η_{int} and η_{ext}, respectively) (Table 3). η_{int} and η_{ext} were obtained according to the recently published protocols[35] and calculated from eqn (S1) and (S2) (ESI†). In detail, η_{int} represents the ratio of photons collected at the LSC edges to the number of absorbed photons by the embedded fluorophores, and it is a key parameter to determine all lightguide losses. η_{ext} is the ratio of photons collected at the LSC edges to the number of total incident photons, and it also provides information about the solar harvesting features of the device.

It is worth noting that for both the η_{int} and η_{ext} parameters, **DQ1** was the best fluorophore in providing the highest LSC efficiencies with values of 42.9% and 6.2%, respectively. Surprisingly, the η_{int} of the LSC based on **LR305** resulted the lowest (16.6%). According to the η_{int} determination, the broadest absorption band of **LR305** adversely affects this parameter in largest extent.

Conversely, η_{ext} shows a different trend of performances, *i.e.*, with **DQ1** as the best fluorophore followed by the state-of-the-art **LR305**. **DQ4**, notwithstanding the higher but similar Φ_f values (64.4 against 59.3%), possibly suffers from inferior solar harvesting characteristics with respect to the perylene bisimide chromophore.

Moreover, the photon efficiencies obtained here appear to be higher than those reported in a recent study.[56] Overall, **DQ1** turns out to be a very promising fluorophore for employment in LSCs.

However, for LSC practical applications, **DQ1**/PMMA stability must be assessed through performance measurements over time.

Table 3 Best Φ_f (%) and optical performances obtained for fluorophores **DQ1** and **DQ4** dispersed in PMMA in comparison with **LR305**

Chromophore	Matrix	Concentration (wt%)	Φ_f (%)	η_{int} (%)	η_{ext} (%)
LR305	PMMA	1.0	59.3	16.6	4.7
DQ1	PMMA	1.4	96.7	42.9	6.2
DQ4	PMMA	1.4	64.4	27.9	3.6

Notably, **DQ1**/PMMA films did not show any noticeable variation in their visible appearance following their preparation, and with optical performances maintained over months. Also, the thermal stability of the fluorophore was evaluated through thermogravimetric analysis showing that the samples maintained at least 95% of their weight up to 300 °C (Fig. S25, ESI†). The photostability of **DQ1**/PMMA LSCs was then preliminarily investigated by continuously irradiating a 0.25 cm^2 spot of the film at 430 nm with a 450 W Xe arc lamp under aerobic conditions. The film samples were placed in the spectrofluorometer chamber and fixed in the solid-state holder, thus receiving irradiances of about 50 μW cm^{-2}. Notably, **DQ1** retained 97.8% of its emission after two hours of continuous excitation compared to the 98.8% of **LR305** (Fig. S26, ESI†), thus suggesting a potentially sufficient photostability. Further experiments will be carried out in order to definitely assess this behaviour.

4. Conclusions

In conclusion, we have reported the preparation of thin-film LSCs having optical properties superior to those of the state-of-the-art solar collectors. This result was obtained by replacing the reference fluorophore **LR305** in PMMA and PCMA films with a series of new high quantum yield, donor–acceptor–donor (D–A–D) photostable fluorophores (**DQ1–5**) characterized by a central quinoxalinic acceptor core and triarylamines or phenothiazine as donor groups. Thanks to their structures, all fluorophores presented excited states characterized by a high degree of intramolecular charge transfer, which was confirmed by both DFT computational analysis and transient absorption spectroscopy studies. Notably, they displayed intense emissions between 550 and 600 nm with Stokes shifts at about 80–120 nm that helped in minimizing the auto-absorption effects when dispersed in polymers at high content. Furthermore, decoration with long alkyl chains at different parts of the molecular backbone allowed tuning their dispersibility in polymer films. It is worth noting that **DQ1** in PMMA provided outstanding LSC η_{int} and η_{ext} values of 42.9 and 6.2%, respectively. This result was addressed to the effective combination between high phase compatibility and excellent quantum yield, which for **DQ1** reached remarkable values of >95% in both PMMA and PCMA matrices.

In view of these performances, our findings provide new advances for the widespread distribution of the LSC/PV system in the integrated photovoltaics, which is the backbone of the zero-energy building European target.

Conflicts of interest

There are no conflicts to declare.

Acknowledgements

Notes and references

1 N. Armaroli and V. Balzani, *Chem. – Eur. J.*, 2016, **22**, 32–57.
2 G. M. Wilson, M. Al-Jassim, W. K. Metzger, S. W. Glunz, P. Verlinden, G. Xiong, L. M. Mansfield, B. J. Stanbery, K. Zhu, Y. Yan, J. J. Berry, A. J. Ptak, F. Dimroth, B. M. Kayes, A. C. Tamboli, R. Peibst, K. Catchpole, M. O. Reese, C. S. Klinga, P. Denholm, M. Morjaria, M. G. Deceglie, J. M. Freeman, M. A. Mikofski, D. C. Jordan, G. TamizhMani and D. B. Sulas-Kern, *J. Phys. D: Appl. Phys.*, 2020, **53**, 493001.
3 J. S. Batchelder, A. H. Zewai and T. Cole, *Appl. Opt.*, 1979, **18**, 3090.
4 W. H. Weber and J. Lambe, *Appl. Opt.*, 1976, **15**, 2299.
5 J. Roncali, *Adv. Energy Mater.*, 2020, **10**, 2001907.
6 F. Meinardi, F. Bruni and S. Brovelli, *Nat. Rev. Mater.*, 2017, **2**, 17072.
7 G. Griffini, *Front. Mater.*, 2019, **6**, 29.
8 F. J. Ostos, G. Iasilli, M. Carlotti and A. Pucci, *Polymers*, 2020, **12**, 2898.
9 T. M. Clarke, K. C. Gordon, W. M. Kwok, D. L. Phillips and D. L. Officer, *J. Phys. Chem. A*, 2006, **110**, 7696–7702.
10 C. Papucci, A. Dessì, C. Coppola, A. Sinicropi, G. Santi, M. di Donato, M. Taddei, P. Foggi, L. Zani, G. Reginato, A. Pucci, M. Calamante and A. Mordini, *Dyes Pigm.*, 2021, **188**, 109207.
11 H. J. Song, D. H. Kim, E. J. Lee and D. K. Moon, *J. Mater. Chem. A*, 2013, **1**, 6010–6020.
12 B. Li, M. Zhao and F. Zhang, *ACS Mater. Lett.*, 2020, **2**, 905–917.
13 P. Y. Gu, J. Zhang, G. Long, Z. Wang and Q. Zhang, *J. Mater. Chem. C*, 2016, **4**, 3809–3814.
14 L. Lyu, R. Su, S. Y. Al-Qaradawi, K. A. Al-Saad and A. El-Shafei, *Dyes Pigm.*, 2019, **171**, 107683.
15 W. Liu, Z. Liu, Z. Yan, L. Wang, H. Xu, H. Wang and B. Zhao, *Dyes Pigm.*, 2021, **191**, 109305.
16 D. Gedefaw, M. Prosa, M. Bolognesi, M. Seri and M. R. Andersson, *Adv. Energy Mater.*, 2017, **7**, 1700575.
17 M. L. Jiang, M. Wen, Z. Chen, W. Tsai, T. Lin, T. J. Chow and Y. J. Chang, *ChemSusChem*, 2019, **12**, 3654–3665.
18 B. D. Lindner, Y. Zhang, S. Höfle, N. Berger, C. Teusch, M. Jesper, K. I. Hardcastle, X. Qian, U. Lemmer, A. Colsmann, U. H. F. Bunz and M. Hamburger, *J. Mater. Chem. C*, 2013, **1**, 5718–5724.

19 H. Zhang, Y. Wu, W. Zhang, E. Li, C. Shen, H. Jiang, H. Tian and W. H. Zhu, *Chem. Sci.*, 2018, **9**, 5919–5928.

20 H. J. Son, W. S. Han, D. H. Yoo, K. T. Min, S. N. Kwon, J. Ko and S. O. Kang, *J. Org. Chem.*, 2009, **74**, 3175–3178.

21 Y. Chen, Y. Ling, L. Ding, C. Xiang and G. Zhou, *J. Mater. Chem. C*, 2016, **4**, 8496–8505.

22 T. A. Geervliet, I. Gavrila, G. Iasilli, F. Picchioni and A. Pucci, *Chem. – Asian J.*, 2019, **14**, 877–883.

23 R. Mori, G. Iasilli, M. Lessi, A. B. Muñoz-García, M. Pavone, F. Bellina and A. Pucci, *Polym. Chem.*, 2018, **9**, 1168–1177.

24 J. Lucarelli, M. Lessi, C. Manzini, P. Minei, F. Bellina and A. Pucci, *Dyes Pigm.*, 2016, **135**, 154–162.

25 G. Iasilli, R. Francischello, P. Lova, S. Silvano, A. Surace, G. Pesce, M. Alloisio, M. Patrini, M. Shimizu, D. Comoretto and A. Pucci, *Mater. Chem. Front.*, 2019, **3**, 429–436.

26 F. De Nisi, R. Francischello, A. Battisti, A. Panniello, E. Fanizza, M. Striccoli, X. Gu, N. L. C. Leung, B. Z. Tang and A. Pucci, *Mater. Chem. Front.*, 2017, **1**, 1406–1412.

27 M. Carlotti, E. Fanizza, A. Panniello and A. Pucci, *Sol. Energy*, 2015, **119**, 452–460.

28 G. Albano, T. Colli, T. Biver, L. A. Aronica and A. Pucci, *Dyes Pigm.*, 2020, **178**, 108368.

29 G. Albano, T. Colli, L. Nucci, R. Charaf, T. Biver, A. Pucci and L. A. Aronica, *Dyes Pigm.*, 2020, **174**, 108100.

30 P. L. Gentili, M. Mugnai, L. Bussotti, R. Righini, P. Foggi, S. Cicchi, G. Ghini, S. Viviani and A. Brandi, *J. Photochem. Photobiol., A*, 2007, **187**, 209–221.

31 M. Di Donato, A. Iagatti, A. Lapini, P. Foggi, S. Cicchi, L. Lascialfari, S. Fedeli, S. Caprasecca and B. Mennucci, *J. Phys. Chem. C*, 2014, **118**, 23476–23486.

32 E. R. Henry, *Biophys. J.*, 1997, **72**, 652–673.

33 I. H. M. Van Stokkum, D. S. Larsen and R. Van Grondelle, *Biochim. Biophys. Acta, Bioenerg.*, 2004, **1657**, 82–104.

34 J. J. Snellenburg, S. Laptenok, R. Seger, K. M. Mullen and I. H. M. van Stokkum, *J. Stat. Softw.*, 2012, **49**, 1–22.

35 M. G. Debije, R. C. Evans and G. Griffini, *Energy Environ. Sci.*, 2021, **14**, 293–301.

36 C. Yang, D. Liu and R. R. Lunt, *Joule*, 2019, **3**, 2871–2876.

37 B. Mátravölgyi, T. Hergert, A. Thurner, B. Varga, N. Sangiorgi, R. Bendoni, L. Zani, G. Reginato, M. Calamante, A. Sinicropi, A. Sanson, F. Faigl and A. Mordini, *Eur. J. Org. Chem.*, 2017, 1843–1854.

38 G. Qian, B. Dai, M. Luo, D. Yu, J. Zhan, Z. Zhang, M. Dongge and Z. Y. Wang, *Chem. Mater.*, 2008, **20**, 6208–6216.

39 A. Dessì, M. Calamante, A. Mordini, M. Peruzzini, A. Sinicropi, R. Basosi, F. Fabrizi De Biani, M. Taddei, D. Colonna, A. Di Carlo, G. Reginato and L. Zani, *RSC Adv.*, 2015, **5**, 32657–32668.

40 M. J. Frisch, G. W. Trucks, H. B. Schlegel, G. E. Scuseria, M. A. Robb, J. R. Cheeseman, G. Scalmani, V. Barone, G. A. Petersson, H. Nakatsuji, X. Li, M. Caricato, A. V. Marenich, J. Bloino, B. G. Janesko, R. Gomperts,

B. Mennucci, H. P. Hratchian, J. V. Ortiz, A. F. Izmaylov, J. L. Sonnenberg, D. Williams-Young, F. Ding, F. Lipparini, F. Egidi, J. Goings, B. Peng, A. Petrone, T. Henderson, D. Ranasinghe, V. G. Zakrzewski, J. Gao, N. Rega, G. Zheng, W. Liang, M. Hada, M. Ehara, K. Toyota, R. Fukuda, J. Hasegawa, M. Ishida, T. Nakajima, Y. Honda, O. Kitao, H. Nakai, T. Vreven, K. Throssell, J. A. Montgomery Jr, J. E. Peralta, F. Ogliaro, M. J. Bearpark, J. J. Heyd, E. N. Brothers, K. N. Kudin, V. N. Staroverov, T. A. Keith, R. Kobayashi, J. Normand, K. Raghavachari, A. P. Rendell, J. C. Burant, S. S. Iyengar, J. Tomasi, M. Cossi, J. M. Millam, M. Klene, C. Adamo, R. Cammi, J. W. Ochterski, R. L. Martin, K. Morokuma, O. Farkas, J. B. Foresman and D. J. Fox, *GAUSSIAN16: Gaussian 16, Revision C.01*, Gaussian, Inc., Wallingford CT, 2016.

41 A. D. Becke, *J. Chem. Phys.*, 1993, **98**, 5648–5652.

42 C. Lee, W. Yang and R. G. Parr, *Phys. Rev. B: Condens. Matter Mater. Phys.*, 1988, **37**, 785–789.

43 J. Tomasi, B. Mennucci and R. Cammi, *Chem. Rev.*, 2005, **105**, 2999–3093.

44 X. Lu, S. Fan, J. Wu, X. Jia, Z.-S. Wang and G. Zhou, *J. Org. Chem.*, 2014, **79**, 6480–6489.

45 K. Lušpai, A. Staško, V. Lukeš, D. Dvoranová, Z. Barbieriková, M. Bella, V. Milata, P. Rapta and V. Brezová, *J. Solid State Electrochem.*, 2015, **19**, 113–122.

46 K. Y. Chiu, T. X. Su, J. H. Li, T. H. Lin, G. S. Liou and S. H. Cheng, *J. Electroanal. Chem.*, 2005, **575**, 95–101.

47 F. Donati, A. Pucci, C. Cappelli, B. Mennucci and G. Ruggeri, *J. Phys. Chem. B*, 2008, **112**, 3668–3679.

48 J. M. Drake, M. L. Lesiecki, J. Sansregret and W. R. L. Thomas, *Appl. Opt.*, 1982, **21**, 2945.

49 M. G. Debije and P. P. C. Verbunt, *Adv. Energy Mater.*, 2012, **2**, 12–35.

50 J. Donovalová, M. Cigáň, H. Stankovičová, J. Gašpar, M. Danko, A. Gáplovský and P. Hrdlovič, *Molecules*, 2012, **17**, 3259–3276.

51 M. Kaholek and P. Hrdlovič, *J. Photochem. Photobiol., A*, 1997, **108**, 283–288.

52 F. Gianfaldoni, F. De Nisi, G. Iasilli, A. Panniello, E. Fanizza, M. Striccoli, D. Ryuse, M. Shimizu, T. Biver and A. Pucci, *RSC Adv.*, 2017, **7**, 37302–37309.

53 C. Papucci, T. A. Geervliet, D. Franchi, O. Bettucci, A. Mordini, G. Reginato, F. Picchioni, A. Pucci, M. Calamante and L. Zani, *Eur. J. Org. Chem.*, 2018, 2657–2666.

54 A. Pucci, N. Tirelli, G. Ruggeri and F. Ciardelli, *Macromol. Chem. Phys.*, 2005, **206**, 102–111.

55 N. Tirelli, S. Amabile, C. Cellai, A. Pucci, L. Regoli, G. Ruggeri and F. Ciardelli, *Macromolecules*, 2001, **34**, 2129–2137.

56 F. Corsini, A. Nitti, E. Tatsi, G. Mattioli, C. Botta, D. Pasini and G. Griffini, *Adv. Opt. Mater.*, 2021, **9**, 2100182.

4.7.1. Additional Computational Results

Computational details

Molecular and electronic properties of compounds **DQ1**, **DQ2**, **DQ3**, **DQ4** and **DQ5** have been computed *via* Density Functional Theory (DFT) [2,3] and Time Dependent DFT (TDDFT) [4,5] methods, using Gaussian 16, Revision C.01 suite of programs [6]. The S_0 optimized geometries of compounds **DQ1-5** have been obtained at B3LYP [7,8]/6-31G* level of theory in *vacuo*. The same level of theory has been employed to calculate the energy and the wavefunction plots of frontier molecular orbitals (FMOs) in solvent (toluene), while the S_1 optimized geometries have been computed at TD-CAM-B3LYP [9]/6-31G* level of theory. The UV–Vis spectroscopic properties of the analyzed compounds, including absorption (λ_{max}^{abs}) and emission (λ_{max}^{emi}) maxima, vertical excitation (E_{exc}) and emission (E_{emi}) energies, oscillator strengths (f) and composition (%) in terms of molecular orbitals for the lowest singlet-singlet excitations and the singlet-singlet emissions, $S_0{\rightarrow}S_1$ and $S_1{\rightarrow}S_0$ respectively, have been computed in toluene on the minimized structures at TD-MPW1K [10]/6-311+G(2d,p) level of theory. Solvent effects have been included by using the polarizable continuum model (PCM) and, in the case of the emission maxima, using the Linear-Response implementation (LR-PCM) [11,12]. The electronic properties and the absorption maxima of compound **DQ3** have been further investigated including the solvent effects by means of the Averaged Solvent Electrostatic Potential from Molecular Dynamics (ASEP/MD) method [13], using Gaussian09 and Gromacs-4.5 programs for QM calculations and MD simulations, respectively [14,15]. Geometry optimization of the solute (**DQ3**) has been carried out *via* DFT at B3LYP/6-31G* level of theory in toluene, while absorption maxima and vertical excitation energies have been calculated by means of TDDFT method at MPW1K/6-311+G(2d,p) level of theory. MD simulations included 1168 toluene molecules and one molecule of solute in a dodecahedral rhomboid box of 7 nm, to reproduce the experimental solvent density. All the molecules have been simulated at fixed intramolecular geometry and the Lennard-Jones parameters for the solvent and the solute have been taken from the optimized potentials for liquid simulations all atoms (OPLS-AA) force field [16]. The electrostatic interaction has been calculated with the Ewald method [17] at fixed temperature (298 K) using the Nose-Hoover thermostat [18]. Each simulation has been run in the NVT ensemble for 1.000 ps, with a time step of 1 fs, where the first 250 ps have been used for

equilibration and the last 750 ps for production. The solute atomic charges have been obtained from QM calculations using the CHELPG (Charges from Electrostatic Potential, Grid) method [19,20] and they have been updated at each ASEP/MD cycle. The iterative ASEP/MD procedure stops when convergence in the QM energy (0.0001 au) is reached. Here, 15 cycles of ASEP/MD have been performed. Final results have been obtained by averaging the last four ASEP/MD cycles, hence they represent an effective simulation time of 3.0 ns.

Results

The ground- (S_0) and excited-states (S_1) optimized geometries of compounds **DQ1-5** are shown in Figure 4.7.1. The S_0 optimized geometries in *vacuo* show dihedral angles between the quinoxaline acceptor core and the donor groups in the range of 43.1° and 44.6°, whereas calculated geometries for S_1 show an overall increased planarity of the molecules (dihedral angles between 21.0° and 28.4°).
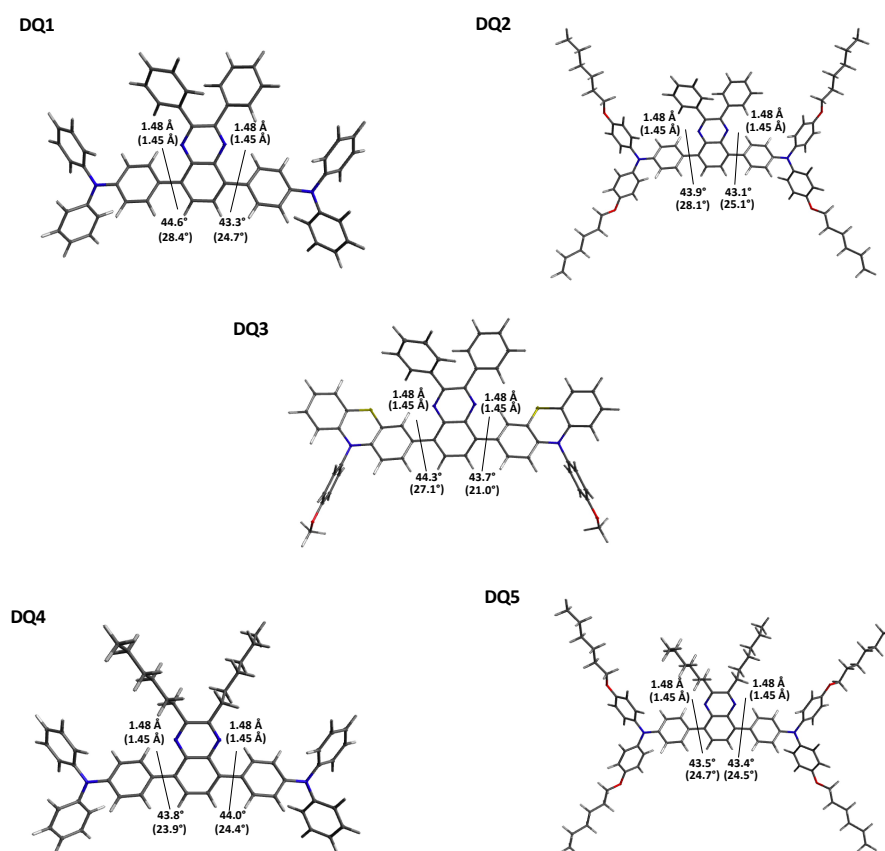
Figure 4.7.1. Bond lengths (Å) and dihedral angles (degrees) of S_0 and S_1 (in brackets) optimized geometries of compounds **DQ1-5**.

154

The analysis of the Kohn-Sham frontier molecular orbitals (FMOs) energies revealed that the HOMO-1 and the HOMO energies resulted to be more stabilized, while those of the LUMO and the LUMO+1 are less stabilized moving from S_0 to S_1 (Tables 4.7.1 and 4.7.2). From the inspection of wavefunction plots, it emerges that the LUMO and the LUMO+1 electron densities are mainly confined on the quinoxaline core, while those of the HOMO-1 and the HOMO are mostly delocalized on the triarylamines and phenothiazine donor groups, both in S_0 and S_1 (Figures 4.7.2 and 4.7.3).

Table 4.7.1. S_0 B3LYP/6-31G* FMOs energies (eV) of compounds **DQ1-5** computed in toluene (using PCM).

Molecule	HOMO-1	HOMO	LUMO	LUMO+1
DQ1	-5.057	-4.864	-2.015	-1.280
DQ2	-4.718	-4.544	-1.923	-1.223
DQ3	-5.001	-4.863	-1.980	-1.234
DQ4	-5.032	-4.837	-1.798	-0.680
DQ5	-4.689	-4.513	-1.682	-0.508

Table 4.7.2. S_1 TD-CAM-B3LYP/6-31G* FMOs energies (in eV) of compounds **DQ1-5** computed in toluene (using PCM).

Molecule	HOMO-1	HOMO	LUMO	LUMO+1
DQ1	-6.347	-5.718	-1.203	-0.017
DQ2	-6.003	-5.487	-1.117	0.054
DQ3	-6.172	-5.707	-1.233	0.011
DQ4	-6.325	-5.677	-1.059	0.514
DQ5	-5.979	-5.441	-0.952	0.654
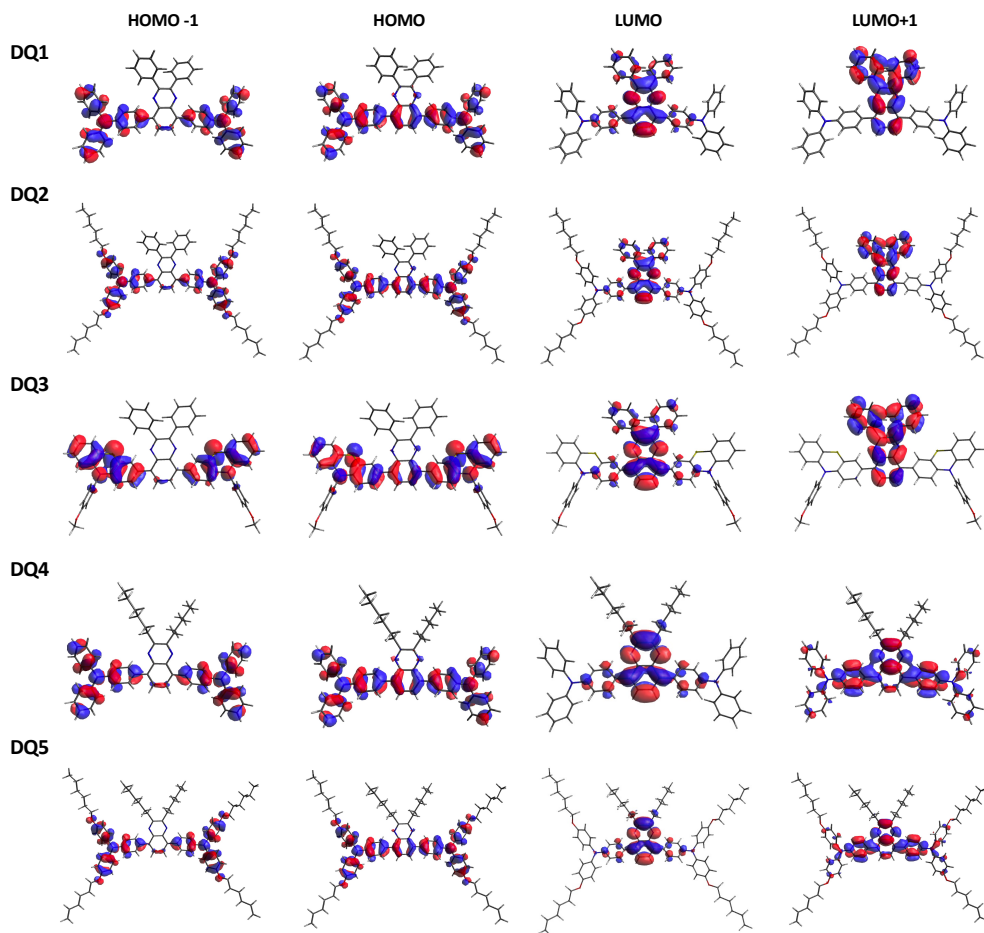
Figure 4.7.2. S$_0$ FMOs plots of compounds **DQ1-5** computed in toluene at B3LYP/6-31G* level of theory (using PCM).
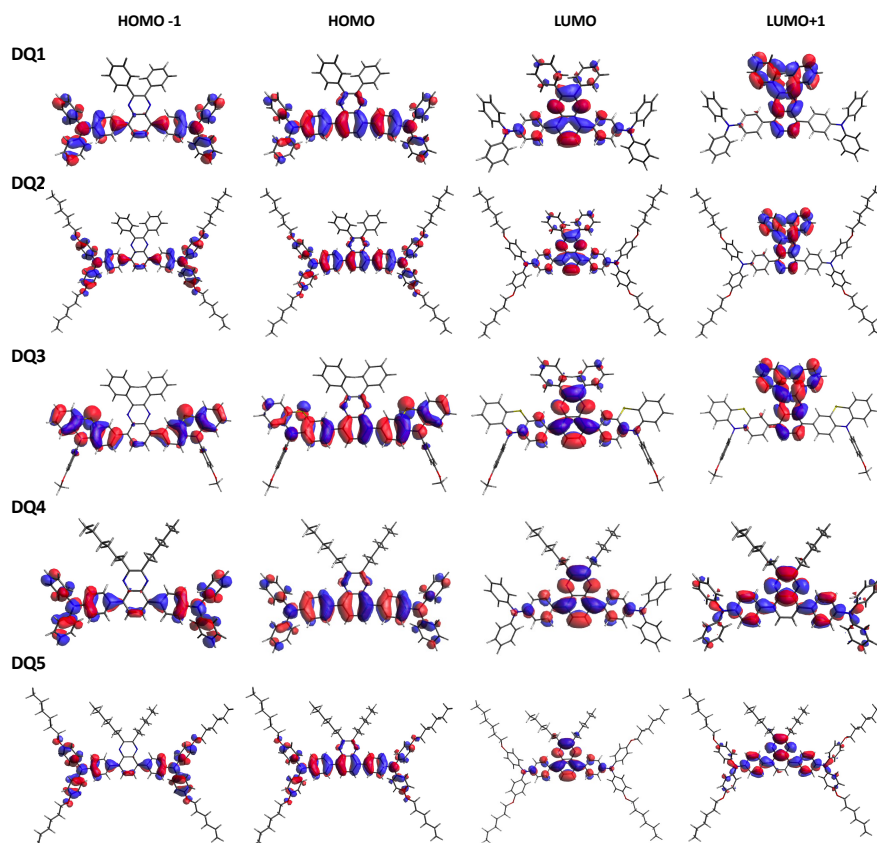
Figure 4.7.3. S$_1$ FMOs plots of compounds **DQ1-5** computed in toluene with TD-CAM-B3LYP/6-31G* (using PCM).

TD-MPW1K/6-311+G(2d,p) absorption (λ_{max}^{abs}) and emission λ_{max}^{emi} maxima, vertical excitation (E$_{exc}$) and emission (E$_{emi}$) energies, oscillator strengths (f) and composition (%) in terms of molecular orbitals for the lowest singlet-singlet excitations (S$_0$→S$_1$) and emissions (S$_1$→S$_0$) in toluene of compounds **DQ1-5** are shown in Table 4.7.3 and 4.7.4, respectively.

Table 4.7.3. TD-MPW1K/6-311+G(2d,p) absorption maxima (λ_{max}^{abs} in nm), excitation energies (E$_{exc}$ in eV), oscillator strengths (f) and contributions (%) to S$_0$→S$_1$transition in toluene (by using PCM) of compounds **DQ1-5.**

Molecule	λ_{max}^{abs}	E$_{exc}$	f	Contribution (%)	Exp (eV) (ΔE in eV)
DQ1	409	3.02	0.66	90% H→L	2.86 (0.16)
DQ2	434	2.85	0.66	90 % H→L	2.71 (0.14)
DQ3	404	3.07	0.51	88% H→L	2.74 (0.33)
DQ4	386	3.21	0.94	89% H→L	3.12 (0.09)
DQ5	406	3.06	0.94	89% H→L	2.98 (0.08)

DQ1-5 compounds show absorption maxima between 386 and 434 nm, corresponding to 3.21-2.85 eV. Looking at the wavefunction plots of MOs involved in the lowest energy transitions (Figures 4.7.2 and 4.7.3), it is evident that the $S_0 \rightarrow S_1$ excitations are characterized by an intramolecular charge transfer from the donors to the acceptor group, involving HOMO→LUMO orbitals. The computed excitation energies are in good agreement with the experimental values. Indeed, even if the TDDFT accuracy for the determination of transition energies is strictly dependent on: i) the selected functional (i.e. functionals containing a small fraction of exact HF exchange tend to underestimate the transition energies, while functionals incorporating $\cong$ 40-50% of exact HF exchange tend to overestimate them), ii) the set of considered molecules and iii) a good description of the surrounding environment [21,22], it has been recently reported that with hybrid functionals for low-lying valence excited states of organic molecules there is a typical error of 0.2-0.4 eV [23]. Hence, the vertical excitation energies of **DQ1-5** compounds fall in the expected accuracy of the TDDFT method. However, the error found for compound **DQ3** is larger than the others.

Table 4.7.4. TD-MPW1K/6-311+G(2d,p) emission maxima (λ_{max}^{emi} in nm), emission energies (E_{emi} in eV), oscillator strengths (f) and contributions (%) to the transition $S_1 \rightarrow S_0$ in toluene (by using PCM) of compounds **DQ1-5**.

Molecule	λ_{max}^{emi}	E_{emi}	f	Contribution (%)	Exp (eV) (ΔE in eV)
DQ1	537	2.31	0.83	96% L→H	2.30 (0.01)
DQ2	561	2.21	0.83	95% L→H	2.19 (0.02)
DQ3	542	2.29	0.77	95% L→H	2.06 (0.23)
DQ4	514	2.41	1.07	96% L→H	2.42 (0.01)
DQ5	532	2.33	1.08	95% L→H	2.34 (0.01)

The LR-PCM computed emission maxima in toluene fall in the 514-561 nm range, corresponding to 2.41-2.21 eV. They are in very good agreement with the experimental values, as the energy difference is at maximum 0.02 eV for compounds **DQ1**, **DQ2**, **DQ4** and **DQ5**, while an energy difference of 0.23 eV is found for compound **DQ3**. However, these values are all in the expected accuracy of the TDDFT method for the transition energies calculations [12, 21-23]. The Stokes Shift of compounds **DQ1-5**, which have been determined starting from the calculated absorption and emission maxima, have been compared with those obtained from experimental results and they are reported in Table 4.7.5. It is possible to notice that even if calculated Stokes Shifts tend to overestimate the

experimental ones, they are in very good agreement, as the energy difference is at maximum 0.15 eV.

Table 4.7.5. Calculated and experimental Stokes Shift values (eV).

Molecule	Calculated Stokes Shift (eV)	Experimental Stokes Shift (eV)
DQ1	0.71	0.56
DQ2	0.64	0.53
DQ3	0.78	0.68
DQ4	0.80	0.71
DQ5	0.73	0.62

All the results obtained from the computational investigation are very closed to the experimental ones, except for the estimation of the vertical excitation energy of **DQ3**. For this reason, the electronic properties and the absorption maxima of this molecule have been further investigated including the solvent effects by means of the ASEP/MD method, in order to deep examine the possible influence of the solute-solvent interactions on **DQ3** spectroscopic properties [13]. The internal energy (a.u.) and the dipole moment (D) variations throughout the 15 ASEP/MD cycles for compound **DQ3** are reported in Figures 4.7.4 and 4.7.5, respectively.
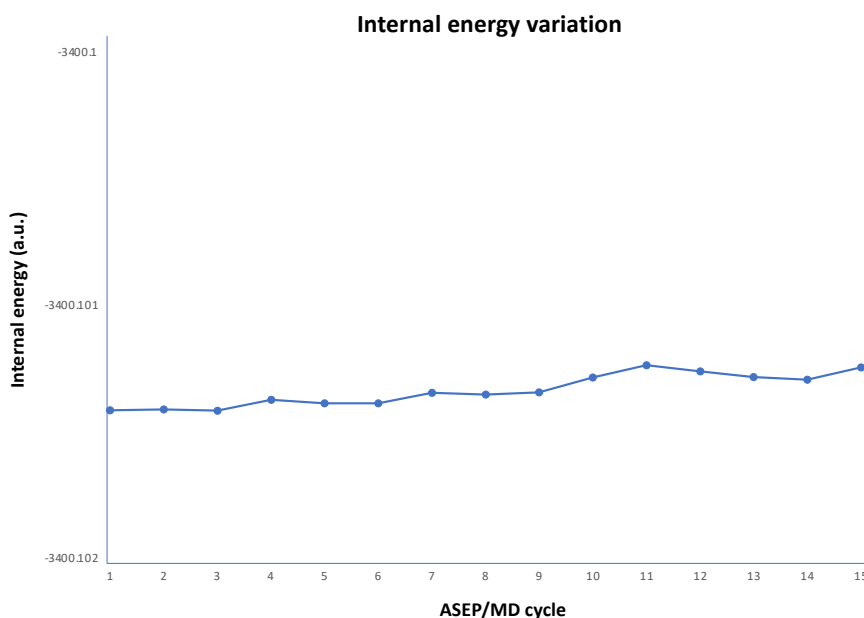
Figure 4.7.4. Internal energy variation (a.u) of compound **DQ3** throughout the 15 ASEP/MD cycles.
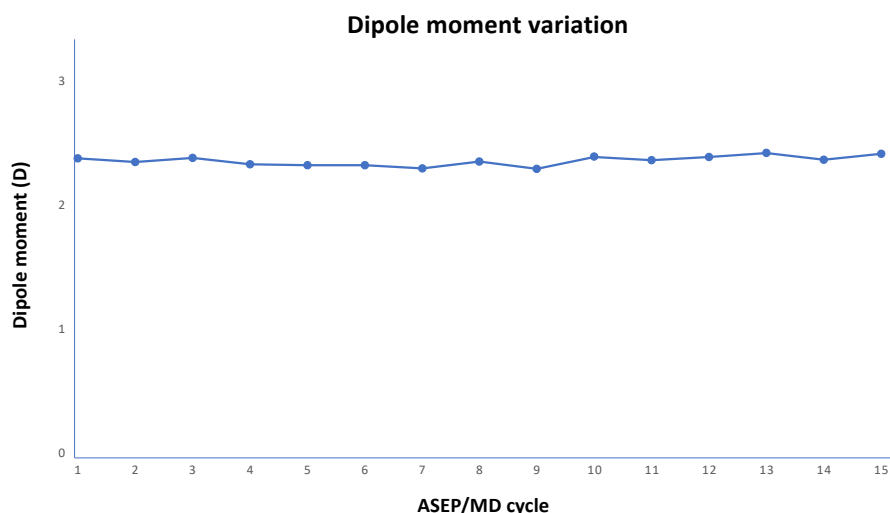
Figure 4.7.5. Dipole moment variation of compound **DQ3** throughout the 15 ASEP/MD cycles.

The plots of the internal energy and the dipole moment variations show that there are not consistent fluctuations between cycles, hence the last four ASEP/MD cycles have been considered for the calculation of the vertical excitation energy of compound **DQ3**. In Table 4.7.6 the S_0 optimized bond lengths (Å) and dihedral angles (degrees) between the quinoxaline acceptor core and the phenothiazine donor groups for the last four considered ASEP/MD cycles are shown. In Figure S2 the involved atoms are highlighted.

Table 4.7.6. Bond lengths (Å) and dihedral angles (degrees) of S_0 optimized geometries at B3LYP/6-31G* in toluene of compound **DQ3** for the last four considered ASEP/MD cycles.

ASEP/MD cycle	Bond lengths (Å)		Dihedral angles (degrees)	
	C28-C7	C8-C46	C35-C28-C7-C2	C1-C8-C46-C52
12	1.48	1.48	42.2	41.6
13	1.48	1.48	42.0	41.3
14	1.48	1.48	42.0	41.4
15	1.48	1.48	42.3	41.5

TD-MPW1K/6-311+G(2d,p) absorption (λ_{max}^{abs}) maxima, vertical excitation (E_{exc}) energies, oscillator strengths (f) and composition (%) in terms of molecular orbitals for the lowest singlet-singlet excitations ($S_0 \rightarrow S_1$) in toluene of compounds **DQ3** for the last four ASEP/MD cycles are shown in Table 4.7.7.

160

Table 4.7.7. TD-MPW1K/6-311+G(2d,p) absorption maxima (λ_{max}^{abs} in nm), excitation energies (E_{exc} in eV), oscillator strengths (f) and contributions (%) to $S_0 \rightarrow S_1$ transition in toluene (by using ASEP/MD) of compound **DQ3.**

ASEP/MD cycle	λ_{max}^{abs}	E_{exc}	f	Contribution (%)
12	404	3.07	0.46	89% H→L
13	403	3.08	0.46	89% H→L
14	404	3.07	0.45	89% H→L
15	403	3.08	0.46	89% H→L

Within the ASEP/MD method, the vertical excitation energy value is taken as the average value of the calculated vertical excitation energies of the four considered cycles, corresponding to 3.075 eV $\cong$ 3.08 eV (403 nm), hence the energy difference with the experimental **DQ3** absorption value is 0.34 eV. Additionally, the vertical excitation energy calculated with ASEP/MD method is in very good agreement with that obtained employing PCM as solvation method (3.07 eV – 404 nm), hence it is possible to assume that the solvent does not have an important effect on the solute properties. To further confirm this assumption, the vertical excitation energy of **DQ3** has been also calculated in *vacuo* and it has been compared to calculated values in toluene by using PCM and ASEP/MD solvation methods (Table 4.7.8).

Table 4.7.8. TD-MPW1K/6-311+G(2d,p) absorption maxima (λ_{max}^{abs} in nm), excitation energies (E_{exc} in eV), oscillator strengths (f) and contributions (%) to $S_0 \rightarrow S_1$ transition in *vacuo* and in toluene by using PCM and ASEP/MD of compound **DQ3.**

Medium	λ_{max}^{abs}	E_{exc}	f	Contribution (%)
Vacuo	401	3.09	0.42	89% H→L
Toluene (by PCM)	404	3.07	0.51	88% H→L
Toluene (by ASEP/MD)	403	3.08	0.46	89% H→L

From this preliminary study, it has not been possible to correctly reproduce the experimental absorption value of compound **DQ3** and it has been shown that the solvent does not have an important effect on the solute properties. To deeply examine this aspect, further computational studies could be carried out including the polarizable solvent in

ASEP/MD. An additional strategy could also consist in modifying the radius of the cavity within the PCM solvation method. Indeed, a reduced radius' cavity should stabilize the excited state of the solute, leading to smaller values of excitation energy.

In Supporting Information, additional results are reported, including the absorption maxima values of compound **DQ3** calculated with different levels of theory (using PCM). Moreover, the results obtained employing ASEP/MD method to one of the higher energy conformers of **DQ3**, here identified as **DQ3-a**, are reported too.

Supporting Information

Table S1. B3LYP/6-31G* relative energies (kcal/mol) *in vacuo* of different conformations of **DQ3**.

Conformers	ΔE
Selected DQ3	0.0
DQ3-a	+7.86
DQ3-b	+7.73
DQ3-c	+7.63
DQ3-d	+0.14
DQ3-e	+0.04
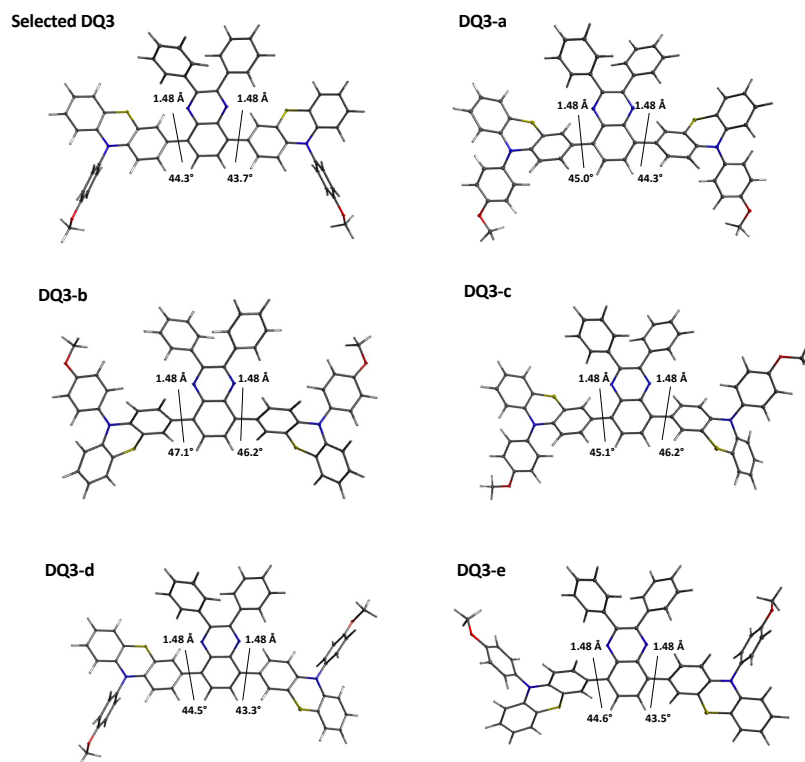
Figure S1. Bond lengths (Å) and dihedral angles (degrees) of S_0 optimized geometries of **DQ3** conformers.

Table S2. Absorption (λ_{max}^{abs}) maxima, vertical excitation (E_{exc}) energy, oscillator strengths (f) and composition (%) in terms of molecular orbitals for the lowest singlet-singlet excitations ($S_0 \rightarrow S_1$) in toluene (using PCM) of compound **DQ3** at different levels of theory.

Level of theory	λ_{max}^{abs}	E_{exc}	f	Contribution (%)	(ΔE in eV)
MPW1K/6-311++G(2d,2p)	404	3.07	0.51	88% H→L	0.33
CAM-B3LYP/6-311+G(2d,p)	384	3.23	0.61	76% H→L	0.49
CAM-B3LYP/6-311++G(2d,2p)	384	3.23	0.61	76% H→L	0.49
B3LYP/6-311+G(2d,p)	528	2.35	0.25	99% H→L	0.39
B3LYP/6-311++G(2d,2p)	528	2.35	0.25	99% H→L	0.39
wB97XD/6-311+G(2d,p)	371	3.35	0.66	61% H→L	0.61
wB97XD/6-311++G(2d,2p)	371	3.35	0.66	65% H→L	0.61
PBE0/6-311+G(2d,p)	493	2.51	0.30	98% H→L	0.23
PBE0/6-311++G(2d,2p)	493	2.51	0.30	98% H→L	0.23
PBE0/Def2TZVP	492	2.52	0.30	97% H→L	0.22
M062X/6-311+G(2d,p)	388	3.19	0.60	81% H→L	0.45
M062X/6-311++G(2d,2p)	388	3.19	0.60	81% H→L	0.45
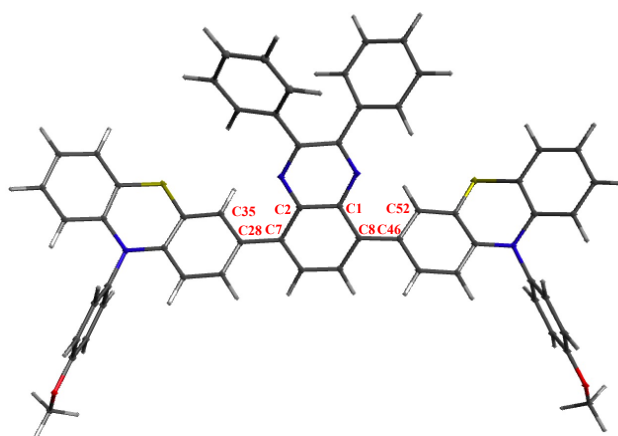
Figure S2. Atoms involved in the considered bond lengths (Å) and dihedral angles (degrees) between the quinoxaline acceptor core and the phenothiazine donor groups.
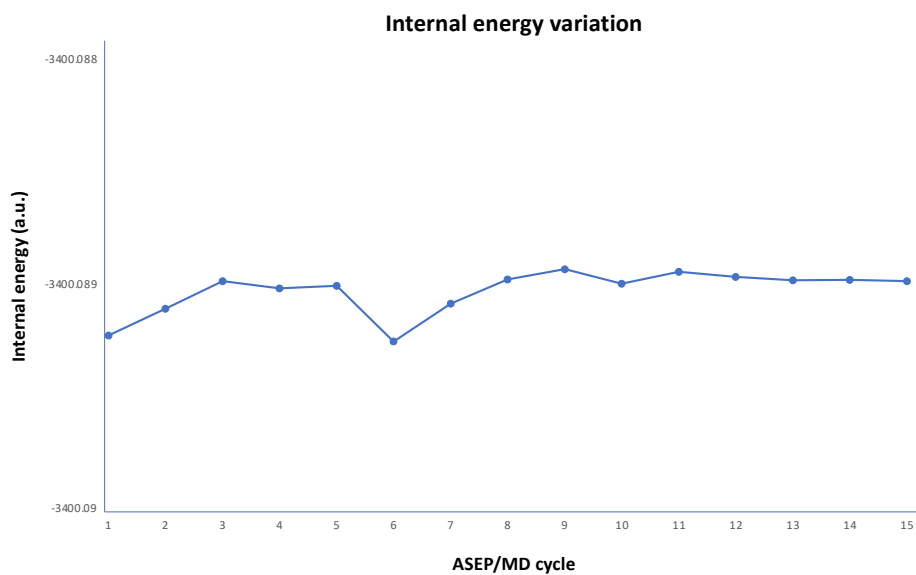
Figure S3. Internal energy variation (a.u) of compound **DQ3-a** throughout the 15 ASEP/MD cycles.
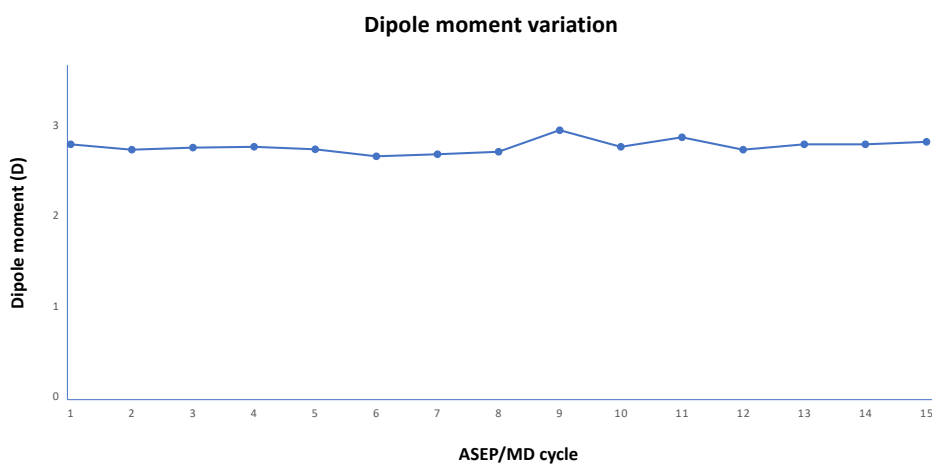
Figure S4. Dipole moment variation of compound **DQ3-a** throughout the 15 ASEP/MD cycles.

Table S3. Bond lengths (Å) and dihedral angles (degrees) of S_0 optimized geometries at B3LYP/6-31G* in toluene of compound **DQ3-a** for the last four considered ASEP/MD cycles.

ASEP/MD cycle	Bond lengths (Å)		Dihedral angles (degrees)	
	C28-C7	C8-C46	C35-C28-C7-C2	C1-C8-C46-C52
12	1.48	1.48	41.8	41.4
13	1.48	1.48	41.8	41.4
14	1.48	1.48	41.7	41.4
15	1.48	1.48	41.6	41.3

Table S4. TD-MPW1K/6-311+G(2d,p) absorption maxima (λ_{max}^{abs} in nm), excitation energies (E_{exc} in eV), oscillator strengths (f) and contributions (%) to $S_0 \rightarrow S_1$ transition in toluene (by using ASEP/MD) of compound **DQ3-a**.

ASEP/MD cycle	λ_{max}^{abs}	E_{exc}	f	Contribution (%)
12	385	3.22	0.39	75% H$\rightarrow$L
13	385	3.22	0.39	79% H$\rightarrow$L
14	386	3.21	0.38	77% H$\rightarrow$L
15	385	3.22	0.39	80% H$\rightarrow$L

Table S5. TD-MPW1K/6-311+G(2d,p) absorption maxima (λ_{max}^{abs} in nm), excitation energies (E_{exc} in eV), oscillator strengths (f) and contributions (%) to $S_0 \rightarrow S_1$ transition in *vacuo* and in toluene by using PCM and ASEP/MD of compound **DQ3-a.**

Medium	λ_{max}^{abs}	E_{exc}	f	Contribution (%)
Vacuo	382	3.24	0.33	79% H$\rightarrow$L
Toluene (by PCM)	381	3.25	0.41	77% H$\rightarrow$L
Toluene (by ASEP/MD)	385	3.22	0.39	78% H$\rightarrow$L

References

[1] J. Roncali, Luminescent Solar Collectors: Quo Vadis?, Advanced Energy Materials 10, 2001907 (2020). https://doi.org/10.1002/aenm.202001907

[2] P. Hohenberg, and W. Kohn, Inhomogeneous Electron Gas, Phys. Rev. 136, B864–B871 (1964). https://doi.org/10.1103/PhysRev.136.B864

[3] W. Kohn, and L. J. Sham, Self-consistent Equations Including Exchange and Correlation Effects, Phys. Rev. 140, A1133–A1138 (1965). https://doi.org/10.1103/PhysRev.140.A1133

[4] C. Adamo, and D. Jacquemin, The calculations of excited-state properties with Time-Dependent Density Functional Theory, Chem. Soc. Rev. 42, 845-856 (2013). https://doi.org/10.1039/C2CS35394F

[5] A. D. Laurent, C. Adamo, and D. Jacquemin, Dye chemistry with time-dependent density functional theory, Phys. Chem. Chem. Phys. 16, 14334-14356 (2014). https://doi.org/10.1039/C3CP55336A

[6] Gaussian 16, Revision C.01, M. J. Frisch, G. W. Trucks, H. B. Schlegel, G. E. Scuseria, M. A. Robb, J. R. Cheeseman, G. Scalmani, V. Barone, G. A. Petersson, H. Nakatsuji, X. Li, M. Caricato, A. V. Marenich, J. Bloino, B. G. Janesko, R. Gomperts, B. Mennucci, H. P. Hratchian, J. V. Ortiz, A. F. Izmaylov, J. L. Sonnenberg, D. Williams-Young, F. Ding, F. Lipparini, F. Egidi, J. Goings, B. Peng, A. Petrone, T. Henderson, D. Ranasinghe, V. G. Zakrzewski, J. Gao, N. Rega, G. Zheng, W. Liang, M. Hada, M. Ehara, K. Toyota, R. Fukuda, J. Hasegawa, M. Ishida, T. Nakajima, Y. Honda, O. Kitao, H. Nakai, T. Vreven, K. Throssell, J. A. Montgomery, Jr., J. E. Peralta, F. Ogliaro, M. J. Bearpark, J. J. Heyd, E. N. Brothers, K. N. Kudin, V. N. Staroverov, T. A. Keith, R. Kobayashi, J. Normand, K. Raghavachari, A. P. Rendell, J. C. Burant, S. S. Iyengar, J. Tomasi, M. Cossi, J. M. Millam, M. Klene, C. Adamo, R. Cammi, J. W. Ochterski, R. L. Martin, K. Morokuma, O. Farkas, J. B. Foresman, and D. J. Fox, Gaussian, Inc.: Wallingford CT, USA (2016).

[7] A. D. Becke, Density-functional thermochemistry. III. The role of exact exchange, J. Chem. Phys. 98, 5648 (1993). https://doi.org/10.1063/1.464913

[8] C. Lee, W. Yang, and R. G. Parr, Development of the Colle-Salvetti correlation-energy formula into a functional of the electron density, Phys. Rev. B. 37, 785-789 (1988). https://doi.org/10.1103/PhysRevB.37.785

[9] T. Yanai, D. P. Tew, and N. C. Handy, A new hybrid exchange–correlation functional using the Coulomb-attenuating method (CAM-B3LYP), Chemical Physics Letters 393, 51–57 (2004). https://doi.org/10.1016/j.cplett.2004.06.011

[10] B. J. Lynch, P. L. Fast, M. Harris, and D. G. Truhlar, Adiabatic Connection for Kinetics, J. Phys. Chem. A 104, 4811–4815 (2000). https://doi.org/10.1021/jp000497z

[11] J. Tomasi, B. Mennucci, and R. Cammi, Quantum Mechanical Continuum Solvation Models, Chem. Rev. 105, 2999−3093 (2005). https://doi.org/10.1021/cr9904009

[12] C. Bernini, L. Zani, M. Calamante, G. Reginato, A. Mordini, M. Taddei, R. Basosi, and A. Sinicropi, Excited State Geometries and Vertical Emission Energies of Solvated Dyes for DSSC: A PCM/TD-DFT Benchmark Study, J. Chem. Theory Comput. 10, 3925–3933 (2014). https://doi.org/10.1021/ct500328t

[13] I. F. Galván, M. L. Sánchez, M. E. Martín, F. J. Olivares del Valle, and M. A. Aguilar, ASEP/MD: A program for the calculation of solvent effects combining QM/MM methods and the mean field approximation, Computer Physics Communications 155, 244–259 (2003). https://doi.org/10.1016/S0010-4655(03)00351-5

[14] Gaussian 09, Revision C.01, M.J. Frisch, G.W. Trucks, H.B. Schlegel, G.E. Scuseria,

M.A. Robb, J.R. Cheeseman, G. Scalmani, V. Barone, B. Mennucci, G.A. Petersson, H. Nakatsuji, M. Caricato, X. Li, H.P. Hratchian, A.F. Izmaylov, J. Bloino, G. Zheng, J.L. Sonnenberg, M. Hada, M. Ehara, K. Toyota, R. Fukuda, J. Hasegawa, M. Ishida, T. Nakajima, Y. Honda, O. Kitao, H. Nakai, T. Vreven, J.A. Montgomery, Jr., J.E. Peralta, F. Ogliaro, M. Bearpark, J.J. Heyd, E. Brothers, K.N. Kudin, V.N. Staroverov, T. Keith, R. Kobayashi, J. Normand, K. Raghavachari, A. Rendell, J.C. Burant, S.S. Iyengar, J. Tomasi, M. Cossi, N. Rega, J.M. Millam, M. Klene, J.E. Knox, J.B. Cross, V. Bakken, C. Adamo, J. Jaramillo, R. Gomperts, R.E. Stratmann, O. Yazyev, A.J. Austin, R. Cammi, C. Pomelli, J.W. Ochterski, R.L. Martin, K. Morokuma, V.G. Zakrzewski, G.A. Voth, P. Salvador, J.J. Dannenberg, S. Dapprich, A.D. Daniels, O. Farkas, J.B. Foresman, J.V. Ortiz, J. Cioslowski, and D.J. Fox, Gaussian, Inc.: Wallingford, CT, USA (2010).

[15] H. J. C. Berendsen, D. van der Spoel, and R. van Drunen, GROMACS: A message-passing parallel molecular dynamics implementation, Computer Physics Communications 91, 43-56 (1995). https://doi.org/10.1016/0010-4655(95)00042-E

[16] W. Jorgensen, D. S. Maxwell, and J. Tirado-Rives, Development and Testing of the OPLS All-Atom Force Field on Conformational Energetics and Properties of Organic Liquids, J. Am. Chem. Soc. 118, 11225–11236 (1996). https://doi.org/10.1021/ja9621760

[17] M. P Allen, and D.J. Tildesley, Computer Simulation of Liquids, Oxford University Press: London (1987).

[18] W. G. Hoover, Canonical dynamics: Equilibrium phase-space distributions, Phys. Rev. A 31, 1695 (1985). https://doi.org/10.1103/PhysRevA.31.1695

[19] L. E. Chirlian, and M. M Francl, Atomic charges derived from electrostatic potentials: A detailed study, J. Comput. Chem. 8, 894-905 (1987). https://doi.org/10.1002/jcc.540080616

[20] M. Breneman, and K. B. Wiberg, Determining atom-centered monopoles from molecular electrostatic potentials. The need for high sampling density in formamide conformational analysis, J. Comput. Chem. 11, 361-373 (1990). https://doi.org/10.1002/jcc.540110311

[21] D. Jacquemin, V. Wathelet, E. A. Perpète, and C. Adamo, Extensive TD-DFT Benchmark: Singlet-Excited States of Organic Molecules, J. Chem. Theory Comput. 5, 2420–2435 (2009). https://doi.org/10.1021/ct900298e

[22] D. Jacquemin, B. Mennucci, and C. Adamo, Phys. Chem. Chem. Phys. 13, 16987–16998 (2011). https://doi.org/10.1039/C1CP22144B

[23] P.-F. Loos, A. Scemama, and D. Jacquemin, The Quest For Highly Accurate Excitation Energies: A Computational Perspective, J. Phys. Chem. Lett. 11, 2374–2383 (2020). https://doi.org/10.1021/acs.jpclett.0c00014

4.8. Manuscript 8: "Donor-Acceptor-Donor Thienopyrazine-Based Dyes as NIR-Emitting AIEgens"

In this work, three novel molecules, **TPa-c**, have been designed and synthetized for a possible application as NIR-emitting AIEgens in luminescent devices. They possess the peculiar D-A-D structure, carrying the thieno[3,4-*b*]pyrazine acceptor core (A) connected to two triarylamine donor groups (D), which are substituted to a tetraphenylethylene (TPE) moiety, whose introduction is a common strategy to enhance emission from the condensed phase (AIE properties). From the computational investigation and the experimental characterization carried out in different solvents, it emerged that **TPa-c** have intense light-harvesting ability and emissions in the NIR region of the spectrum. Additionally, they possess large Stokes Shift values and AIE properties, which have been observed upon the formation of nanoaggregates in THF/water mixtures. These outcomes revealed that **TPa-c** can be considered as promising candidates for the development of new emissive devices.

The PhD candidate's contribution refers to the application of DFT and TDDFT methods to rationalize the structural, the electronic and the photophysical properties of the designed compounds in toluene and in dichloromethane, by using PCM. The Stokes Shifts values have been evaluated from the computed vertical absorption and the emission energies. Additionally, the PhD candidate also contributed to the writing of the manuscript.

Check for updates

Chemistry Europe
European Chemical
Societies Publishing

Donor-Acceptor-Donor Thienopyrazine-Based Dyes as NIR-Emitting AIEgens

Giulio Goti,*[a, b] Massimo Calamante,[a, b] Carmen Coppola,[c, d] Alessio Dessì,[a]
Daniele Franchi,[a] Alessandro Mordini,*[a, b] Adalgisa Sinicropi,[a, c, d] Lorenzo Zani,[a] and
Gianna Reginato[a]

Dedicated to Professor Franco Cozzi on the occasion of his 70th birthday.

Organic Near-Infrared luminophores have found broad application as functional materials, but the development of efficient NIR emitters is still a challenging goal. Here we report on a new class of thieno[3,4-*b*]pyrazine-based NIR emitting materials with Aggregation Induced Emission (AIE) properties. The dyes feature a donor–acceptor–donor (D–A–D) structure, with a thienopyrazine acceptor core connected to two triarylamine donor groups bearing a tetraphenylethylene (TPE) moiety. Fast and efficient synthesis allowed the modular preparation of three dyes of tunable absorption and emission profiles. These constructs were extensively characterized by spectroscopic studies in different solvents, which revealed intense light-harvesting ability and emissions in the deep-red and NIR region with large Stokes shift values. Remarkably, the dyes exhibited AIE properties, retaining emissive ability in the aggregate state, thus emerging as attractive materials for their potential application in the development of luminescent devices.

Introduction

Deep-red and Near-infrared (NIR) light-emitting materials have attracted increasing attention over the past few years for their use in a plethora of applications, ranging from photovoltaics, night vision, optical communication, organic light-emitting diodes (OLEDs), and bioimaging.[1] Ideal NIR emitters are able to harvest photons in the visible region with high molar attenuation coefficients (ε) and efficiently emit NIR radiation ($\lambda >$ 650 nm). Although efficient NIR emitters have been successfully developed relying both on rare-earth metals and transition metal complexes,[2] their poor availability and high costs limit their wide applicability and scalability. In this regard, purely organic NIR emitting molecules represent a valuable alternative,

offering advantages in terms of ease of preparation, tunability of their photophysical properties, and reduced costs.[3]

A common strategy in designing organic NIR molecules is based on a donor-acceptor (D–A) architecture, where one (or more) strong electron-donating moiety, the donor (D), is connected to a highly electron-poor motif, the acceptor (A).[4] This approach grants access to molecules with intramolecular charge-transfer (ICT) excited state and low energy band gaps, which are ultimately responsible for the desired NIR emission. While effective, this strategy is affected by two main drawbacks: 1) as a direct consequence of the energy-gap law, radiative decay from low lying excited states is commonly associated with low emission quantum yields,[5] and 2) due to their rigid conjugated structure, D–A compounds are prone to aggregation-caused quenching (ACQ), a behavior that poses limits to their application in the solid-state.[6] Altogether, these aspects make the development of efficient organic NIR emitters challenging.

A solution to the ACQ affecting molecular dyes is provided by the aggregation-induced emission (AIE) phenomenon. Specifically, AIE luminogens (AIEgens) are molecules that, upon aggregation, exhibit enhanced emissive properties by avoiding deactivation pathways. Such AIE behavior is achieved through a combination of mechanisms, encompassing restriction of molecular motions, which also prevents deleterious π–π stacking interactions, and control of the conical intersection accessibility (CCIA).[7] During the past two decades, the deep understanding of the principles governing AIE has fostered the generation of a myriad of new AIEgens, which revealed AIE as a powerful strategy for the preparation of efficient organic NIR emitters.[8]

As part of our research interest in the synthesis and characterization of luminescent organic materials,[9] we have focused our attention on thieno[3,4-*b*]pyrazine-based dyes as

[a] *Dr. G. Goti, Dr. M. Calamante, Dr. A. Dessì, Dr. D. Franchi, Dr. A. Mordini,*
    Dr. A. Sinicropi, Dr. L. Zani, Dr. G. Reginato
    Institute of Chemistry of Organometallic Compounds (ICCOM)
    National Research Council (CNR)
    Via Madonna del Piano 10, 50019 Sesto Fiorentino, Italy
    E-mail: ggoti@iccom.cnr.it
        alessandro.mordini@iccom.cnr.it
[b] *Dr. G. Goti, Dr. M. Calamante, Dr. A. Mordini*
    Department of Chemistry "Ugo Schiff"
    University of Florence
    Via della Lastruccia 13,
    50019 Sesto Fiorentino, Italy
[c] *Dr. C. Coppola, Dr. A. Sinicropi*
    Department of Biotechnology, Chemistry and Pharmacy
    University of Siena
   *Via A. Moro 2, 53100, Siena, Italy*
[d] *Dr. C. Coppola, Dr. A. Sinicropi*
    Consorzio per lo Sviluppo dei Sistemi a Grande Interfase (CSGI)
    Via della Lastruccia 3,
    Sesto Fiorentino, 50019, Italy

    Supporting information for this article is available on the WWW under
    https://doi.org/10.1002/ejoc.202100199

    Part of the "Franco Cozzi's 70th Birthday" Special Collection.

potential NIR emitters. The thieno[3,4-*b*]pyrazine core is a relevant and versatile acceptor moiety in the synthesis of D–A–D molecules: *i*) its electron deficiency and poor aromaticity impart a high ICT character to the dye excited state, resulting in a deeply red-shifted absorption and emission bands; *ii*) importantly, judicious functionalization of the acceptor core enables additional tuning of the dye photophysical properties.[10] While these unique features have enabled the preparation of efficient organic NIR luminophores, the use of thieno[3,4-*b*]pyrazine in the development of NIR emitters with AIE properties has remained poorly investigated.[11]

Here we report on a new class of NIR emitting AIEgens **TP** (Scheme 1) featuring a D–A–D structure, with a thieno[3,4-*b*] pyrazine acceptor core connected to two triarylamine donor groups. Importantly, to bestow the dyes with AIE properties, we envisioned adorning the triarylamine donors with a tetraphenyl-ethylene (TPE) moiety, whose introduction within luminophores structures is an established strategy to enhance emission from the condensed phase.[7c,8a,12] As depicted in Scheme 1, from a retrosynthetic point of view, the **TP** dyes can be obtained following a C–H functionalization logic,[10d,13] where the two C–H bonds within the acceptor core **1** are directly functionalized in the presence of an excess of the triarylamine bromide **2**. The high modularity of this approach provides straightforward access to different **TP** emitters by simple variation of the substitution pattern of acceptor **1**, which can be directly connected to the donors **2** without the need for pre-activation. Following this route, three **TP** NIR AIEgens were successfully prepared and fully characterized in solution for their photophysical and AIE properties.
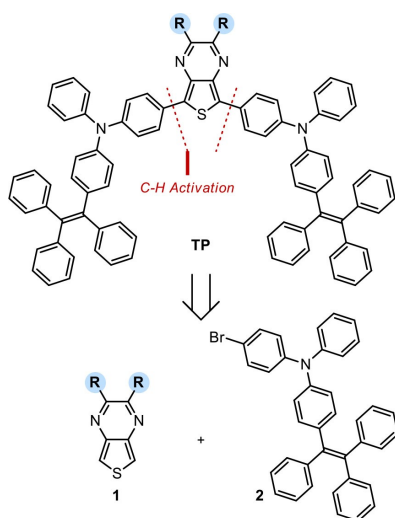
Scheme 1. Retrosynthetic analysis for **TP** emitters.

Results and Discussion

Synthesis of Compounds

Keeping in mind our retrosynthetic plan (Scheme 1), we envisaged a convergent strategy for the preparation of thieno [3,4-*b*]pyrazine dyes **TP**, where the acceptors **1** and the donor **2** are accessed through two different synthetic routes and finally assembled in a modular fashion. This synthetic strategy, depicted in Scheme 2, has allowed straightforward access to three different NIR emitters **TPa-c**. Importantly, the synthetic route strives for minimizing purification steps and is remarkable for its efficiency, both crucial aspects to be considered in view of the potential processability of the compounds.

The three thieno[3,4-*b*]pyrazine acceptor cores **1a-c** were synthesized following a reported procedure,[14] using thiophene (**3**) as an inexpensive and readily available starting material (Scheme 2a). Thiophene (**3**) was readily brominated in the presence of NBS and, after a chromatographic purification, subjected to electrophilic nitration to provide the 2,5-dibromo-3,4-dinitrothiophene **4**, which was recovered as a pure solid upon filtration (50% yield over 2 steps). Reduction of the nitro groups within **4**, along with debromination of the heteroaromatic ring, was accomplished by treatment with an excess of tin in HCl, yielding the 3,4-diaminothiophene **5**, that was isolated in gram scale upon simple filtration as a mixture of chloride and hexachlorostannate $(SnCl_6)^{2-}$ diammonium salt.[14] Finally, condensation of **5** with the 1,2-dicarbonyl compounds **6a-c** provided the three thieno[3,4-*b*]pyrazine acceptors **1a-c**. Specifically, condensation with benzil **6a** was achieved upon *in situ* deprotection of the ammonium salt **5** with an excess of triethylamine, obtaining the 2,3-diphenylthieno[3,4-*b*]pyrazine **1a** in 60% yield over two steps after chromatographic purification. The same procedure allowed the condensation of the diamine **5** with 2,3-butandione **6c** to give the 1,2-dimethyl substituted core **1c** in 81% yield over two steps, which was pure enough to be used in the next synthetic step without further manipulation. On the other hand, condensation of **5** with an excess of glyoxal **6b** occurred in basic water solution, delivering core **1b** in 79% yield over two steps with no purification needed.

The triarylamine donor **2** was synthesized starting from the commercially available bromide **7** (Scheme 2b), which was submitted to Buchwald-Hartwig coupling with aniline **8** using Pd₂(dba)₃ and tri-*tert*-butylphosphine as catalyst/ligand combination, furnishing the coupling product **9** in gram scale with 85% yield.[15] Following a reported procedure, the bis-arylamine **9** was then reacted with a slight excess of 1-bromo-4-iodobenzene **10** in a second C–N coupling, catalyzed by Pd(OAc)₂ and tri-*tert*-butylphosphine.[16] However, in our hands, these conditions led to the triarylamine product **2** only in poor yields (33%), along with the formation of a side-product (22% yield) arising from the overreaction of **2** with the starting amine **9**. To solve this issue, we conducted a short optimization (see Supporting Information, Section A), finding that an excellent balance between reactivity and selectivity is achieved using Pd(OAc)₂ (10 mol%) and Xantphos (15 mol%) as catalysts at
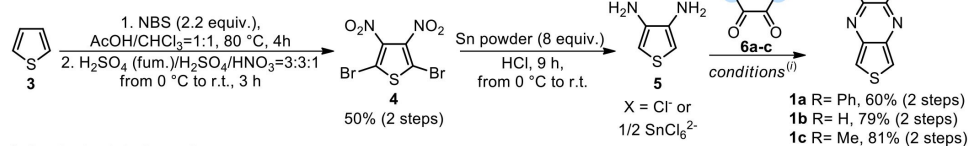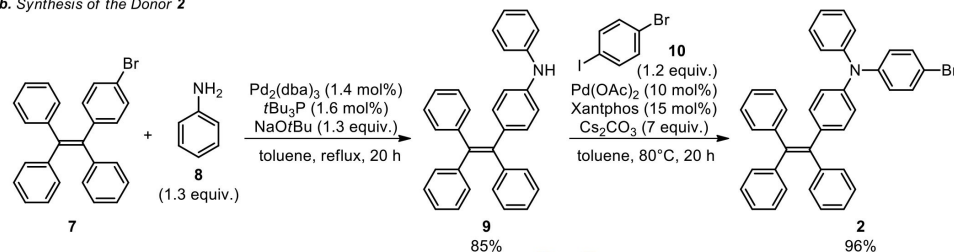
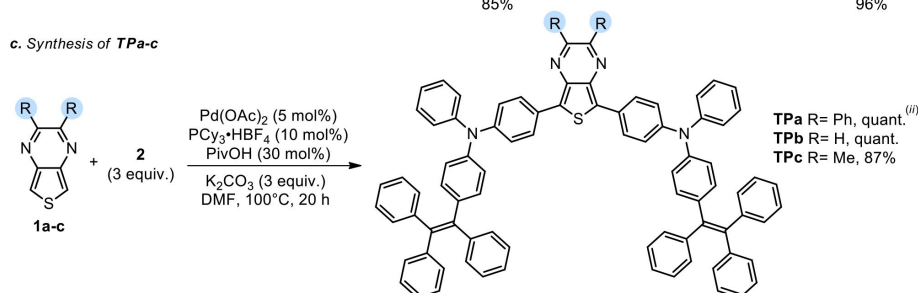**Scheme 2.** Convergent synthetic route for constructs **TPa-c**. *i*) Conditions for **1a**, R = Ph: benzil **6a** (1.05 equiv.), Et₃N (4 equiv.), EtOH/DCM = 1:1, r.t., 3 h; for **1b**, R = H: glyoxal **6b** (40% wt in H₂O, 1.9 equiv.), H₂O, r.t., o.n.; for **1c**, R = Me: 2,3-butanedione **6c** (1 equiv.), Et₃N (4 equiv.), EtOH/DCM = 2:1, r.t., o.n. *ii*) Reaction time for **TPa**: 30 min. NBS = *N*-bromosuccinimide, DMF = *N,N*-dimethylformamide.

80 °C, which allowed the gram-scale synthesis of triarylamine **2** in 96% yield. We further found that the amount of Pd/ligand catalysts can be reduced as low as 5 mol% in palladium without loss in performance.

With all the synthons in our hands, we investigated the direct arylation of the acceptor cores **1a–c** with the donor **2** to finally obtain the targeted constructs **Tpa–c** (Scheme 2c). To our delight, arylation of both C–H bonds within the thienyl ring of cores **1a-c** occurred cleanly using Pd(OAc)₂ (5 mol%) and PCy₃·HBF₄ (10 mol%) as a catalytic system, along with pivalic acid (30 mol%) as co-catalyst.[17] Under these conditions, we successfully synthesized the desired **Tpa–c** compounds, that were obtained after chromatographic purification with good to excellent yields (quantitative, quantitative, and 87% respectively).

Photophysical Characterization

To evaluate the ability of **Tpa–c** dyes to perform as NIR emitters, we conducted UV-Vis and emission studies to determine their photophysical properties, which are summarized below in Table 1.

Absorption spectra of **Tpa–c** solutions in dichloromethane (DCM) revealed three main absorption bands (Figure 1A): two with higher intensity in the UV region, with λ_max approximately centered at 310 nm and 350 nm respectively, and a third one at longer wavelengths, ascribed to the intramolecular charge transfer (ICT) transition. As it can be noted, the substitution of the thienopyrazine core strongly influences the position of the ICT absorption band. Specifically, while the non-substituted **TPb** showed an absorption maximum at 550 nm, the introduction of electron-donating methyl groups within **TPc** reduced the ICT character of the molecule, thus inducing a blue shift of the ICT band absorption maximum to 518 nm; on the contrary, a red-

172

EurJOC
European Journal of Organic Chemistry

Full Papers
doi.org/10.1002/ejoc.202100199

Chemistry Europe
European Chemical Societies Publishing

Table 1. Photophysical characterization of **TPa-c** dyes in solution.

Compound	λ_{abs} [nm][a]	ε [M^{-1}cm^{-1}]	λ_{emi} [nm][a]	E_{0-0} [eV][a]	Stokes shift [nm, eV]	Φ [%][a]	λ_{abs} [nm][b]	λ_{emi} [nm][b]	E_{0-0} [eV][b]	Stokes shift [nm, eV]	Φ [%][b]
TPa	576	16876	750	1.84	174, 0.50	0.6	580	714	1.86	134, 0.40	5
TPb	550	15025	738	1.89	188, 0.57	0.3	556	703	1.92	150, 0.47	6
TPc	518	18820	679	2.02	161, 0.57	5	521	663	2.03	142, 0.51	22

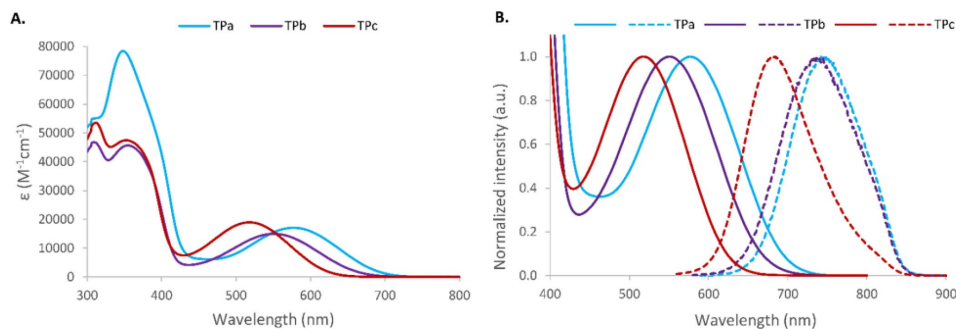[a] Measured in DCM. [b] Measured in toluene.

Figure 1. A) Absorption spectra of **TPa-c** solutions in DCM. B) Normalized ICT absorption bands (solid lines) and normalized emission bands (dotted lines) of **TPa-c** solutions in DCM (1×10^{-5} M, $\lambda_{exc.}$ 576 nm, 550 nm, 518 nm respectively).

shifted ICT band was observed for the highly conjugated diphenyl substituted **TPa** ($\lambda_{max} = 576$ nm).
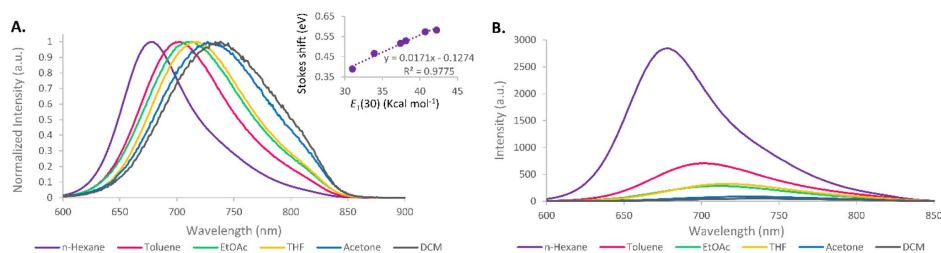
Importantly, all the **TPa-c** molecules showed deep-red to NIR emissions in DCM solution. The emission spectra (Figure 1B, dotted lines) are characterized by broad bands that mirror the corresponding ICT absorption bands well, featuring no significant vibronic structure, and considerably large Stokes shifts, >150 nm. The most blue-shifted emission in the **TP** series is observed for the dimethyl substituted **TPc** ($\lambda_{max} = 679$ nm), while the emission of the diphenyl substituted **TPa** is the most red-shifted ($\lambda_{max} = 750$ nm). Interestingly, the non-substituted **TPb** possesses the highest Stokes shift of the series, 188 nm (0.57 eV), thus displaying a noticeable red-shifted emission with a maximum at 738 nm.

To gain information about the influence of the solvent on the optical properties of the **TPa–c** dyes, we analyzed their absorption and emission spectra in six different media (see Supporting Information, Section D). This study showed that, while the absorption properties of **TPa–c** are only moderately affected by the nature of the solvent, the emission spectra present a marked positive solvatochromism, with maxima shifting towards longer wavelength with increasing solvent polarities. Such effect is particularly pronounced for the non-substituted **TPb**, where the emission maximum in *n*-hexane, λ_{max} 678 nm, is red-shifted by 60 nm when the solvent is changed to DCM, λ_{max} 738 nm (Figure 2A). Remarkably, a strong linear correlation between Stokes shift and the solvent polarity was observed for all **TPa–c** dyes (inset in Figure 2A for **TPb**).[18] This phenomenon is typical of push-pull organic emitters and

can be ascribed to a pronounced stabilization of the highly polar charge-transfer excited states in more polar solvents. Consequently, as for the energy-gap law, narrower band-gap transitions are more susceptible to non-radiative decay, a decrease in emission intensity is observed when passing from apolar to highly polar solvents (Figure 2B). Accordingly, fluorescence quantum yields for **TPa–c** solutions in toluene, $\Phi_{Toluene}$ 5%, 6%, 22% respectively, are about one order of magnitude higher than the corresponding quantum yields measured for **TPa-c** DCM solutions, Φ_{DCM} 0.6%, 0.3%, 5% (Table 1); such quantum yield values are comparable with those of previously reported thieno[3,4-*b*]pyrazine based D–A–D emitters.[10d] Notably, the highest fluorescence quantum yield among the series of compounds is displayed by the methyl disubstituted **TPc**, as it is characterized by the highest energy band-gap.

Computational Investigation

A computational investigation based on Density Functional Theory (DFT) and time-dependent DFT (TD-DFT) methods was carried out to further rationalize the structural, electronic and photophysical properties of compounds **TPa–c**. The ground (S_0) and excited states (S_1) geometries of **TPa–c** were optimized both in DCM and in toluene and are shown in Figure S19. The S_0 optimized geometries show dihedral angles between the thieno[3,4-*b*]pyrazine acceptor core and the triarylamine donor between 10.3° and 18°, whereas calculated geometries for S_1

173

EurJOC
European Journal of Organic Chemistry

Full Papers
doi.org/10.1002/ejoc.202100199

Chemistry
Europe
European Chemical
Societies Publishing

Figure 2. A) Normalized emission spectra of **TPb** solutions in different media. *Inset*: linear correlation between Stokes shift and solvent polarity. B) Variation of emission spectra intensities for **TPb** solutions (1×10^{-5} M) as a function of solvent.

show an overall increased planarity of the molecules in both solvents (dihedral angles between 0.2° and 1.2°).

TD-CAM-B3LYP/6-311+G(2d,p) absorption (λ_{max}^{abs}) and emission (λ_{max}^{emi}) maxima, vertical excitation (E_{exc}) and emission (E_{emi}) energies, oscillator strengths (f) and composition (%) in terms of molecular orbitals for the lowest singlet-singlet excitations ($S_0 \rightarrow S_1$) and the singlet-singlet emissions ($S_1 \rightarrow S_0$) in DCM and toluene of compounds **TPa-c** are shown in Table 2 and Table 3, respectively.

TPa–c show absorption maxima in DCM between 515 and 563 nm, corresponding to 2.41-2.20 eV, while absorption maxima between 520 and 566 nm, corresponding to 2.38-2.19 eV, are calculated in toluene (Table 2). Looking at the wavefunction plot of molecular orbitals (MOs) involved in the lowest energy transitions (Figure 3), it is evident that the $S_0 \rightarrow S_1$ excitations are characterized by an intramolecular charge transfer from the donor to the acceptor group, involving HOMO→LUMO orbitals. The experimental absorption maxima are in very good agree-

ment with the computed values in both solvents, reproducing the red-shift of the lowest energy transition going from **TPc** to **TPa**, with energy differences ≤ to 0.05 eV.

The LR-PCM computed emission maxima in DCM (Table 3) fall in the 705–769 nm range, corresponding to 1.76–1.61 eV, while emission maxima between 706–764 nm (1.76–1.62 eV) are calculated in toluene. The experimental emission maxima are also in good accordance with the computed vertical $S_1 \rightarrow S_0$ emission energies in both solvents, as the energy difference is ≤ to 0.13 eV. The calculated Stokes shifts values of **TPa–c** compounds are, respectively, 0.59, 0.63 and 0.65 eV in DCM, while 0.57, 0.60 and 0.62 eV in toluene. The wavefunction plot of molecular orbitals (MOs) involved in the lowest energy radiative transitions is shown in Figure S20 in the Supporting Information, Section F.

Table 2. TD-CAM-B3LYP/6-311+G(2d,p) absorption maxima (λ_{max}^{abs} in nm), excitation energies (E_{exc} in eV), oscillator strengths (f) and contributions (%) to the $S_0 \rightarrow S_1$ transition in [a] DCM and [b] toluene for **TPa–c** compounds.

Compound	λ_{max}^{abs} [nm] [a]	[b]	E_{exc} [eV] [a]	[b]	f [a]	[b]	Contribution [%] [a]	[b]
TPa	563	566	2.20	2.19	0.71	0.71	86% H→L	89% H→L
TPb	551	556	2.25	2.23	0.81	0.80	84% H→L	85% H→L
TPc	515	520	2.41	2.38	0.95	0.93	86% H→L	86% H→L

Table 3. TD-CAM–B3LYP/6-311+G(2d,p) emission maxima (λ_{max}^{emi} in nm), emission energies (E_{emi} in eV), oscillator strengths (f) and contributions (%) to the $S_1 \rightarrow S_0$ transition in [a] DCM and [b] toluene for **TPa–c** compounds.

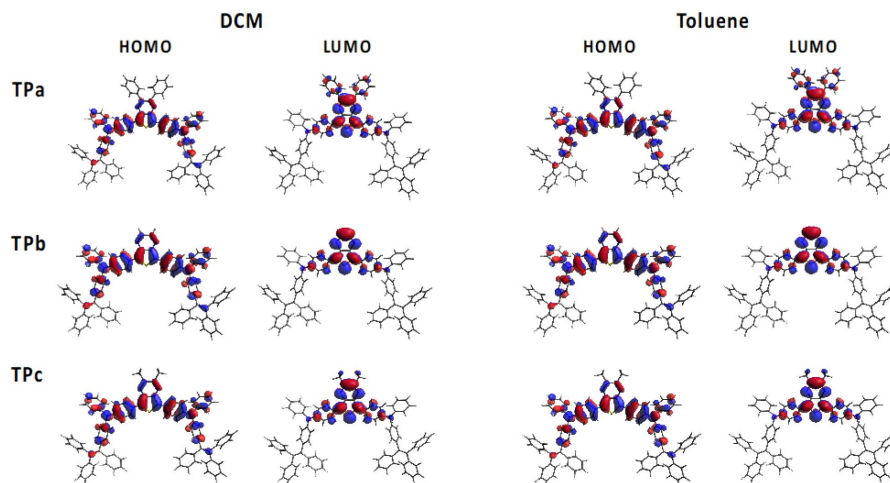| Compound	λ_{max}^{emi} [nm] [a]	[b]	E_{emi} [eV] [a]	[b]	f [a]	[b]	Contribution [%] [a]	[b]
TPa	769	764	1.61	1.62	0.59	0.58	94% L→H	94% L→H
TPb	765	763	1.62	1.63	0.66	0.65	94% L→H	93% L→H
TPc	705	706	1.76	1.76	0.77	0.75	94% L→H	94% L→H

Figure 3. DFT–B3LYP/6-31G* HOMO and LUMO ground-state electron density distributions in DCM and toluene using the polarizable continuum model (PCM) of **TPa-c** compounds.

AIE Studies

The AIE properties of the **TPa-c** luminophores were investigated to assess their emission ability in the aggregated phase, an important parameter for their application as functional materials in the development of new devices. To this end, we analyzed the emission of **TPa–c** dyes in THF/water mixtures (1×10^{-5} M) with increasing water fractions, f_w (%) (Figure 4).

A moderate positive solvatochromic effect, along with a decrease in photoluminescence intensity was generally observed when going from $f_w = 0\%$ to $f_w = 50\%$ ($I/I_0 \approx 0.6$ for **TPa** and $I/I_0 \approx 0.2$ for **TPb,c**), which is likely due to an increase of the ICT character of the dyes excited state in more polar solvent mixtures. On the other hand, **TPa–c** formed soluble nano-aggregates when dissolved in solutions with $f_w \geq 60\%$, which induced a slight shift of emission maxima towards shorter wavelengths and an increase of photoluminescence intensity,
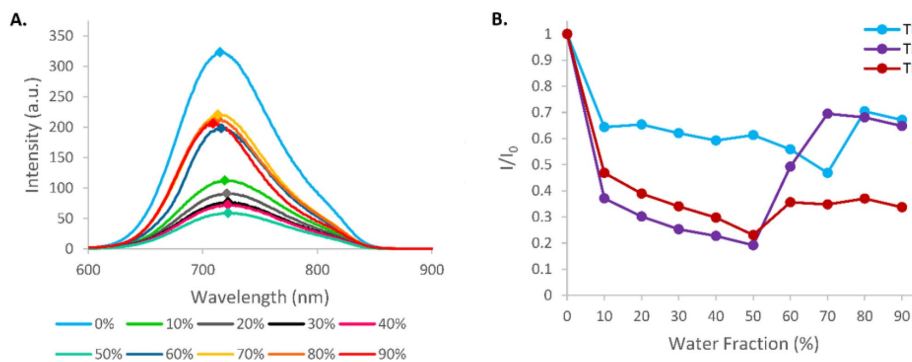
Figure 4. A) Emission spectra of **TPb** solutions in THF/water mixtures (1×10^{-5} M, $\lambda_{exc.}$ 551 nm) with increasing water fractions (%). Emission maxima are labelled as follows: ♦. B) Relative emission intensities (I/I_0) of **TPa-c** solutions in THF/water mixtures (1×10^{-5} M, $\lambda_{exc.}$ 576 nm, 551 nm, 518 nm respectively) as a function of water fraction, f_w. I and I_0 are emission intensities at the emission maximum for the compounds in THF/water mixtures ($f_w \geq 10$) and pure water ($f_w = 0$) respectively. I and I_0 values for **TPa-c** solutions have been weighted for their absorption at the excitation wavelength.

with a maximum effect at f_W of about 70%-80%. Such AIE effect was particularly marked for the **TPb** dye, with a relative intensity variation from $I/I_0 = 0.2$ to 0.7, while it was found to be less important for **TPa** and **TPc** (maximum $I/I_0 = 0.7$ and 0.37 respectively). Notably, nano-aggregates formation for **TPa–c** solutions at $f_W \geq 60\%$ was confirmed by UV-vis analysis with the onset of light scattering effects;[19] it is worth noting that such phenomenon introduces an overestimation of **TPa–c** absorbances, with consequent underestimation of the corresponding I/I_0 values.

Conclusion

In summary, we have developed new thienopyrazine based D–A–D dyes as deep-red and NIR emitters with AIE properties. A streamlined and modular synthesis enabled the straightforward assembly of three different **TPa–c** dyes with distinct photophysical properties. Importantly, all the dyes were found to strongly absorb light in the UV and visible region and to re-emit it at $\lambda_{max} > 650$ nm, with Φ values that are comparable with previously reported thienopyrazine based D–A–D luminophores. The introduction of TPE moieties within **TPa–c** structures is a key design element intended to provide the dyes with AIE properties, that were fully characterized in solution. Although moderate in some cases, an AIE effect was observed for all **TPa–c** molecules, which retained their emissive ability upon the formation of nano-aggregates in THF/water mixtures. Altogether these studies highlight thienopyrazine based D–A–D architectures as promising and versatile structures for the development of efficient NIR emitters, and will likely guide the generation of dyes with higher performances. The high processability and the advantageous photophysics of these systems suggest their potential application for the development of new emissive devices, a goal that is currently being pursued by our group.

Experimental Section

General Information

All commercially available compounds were purchased from *Merck KgaA, Fluorochem Ltd.,* and *T.C.I. Co. Ltd.,* and were used without further purification unless otherwise stated. Aniline **8** was distilled from KOH and stored over 4 Å molecular sieves. Anhydrous toluene, *N,N*-dimethylformamide (DMF), DCM, and tetrahydrofuran (THF) were obtained after drying with a PureSolv Micro apparatus (Inert). Organometallic reactions were carried out under dry nitrogen using Schlenk techniques. Reactions were monitored by TLC on Kieselgel 60 F254 (*Merck*) aluminum sheets and the products were visualized by exposing the plate to UV light or by staining it with basic aqueous potassium permanganate ($KMnO_4$) solution. Flash column chromatography[20] was performed using *Merck* Kieselgel 60 (300–400 mesh) as the stationary phase. NMR spectra were recorded on *Varian* Gemini/Mercury/INOVA instruments at 200 or 400 MHz for ^1H, and 50.3–100.6 MHz for ^{13}C respectively. Chemical shifts (δ) are reported in parts per million (ppm) and are referenced to the residual solvent peak ($CDCl_3$, $\delta = 7.26$ ppm for ^1H NMR and $\delta = 77.16$ ppm for ^{13}C NMR; THF-d_8, $\delta = 3.58$ ppm for ^1H NMR and $\delta =$

67.21 ppm for ^{13}C NMR; DMSO-d_6, $\delta = 2.50$ ppm for ^1H NMR). The following abbreviations are used to indicate the multiplicity: s, singlet; d, doublet; q, quartet; m, multiplet; bs, broad signal. GC-MS analyses were performed with a *Varian* CP-3800 gas-chromatograph coupled to a *Varian* Saturn 2200 GC/MS/MS detector and equipped with a *Varian* Chrompack Capillary Column CP-Sil 8 CB (30 m × 0.25 mm I.D. 0.25 μm df), using the following parameters: Injector temperature: 280 °C, carrier gas: He 1 mL/min, Column Temperature: 60 °C (2.5 min)–9.4 °C/min-300 °C (2 min). ESI-MS spectra were obtained by direct injection of the sample solution using a *Thermo Scientific* LCQ-FLEET instrument, while HRMS spectra were measured using a *Thermo Scientific* LTQ Orbitrap (FT-MS) instrument (carried out at the Interdepartmental Center for Mass Spectroscopy of the University of Florence, CISM); both are reported as *m/z*. UV-Vis spectra in solution were recorded with a *Varian Cary* 4000 spectrophotometer, and fluorescence spectra in solution were recorded with a *Jasco* FP-8300 spectrofluorometer, equipped with a 150 W Xenon arc lamp, irradiating the sample at the wavelength corresponding to maximum absorption in the UV spectrum (no spectral correction has been applied). Fluorescence quantum yields (Φf) in solution were measured at room temperature irradiating the sample at the wavelength corresponding to maximum absorption in the UV spectrum by means of a 152 mm diameter *Quanta-ϕ* Integrating sphere coated with *Spectralon*, that was coupled by a 1.5 m fiber optic bundle (PVC monocoil sheath, slit-round configuration, 180 fibers; slit-end termination 10 mm O.D. × 50 mm long; round-end termination FR-274) to a *HORIBA Jobin-Yvon* Fluorolog-3 spectrofluorometer, equipped with a 450 W Xenon arc lamp and double-grating excitation and single-grating emission monochromator.

Synthetic Procedures

2,5-Dibromo-3,4-dinitrothiophene (4):[21] To a solution of thiophene **3** (10.0 g, 119 mmol) in a 1:1 mixture of glacial acetic acid and $CHCl_3$ (v/v) (100 mL), *N*-bromosuccinimide (46.4 g, 263 mmol) was added portion-wise and the reaction stirred vigorously at 80 °C for 4 h. Complete conversion was assessed by TLC monitoring (petroleum ether:EtOAc, 2:1), then the reaction was diluted with EtOAc (50 mL), poured in an extraction funnel, and washed with Na_2CO_3 saturated aqueous solution (2 × 50 mL), water (50 mL) and Brine (50 mL). The organic phase was dried over anhydrous Na_2SO_4, filtered and the solvent removed under rotatory evaporation. The crude was filtered through a pad of silica eluting with petroleum ether to get the pure 2,5-dibromothiophene as an oil (29.3 g, 90% yield). ^1H NMR (200 MHz, $CDCl_3$): $\delta = 6.84$ (s, 2H). Spectroscopic data are in agreement with those reported in the literature.[14] Concentrated sulfuric acid (96%, 25 mL), fuming sulfuric acid (20% SO_3, 25 mL), and concentrated nitric acid (65%, 8.3 mL) were combined in a three-neck flask equipped with a mechanical stirrer and a thermometer. The flask was cooled at 0 °C and 2,5-dibromothiophene (14.6 g, 60.2 mmol) was added maintaining the temperature below 20 °C. The reaction was stirred at room temperature for 3 h and then poured into a beaker containing 350 g of ice. Once the ice had melted, the precipitate was filtered and the solid residue extensively washed with water, obtaining 2,5-dibromo-3,4-dinitrothiophene **4** as a dark reddish solid (11.0 g, 55% yield). GC-MS (EI): $t = 18.3$ min; *m/z* (%): 161 (14), 302 (19) $[M-S]^+$, 330 (24) $[M^{79}Br^{79}Br]^+$, 332 (100) $[M^{79}Br^{81}Br]^+$, 333 (52) $[M^{81}Br^{81}Br]^+$.

3,4-Diaminothiophene salt [5·2H$^+$]$_x$[SnCl$_6$$^{2-}$]$_{(x-1/2y)}$[Cl$^-$]$_y$ (5): Compound **5** was prepared by modification of a previously reported procedure.[14] 2,5-dibromo-3,4-dinitrothiophene **4** (7.9 g, 24 mmol) and concentrated HCl (37%, 40 mL) were added to a flask, the mixture was cooled to 0 °C and tin metal powder (23 g, 194 mmol)

176

was added portionwise. The reaction was vigorously stirred at 0 °C for 3 h, then it was allowed to reach room temperature and stirred for an additional 6 h. The mixture was cooled down in the freezer (-20 °C) to allow the formation of a precipitate, that was filtered through a fritted funnel. The solid residue was washed with cold acetonitrile (100 mL) and cold diethyl ether (100 mL), obtaining compound **5** as a pale grey solid (4.4 g). *Note*: while the corresponding free amine of derivative **5** is prone to oxidation,[22] the diammonium salt **5** is stable and could be stored in the freezer for months. ^{1}H NMR (400 MHz, DMSO-d_6): $\delta = 7.09$ (s, 2H), 5.19 (bs, 6H). MS (ESI) *m/z*: 114.96 $[M+H]^+$. Spectroscopic data are in agreement with those reported in the literature.[14]

2,3-Diphenylthieno[3,4-*b*]pyrazine (1 a):[14] In a round bottom flask, diammonium salt **5** (500 mg, 2.67 mmol) and benzil (diphenyletha-nedione) **6 a** (590 mg, 2.80 mmol) were suspended in an EtOH:DCM, 1:1 mixture (27 mL), then triethylamine (1.50 mL, 10.7 mmol) was added and the reaction stirred at 50 °C for 5 h. Complete conversion was assessed by TLC monitoring (petroleum ether:EtOAc, 1:1). Water (40 mL) was added to the reaction and the mixture extracted with EtOAc (3x30 mL). The reunited organic phases were dried over anhydrous Na$_2$SO$_4$, the solution was filtered, and the solvent was evaporated under reduced pressure. The crude was purified by flash chromatography (gradient: from petroleum ether:EtOAc, 20:1 to 10:1) to give pure **1 a** as a yellow solid (464 mg, 60% yield over 2 steps). ^{1}H NMR (400 MHz, CDCl$_3$): $\delta = 8.07$ (s, 2H), 7.46–7.42 (m, 4H), 7.38–7.28 (m, 6H); Spectroscopic data are in agreement with those reported in the literature.[14]

Thieno[3,4-*b*]pyrazine (1 b):[14] In a round bottom flask, diammonium salt **5** (381 mg, 3.33 mmol) was dissolved in a Na$_2$CO$_3$ aqueous solution (5% w/w, 18 mL), followed by the addition of glyoxal **6 b** (358 mg, 6.17 mmol) as a 0.65 M aqueous solution, prepared by diluting 895 mg of a 40% wt glyoxal solution in water to 9.5 mL. The reaction was stirred at room temperature overnight, then poured in an extraction funnel and extracted with diethyl ether (7x30 mL). The reunited organic phases were dried over anhydrous Na$_2$SO$_4$, the solution was filtered, and the solvent was evaporated under reduced pressure to give crude **1 b** as a brownish solid (357 mg), which was judged pure enough to be used in the next synthetic step without further purification. ^{1}H NMR (200 MHz, CDCl$_3$): $\delta = 8.52$ (s, 2H), 8.05 (s, 2H). Spectroscopic data are in agreement with those reported in the literature.[14]

2,3-Dimethylthieno[3,4-*b*]pyrazine (1 c):[14] In a round bottom flask, diammonium salt **5** (500 mg, 2.67 mmol) and 2,3-butanedione **6 c** (253 mg, 2.94 mmol) were suspended in a EtOH:DCM, 2:1 mixture (40 mL), then triethylamine (1.5 mL, 10.68 mmol) was added and the reaction stirred at 50 °C for 16 h. Water (50 mL) was added to the reaction and the mixture extracted with EtOAc (3x30 mL). The reunited organic phases were dried over anhydrous Na$_2$SO$_4$, the solution was filtered, and the solvent was evaporated under reduced pressure to give crude **1 c** as a tan solid (354 mg), which was judged pure enough to be used in the next synthetic step without further purification. ^{1}H NMR (200 MHz, CDCl$_3$): $\delta = 7.79$ (s, 2H), 2.62 (s, 6H). Spectroscopic data are in agreement with those reported in the literature.[14]

N-Phenyl-4-(1,2,2-triphenylvinyl)aniline (9):[15] To a Schlenk tube under nitrogen atmosphere, Pd$_2$(dba)$_3$ (64 mg, 0.070 mmol) was added and dissolved in dry toluene (30 mL), followed by the addition of tri-*tert*-butylphosphine (20 μL, 0.080 mmol) and (2-(4-bromophenyl)ethene-1,1,2-triyl)tribenzene **7** (2.1 g, 5.0 mmol). The mixture was stirred for 10 minutes, then aniline **8** (59 μL, 6.5 mmol) and sodium *tert*-butoxide (625 mg, 6.50 mmol) were added and the reaction stirred at 120 °C for 20 h. Then the reaction was cooled down to room temperature, concentrated under reduced pressure, water (100 mL) was added and the mixture was extracted with

CHCl$_3$ (3x50 mL). The organic phases were reunited and dried over anhydrous Na$_2$SO$_4$, filtered and the solvent evaporated under reduced pressure. The crude was purified by flash chromatography (gradient: from petroleum ether 90% - DCM 10%, to petroleum ether 85% – DCM 15%) to give compound **9** as a bright yellow solid (1.8 g, 85% yield). ^{1}H NMR (400 MHz, THF-d_8): $\delta = 7.34$ (s, 1H), 7.15 (t, *J* = 7.7 Hz, 2H), 7.12-6.96 (m, 17H), 6.83 (d, *J* = 8.6 Hz, 2H), 6.79 (d, *J* = 8.8 Hz, 2H), 6.76 (t, *J* = 7.5 Hz, 1H). ^{13}C NMR (100 MHz, THF-d_8): $\delta = 145.2$, 145.0, 144.9, 144.1, 143.3, 141.8, 140.2, 135.7, 132.9, 132.1, 132.04, 132.01, 129.5, 128.2, 128.11, 128.11, 126.8, 126.7, 126.65, 120.7, 118.2, 116.2. MS (ESI) *m/z*: 424.18 $[M+H]^+$.

4-Bromo-N-phenyl-N-(4-(1,2,2-triphenylvinyl)phenyl)aniline (2): Pd(OAc)$_2$ (48 mg, 0.21 mmol) and Xantphos (184 mg, 0.318 mmol) were added to a Schlenk tube and put under inert atmosphere by performing three vacuum-nitrogen cycles. The solids were then dissolved in dry toluene (85 mL) and the solution was stirred for 5 minutes. Then 1-bromo-4-iodobenzene **10** (720 mg, 2.54 mmol), *N*-phenyl-4-(1,2,2-triphenylvinyl)aniline **9** (900 mg, 2.12 mmol) and caesium carbonate (4.82 g, 14.8 mmol) were added in the order and the reaction was stirred at 80 °C for 20 h. The reaction was allowed to cool down to room temperature, water (300 mL) was added, and the mixture extracted with CHCl$_3$ (3x150 mL). The organic phases were reunited and dried over anhydrous Na$_2$SO$_4$, filtered and the solvent evaporated under reduced pressure. The crude was purified by flash chromatography (gradient: from petroleum ether 98% – DCM 2%, to petroleum ether 90% - DCM 10%) to give compound **2** as a bright yellow solid (1.17 g, 96% yield). ^{1}H NMR (400 MHz, THF-d_8): $\delta = 7.33$ (d, *J* = 8.9 Hz, 2H), 7.23 (t, *J* = 7.8 Hz, 2H), 7.16–6.97 (m, 18H), 6.89 (dd, *J* = 8.8, 2.1 Hz, 4H), 6.76 (d, *J* = 8.6 Hz, 2H). ^{13}C NMR (100 MHz, THF-d_8): $\delta = 148.0$, 147.8, 146.4, 144.8, 144.5, 144.2, 141.7, 141.4, 139.5, 133.0, 132.7, 131.99, 131.95, 131.93, 130.0, 128.3, 128.20, 128.19, 127.1, 127.02, 126.95, 125.9, 125.2, 124.0, 123.7, 115.3. MS (ESI) *m/z*: 577.17 $[M]^+$.

General Procedure for the synthesis of TPa-c dyes: The pyrazine derivative **1** (0.05 mmol), 4-bromo-*N*-phenyl-*N*-(4-(1,2,2-triphenyl-vinyl)phenyl)aniline **2** (86.8 mg, 0.150 mmol), and potassium carbonate (20.8 mg, 0.150 mmol) were added to a Schlenk tube and put under inert atmosphere by performing three vacuum-nitrogen cycles. The solids were dissolved in dry DMF (620 μL) and a solution of Pd(OAc)$_2$ (0.56 mg, 2.50 μmol), tricyclohexylphospho-nium tetrafluoroborate (1.84 mg, 5.00 μmol) and pivalic acid (1.54 mg, 15.0 μmol) in DMF (100 μL) was added. Unless otherwise stated, the reaction was stirred at 100 °C for 20 h, then was allowed to cool down to room temperature, water (30 mL) was added, and the mixture extracted with CHCl$_3$ (3x10 mL). Reunited organic phases were dried over anhydrous Na$_2$SO$_4$, the solution filtered, and the solvent evaporated under reduced pressure. The crude was purified by flash chromatography to give the corresponding **TP** compound.

4,4′-(2,3-Diphenylthieno[3,4-*b*]pyrazine-5,7-diyl)bis(N-phenyl-N-(4-(1,2,2-triphenylvinyl)phenyl)aniline) (TPa): Prepared following the *general procedure* using 2,3-diphenylthieno[3,4-*b*]pyrazine **1 a** (14.4 mg, 50.0 μmol). The reaction was stirred at 100 °C for 30 minutes, then was allowed to cool down to room temperature and directly purified by flash chromatography (gradient: from petroleum ether 90% - DCM 10%, to petroleum ether 70%–DCM 30%) to give compound **TPa** as a dark blue solid (65.0 mg, quant.). ^{1}H NMR (400 MHz, THF-d_8): $\delta = 8.25$ (d, *J* = 8.6 Hz, 4H), 7.52 (d, *J* = 7.1 Hz, 4H), 7.35–7.22 (m, 10H), 7.18–6.98 (m, 40H), 6.92 (d, *J* = 8.4 Hz, 4H), 6.85 (d, *J* = 8.5 Hz, 4H). ^{13}C NMR (100 MHz, THF-d_8; two signals are overlapped): $\delta = 153.0$, 148.0, 147.9, 146.4, 144.8, 144.5, 144.3, 141.7, 141.5, 140.5, 139.5, 139.2, 133.0, 132.02, 131.97, 130.6, 130.5, 130.0, 129.2, 128.9, 128.6, 128.4, 128.3, 128.22, 128.21, 127.1, 127.0, 125.5, 124.1, 124.0, 123.7. HRMS (ESI): *m/z* calcd for C$_{94}$H$_{66}$N$_4$S$^+$: 1282.50027 $[M]^+$; found: 1282.49963.

177

EurJOC
European Journal of Organic Chemistry

Full Papers
doi.org/10.1002/ejoc.202100199

Chemistry
Europe
European Chemical
Societies Publishing

4,4′-(Thieno[3,4-*b*]pyrazine-5,7-diyl)bis(*N*-phenyl-*N*-(4-(1,2,2-tri-phenylvinyl)phenyl)aniline) (TPb): Prepared following the *general procedure* using thieno[3,4-*b*]pyrazine **1b** (6.8 mg, 0.050 mmol). The crude was purified by flash chromatography (gradient: from petroleum ether 80% - DCM 20%, to petroleum ether 50% - DCM 50%) to give compound **TPb** as a light purple solid (59 mg, quant. over 3 steps). ^{1}H NMR (400 MHz, THF-d_8): $\delta = 8.47$ (d, $J = 0.7$ Hz, 2H), 8.17–8.10 (m, 4H), 7.30–7.22 (m, 4H), 7.19–6.97 (m, 40H), 6.96–6.90 (m, 4H), 6.88–6.83 (m, 4H). ^{13}C NMR (100 MHz, THF-d_8; three signals are overlapped): $\delta = 147.98, 147.96, 146.4, 144.8, 144.5, 144.3, 141.7, 141.5, 140.7, 139.5, 133.0, 132.02, 131.97, 131.96, 131.3, 129.9, 129.1, 128.3, 128.22, 128.21, 128.1, 127.1, 126.9, 125.4, 124.0, 123.8$. HRMS (ESI): *m/z* calcd for $C_{82}H_{58}N_4S^+$: 1130.43767 [*M*]$^+$; found: 1130.43677.

4,4′-(2,3-Dimethylthieno[3,4-*b*]pyrazine-5,7-diyl)bis(*N*-phenyl-*N*-(4-(1,2,2-triphenylvinyl)phenyl)aniline) (TPc): Prepared following the *general procedure* using 2,3-dimethylthieno[3,4-*b*]pyrazine **1c** (8.2 mg, 0.050 mmol). Respect to the *general procedure*, during the reaction work-up increased extractions from water (30 mL) with CHCl₃ (6x10 mL) were necessary. The crude was purified by flash chromatography (gradient: from *n*-hexane 80% - DCM 20%, to *n*-hexane 50% - DCM 50%) to give compound **TPc** as a dark red solid (50.7 mg, 70% over 3 steps). ^{1}H NMR (400 MHz, THF-d_8): $\delta = 8.16$ (d, $J = 8.8$ Hz, 4H), 7.25 (t, $J = 7.9$ Hz, 4H), 7.19–6.97 (m, 40H), 6.85 (d, $J = 8.6$ Hz, 4H), 2.60 (s, 6H). ^{13}C NMR (100 MHz, THF-d_8): $\delta = 153.4, 148.1, 147.5, 146.6, 144.9, 144.5, 144.3, 141.6, 141.5, 139.7, 139.3, 133.0, 132.02, 131.98, 131.97, 129.9, 129.3, 128.82, 128.81, 128.3, 128.22, 128.20, 127.04, 127.02, 126.9, 125.4, 124.0, 123.88, 123.86, 23.5$. HRMS (ESI): *m/z* calcd for $C_{84}H_{62}N_4S^+$: 1158.46897 [*M*]$^+$; found: 1158.46826.

Computational details

Molecular and electronic properties of compounds **TPa**, **TPb**, and **TPc** have been computed via Density Functional Theory (DFT)[23,24] and Time-Dependent DFT (TDDFT)[25,26] methods, using Gaussian 16, Revision C.01 suite of programs.[27] The S_0 optimized geometries of compounds **TPa–c** have been obtained at B3LYP[28,29]/6-31G* level of theory *in vacuo*, as well as the ground-state electron density delocalization and the energy of frontier molecular orbitals (FMOs) in DCM and toluene, while the S_1 optimized geometries have been computed at TD-CAM-B3LYP[30]/6-31G* level of theory including the effects of solvent (DCM and toluene). The UV–Vis spectroscopic properties of the analyzed compounds, including absorption (λ_{max}^{abs}) and emission (λ_{max}^{emi}) maxima, vertical excitation (E_{exc}) and emission (E_{emi}) energies, oscillator strengths (f) and composition (%) in terms of molecular orbitals for the lowest singlet-singlet excitations and the singlet-singlet emissions, $S_0 \rightarrow S_1$ and $S_1 \rightarrow S_0$ respectively, in DCM and toluene, have been computed on the minimized structures at TD-CAM–B3LYP[30]/6-311+G(2d,p) level of theory. Solvent effects have been included by using the polarizable continuum model (PCM) and, in the case of the emission maxima, using the Linear-Response implementation (LR-PCM).[31]

Conflict of Interest

The authors declare no conflict of interest.

[1] a) H. Nakazumi, M. Matsuoka, *Chem. Rev.* **1992**, *92*, 1197–1226; b) G. Qian, Z. Y. Wang, *Chem. Asian J.* **2010**, *5*, 1006–1029; c) R. Wang, F. Zhang, *J. Mater. Chem. B* **2014**, *2*, 2422–2443; d) Y. Zhang, Y. Wang, J. Song, J. Qu, B. Li, W. Zhu, W.-Y. Wong, *Adv. Opt. Mater.* **2018**, *6*, 1800466; e) F. Ding, Y. Zhan, X. Lu, Y. Sun, *Chem. Sci.* **2018**, *9*, 4370–4380; f) Q. Wei, N. Fei, A. Islam, T. Lei, L. Hong, R. Peng, X. Fan, L. Chen, P. Gao, Z. Ge, *Adv. Opt. Mater.* **2018**, *6*, 1800512.

[2] a) E. Hemmer, N. Venkatachalam, H. Hyodo, A. Hattori, Y. Ebina, H. Kishimoto, K. Soga, *Nanoscale* **2013**, *5*, 11339–11361; b) Y. Zhuang, Y. Katayama, J. Ueda, S. Tanabe, *Opt. Mater.* **2014**, *36*, 1907–1912; c) A. Barbieri, E. Bandini, F. Monti, V. K. Praveen, N. Armaroli, *Top. Curr. Chem.* **2016**, *374*, 47; d) J. Li, J. Yan, D. Wen, W. U. Khan, J. Shi, M. Wu, Q. Sua, P. A. Tanner, *J. Mater. Chem. C* **2016**, *4*, 8611–8623; e) K. T. Ly, R.-W. Chen-Cheng, H.-W. Lin, Y.-J. Shiau, S.-H. Liu, P.-T. Chou, C.-S. Tsao, Y.-C. Huang, Y. Chi, *Nat. Photonics* **2017**, *11*, 63–68.

[3] a) C.-T. Chen, *Chem. Mater.* **2004**, *16*, 4389–4400; b) Z. Sun, Q. Ye, C. Chi, J. Wu, *Chem. Soc. Rev.* **2012**, *41*, 7857–7889; c) M. Y. Wong, E. Zysman-Colman, *Adv. Mater.* **2017**, *29*, 1605444; d) Y. Liu, C. Li, Z. Ren, S. Yan, M. R. Bryce, *Nat. Rev. Mater.* **2018**, *3*, 18020; e) P. Data, Y. Takeda, *Chem. Asian J.* **2019**, *14*, 1613–1636; f) A. Zampetti, A. Minotto, F. Cacialli, *Adv. Funct. Mater.* **2019**, *29*, 1807623; g) Y. Xu, P. Xu, D. Hu, Y. Ma, *Chem. Soc. Rev.* **2021**, *50*, 1030–1069; h) B. Li, M. Zhao, F. Zhang, *ACS Materials Lett.* **2020**, *2*, 905–917; i) S. Liu, Y. Li, R. T. K. Kwok, J. W. Y. Lama, B. Z. Tang, *Chem. Sci.* **2021**, DOI: 10.1039/d0sc02911d.

[4] a) K. Umezawa, Y. Nakamura, H. Makino, D. Citterio, K. Suzuki, *J. Am. Chem. Soc.* **2008**, *130*, 1550–1551; b) T. Weil, T. Vosch, J. Hofkens, K. Peneva, K. Müllen, *Angew. Chem. Int. Ed.* **2010**, *49*, 9068–9093; *Angew. Chem.* **2010**, *122*, 9252–9278; c) H. Bürckstümmer, A. Weissenstein, D. Bialas, F. Würthner, *J. Org. Chem.* **2011**, *76*, 2426–2432; d) U. Mayerhöffer, B. Fimmel, F. Würthner, *Angew. Chem. Int. Ed.* **2012**, *51*, 164–167; *Angew. Chem.* **2012**, *124*, 168–171; e) Y. Koide, Y. Urano, K. Hanaoka, W. Piao, M. Kusakabe, N. Saito, T. Terai, T. Okabe, T. Nagano, *J. Am. Chem. Soc.* **2012**, *134*, 5029–5031; f) M. Shimizu, R. Kaki, Y. Takeda, T. Hiyama, N. Nagai, H. Yamagishi, H. Furutani, *Angew. Chem. Int. Ed.* **2012**, *51*, 4095–4099; *Angew. Chem.* **2012**, *124*, 4171–4175; g) L. Yao, S. Zhang, R. Wang, W. Li, F. Shen, B. Yang, Y. Ma, *Angew. Chem. Int. Ed.* **2014**, *53*, 2119–2123; *Angew. Chem.* **2014**, *126*, 2151–2155; h) Y. Yuan, Y. Hu, Y.-X. Zhang, J.-D. Lin, Y.-K. Wang, Z.-Q. Jiang, L.-S. Liao, S.-T. Lee, *Adv. Funct. Mater.* **2017**, *27*, 1700986; i) C. Li, R. Duan, B. Liang, G. Han, S. Wang, K. Ye, Y. Liu, Y. Yi, Y. Wang, *Angew. Chem. Int. Ed.* **2017**, *56*,11525–11529; *Angew. Chem.* **2017**, *129*, 11683–11687; j) D.-H. Kim, A. D'Aléo, X.-K. Chen, A. D. S. Sandanayaka, D. Yao, L. Zhao, T. Komino, E. Zaborova, G. Canard, Y. Tsuchiya, E. Choi, J. W. Wu, F. Fages, J.-L. Brédas, J.-C Ribierre, C. Adachi, *Nat. Photonics* **2018**, *12*, 98–104; k) S. Wang, J. Liu, C. C. Goh, L. G. Ng, B. Liu, *Adv. Mater.* **2019**, *31*, 1904447; l) C. Lv, W. Liu, Q. Luo, H. Yi, H. Yu, Z. Yang, B. Zou, Y. Zhang, *Chem. Sci.* **2020**, *11*, 4007–4015.

[5] a) W. Siebrand, *J. Chem. Phys.* **1967**, *46*, 440–447; b) J. V. Caspar, E. M. Kober, B. P. Sullivan, T. J. Meyer, *J. Am. Chem. Soc.* **1982**, *104*, 630–632.

[6] a) Y. Huang, J. Xing, Q. Gong, L.-C. Chen, G. Liu, C. Yao, Z. Wang, H.-L. Zhang, Z. Chen, Q. Zhang, *Nat. Commun.* **2019**, *10*, 169; b) K. Zhang, J. Liu, Y. Zhang, J. Fan, C.-K. Wang, L. Lin, *J. Phys. Chem. C* **2019**, *123*, 24705–24713.

[7] a) J. Luo, Z. Xie, J. W. Y. Lam, L. Cheng, H. Chen, C. Qiu, H. S. Kwok, X. Zhan, Y. Liu, D. Zhuc, B. Z. Tang, *Chem. Commun.* **2001**, 1740–1741; b) J. Mei, Y. Hong, J. W. Y. Lam, A. Qin, Y. Tang, B. Z. Tang, *Adv. Mater.* **2014**, *26*, 5429–5479; c) J. Mei, N. L. C. Leung, R. T. K. Kwok, J. W. Y. Lam, B. Z. Tang, *Chem. Rev.* **2015**, *115*, 11718–11940; d) K. Kokado, K. Sada, *Angew. Chem. Int. Ed.* **2019**, *58*, 8632–8639; *Angew. Chem.* **2019**, *131*, 8724–8731; e) S. Suzuki, S. Sasaki, A. S. Sairi, R. Iwai, B. Z. Tang, G. Konishi, *Angew. Chem. Int. Ed.* **2020**, *59*, 9856–9867; *Angew. Chem.* **2020**, *132*, 9940–9951.

[8] a) Q. Zhao, J. Z. Sun, *J. Mater. Chem. C* **2016**, *4*, 10588–10609; b) W. Xu, D. Wang, B. Z. Tang, *Angew. Chem. Int. Ed.* **2020**, DOI:10.1002/anie.202005899.

[9] a) C. Papucci, T. A. Geervliet, D. Franchi, O. Bettucci, A. Mordini, G. Reginato, F. Picchioni, A. Pucci, M. Calamante, L. Zani, *Eur. J. Org. Chem.* **2018**, 2657–2666; b) A. Dessì, M. Bartolini, M. Calamante, L. Zani, A. Mordini, G. Reginato, *Synthesis* **2018**, *50*, 1284–1292; c) C. Papucci, A. Dessì, C. Coppola, A. Sinicropi, G. Santi, M. Di Donato, M. Taddei, P. Foggi, L. Zani, G. Reginato, A. Pucci, M. Calamante, A. Mordini, *Dyes Pigm.* **2021**, *188*, 109207.

[10] a) S. C. Rasmussen, R. L. Schwiderski, M. E. Mulholland, *Chem. Commun.* **2011**, *47*, 11394–11410; b) R. L. Schwiderski, S. C. Rasmussen, *J. Org. Chem.* **2013**, *78*, 5453–5462; c) X. Lu, S. Fan, J. Wu, X. Jia, Z.-S. Wang, G. Zhou, *J. Org. Chem.* **2014**, *79*, 6480–6489; d) L. E. McNamara, N. Liyanage, A. Peddapuram, J. S. Murphy, J. H. Delcamp, N. I. Hammer, *J. Org. Chem.* **2016**, *81*, 32–42.

[11] J. Qi, X. Duan, Y. Cai, S. Jia, C. Chen, Z. Zhao, Y. Li, H.-Q. Peng, R. T. K. Kwok, J. W. Y. Lam, D Ding, B. Z. Tang, *Chem. Sci.* **2020**, *11*, 8438–8447.

[12] a) W. Qin, K. Li, G. Feng, M. Li, Z. Yang, B. Liu, B. Z. Tang, *Adv. Funct. Mater.* **2014**, *24*, 635–643; b) Z. Sheng, B. Guo, D. Hu, S. Xu, W. Wu, W. H. Liew, K. Yao, J. Jiang, C. Liu, H. Zheng, B. Liu, *Adv. Mater.* **2018**, *30*, 1800766.

[13] a) N. P. Liyanage, A. Yella, M. Nazeeruddin, M. Grätzel, J. H. Delcamp, *ACS Appl. Mater. Interfaces* **2016**, *8*, 5376–5384; b) N. P. Liyanage, H. Cheema, A. R. Baumann, A. R. Zylstra, J. H. Delcamp, *ChemSusChem* **2017**, *10*, 2635–2641; Selected reviews on C–H activation:; c) X. Chen, K. M. Engle, D.-H. Wang, J.-Q. Yu, *Angew. Chem. Int. Ed.* **2009**, *48*, 5094–5115; *Angew. Chem.* **2009**, *121*, 5196–5217; d) J. Wencel-Delord, F. Glorius, *Nat. Chem.* **2013**, *5*, 369–375.

[14] D. D. Kenning, K. A. Mitchell, T. R. Calhoun, M. R. Funfar, D. J. Sattler, S. C. Rasmussen, *J. Org. Chem.* **2002**, *67*, 9073–9076.

[15] K. Li, W. Qin, D. Ding, N. Tomczak, J. Geng, R. Liu, J. Liu, X. Zhang, H. Liu, B. Liu, B. Z. Tang, *Sci. Rep.* **2013**, *3*, 1150.

[16] T. Jiang, Y. Qu, B. Li, Y. Gao, J. Hua, *RSC Adv.* **2015**, *5*, 1500–1506.

[17] a) S. I. Gorelsky, D. Lapointe, K. Fagnou, *J. Am. Chem. Soc.* **2008**, *130*, 10848–10849; b) B. Liégault, D. Lapointe, L. Caron, A. Vlassova, K. Fagnou, *J. Org. Chem.* **2009**, *74*, 1826–1834.

[18] C. Reichardt, *Chem. Rev.* **1994**, *94*, 2319–2358.

[19] a) A. Qin, L. Tang, J. W. Y. Lam, C. K. W. Jim, Y. Yu, H. Zhao, J. Sun, B. Z. Tang, *Adv. Funct. Mater.* **2009**,*19*,1891–1900; b) M. P. Aldred, C. Li, M.-Q.

[20] W. C. Still, M. Kahn, A. Mitra, *J. Org. Chem.* **1978**, *43*, 2923–2925.

Zhu, *Chem. Eur. J.* **2012**, *18*, 16037–16045; c) S. Sasaki, Y. Niko, K. Igawa, G. Konishi, *RSC Adv.* **2014**, *4*, 33474–33477.

[21] The procedure for the bromination reaction to give 2,5-dibromothiophene was adapted from: a) R. M. Kellogg, A. P. Schaap, E. T. Harper, H. Wynberg, *J. Org. Chem.* **1968**, *33*, 29022909; the procedure for the nitration reaction to give **4** was adapted from: b) L. Wen, S. C. Rasmussen, *J. Chem. Crystallogr.* **2007**, *37*, 387–398.

[22] N. I. Abdo, A. A. El-Shehawy, A. A. El-Barbary, J.-S. Lee, *Eur. J. Org. Chem.* **2012**, 5540–5551.

[23] P. Hohenberg, W. Kohn, *Phys. Rev.* **1964**, *136*, B864-B871.

[24] W. Kohn, L. J. Sham, *Phys. Rev.* **1965**, *140*, A1134-A1138.

[25] C. Adamo, D. Jacquemin, *Chem. Soc. Rev.* **2013**, *42*, 845–856.

[26] A. D. Laurent, C. Adamo, D. Jacquemin, *Phys. Chem. Chem. Phys.* **2014**, *16*, 14334–14356.

[27] Gaussian 16, Revision C.01, M. J. Frisch, G. W. Trucks, H. B. Schlegel, G. E. Scuseria, M. A. Robb, J. R. Cheeseman, G. Scalmani, V. Barone, G. A. Petersson, H. Nakatsuji, X. Li, M. Caricato, A. V. Marenich, J. Bloino, B. G. Janesko, R. Gomperts, B. Mennucci, H. P. Hratchian, J. V. Ortiz, A. F. Izmaylov, J. L. Sonnenberg, D. Williams-Young, F. Ding, F. Lipparini, F. Egidi, J. Goings, B. Peng, A. Petrone, T. Henderson, D. Ranasinghe, V. G. Zakrzewski, J. Gao, N. Rega, G. Zheng, W. Liang, M. Hada, M. Ehara, K. Toyota, R. Fukuda, J. Hasegawa, M. Ishida, T. Nakajima, Y. Honda, O. Kitao, H. Nakai, T. Vreven, K. Throssell, J. A. Montgomery, Jr., J. E. Peralta, F. Ogliaro, M. J. Bearpark, J. J. Heyd, E. N. Brothers, K. N. Kudin, V. N. Staroverov, T. A. Keith, R. Kobayashi, J. Normand, K. Raghavachari, A. P. Rendell, J. C. Burant, S. S. Iyengar, J. Tomasi, M. Cossi, J. M. Millam, M. Klene, C. Adamo, R. Cammi, J. W. Ochterski, R. L. Martin, K. Morokuma, O. Farkas, J. B. Foresman, and D. J. Fox, Gaussian, Inc., Wallingford CT, **2016**.

[28] A. D. Becke, *J. Chem. Phys.* **1993**, *98*, 5648–5652.

[29] C. Lee, W. Yang, R. G. Parr, *Phys. Rev. B.* **1988**, *37*, 785–789.

[30] T. Yanai, D. P. Tew, N. C. Handy, *Chem. Phys. Lett.* **2004**, *393*, 51–57.

[31] J. Tomasi, B. Mennucci, R. Cammi, *Chem. Rev.* **2005**, *105*, 2999–3094.

179

Chapter 5. Conclusions

The research carried out in the present PhD thesis focused onto the design of novel organic compounds for solar energy conversion devices: perovskite solar cells (PSCs), dye-sensitized solar cells (DSSCs) and luminescent solar concentrators (LSCs). These technologies are included in the so-called "emerging photovoltaics", and they represent innovative alternatives to silicon-based solar cells, which are still the most efficient commercially available technology.

Efficiency and stability issues related to these device's components should be overcome to let PSCs, DSSCs and LSCs really competitive to Si-based solar cells on the photovoltaic market. In this regard, the design of novel materials and a deep understanding of their working principles play a key role for the optimization of the performances of these devices.

Large-scale PSCs commercialization is still hindered by some instability issue that can be mainly ascribed to the hole transport materials intrinsic properties and to their inefficient contact with the perovskite layer. In this regard, in this thesis, a novel family of phenothiazine and triphenylamine-based molecules (**HTM1-4**) to be employed as potential hole transport materials (HTMs) candidates in PSCs has been designed. A deep DFT and TDDFT investigation of their structural and electronic properties, as well as the investigation of interfacial phenomena occurring between the MAPI perovskite and **HTM1** have been carried out. The results of these studies showed that **HTM1-4** fulfill all the requirements to be considered suitable HTMs candidates for PSCs and provide new insights into the hole transport process that should be taken into account for the construction of potentially more efficient PSCs.

DSSCs commercialization is still limited due to their poor efficiency in comparison to Si-based solar cells, which is partially due to the intrinsic properties of the sensitizers and to their inappropriate energy levels matching with the other DSCCs components. For this reason, in this thesis, the design of a novel indigo-based D-A-π-A dye (**DF90**) to be employed has a sensitizer in DSSCs has been carried out. From the investigation of its electronic and spectroscopic properties, it emerged that **DF90** can be considered as a valid candidate in DSSCs. Moreover, to extend the possibility to use the indigo scaffold for the design of novel dyes, a new family of D-A-D indigo-based dyes has been presented as well. Additionally, a fully *in silico* study concerning the prediction of ground state oxidation potentials of 16 D-π-A and D-A-π-A dyes, having medium to large size of the

conjugated scaffold, has been reported. The results of this study demonstrated that the applied strategy consents to accurately predict the dye regeneration driving force, hence it can be very useful for the identification of the most promising dyes to be used in DSSCs. Additionally, the design of a novel series of catechol-based molecules, **Cat-I-XV**, has been reported for their potential application as sensitizers in type-II DSSCs. The effect of the substituents and the effect of enhanced conjugation by inserting a π spacer have been deeply investigated in relation to the *one-step* (type-II) mechanism and the dye-to-TiO$_2$ charge transfer (DTCT) features, to provide additional knowledge for the design of more efficient dyes for such application.

To boost LSCs commercialization, a key point to address is the optimization of the fluorophores which are responsible for self-absorption and aggregation-caused quenching (ACQ) phenomena. For such reasons, in this thesis three novel series of D-A-D fluorophores (**BBT2-4, DQ1-5 and TPa-c**) have been presented and a deep investigation of their structural, electronic and photophysical properties has been carried out. The results of these studies demonstrated that **BBT2-4, DQ1-5 and TPa-c** can be considered as promising fluorophores in LSCs devices for their good light-harvesting ability and intense emission properties, associated also to large Stokes Shift values. Hence, they are responsible for limited self-absorption phenomena. Additionally, **TPa-c** molecules also possess good aggregation-induced emission (AIE) properties, which is a fundamental feature to allow their application in solid state luminescent devices.

In conclusion, the results presented in this thesis' research work provide new insights in the applications of organic materials for solar energy conversion devices that could hopefully contribute to the development of more efficient materials for PSCs, DSSCs and LSCs, and make these technologies more competitive to Si-based solar cells in the PV market.

Appendix A. Photovoltaic parameters of solar cells

All the photovoltaic devices exploit the photovoltaic effect to directly convert sunlight into electricity, thus they are characterized by the same electrical parameters, regardless of the light-harvesting material. The main parameters defining the performances of solar cells, apart from the power conversion efficiency η, are the short-circuit current I_{sc}, the peak of maximum power P_{mp}, the open-circuit voltage V_{oc} and the fill factor *FF*, which are generally represented in the Current-Voltage Curves (I-V) that define the relationship between the flow of the current through the external circuit and the applied voltage (Figure A1). They are briefly presented here [1-3].
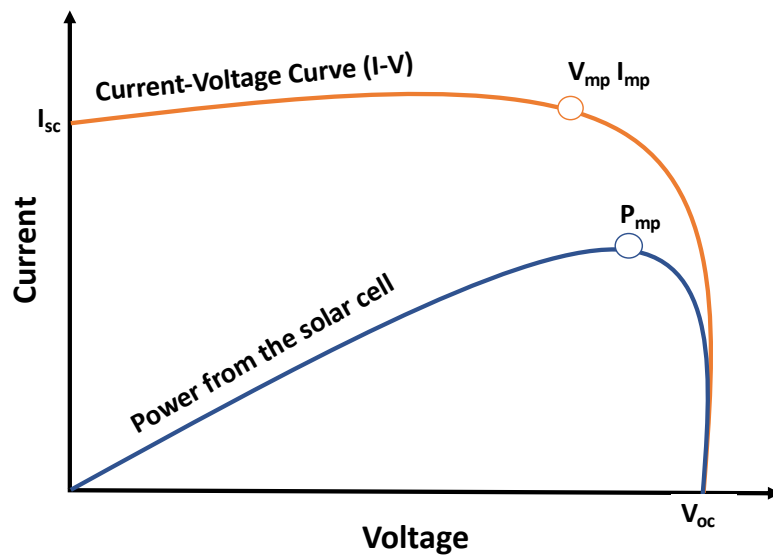

Figure A1. Schematic representation of the Current-Voltage Curve (I-V) and of the main photovoltaic parameters.

Short-circuit current I_{sc}

It represents the current that flows in the external circuit and it mainly depends on: i) the flux of the incident photons, ii) the spectrum of the incident light, which is often standardized to AM1.5 spectrum, iii) the area (A) of the solar cell. To remove this last dependence, it is often used the short-circuit current density J_{sc}, which is the maximum current delivered by a solar cell without the presence of a load (Eq. A1).

$$J_{SC} = \frac{I_{SC}}{A} \quad \text{(Eq. A1)}$$

Peak of maximum power P$_{mp}$

It represents the maximum electrical power that a solar cell in its standard conditions can deliver and it is defined as follows (Eq. A2):

$$P_{mp} = I_{mp} * V_{mp} \quad \text{(Eq. A2)}$$

where I_{mp} is the current at maximum power and V_{mp} is the voltage at maximum power.

Open-circuit voltage V$_{oc}$

It represents the voltage when the current does not flow through the external circuit, and it is the maximum voltage that a solar cell can deliver. Considering the net current set to zero, the V$_{oc}$ can be defined as follows (Eq. A3):

$$V_{oc} = \frac{k_B T}{q} \ln \left(\frac{J_{ph}}{J_0} + 1 \right) \quad \text{(Eq. A3)}$$

where k_B is the Boltzmann constant, T is the operating temperature of the cell, q is the fundamental charge, J_{ph} is the photo-generated current density and J_0 is the saturation current density. J_{ph} has generally small variations, while J_0 can vary by orders of magnitude and it depends on the recombination in the solar cell. Therefore, V$_{oc}$ can be defined as a measure of the amount of recombination in the device.

Fill Factor FF

It represents the performance of the cells in comparison with that of an ideal diode and it is expressed by the ratio between the product of the V_{oc} with the I$_{sc}$ and the maximum power generated by a solar cell (Eq. A4).

$$FF = \frac{I_{sc} V_{oc}}{I_{mp} V_{mp}} \quad \text{(Eq. A4)}$$

Increasing the illumination on the cell, the short-circuit current will increase without affecting the open-circuit voltage, while increasing the temperature, the open-circuit voltage will decrease and the short-circuit current will slightly increase.

Power conversion efficiency η

It is the most common parameter used to compare the performances among solar cells and it is defined as the ratio between the maximum generated power (P_{max}) and the incident power (I_{in}), as reported in Eq. A5.

$$\eta = \frac{P_{max}}{I_{in}} = \frac{J_{mp}V_{mp}}{I_{in}} = \frac{J_{sc}V_{oc}FF}{I_{in}} \quad \text{(Eq. A5)}$$

It is clearly dependent on the solar spectrum, on the operating temperature of the solar cell and on the intensity of the incident light. For this reason, the η of different solar cells can be compared only if the measurement conditions are the same.

References

[1] A.E Brooks, Solar Energy: Photovoltaics, Future Energy, Ed Trevor Letcher. New York: Elsevier 2nd Ed., 383-404 (2014).

[2] A. Reinders, P. Verlinden, W. Sark, A. Freundlich, Photovoltaic Solar Energy from Fundamentals to Applications, Wiley & Sons, (2017).

[3] T. Dittrich, Materials Concepts for Solar Cells, World Scientific 2nd Ed., 3-43 (2018).

Appendix B. Additional Manuscripts

L. A. Castriotta, R. Infantino, L. Vesce, M. Stefanelli, A. Dessì, C. Coppola, M. Calamante, G. Reginato, A. Mordini, A. Sinicropi, A. Di Carlo, and L. Zani, Methylammonium-Free Wide Band-Gap p-i-n Perovskite Solar Cells and Mini-Modules with Phenothiazine Dimers as Dopant-Free Hole Transporting Materials, submitted manuscript, 2022.

M. Paolino, A. Reale V. Razzano, G. Giorgi, G. Giuliani, F. Villafiorita-Monteleone, C. Botta, C. Coppola, A. Sinicropi, and A. Cappelli, Design, synthesis, structure, and photophysical features of highly emissive cinnamic derivatives, New J. Chem. 44, 13644-13653 (2020). https://doi.org/10.1039/D0NJ02429E